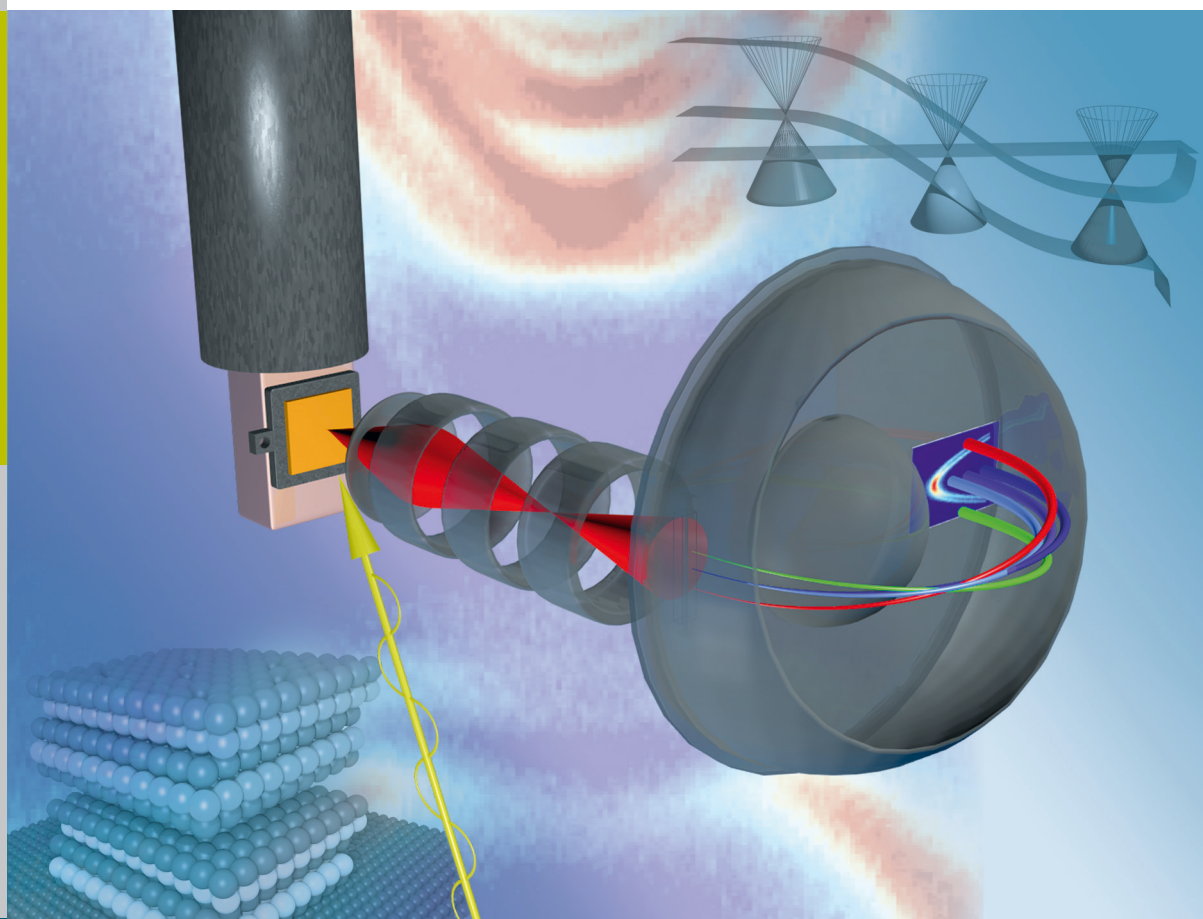


Band Structure Engineering in 3D Topological Insulators Investigated by Angle-Resolved Photoemission Spectroscopy

Markus Eschbach



Forschungszentrum Jülich GmbH
Peter Grünberg Institute (PGI)
Electronic Properties (PGI-6)

Band Structure Engineering in 3D Topological Insulators Investigated by Angle-Resolved Photoemission Spectroscopy

Markus Eschbach

Schriften des Forschungszentrums Jülich
Reihe Schlüsseltechnologien / Key Technologies

Band / Volume 126

ISSN 1866-1807

ISBN 978-3-95806-149-1

Bibliographic information published by the Deutsche Nationalbibliothek.
The Deutsche Nationalbibliothek lists this publication in the Deutsche
Nationalbibliografie; detailed bibliographic data are available in the
Internet at <http://dnb.d-nb.de>.

Publisher and
Distributor: Forschungszentrum Jülich GmbH
Zentralbibliothek
52425 Jülich
Tel: +49 2461 61-5368
Fax: +49 2461 61-6103
Email: zb-publikation@fz-juelich.de
www.fz-juelich.de/zb

Cover Design: Grafische Medien, Forschungszentrum Jülich GmbH

Printer: Grafische Medien, Forschungszentrum Jülich GmbH

Copyright: Forschungszentrum Jülich 2016

Schriften des Forschungszentrums Jülich
Reihe Schlüsseltechnologien / Key Technologies, Band / Volume 126

D 464 (Diss., Duisburg, Univ., 2016)

ISSN 1866-1807
ISBN 978-3-95806-149-1

The complete volume is freely available on the Internet on the Jülicher Open Access Server (JuSER)
at www.fz-juelich.de/zb/openaccess.



This is an Open Access publication distributed under the terms of the [Creative Commons Attribution License 4.0](https://creativecommons.org/licenses/by/4.0/),
which permits unrestricted use, distribution, and reproduction in any medium, provided the original work is properly cited.

Zusammenfassung

Drei-dimensionale topologische Isolatoren (3D TIs) stellen einen neuen Zustand der Quanten-Materie dar und eröffnen aufgrund ihrer einzigartigen elektronischen Eigenschaften faszinierende Möglichkeiten für moderne spintronische Anwendungen: sie besitzen gleichzeitig vorliegende isolierende Eigenschaften im Volumen sowie leitfähige, spinpolarisierte elektronische Zustände auf der Oberfläche. Im Gegensatz zu herkömmlichen (topologisch trivialen) Oberflächenzuständen werden diese (topologisch nicht-trivialen) Zustände durch Zeitumkehr-Symmetrie sowie eine neuartige Volumeneigenschaft, genannt Topologie, hervorgerufen und geschützt. Für die Nutzbarkeit dieser TI Materialien in spintronischen Anwendungen müssen jedoch Wege gefunden werden, ihre elektronische Bandstruktur zu manipulieren und einzustellen, da die meisten 3D TI Materialien sich leider durch eine ebenfalls signifikante Volumenleitfähigkeit an den Oberflächen auszeichnen.

In dieser Arbeit werden verschiedene Methoden vorgestellt, um die Fermi-Energie und damit die elektronischen Eigenschaften von 3D TI Dünnschichtfilmen (u.a. Bi_2Se_3 , Bi_2Te_3 und Sb_2Te_3), die mittels Molekularstrahlepitaxie gewachsen wurden, einzustellen und maßzuschneidern. Die elektronische Struktur ihrer Oberflächen wird mittels der Methode der winkelaufgelösten Photoemissionsspektroskopie untersucht.

Neben den konventionellen Methoden des Dotierens der Oberfläche oder des Volumens, wird zum ersten Mal die erfolgreiche Realisierung eines vertikalen topologischen p-n Überganges in epitaktisch gewachsenen $\text{Sb}_2\text{Te}_3/\text{Bi}_2\text{Te}_3/\text{Si}(111)$ Heterostrukturen demonstriert. Neben der Überprüfung der Kristallqualität der Doppellagen und der Beschaffenheit der Grenzfläche, wird gezeigt, dass es möglich ist die Oberfläche von Sb_2Te_3 von p -dotiert nach n -dotiert zu verändern. Dies geschieht durch den variierenden Einfluss der unteren Bi_2Te_3 Schicht, oder gleichbedeutend des internen elektrostatischen Potentials, welches durch die entstehende Raumladungszone hervorgerufen wird. Die experimentellen Ergebnisse werden durch Simulationen unterstützt, die durch das selbstkonsistente Lösen der Schrödinger- sowie der Poissonsgleichung das Banddiagramm der Heterostruktur nachbilden.

Des Weiteren wird eine umfassende Untersuchung der Kristallstruktur sowie der reichhaltigen elektronischen (Spin-) Struktur des natürlich vorkommenden Übergitter-Phase $\text{Bi}_1\text{Te}_1 = (\text{Bi}_2)_1(\text{Bi}_2\text{Te}_3)_2$ präsentiert. Die Dichtefunktionaltheorie zeigt, dass Bi_1Te_1 , im Gegensatz zu dem eng verwandten Prototypen eines 3D TI Bi_2Te_3 , ein sogenannter schwacher topologischer Isolator mit $\nu_0; (\nu_1\nu_2\nu_3) = 0; (001)$ ist. Demzufolge wird erwartet, dass alle Oberflächen, die senkrecht zur Stapelrichtung, d.h. parallel zu den natürlichen Spaltrichtungen sind, frei von topologischen Oberflächenzuständen sind. In der Tat wird gezeigt werden, dass eine solche Oberfläche lediglich Zustände besitzt, die leicht mit topologischen Dirac-Kegeln verwechselt werden können, jedoch keinerlei nachweisbare helikale Spinpolarisierung besitzen. Letzteres bestätigt die schwache topologische Natur von Bi_1Te_1 .

Abstract

Three-dimensional topological insulators (3D TIs) are a new state of quantum matter and open up fascinating opportunities for novel spintronic devices due to their unique electronic properties: the simultaneous presence of an insulating energy gap in the bulk and conductive, spin-polarized electronic states at their surface. Unlike the metallic surface states of ordinary (topologically trivial) materials, these (topologically non-trivial) surface states are induced and protected by time reversal symmetry and by a new bulk property, called topology. However, for the usability of TI materials in spintronic devices one needs to find means to engineer their electronic band structure such that the Fermi level falls into the band gap, since most of the 3D TI materials suffer from significant bulk conductivity also at their surfaces.

In this thesis different approaches are presented to manipulate the Fermi level and thereby engineer the electronic properties of thin films of typical 3D TI materials, such as Bi_2Se_3 , Bi_2Te_3 , and Sb_2Te_3 , which were grown by molecular beam epitaxy. Their surface electronic structure is investigated using angle-resolved photoelectron spectroscopy.

Besides conventional approaches like surface or bulk doping, the successful realization of a vertical topological p-n junction in epitaxial $\text{Sb}_2\text{Te}_3/\text{Bi}_2\text{Te}_3/\text{Si}(111)$ heterostructures is demonstrated for the first time. Besides the verification of the crystalline quality of the bilayers and integrity of the interface, it is shown that it is possible to drive the surface of Sb_2Te_3 from being *p*-type into *n*-type by varying the influence from the lower Bi_2Te_3 layer, i.e. the built-in electrostatic potential caused by the depletion layer. The experimental findings are supported by solving the Schrödinger and Poisson equations self-consistently and thus simulating the band diagram throughout the heterostructure.

Further, a thorough investigation of the crystal structure as well as the rich electronic (spin-) structure of the natural superlattice phase $\text{Bi}_1\text{Te}_1 = (\text{Bi}_2)_1(\text{Bi}_2\text{Te}_3)_2$ is presented. It is shown by density functional theory that Bi_1Te_1 , contrary to the closely related, prototypical strong 3D TI Bi_2Te_3 , is a weak topological insulator with $\nu_0; (\nu_1\nu_2\nu_3) = 0; (001)$. According to this, surfaces, which are perpendicular to the stacking direction, i.e. parallel to the natural cleavage planes, are expected to be free of topological surface states. Indeed, such surface is shown to exhibit surface states which in fact can easily be confused with topological Dirac cones but do not possess a measurable helical spin polarization which thus confirms the weak topological nature of Bi_1Te_1 .

Contents

1	Introduction	1
2	Theoretical Background	7
2.1	Spin-Orbit Coupling	8
2.2	Rashba-Effect	10
2.3	An Introduction into Topological Insulators	12
2.3.1	Topological Band Theory	12
2.3.2	Experimental Realization of Topological Insulators	23
2.3.3	Defect Chemistry	30
2.4	Photoemission Theory	32
2.4.1	The Photoemission Process	32
2.4.2	Single-Particle Spectral Function $A(\mathbf{k}, E)$ and Electron Self-Energy $\Sigma(\mathbf{k}, E)$	40
2.4.3	Spin-Resolved Photoemission	43
2.5	Surface Electronic Structure	44
2.6	Density Functional Theory	46
3	Experimental Setup	49
3.1	The High-Resolution ARPES apparatus at PGI-6	49
3.2	Spin-Resolved Photoelectron Spectroscopy	65
4	Prototypical Binary 3D Topological Insulators	67
4.1	Cleaning of MBE-Grown 3D TI Thin Films	67
4.2	Comparison of the Binary Compounds Bi_2Se_3 , Bi_2Te_3 , and Sb_2Te_3	69
4.2.1	Cleaved Single Crystals Compared to MBE-Grown Thin Films	69
4.2.2	Comparison of the Surface Electronic Structure	72
5	Band Structure Engineering by Doping	79
5.1	Unintentional Surface Doping or the 'Aging' Effect in Bi_2Se_3	79
5.1.1	Sample Design and Preparation	80
5.1.2	Pristine and Aged Bi_2Se_3	80
5.1.3	Evolution of the Surface Electronic Structure	83
5.1.4	Conclusion	85
5.2	Active Surface Doping of 3D TIs with Sub-ML Impurities	87
5.2.1	Sample Preparation and <i>in situ</i> Deposition	87

5.2.2	Electron Doping of the p -type TI Sb_2Te_3 with Magnetic Fe	88
5.2.3	Hole Doping of the n -type TI Bi_2Te_3 with Non-Magnetic MgO	89
5.2.4	Conclusion	91
5.3	Bulk Doping in Ternary Topological Insulators $(\text{Bi}_{1-x}\text{Sb}_x)_2\text{Te}_3$	92
6	Realization of a Topological p-n Junction in $\text{Sb}_2\text{Te}_3/\text{Bi}_2\text{Te}_3$ Heterostructures	95
6.1	Sample Design and Preparation	96
6.2	Experimental Characterization	97
6.2.1	Structural Analysis by HR-STEM	97
6.2.2	Depth Profiling by AES	98
6.2.3	Transport Properties	100
6.3	Engineering of the Surface States by the Built-In Electric Field	101
6.3.1	1D Schrödinger-Poisson Model	104
6.4	Discussion and Outlook	106
6.4.1	Topological Exciton Condensate	107
7	Natural Superlattice and Weak Topological Insulator Bi_1Te_1	109
7.1	Crystal Structure of the Natural Superlattice Series $[\text{Bi}_2]_x[\text{Bi}_2\text{Te}_3]_y$	110
7.2	Topological Invariants Revealed by DFT	111
7.2.1	Bulk Band Structure and Topology	112
7.2.2	Surface Band Structure and Termination	114
7.3	Experimental Characterization	115
7.3.1	Stoichiometry by RBS	115
7.3.2	Bulk Crystal Structure by XRD	116
7.3.3	Unit Cell by STEM	116
7.3.4	Surface Chemistry by XPS and the Influence of Sputtering	118
7.4	Surface Electronic Structure of Bi_1Te_1 vs. Bi_2Te_3	119
7.4.1	Off-Normal Emission and the Appearance of New Dirac Cones?	122
7.4.2	The Influence of Sputtering on the Surface Electronic Structure	123
7.4.3	Spin-Resolved ARPES	124
7.5	Conclusion and Outlook	125
8	Summary and Outlook	127
	Appendix	129
	Bibliography	133
	Publications	149
	Curriculum Vitae	151
	Acknowledgements	152

CHAPTER 1

Introduction

In elementary school one is taught that there are three states of matter: solid, liquid and gas. In rare cases the plasma phase is added. However, this fundamental classification is only valid for simple everyday life observations. As our knowledge of condensed matter physics and emergent phenomena keeps on growing, we learn that there is a countless number of material properties and ways how the atoms are organized, which we call states or phases of matter (solid, liquid, gas, plasma, superfluids, liquid crystals, spin-glasses, Bose-Einstein condensates, etc.). And the discovery of novel and fascinating new phases of matter has not stopped until now.

For a long time it was possible, for example, to categorize materials based on their ability to conduct electrical current either into the metallic, semiconducting, or insulating phases. In the last decades, however, a new class or state of matter that does not fit into this classification scheme, has been found and attracted tremendous attention among both theoretical as well as experimental scientists. Materials belonging to this class are called *topological insulators* (TIs)¹ [1–8]. Their unique electronic property is that they intrinsically behave as insulators in their interior (bulk), i.e. they possess an electronic band gap, while at the same time they exhibit gapless, highly conducting boundary states at their exterior (surfaces in 2D or edges in 1D). Moreover, the bulk band gap is different to the gap of a conventional insulator, because it is partially inverted due to strong spin-orbit coupling (SOC), being a prerequisite for the existence of this new state. An electronic bulk ‘band gap inversion’ means that at certain points in the band structure the characters of the lowest unoccupied and highest occupied electronic levels are intermixed, but the band gap remains finite. In order to differentiate between the electrically distinct topological insulator and conventional insulator state, a novel *topological band theory* has been developed, which classifies the materials in an analogy to the mathematical concept of topology and successfully deduces the existence of conducting boundary states [1, 9–11]. At first glance the concept of topology in the electronic band structure of materials seems rather abstract. But in principle it just introduces (topological) invariants distinguishing materials based on the existence

¹ The concept can be applied both in two and three dimensions; the materials are then called 2D or 3D TIs, respectively. In this thesis 3D TIs are investigated, which is why ‘TI’ corresponds to ‘3D TI’ if not stated differently.

or absence of a bulk electronic band gap². Moreover, in analogy to the mathematical Möbius strip, it tells that an inverted band gap cannot be transformed into a standard one without closing the gap, which additionally differentiates between topologically non-trivial (TIs) and trivial (conventional) insulators. Therefore, topological band theory allows a full classification of materials according to their ability to conduct electric current including the newly found TI states.

Interestingly, the topological insulator phase is invariant under time-reversal symmetry and electrons occupying the interesting metallic boundary states are highly spin-polarized with their wave functions further confined to certain momenta, effectively providing the material a helical spin texture [12–14]. This means that spin up and spin down electrons can only occupy states with opposite momentum (propagate into opposite directions), which immediately promises a way to produce efficient spin currents. Further, a spin up electron propagating to the right can also not scatter into a left-moving spin down channel, meaning that backscattering is prohibited and spin currents without (or little) dissipation loss are conceivable. These fascinating properties make topological insulators an interesting field of research for novel spin electronics (spintronics) and future devices.

The great enthusiasm after the theoretical introduction of the topological band theory and short-after experimental realization of the first 3D TIs [12, 15–17], was followed by what can be seen as a mild frustration among experimentalists. TIs provide a huge playground for theoretical physicists for the investigation of novel and exotic fundamental phenomena. Likewise, also spectroscopists have very successfully studied the TIs electronic properties and the (2D) *topologically protected surface states* (TSS). However, the results from scientists studying transport properties are rather frustrating. Unfortunately, the band gaps of typical TI materials are considerably small ($\sim 100 - 200$ meV) and, moreover, the intrinsic defect densities and related bulk carrier concentrations are very high, and the desired surface electrical transport is usually strongly obscured by trivial bulk transport. In reality this means that very few of the 3D TI materials studied so far are actually intrinsic insulators. Typically they are comparatively low-resistive and suffer from significant (3D) bulk charge carriers that pushes the Fermi level into the conduction or valence band, effectively making them ‘bad metals’ [18, 19].

Therefore, the second stage of TI research is dedicated to find routes to *engineer the electronic band structure* of TI materials and to controllably tune the position of the Fermi level in order to exploit the interesting properties of the TSS for electrical transport. Many different approaches, such as external electrostatic gating [20] or composition bulk doping, have been pursued in the recent years to suppress the bulk carriers and to tune the surface states. Bulk doping can be realized by alloying the TI materials in ternary [21–23] or quarternary alloys [24, 25]. In this thesis, another novel approach will be presented, where an influence on the electronic structure by the combination of *p*- and *n*-type TIs in a heterostructure resulting in the creation of a topological p-n junction, is demonstrated.

Most of the research on topological insulators in literature has been performed on epitaxially grown bulk single crystals. These crystals typically exhibit highest possible

² Or any smooth transformations of the band structure that do not open or close the band gap.

quality and are well-suited for the fundamental study of the basic properties of a material. However, for possible device application and in order to apply more advanced band structure engineering approaches, like the creation of heterostructures, different synthesis techniques have to be employed. This is why this thesis mainly focuses on results that were obtained on high-quality thin films of 3D TIs created by means of *molecular beam epitaxy* (MBE) grown on Si(111) or InP(111) substrates. MBE is nowadays one of the best methods for deposition of thin epitaxial films and is widely used in high-quality semiconductor device manufacturing. It allows epitaxial growth with high control of purity, doping concentrations and film thickness and, moreover, the creation of heterostructures or superlattices.

In this thesis, different approaches to manipulate and engineer the electronic band structure of 3D topological insulator thin films are studied by means of *angle-resolved photoelectron spectroscopy* (ARPES), which is one of the most powerful tools for the investigation of new phases and physical phenomena in condensed matter physics. In analogy to the historic development in semiconductor physics, this thesis applies this knowledge to 3D topological insulators and summarizes the different approaches to manipulate the electronic structure. Figure 1.1 summarizes these approaches graphically.

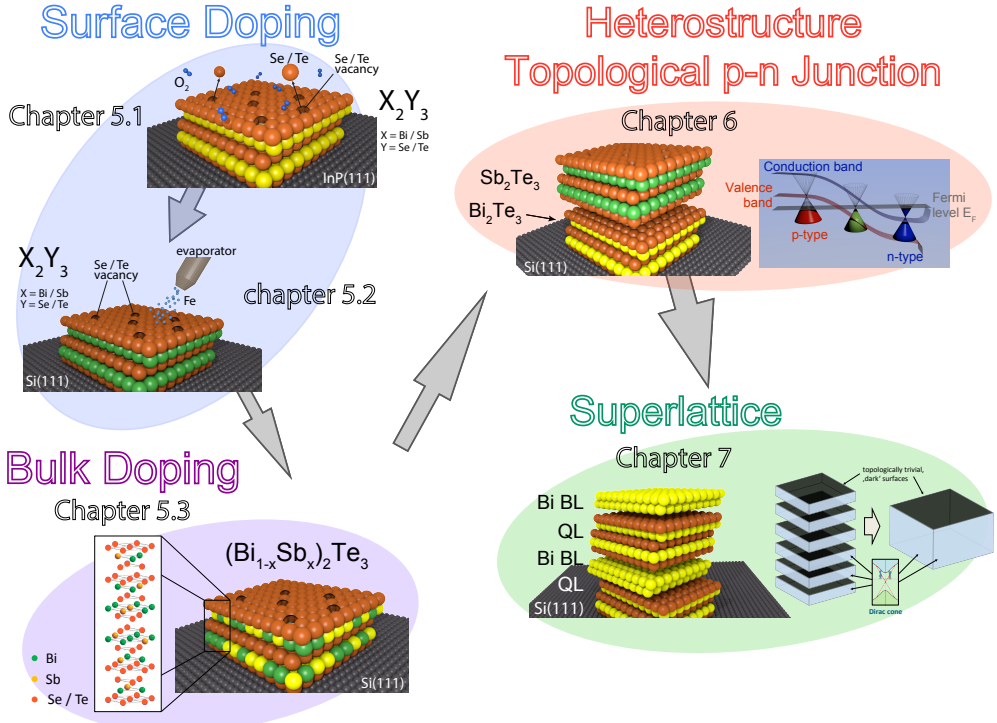


Figure 1.1: Graphical illustration of the different approaches to engineer the electronic band structure of 3D topological insulators summarized in this thesis. The individual pictures represent one chapter or section in the thesis, as labeled.

According to Fig. 1.1, this work is organized as follows:

Chapter 2 gives a detailed introduction to topological insulators and illustrates the development of topological band theory as well as the first experimental realization of this new fascinating state of matter. Additionally, the technique of photoemission spectroscopy is introduced and explained, since it is the main method employed in this thesis.

Chapter 3 depicts the experimental setup of the high-resolution ARPES laboratory at the Peter Grünberg Institute 6 of the Forschungszentrum Jülich.

Chapter 4 presents an analysis of the surface electronic structure of the three prototypical 3D TIs Bi_2Se_3 , Bi_2Te_3 , and Sb_2Te_3 , after a short introduction of the standard thin film cleaning procedure. Further, it compares results obtained on MBE-grown thin films and cleaved bulk single crystals and divides these materials as either *n*-type or *p*-type TIs, respectively.

Chapter 5 summarizes the 'conventional' examples of manipulating the electronic band structure by doping or alloying, which is shown in the left half of Fig. 1.1. Doping can

occur either at the sample surface as adsorbates or deposited material or in the bulk of the sample as defects or controllably implanted dopants.

The upper left panel in Fig. 1.1 refers to **Sec. 5.1**, which deals with the time- and temperature dependent electronic structure of Bi_2Se_3 , i.e. the so-called 'aging' effect and can be understood as unintentional surface doping. The next panel describes active surface doping by deposition of sub-ML impurities, as it will be discussed in **Sec. 5.2.2** for the deposition of Fe on Sb_2Te_3 and **Sec. 5.2.3** dealing with depositing MgO on Bi_2Te_3 . The lower left panel addresses bulk doping in the ternary topological insulators $(\text{Bi}_{1-x}\text{Sb}_x)_2\text{Te}_3$ for variable stoichiometry x (**Sec. 5.3**). It should be noted that these approaches are rather well-established and are shown only for the sake of completeness and to integrate this study into the scientific context and provide a more complete picture of band structure engineering.

Chapter 6 presents the above mentioned results on the realization of a vertical p-n junction in $\text{Sb}_2\text{Te}_3/\text{Bi}_2\text{Te}_3/\text{Si}(111)$ heterostructures, which represents a more complicated approach to engineer the electronic band structure and is illustrated in the upper right panel of Fig. 1.1. Depending on the size of the upper Sb_2Te_3 layer, an evolution of the surface electronic structure from p -type to n -type (for decreasing upper layer thickness) is observed. The effect is explained by a varying influence of the built-in electric field at the interface of the two TI materials on the probed upper surface. The results of self-consistent Schrödinger-Poisson simulations of such heterostructures that support this explanation are presented.

The last **chapter 7** addresses the creation of more complicated TI structures, such as superlattices, which is displayed in the lower right panel of Fig. 1.1. Interestingly, the stoichiometric stable compound $[\text{Bi}_2]_x[\text{Bi}_2\text{Te}_3]_y$ with $x = 1$ and $y = 2$, i.e. Bi_1Te_1 , of the Bi-Te family forms a natural superlattice phase. Contrary to the closely related, prototypical 3D strong topological insulator Bi_2Te_3 ($x = 0, y = 1$), the electronic structure as well as topological properties of Bi_1Te_1 have not been addressed so far. After a thorough investigation of the structural and (spin-polarized) electronic properties, we find that certain states of the rich surface electronic structure can be easily confused with Dirac cone-like topological surface states. However, we show by experiment and comprehensive *ab initio* density functional theory calculations that Bi_1Te_1 is a weak topological insulator.

Finally, **chapter 8** gives a short summary and outlook of the thesis.

CHAPTER 2

Theoretical Background

One of the greatest achievements in the 20th century in the field of condensed-matter physics was the formulation of the band theory of solids by Felix Bloch (among others) [26]. It successfully describes properties like electrical conductivity / resistivity, or optical absorption, and led to the development of transistors or solar cells. The band theory of solids derives the allowed quantum mechanical energy states of electrons in a periodic lattice of atoms or molecules (like a crystal) by exploiting its symmetry properties, such as the discrete translational symmetry. Further, band theory describes electronic states in terms of their crystal momentum \mathbf{k} , which is defined in a periodic *Brillouin zone* (BZ), being the unit cell in reciprocal space [27].

Bloch's theorem states that electrons in a periodic potential $u_k(\mathbf{r})$ (e.g. a solid with a periodic crystal lattice and certain boundary conditions) form Bloch waves with eigenfunctions as

$$|\Psi_k(\mathbf{r})\rangle = e^{i\mathbf{k}\cdot\mathbf{r}} |u_k(\mathbf{r})\rangle, \quad (2.1)$$

where $u_k(\mathbf{r})$ has the same periodicity as the crystal lattice with $u_k(\mathbf{r}) = u_k(\mathbf{r} + \mathbf{R})$ and lattice vector \mathbf{R} . These Bloch waves are the solution of the single-electron Schrödinger equation

$$\mathcal{H} |\Psi_k(\mathbf{r})\rangle = \left[-\frac{\hbar^2}{2m} \nabla^2 + V(\mathbf{r}) \right] |\Psi_k(\mathbf{r})\rangle = E_n(\mathbf{k}) |\Psi_k(\mathbf{r})\rangle. \quad (2.2)$$

Here, $\mathbf{k} = (k_x, k_y, k_z)$ is the electron wave vector in reciprocal space, i.e. crystal momentum, and n is an (band) index identifying the discrete energy eigenvalues $E_n(\mathbf{k})$, which are themselves periodic $E_n(\mathbf{k}) = E_n(\mathbf{k} + \mathbf{G})$ with the reciprocal lattice vector \mathbf{G} and vary continuously with the wave vector. This continuum of quantum mechanical states with the same n index form an *energy band* and $E_n(\mathbf{k})$ describes the dispersion relation of electrons within this band. Due to the periodic boundary conditions and the non-uniqueness of the wave vector $\mathbf{k} = \mathbf{k} + \mathbf{G}$, one can always find an equivalent electronic wave vector inside the first Brillouin zone, which is the unit cell in reciprocal space related to the specific crystal lattice. In the ground state of the system, the electronic states are filled up with electrons successively, starting with the lowest states of highest binding energy. Further, each electronic state can be occupied by only one electron due to Pauli's exclusion principle. The highest occupied state is called the Fermi

level E_F or Fermi energy and, in general, mostly the states at or near E_F contribute to electronic transport or optoelectronics. The entirety of the filled and unfilled electronic states is called the *electronic band structure* of a material [28]. Besides filled or unfilled bands there exists also ranges of energy that are free of any electronic states, those regions are called *band gaps* or *forbidden bands*.

Consequently, the band theory can be used to classify materials as electrically conducting (metals) or electrically non-conducting (insulators or semiconductors). In the case of metals, the Fermi level coincides with filled electronic bands (leaving certain states unoccupied) and an arbitrarily small amount of energy is needed for the excitation of an electron at the Fermi level into an unoccupied state, which leads to a gain of non-zero total momentum in form of an electric current flow. In the insulating state (often referred to as *band insulator*), the highest energetic band is fully filled and there exists a band gap between the highest occupied, so-called *valence band*, and the lowest unoccupied, which is called *conduction band*. In this case a substantial amount of energy is necessary in order to lift an electron across the band gap and thus the state is electrically inert. The only difference to semiconductors is that the band gap is smaller and thus smaller amounts of energy are needed to excite electrons into the conduction band. Additionally, it is possible to controllably create acceptor or donor states close to the valence band maximum or conduction band minimum (the material is then called *p-type doped* or *n-type doped*, respectively) in order to make the material more conductive.

2.1 Spin-Orbit Coupling

Spin-orbit coupling (SOC) is a relativistic quantum-mechanical effect that describes the interaction of the spin of an electron, which is a fundamental property of elemental particles [29], and its angular momentum, which is a result of the orbital motion of the electron. An electron that travels around a nucleus will experience an electric field gradient from the nucleus as an effective magnetic field¹ which will couple to the spin of the electron [30]. The first experimental evidence of an effect due to spin was observed in atomic physics in the fine structure of atomic spectral lines. For example the electron energy level p is split into two separated $p_{1/2}$ and $p_{3/2}$ states by SOC as a result of the two possible relative orientations of the electron spin and angular momentum [31].

Although, the strength of SOC is typically among the smaller energy scales in a band system (up to 10 eV in the core levels but only ~ 100 meV in the valence band) and can thus often be safely neglected, SOC appears in magnetic and non-magnetic materials and is the driving force of many interesting phenomena. In particular, SOC is essential in the field of topological insulators (TIs), where it acts as a kind of a built-in magnetic field in an otherwise non-magnetic solid, resulting in a technologically-relevant phenomenon called *spin-momentum locking* [31].

Following the Schrödinger formalism the state of an electron is described by a wave function $\Psi(\mathbf{r}) = \phi(\mathbf{r}) \cdot \chi$ with a spatially dependent part $\phi(\mathbf{r})$ and the electron spin

¹ Due to Lorentz transformation: $\mathbf{B} = \frac{1}{c}(\mathbf{v} \times \mathbf{E})$.

state χ given by a linear combination as

$$|\chi\rangle = a|\alpha\rangle + b|\beta\rangle \quad \text{with} \quad |\alpha\rangle = \begin{pmatrix} 1 \\ 0 \end{pmatrix} = |\uparrow\rangle \text{ and } |\beta\rangle = \begin{pmatrix} 0 \\ 1 \end{pmatrix} = |\downarrow\rangle, \quad (2.3)$$

where $|\alpha\rangle$ and $|\beta\rangle$ represent two-component spinors of spin up and spin down electrons depending on a certain quantization axis and a and b are two complex numbers [32]. Further, to address the actual spin of an electron, one has to introduce the expectation value of the spin operator σ which is determined by the three Pauli matrices σ_x , σ_y and σ_z :

$$\mathbf{s} = \langle \Psi | \sigma | \Psi \rangle; \quad \sigma = \sigma_x \hat{x} + \sigma_y \hat{y} + \sigma_z \hat{z}; \quad (2.4)$$

$$\sigma_x = \begin{pmatrix} 0 & 1 \\ 1 & 0 \end{pmatrix}, \sigma_y = \begin{pmatrix} 0 & -i \\ i & 0 \end{pmatrix}, \sigma_z = \begin{pmatrix} 1 & 0 \\ 0 & -1 \end{pmatrix}. \quad (2.5)$$

In the relativistic limit the Schrödinger equation is not sufficient to include the spin-operator. Therefore, a new term that connects the spin-orientation to the axes of the crystal (SOC) has to be introduced and the derivation starts from the fully relativistic one-electron Dirac equation [30, 33]. A thorough derivation of the Dirac theory can be found in quantum mechanics textbooks as refs. [32, 34] and a short derivation is also given in the appendix. The Dirac equation can be simplified² into a form which is often called *Pauli equation*, which takes the electron spin into account,

$$\left[\underbrace{-\frac{1}{2m} \left(\mathbf{p}(\mathbf{r}) + \frac{e}{c} \mathbf{A}(\mathbf{r}) \right)^2 + e\phi(\mathbf{r})}_{\text{classical Schrödinger eq.}} + \underbrace{i \frac{e\hbar}{(2mc)^2} \mathbf{E}(\mathbf{r}) \cdot \mathbf{p}}_{\text{Darwin term}} - \underbrace{\frac{e\hbar}{2mc} \sigma \cdot \mathbf{B}(\mathbf{r})}_{\text{ext. magnetic field}} - \underbrace{\frac{e\hbar}{(2mc)^2} \sigma (\mathbf{E}(\mathbf{r}) \times \mathbf{p})}_{\text{spin-orbit coupling}} \right] \psi = E\psi \quad (2.6)$$

The first two terms are the conventional Schrödinger equation in the non-relativistic limit. The third term is the only real relativistic term, the so-called Darwin term which has no classical analogon. Finally, the last two terms describe the interaction of the electron spin with an external magnetic field (Zeeman term) and the internal SOC coupling due to the electrons own orbital motion through an electric field of the nucleus. If one assumes this electric field in the vicinity of a nucleus to be spherically symmetric $V(r)$, the last term transforms to

$$\sigma \cdot (\mathbf{E}(\mathbf{r}) \times \mathbf{p}) = \sigma \cdot (\nabla V(r) \times \mathbf{p}) = \frac{1}{r} \frac{\partial V(r)}{\partial r} \sigma \cdot (\mathbf{r} \times \mathbf{p}) = \frac{1}{r} \frac{\partial V(r)}{\partial r} \sigma \cdot \mathbf{L} = \zeta \sigma \cdot \mathbf{L} \quad (2.7)$$

² Here only the large component spinor $\psi = (\psi_1, \psi_2)^T$ of the four-component (bi-spinor) wavefunction $\Psi = (\psi_1, \psi_2, \chi_1, \chi_2)^T$ will be considered. Electromagnetic fields are introduced by $\mathbf{p} \rightarrow \mathbf{p} - \frac{e}{c} \mathbf{A}$ with the vector potential $\mathbf{B} = \nabla \times \mathbf{A}$ and $\mathcal{H} \rightarrow \mathcal{H} - e\phi$ with the electric potential ϕ . \mathbf{E} is the electric and \mathbf{B} the magnetic field. Further, the approximation of $E_{kin}, V(\mathbf{r}) \ll mc^2$ was used [32, 35]. This means that for example the so-called mass-velocity term taking into account the relativistic change of the particle mass, which adds additional complications, is neglected here.

with the SOC constant ξ and the orbital angular momentum operator \mathbf{L} [31]. It is important to note that, due to the scalar product $\boldsymbol{\sigma} \cdot \mathbf{L}$, spin-orbit coupling depends on the relative orientation of the electrons spin and orbital angular momentum. Furthermore, the strength of the SOC depends on the size of the nucleus, which is proportional to the atomic Z number, because $\xi = \frac{1}{r} \frac{\partial V}{\partial r} \propto \frac{Z}{r}$ for a Coulomb-like potential $V(r) = -\frac{Z}{r}$. This means that firstly, SOC is strongest for electronic core levels (electrons closely bound to the core), but secondly that SOC increases for heavier elements. Typical strong SOC, high Z materials are gold (Au), bismuth (Bi), or antimony (Sb).

As soon as SOC is taken into account, neither the conventional orbital quantum number l ($0 \leq l \leq n-1$) nor the spin quantum number m_s ($m_s = -1/2, 1/2$) are good quantum numbers any more, which means that their operators \mathbf{L} and $\boldsymbol{\sigma}$ do not commute with the Hamiltonian any more ($[\mathcal{H}, \mathbf{L}] \neq 0$ and $[\mathcal{H}, \boldsymbol{\sigma}] \neq 0$). However, a new quantum number can be constructed out of their sum in a way that this total angular momentum operator $\mathbf{J} = \mathbf{L} + \boldsymbol{\sigma}$ does commute with the SOC-included Hamiltonian ($[\mathcal{H}, \mathbf{J}] = 0$) which makes it a conserved quantity.

2.2 Rashba-Effect

One effect, where spin-orbit coupling is the driving force and which is nowadays relatively easy to observe experimentally, is the Rashba- or Rashba-Bychkov-effect in two-dimensional systems.

Let us consider an electron of energy E , momentum \mathbf{k} and spin (\uparrow or \downarrow) in a system in which both time-reversal symmetry³

$$E(\mathbf{k}, \uparrow) = E(-\mathbf{k}, \downarrow) \quad (2.8)$$

and inversion symmetry

$$E(\mathbf{k}, \uparrow) = E(-\mathbf{k}, \uparrow) \quad \text{and} \quad E(\mathbf{k}, \downarrow) = E(-\mathbf{k}, \downarrow) \quad (2.9)$$

are valid. The band structure of such system will be symmetric around the center of the Brillouin zone and all energy bands for spin up and spin down electrons will be doubly degenerate [30]. If one of these two symmetries is violated, however, in a non-magnetic system the degeneracy of the bands can be lifted due to SOC. Time-reversal symmetry is in general broken in magnetic systems or can be broken by applying an external magnetic field.

Spatial inversion symmetry, on the other hand, will be violated either in non-centrosymmetric crystals (Dresselhaus effect) or at every crystal surface which truncates the periodic crystal potential and thus lifts the spin-degeneracy of the electrons close to the surface (Rashba-effect⁴). Therefore, due to the lack of inversion symmetry at a surface which is accompanied by a strong potential gradient of the electric field perpendicular to the surface, the last SOC term in Eq. 2.6 equals the Rashba-Hamiltonian

$$\mathcal{H}_R = \alpha_R \boldsymbol{\sigma} \cdot (\mathbf{E} \times \mathbf{p}) = \alpha_R |\mathbf{E}| \cdot \boldsymbol{\sigma} \cdot (\mathbf{k} \times \mathbf{e}_z) \quad (2.10)$$

³ Time-reversal symmetry means that changing the direction of the arrow of time does not alter the properties of the system.

⁴ Historically, the Rashba-effect has been used to describe two-dimensional electron gases at semiconductor interfaces [36]

with the material-dependent Rashba-parameter α_R which depends on the potential gradient along z -direction (perpendicular to the surface) and again on the atomic Z number of the nuclei involved.

Strictly speaking, the second equality in Eq. 2.10 is only valid for electronic eigenstates that are plane waves, as they appear in two-dimensional electron gases (2DEGs). However, the sudden truncation of the electronic configuration (and subsequent surface reconstructions) at many metal surfaces can lead to the formation of confined two-dimensional surface states without out-of-plane dispersion (see section 2.5). Metallic surfaces of certain orientation, like Au(111), Ag(111) or Cu(111) support such surface states and thus enable the study of the SOC-induced Rashba-effect. For electrons that are confined to the (x, y) -plane but experience an electric field gradient along the z -direction, the Schrödinger equation with the above Hamiltonian can be analytically solved (see appendix A.2) and the energy eigenstates are then given by

$$E_{\pm}(\mathbf{k}_{\parallel}) = \frac{\hbar^2}{2m^*} \mathbf{k}_{\parallel}^2 \pm \alpha_R \hbar |\mathbf{k}_{\parallel}|, \quad (2.11)$$

where \pm stands for spin up and spin down electrons [30, 37]. This means that, when taking SOC at a crystal surface into account, an originally two-fold degenerate parabolic band of a quasi-free electrons will split into two spin-polarized parabolas that shift away from each other with a shift that is linear in k_{\parallel} . Only at the high-symmetry point $k_{\parallel} = 0$ both spins are still degenerate. Figure 2.1 illustrates this Rashba-splitting in the energy dispersion of a 2DEG. Most interestingly, this effect already induces helical spin textures in k -space where the spin of every electron is ‘locked’ to a certain momentum (spin-momentum locking). Further, it means that an otherwise non-magnetic material with an overall zero net magnetic moment can show spin-polarized states depending on the k -space position, due to spin-orbit coupling. These effects are fundamentally related to the concept of topological insulators where spin-orbit coupling also acts as the driving mechanism.

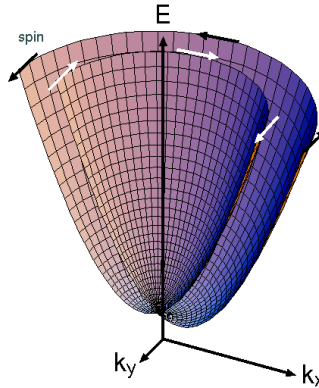


Figure 2.1: Illustration of the Rashba-effect at metallic surfaces. Due to the Rashba-effect, the spin-degenerate parabolic energy dispersion of a two-dimensional electron gas (free electron) will split into a spin up and a spin down electron parabola. This can effectively lead to a k -dependent spin texture in an otherwise non-magnetic solid. (Taken from [30]).

2.3 An Introduction into Topological Insulators

Topological insulators are fundamentally a new state of matter and cannot be classified according to the classical picture of the band theory, since their electronic properties differ in the bulk and at the boundary to a topologically trivial material. They are characterized by an insulating bulk, i.e. the bulk band structure exhibits an energy band gap (with inverted band parity⁵ at certain points in the Brillouin zone, as we will see later), and additionally non-gapped highly conductive states on their boundaries. These boundary states are either 1D edge channels in two-dimensional systems (2D TIs) or 2D surface states in three-dimensional systems (3D TIs) and they are a necessary consequence of the TIs topologically non-trivial nature and the bulk-boundary correspondence (section 2.3.1.1). The existence of these boundary states is due to a combination of strong spin-orbit coupling and the conservation of time-reversal symmetry (TRS) which leads to a robust symmetry protection of those states [3, 4, 9, 38]. In the following, I will try to introduce and explain the most important effects and concepts that lead to these interesting properties on a phenomenological level. For this I will mainly refer to [7, 8, 39, 40] and the references therein, which are already nicely summarized in [41].

2.3.1 Topological Band Theory

To correctly describe properties of the topological insulators, classical band theory needs to be extended to include the concept of topological order. In the extended topological band theory, a new *bulk* property in form of a topological invariant $n \in \mathbb{Z}$ is defined which allows to differentiate between topologically trivial ($n = 0$) and non-trivial ($n \neq 0$) materials [9, 40].

A classical band insulator, such as glass or also vacuum⁶, is the simplest form of matter and is in terms of its electric properties “appreciated for its ability to do nothing” [11]. The electrons are localized in closed shells around the nuclei and the band structure is characterized by a substantial band gap separating valence from conduction band (see (a) in Fig. 2.2). It belongs to the topologically trivial materials with $n = 0$. The mathematical analogon from topology could be a sphere with topological genus $g = 0$, having no hole.

⁵ The parity operator will be introduced at the end of section 2.3.1.3.

⁶ According to Dirac’s relativistic quantum theory, vacuum belongs to the band insulators and possesses a band gap for pair production as well as valence band and conduction band as the positron and electron sea, respectively [7].

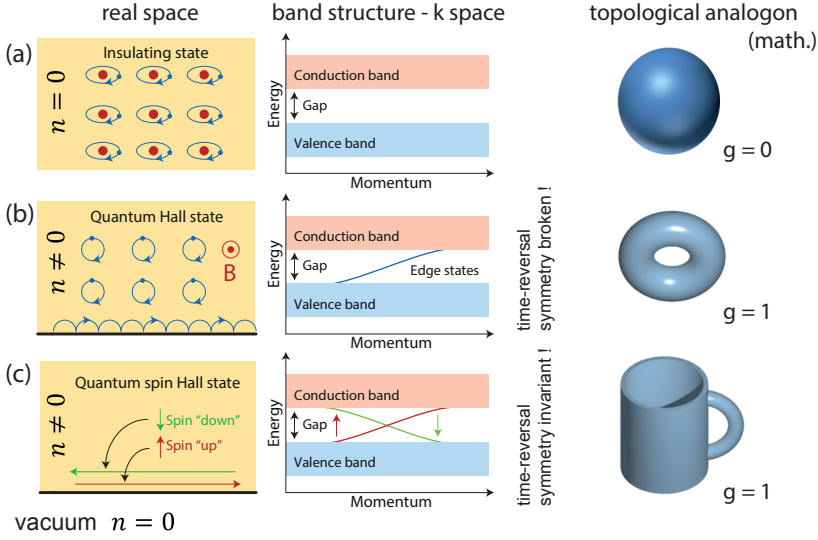


Figure 2.2: The insulating phases in two dimensions. (a) Topologically trivial ($n = 0$) insulating state is electrically inert. A mathematical analogon could be a sphere without any 'holes', thus a topological genus of $g = 0$. (b) The topologically non-trivial ($n \neq 0$) quantum Hall state in which a strong perpendicular magnetic field forces electrons on cyclotron orbits which scatter and bounce along the boundary, leading to 'chiral' spin-degenerate conducting edge states. Here the analogon could be a doughnut having one hole and thus $g = 1$. (c) The similar quantum spin Hall state which is an extension of the quantum Hall effect functioning without any external magnetic field. Here, SOC acts on the electrons and leads to 'helical' spin-polarized conducting states at the boundary. A homeomorphic transformation of the doughnut which does not change the topological invariant could be a coffee mug, having also one hole. The difference between (b) and (c) lies in the time-reversal symmetry which will be distinguished later (see section 2.3.1.2) and in another invariant. (Taken from [11]).

Insulators that are topologically non-trivial ($n \neq 0$), on the other hand, also have a band gap in the bulk (though band character inverted) but possess highly conductive states at their boundaries and thus have to be differentiated. The (b) and (c) of Fig. 2.2 show such examples in form of the quantum Hall state and the quantum spin Hall state which will be explained in more detail below. Here, the mathematical analogon could be a object like a doughnut or a coffee mug which both exhibit one hole ($g = 1$) and can be homeomorphically transformed into one another without changing the topological invariant, i.e. without closing the hole.

In the same sense, clear rules and transformations need to be defined that separate the two insulating phases from each other, in order for the topological distinction to be valid. Thus, in topological insulators the invariant n does not change as long as the band gap (= hole) is not closed or opened up. In other words, the band structure of a trivial band insulator, which is equivalent to the Hilbert space describing all possible electronic wave functions, cannot be continuously transformed (i.e. keeping the topological character equivalent) into that one of a non-trivial TI without closing and

reopening of the band gap [7, 40, 41].

2.3.1.1 Quantum Hall Insulating State

The first example of a state which is topologically not equivalent to a classical band insulator and thus can be seen as the first (TR symmetry broken) topological insulator, was found in 1980 by von Klitzing [42] in form of a quantum-mechanical version of the Hall effect, the (integer) quantum Hall effect (QHE). The effect occurs at low temperatures when electrons which are confined in two dimensions are exposed to a strong magnetic field perpendicular to their confinement forcing them onto quantized circular orbits with the cyclotron frequency ω_c . The confinement also leads to quantized highly degenerate energy levels, called Landau levels, with $E_n = (n + 1/2) \cdot \hbar\omega_c$ which basically can be viewed as a band structure with a band gap between the highest filled Landau level and the lowest unfilled Landau level identical to that of an classical band insulator [7, 28]. Interestingly, in a Hall probe experiment von Klitzing found [42] that the longitudinal conductance σ_{xx} in such systems is zero while the Hall conductance σ_{xy} shows precisely quantized integer multiples of $\frac{e^2}{h}$

$$\sigma_{xy} = N \cdot e^2/h \quad (2.12)$$

with N being an integer and known as the filling factor.

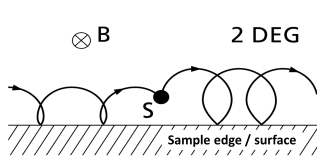


Figure 2.3: Schematic electron trajectory of an edge electron in a confined 2D quantum Hall state material with a perpendicular magnetic field B . S is an impurity causing scattering. (Taken from [28]).

In a semi-classical picture, the ‘bulk’ of the sample is insulating due to the localized cyclotron orbits and the quantization of the Hall conductance can be understood as being entirely caused by boundary edge channels. If an electron, occupying the quantized energy level E_n , comes close to the boundary, it ‘bounces’ off, but the strong magnetic field forces it back on the orbit leading to an effective drift motion along the boundary. This produces backscattering-free, quasi-ballistic conductive edge channels which are not affected or can be even stabilized by scattering centers such as impurities at the boundary [28]. Thus, N filled Landau levels will produce the quantized Hall conductance at the edge. However, these edge channels are spin-degenerate and thus

moving only ‘one-way’ at one boundary and moving in the opposite direction at the opposite boundary and are therefore called *chiral* or *helical*.

Topology of the Quantum Hall State - the TKNN Invariant = the Chern Number

In order to understand the origin of this quantization of a macroscopic transport observable and to differentiate the quantum Hall state from a classical band insulator in which such perfectly conducting boundary channels would not be possible, Thouless, Kohmoto, Nightingale, and den Nijs (TKNN) pointed out in 1982 that difference is not only quantum-mechanical but also topological [43]. Therefore, they introduced the integer TKNN invariant n which was later identified as equivalent to the Chern

number C . The Chern number on the other hand, is the closest analogon to the above described mathematical genus invariant g . Physically, it can be understood in terms of the geometric Berry phase⁷ γ which is a phase factor that a quantum-mechanical system accumulates when completing a closed path in its parameter space [39]. In other words, the TKNN invariant n , i.e. the quantized Hall conductance N , is equal to the phase that a Bloch wavefunction $|u_m(\mathbf{k})\rangle$ accumulates when \mathbf{k} propagates around a closed loop along the Brillouin zone boundary.

$$\underbrace{\sigma_{xy}}_{\text{Hall conductivity}} = e^2/h \cdot \underbrace{N}_{\text{filling factor}} = e^2/h \cdot \underbrace{n}_{\text{TKNN invariant}} = e^2/h \cdot \underbrace{C}_{\text{Chern number}} \quad (2.13)$$

with the total Chern number C , summed over all r occupied bands, being the total Berry phase in the Brillouin zone

$$C = \sum_{m=1}^r C_m = \sum_{m=1}^r \frac{1}{2\pi} \cdot \oint_{\partial\text{BZ}} d\mathbf{k} \underbrace{\nabla_{\mathbf{k}} \times \mathbf{A}_m(\mathbf{k})}_{\text{Berry curvature}} \quad (2.14)$$

Berry phase γ

and the Berry vector potential / Berry connection

$$\mathbf{A}_m(\mathbf{k}) = i\langle u_m(\mathbf{k}) | \nabla_{\mathbf{k}} | u_m(\mathbf{k}) \rangle \quad (2.15)$$

In a trivial band insulator the electron wavefunction will not accumulate any phase when fulfilling a closed loop around the BZ boundary (∂BZ) which means that the Chern number = the TKNN invariant will vanish $C = n = 0$ and thus the state is topologically trivial. In a topological insulator, e.g. the QHE insulating state, on the other hand the phase γ is a single-valued function of \mathbf{k} and can only be an integer multiple of 2π , $\gamma = 2\pi m$ with $m \in \mathbb{Z}$. Therefore, the Chern number $C_m = \frac{1}{2\pi} \cdot \gamma[\partial\text{BZ}]$ will also be an integer value $C = n \neq 0$ which validates the topological distinction [39].

It can not be emphasized enough that the importance of the statements of Thouless et al. lies in the fact that the quantized Hall conductance is equivalent to a topological invariant which means that the QHE state can be assigned to a topologically non-trivial state and, moreover, enjoys robust topological protection and will always be present as long as the topology is not changed [45, 46].

Bulk-Boundary Correspondence

As we have seen already above, in the QHE state there will always exist dissipationless edge states at the 2D sample boundary due to the skipping motion of the bouncing electron orbits in the strong magnetic field. The existence of those states is deeply

⁷ A nice analogy between electromagnetism and quantum anholonomy which explains the concept of the Berry phase in quantum mechanics is explained in [44].

vector potential $\mathbf{A}(\mathbf{r})$ - Berry connection $\mathbf{A}(\mathbf{k})$
 magnetic field $\mathbf{B}(\mathbf{r})$ - Berry curvature $\nabla_{\mathbf{k}} \times \mathbf{A}(\mathbf{k})$
 magnetic monopole - point degeneracy
 magnetic flux $\Phi(C)$ - Berry phase $\gamma(C)$

connected to the non-trivial topological nature of the QHE state and it can be generalized that at any interface where the topological invariant changes, gapless highly-conductive states have to be present [7, 45]. Speaking in terms of band structures, a transformation of the Hilbert space is smooth, i.e. topologically invariant, as long as the band gap does not close. Hence, at the interface between a trivial band insulator like vacuum and a non-trivial insulator like a QHE insulator, the topological invariant changes from $n = 0$ to $n = 1$ and related to this change the band gap has to close and open up again (this we will see on the next page). Connected to this zero-crossing of the band gap, there will be gapless low energy electronic states connecting the valence band to the conduction band (see Fig. 2.2; band structure in (b)). In two-dimensional samples the bulk-boundary correspondence will thus produce 1D edge channels and in three-dimensional samples it will result in 2D surface states.

We will later see that in topologically trivial materials these boundary states have to cross the Fermi level an even number of times (including zero-crossings), whereas in non-trivial materials they intersect E_F an odd number of times. Loosely speaking, the bulk-boundary correspondence relates the change of the topological invariant Δn to the number of Fermi level crossings N_{E_F} of the boundary states

$$N_{E_F} = \Delta n \mod 2 \quad (2.16)$$

Section 2.3.1.3 and Fig. 2.5 will give more insight into this relation.

2.3.1.2 Quantum Spin Hall Insulating State

The major ‘drawbacks’ of the quantum Hall insulating state with respect to any application are its enormous requirements. The state basically only exists at low temperatures and strong magnetic fields in a rather complicated semiconducting heterostructure in which a two-dimensional electron gas (2DEG) is formed. The magnetic field additionally breaks the time-reversal symmetry of the system which is why the QHE phase is also often called a time-reversal broken topological insulating phase. Therefore, physicists tried to extend the theoretical framework in the following years but it was not before 2005 that Kane and Mele [9, 10] introduced a spin-extended version of the QHE, namely the quantum spin Hall effect (QSHE) first for the model system of graphene. Here, instead of the TR symmetry breaking by the Lorentz force due to the magnetic field, spin-orbit coupling (Eq. 2.7) acts as the driving force. It conserves TR invariance and leads to the opening of a non-trivial bulk energy gap (see next paragraph). Therefore, QSH insulating states logically also belong to the topologically non-trivial materials and we will see that further topological invariants are needed to properly classify them as time-reversal invariant topological insulators (see section 2.3.1.3).

Consequently, gapless states will exist at the interface between a QSH insulator and a trivial insulator and moreover, these states will be not spin-degenerate but spin-polarized and electrons of opposite spin will effectively experience a driving force pointing into opposite direction along the boundary. Therefore such states are called *helical* (see Fig. 2.2(c)). In terms of band structure there also have to exist two spin-polarized states connecting the valence band with the conduction band.

The helicity of the boundary states is often referred to as *spin-momentum locking*, be-

cause an electron of certain spin can only travel into a certain direction, thus having certain momentum.

Band Inversion and the Absence of Backscattering

Already earlier it was mentioned that the band structure of topologically non-trivial materials is characterized by a band gap with *inverted* band character. Further we classified that both, conventional trivial insulators as well as topologically non-trivial insulators in the QSHE state exhibit a band gap but are classified by a topological invariant that changes at an interface where also the band structure experiences a transition of closing and reopening of the band gap. The reason for the inversion of certain bands at certain points in the BZ is again spin-orbit coupling. SOC leads to an additional energy splitting of the electronic states which exhibit a non-zero orbital quantum number such as *p*-type ($l = 1$) or *d*-type ($l = 2$) bands and is negligible in bands without orbital character, such as *s*-like bands ($l = 0$). In most common semiconductors, electronic *s* orbitals form the conduction band whereas the valence band is formed by electrons in *p* orbitals [27, 41]. If the band gap of the semiconductor is not too large and/or SOC is strong enough it can happen that the valence band (which is more strongly shifted) crosses the conduction band at certain points in *k*-space. Those crossing points are typically accompanied by a gap opening [41] but the band character of the bands is conserved. Figure 2.4(a) shows a DFT calculation of a bulk band structure of Bi_2Te_3 without (left) and with (right) inclusion of SOC (for the description of DFT see section 2.6). As we will later see in Fig. 2.10, in Bi_2X_3 with $\text{X} = \text{Se}, \text{Te}$ the valence band maximum and conduction band minimum are both originating from electronic p_z orbitals, but with differing parity character (+ or -). In the case of Bi_2Te_3 the calculations shown in Fig. 2.4(a) reveal that the trivial band gap on the left is transformed into a non-trivial inverted band gap with the valence band maximum (and - parity) mixed up with the conduction band minimum (and + parity). Thus, the overall parity of the occupied bands differs at certain points in the *k*-space and in the next paragraph we will see that this change of parity is accompanied by a change of a new time-reversal conserving topological invariant.

Another fascinating property of the helical conduction edge channels in the QSHE state is the absence of backscattering for the case of a time-reversal invariant, i.e. non-magnetic, scattering impurity. Figure 2.4(b) taken from [8] illustrates this effect as an destructive interference effect of two different electron paths, similar like the suppressed reflection of photons in an antireflective coating. Consider a forward moving spin up electron that scatters at a nonmagnetic impurity close to the boundary. Since the backward moving edge channel only allows spin down electrons, the spin of the electron would have to rotate adiabatically, either by an angle π or $-\pi$ from 'up' to 'down'. Consequently, the only two possible paths differ by a precise 2π rotation of its spin. However, the wavefunction picks up a phase of π under a full rotation, which leads to destructive interference and instead perfect transmission [8].

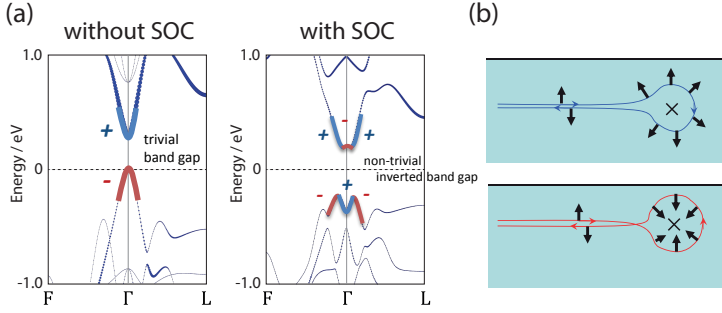


Figure 2.4: Band inversion in a strong topological insulator and the absence of backscattering. (a) calculated electronic bulk structure of semiconducting Bi_2Te_3 without and with inclusion of spin-orbit coupling. Additionally, the valence band (red) and the conduction band (blue), which both stem from electrons in p_z orbitals, as well as their parity character ('-' and '+', respectively) are highlighted. (Taken from [47]) (b) Schematic illustration of the two possible scattering paths of the edge state in a QSHE insulating state. The X marks a time-reversal invariant scattering center. (Taken from [8]).

2.3.1.3 The Topological \mathbb{Z}_2 Invariant

As we have seen, the QHE state and the QSHE state are both topologically distinct from the trivial band insulating state, yet another invariant is needed which distinguishes between these two phases. Since in the QHE state the chiral edge states lead to quantized charge Hall conductance and time-reversal symmetry is explicitly broken by the magnetic field, one needs to separate this phase from the QSHE state. The latter is TR invariant and its helical spin-polarized edge states will lead to a vanishing overall charge conductance (since each edge channel transports the same amount of charge quanta) but a non-zero quantized spin Hall conductivity and an effective spin current from one side to the other. This basically means that the TKNN invariant n (which equals the charge Hall conductivity) is zero in the QSHE state and thus is not sufficient to distinguish it from a trivial band insulator. Therefore, Kane and Mele [9] introduced another new topological \mathbb{Z}_2 invariant⁸ ν_0 in order to classify between time-reversal invariant systems with $\nu_0 = 1$ (and non-trivial spin Hall conductivity) and ordinary insulators with $\nu_0 = 0$ (and trivial spin Hall conductivity).

In order to construct this \mathbb{Z}_2 invariant one has to examine the role of TR symmetry for spin $1/2$ particles [48]. For electrons the anti-unitary TR symmetry operator is given by $\Theta = \exp(i\pi s_y/\hbar) \cdot K$ with s_y being the y-component of the spin and K the complex conjugate and its important property of $\Theta^2 = -1$. If the Hamiltonian \mathcal{H} commutes with the TR operator Θ ($[\mathcal{H}, \Theta] = 0$), then \mathcal{H} satisfies

$$\Theta \mathcal{H}(\mathbf{k}, \uparrow) \Theta^{-1} = \mathcal{H}(-\mathbf{k}, \downarrow) \quad (2.17)$$

⁸ In mathematics the group of integer numbers is called \mathbb{Z} and its subgroup separating between even and odd numbers is called \mathbb{Z}_2 . Hence, a \mathbb{Z}_2 index can take two different values 0 or 1 and can be used, e.g. for topological classification based on parity [39].

which means that for every Bloch energy eigenstate $|\psi_n(\mathbf{k}, \uparrow)\rangle$ the time-reversed state $\Theta|\psi_n(-\mathbf{k}, \downarrow)\rangle$ of opposite wave vector \mathbf{k} and opposite spin σ is also an eigenstate of the same energy. This important constraint is called the Kramers theorem and these two eigenstates are called Kramers partners and are at least two-fold degenerate. Spin-orbit coupling lifts this degeneracy, which means that spin up and spin down states are decoupled at most parts in the BZ, but at certain *time-reversal invariant momentum* (TRIM) points in the BZ this degeneracy persists and so-called Kramers points or *Dirac points* (DP) are formed [39, 40].

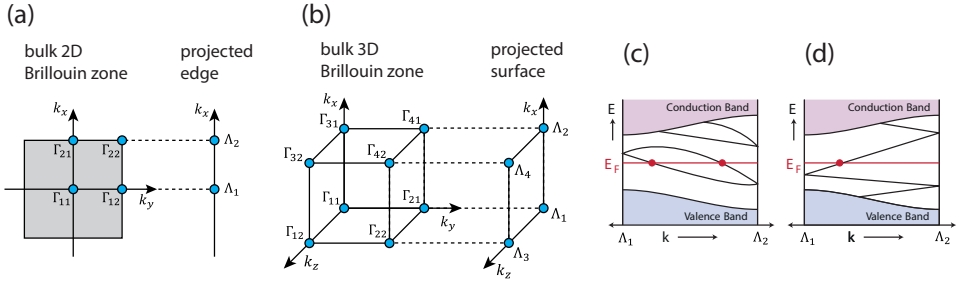


Figure 2.5: Time-reversal invariant momenta (TRIM) points. (a) 4 different bulk TRIM points Γ_{ij} (blue dots) in the 2D Brillouin zone in the case of a square BZ are projected onto the 2 edge TRIM points Λ_a . (b) In the case of a cubic 3D BZ there exist eight different bulk TRIM points which are projected onto four surface BZ TRIM points. (c) and (d) Schematic illustration of the electronic dispersion between two Kramers degenerate boundary TRIM points Λ_1 and Λ_2 for a topologically trivial $\nu_0 = 0$ (c) and non-trivial $\nu_0 = 1$ (d) material, respectively. The latter is related to the number of boundary states crossing the Fermi level (red dots), which is even and odd, respectively. (Adopted from [1, 7]).

Figure 2.5(a) and (b) illustrate the different TRIM points in a square 2D Brillouin zone and a cubic 3D BZ which are projected onto a 1D edge or a 2D surface, respectively. Let us consider the projected band structure $E(k)$ of a two-dimensional square BZ between the two boundary TRIM points Λ_1 and Λ_2 as shown in Fig. 2.5(c) and (d). As we have seen from the bulk boundary correspondence (section 2.3.1.1), the transition between two different topological classes (e.g. at an interface between a TI and a trivial insulator) will result in the existence of boundary states, in this case edge states, in the band gap. At the TRIM points, Kramers theorem requires the degeneracy of those edge states. At any other point along $\overline{\Lambda_1\Lambda_2}$ SOC will lift this degeneracy. Accordingly, there are two different ways how these edge states can connect between the two TRIM points, which are shown by pairwise connection in (c) and a partner switching in (d). In the case of pairwise connection in (c) the edge states will always cross the Fermi level an even number of times, or in other words there has to always exist an energy region without any states. This means that the system is effectively band gapped and thus topologically equivalent to a normal band insulator ($\nu_0 = 0$). On the other hand, the partner switching connection in (d) will always produce an odd number of Fermi level intersections which means that the edge states have to connect the valence band with the conduction band by covering the entire band gap. Such time-reversal invari-

ant systems are effectively metallic at the boundary and are defined as topologically non-trivial and characterized by the \mathbb{Z}_2 index $\nu_0 = 1$.

The mathematical formalism of the \mathbb{Z}_2 invariant has been introduced mainly by Fu and Kane [1, 48] and is nicely summarized in [39–41]. Here I will just briefly state the main conclusions. The most important concept is that ν_0 is defined only by the occupied **bulk band structure at the bulk TRIM points**. In 2D it is given by

$$(-1)^{\nu_0} = \prod_{i=1}^4 \frac{\sqrt{\det[w(\Gamma_i)]}}{\text{Pf}[w(\Gamma_i)]} = \prod_{i=1}^4 \delta(\Gamma_i) \quad (2.18)$$

where $w_{mn}(\mathbf{k})$ is an unitary matrix built from all occupied Bloch wavefunctions $|u_m(\mathbf{k})\rangle$

$$w_{mn}(\mathbf{k}) = \begin{pmatrix} 0 & \langle u_m(\mathbf{k}) | \Theta | u_n(-\mathbf{k}) \rangle \\ -\langle u_m(\mathbf{k}) | \Theta | u_n(-\mathbf{k}) \rangle & 0 \end{pmatrix} \quad (2.19)$$

fulfilling time-reversal invariance and thus $w^T(\mathbf{k}) = -w(-\mathbf{k})$ (i.e. skew symmetric) because $\Theta^2 = -1$. The so-called Pfaffian term $\text{Pf}(w)$ is only non-vanishing for 2×2 skew-symmetric matrices. Then it is defined by

$$\text{Pf}(w)^2 = \det[w] \Leftrightarrow \frac{\sqrt{\det[w]}}{\text{Pf}(w)} = \pm 1 = \delta \quad (2.20)$$

Consequently, $\delta(\Gamma_i)$ is always +1 or -1 which means that according to Eq. 2.18 ν_0 takes the value 0 if there is no change in topology between the projected boundary TRIM point Λ_1 to Λ_2 , which is equal to an even number of band crossings at E_F and means that the system is topologically trivial. Whereas, if ν_0 is equal to 1, there exists a change in topology which results in time-reversal symmetry protected boundary states with an even number of Fermi level crossings. The system then is a topological insulator.

The calculation of the topological invariant ν_0 gets simplified when the crystal has additional symmetries [1]. For inversion symmetric crystals the Hamiltonian additionally commutes with the parity operator

$$P\mathcal{H}(\mathbf{k})P^{-1} = \mathcal{H}(\mathbf{k}) \quad (2.21)$$

with $P|\mathbf{r}, s_z\rangle = P|-\mathbf{r}, s_z\rangle$ with an space coordinate \mathbf{r} and the parity independent spin component s_z . This simplifies the calculation of ν_0 significantly, since at the special bulk TRIM points Γ_i the Bloch states $|u_m(\Gamma_i)\rangle$ are not only time-reversal invariant but also parity invariant with the eigenstates $\zeta_m(\Gamma_i) = \pm 1 = \delta(\Gamma_i)$. Therefore, ν_0 is given by

$$(-1)^{\nu_0} = \prod_{i=1}^4 \delta(\Gamma_i) = \prod_{i=1}^4 \prod_{m=1}^N \zeta_m(\Gamma_i) \quad (2.22)$$

which basically means that one has to determine the parity (even or odd, which can be identified by the ‘curvature’ of the band) of all N occupied bulk bands at all bulk TRIM points Γ_i and calculate their product.

2.3.1.4 Generalization to 3D TIs

In this last step the formalism of the topological \mathbb{Z}_2 invariant has to be generalized into three dimensions. Here, we will again follow the arguments given by Fu and Kane in their subsequent publications [1, 2] and in [5]. As we have seen, the simple 3D cubic BZ consists of eight distinct TRIM points which can be identified by the reciprocal lattice vector $\mathbf{G}_{i=(l_1, l_2, l_3)} = \frac{1}{2}(l_1 \mathbf{b}_1 + l_2 \mathbf{b}_2 + l_3 \mathbf{b}_3)$ with $l_i = 0, 1$ and the primitive (unit) lattice vectors \mathbf{b}_i . Figure 2.6 shows their visualization as vertices of a cubic BZ (as already depicted in Fig. 2.5(b)).

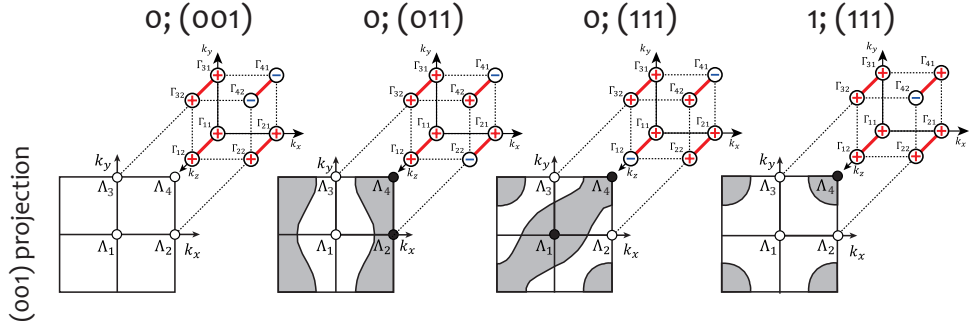


Figure 2.6: Illustration of four different 3D topological classes which can be identified by the topological invariants $\nu_0; (\nu_1 \nu_2 \nu_3)$. Shown is the 3D cubic BZ with its eight TRIM points Γ_i as well as the projected surface BZ along the $k_z = (001)$ direction with its surface TRIM points Λ_a . The latter are marked by white ($\pi = +1$) or black ($\pi = -1$) circles depending on the product of the topology of their producing bulk pairs having '+' ($\delta_i = +1$) or '-' ($\delta_i = -1$). Black lines in the Fermi surface separate white from gray area and represent surface states that have to be present at each path between a black and a white circle as a consequence of the change of topology from trivial to non-trivial. For the first 3 examples ($\nu_0 = 0$) always a completely trivial surface can be found (with four white circles) and all other surfaces will exhibit an even number of black circles, whereas in the last example ($\nu_0 = 1$) all surfaces will have an odd number of black circles. (Adopted from [2])

In this figure, eight bulk TRIMs Γ_i are exemplarily projected along the (001)-direction into 4 surface TRIM points Λ_a . According to Eq. 2.18, the topology of the bulk TRIM points can be determined by $\delta(\Gamma_{i=(l_1, l_2, l_3)}) = \frac{\sqrt{\det[w(\Gamma_i)]}}{\text{Pf}[w(\Gamma_i)]} = \pm 1$, having positive (+) or negative (-) parity. Hence, the character of the projected surface TRIM Λ_a is again defined by the bulk and given by the product of the two paired bulk TRIMs as

$$\pi_a = \delta_{a1} \cdot \delta_{a2} = \pm 1 \quad (2.23)$$

where a denotes the pair of bulk TRIMs.

In the figure, the parity of the bulk TRIMs is depicted with a '+' ($\delta = +1$) or a '-' ($\delta = -1$) and the projected surface TRIM will be a white dot if their product is $\pi = +1$ or a black dot if their product is $\pi = -1$, respectively. This change of the topological

character in the surface BZ (change from black dot to white dot) will again be accompanied by the existence of spin-polarized TR symmetry protected surface states with an odd number of Fermi level crossings. These surface states are visualized as black lines in the Fermi surface BZ separating the gray shaded from the white area which represent a change in the topology. The picture shows four different topological classes with different bulk properties and resulting surface BZs where the relative values of π_n at the four surface TRIMs Λ_n (which are also called Dirac points due to Kramers degeneracy) determine how they are connected to another. If only one of the surface TRIMs has a '-' sign, the surface state forms a Fermi arc around this point which in the extended picture forms a so-called Dirac cone around the Dirac point [41].

Only in this last case, labeled with 1; (111), where only one bulk TRIM has $\delta(\Gamma_i) = -1$ and all other seven have $\delta(\Gamma_i) = +1$, the Fermi surface will always look the same independent on the projection direction / crystal surface. In this case the Fermi surface will consist of an odd number of negative surface TRIMs, which means that the system will have an **odd number of Dirac cones on every surface**.

In all of the other cases the surface projections will differ from another and in total there exist 16 different invariant configurations of $\delta(\Gamma_i)$. This matter is taken into account by the fact that in 3D one needs exactly four \mathbb{Z}_2 invariants $\nu_0; (\nu_1\nu_2\nu_3)$ to fully classify a system [1, 2]. The first one, also called *strong topological invariant*, is the same as in 2D (Eq. 2.18) given by the product of all eight bulk TRIMs

$$(-1)^{\nu_0} = \prod_{i=1}^8 \delta(\Gamma_i) = \prod_{i=1}^8 \prod_{m=1}^N \zeta_m(\Gamma_i), \quad (2.24)$$

while $(\nu_1\nu_2\nu_3)$ are not independent of the choice of the surface projection (defined by $l_1l_2l_3$) and are defined by the product of only four $\delta(\Gamma_i)$ of TRIM points lying in the same plane

$$(-1)^{\nu_{k=1,2,3}} = \prod_{l_i \neq k=0,1;l_k=1} \delta(\Gamma_{l_1,l_2,l_3}). \quad (2.25)$$

This means, that the so-called *weak topological indices* $(\nu_1\nu_2\nu_3)$ can be interpreted as Miller indices of a reciprocal lattice vector $\mathbf{G}_\nu = \nu_1\mathbf{b}_1 + \nu_2\mathbf{b}_2 + \nu_3\mathbf{b}_3$. Concretely, in a 3D crystal a surface, which is perpendicular to the direction denoted by the weak indices, i.e. whose surface normal is along $(\nu_1\nu_2\nu_3)$, will be topologically trivial and free of any surface state and therefore really insulating (as the first example in Fig. 2.6; $(\nu_1\nu_2\nu_3) = (001) \rightarrow 0$ states crossing E_F). All other surfaces in this case have an even number of state crossings at the Fermi level enclosing an even number of Dirac points.

Lets go through the estimation of these invariants on the basis of a concrete example. In the first case in Fig. 2.6 the strong topological index ν_0 is zero, because the product over all eight bulk trim points is

$$\begin{aligned} (-1)^{\nu_0} &= \delta(\Gamma_{11}) \cdot \delta(\Gamma_{21}) \cdot \delta(\Gamma_{12}) \cdot \delta(\Gamma_{22}) \cdot \delta(\Gamma_{31}) \cdot \delta(\Gamma_{41}) \cdot \delta(\Gamma_{32}) \cdot \delta(\Gamma_{42}) \\ &= (+1) \cdot (+1) \cdot (+1) \cdot (+1) \cdot (+1) \cdot (-1) \cdot (+1) \cdot (-1) = +1 \\ \Rightarrow \nu_0 &= 0 \end{aligned}$$

and the three weak indices are calculated from the respective four TRIMs which lie in

the (100), (010) and (001) plane as

$$\begin{aligned} (-1)^{\nu_1} &= \delta(\Gamma_{21}) \cdot \delta(\Gamma_{22}) \cdot \delta(\Gamma_{41}) \cdot \delta(\Gamma_{42}) = (+1)(+1)(-1)(-1) = +1 \Rightarrow \nu_1 = 0 \\ (-1)^{\nu_2} &= \delta(\Gamma_{31}) \cdot \delta(\Gamma_{32}) \cdot \delta(\Gamma_{41}) \cdot \delta(\Gamma_{42}) = (+1)(+1)(-1)(-1) = +1 \Rightarrow \nu_2 = 0 \\ (-1)^{\nu_3} &= \delta(\Gamma_{12}) \cdot \delta(\Gamma_{22}) \cdot \delta(\Gamma_{32}) \cdot \delta(\Gamma_{42}) = (+1)(+1)(+1)(-1) = -1 \Rightarrow \nu_3 = 1 \end{aligned}$$

Therefore, this situation is fully described by 0; (001) and additionally (001) indicates the only surface which is entirely trivial.

To summarize, in 3D there are four topological \mathbb{Z}_2 invariants $\nu_0; (\nu_1\nu_2\nu_3)$ necessary to categorize the topological classes. In general, all topological properties are defined by the time-reversal invariant momenta of the bulk band structure. The strong topological insulator (STI) state is given if $\nu_0 = 1$, which means that all surfaces of the crystal will be equivalent and will possess an odd number of Dirac points being enclosed by an odd number of spin-polarized surface states (Dirac cones) which connect valence and conduction band, making the surfaces highly conducting. The term *strong*, is related to the robustness of the surface state against any kind of time-reversal invariant perturbation or changes of the Hamiltonian which do not close the band gap (the protection can only be broken by an external magnetic field or magnetic impurities).

However, if $\nu_0 = 0$ the system is either a trivial band insulator ($\nu_0; (\nu_1\nu_2\nu_3)$ are all zero) or in a weak topological insulator (WTI) state depending on the other three invariants ($\nu_1\nu_2\nu_3$) which mark the surface normal of the only surface that is trivial, i.e. showing no conductivity. Moreover, in that case, any other surface exhibit an even number of topologically protected surface states [41]. Here, the term *weak* relates to the early claims that perturbations might easily be able to gap the surface states. However, recently theorists have shown that the WTI phase is highly robust against time-reversal invariant perturbations [49, 50].

The next chapters will very shortly review how both 2D and 3D as well as strong and weak 3D topological insulators can actually be realized.

2.3.2 Experimental Realization of Topological Insulators

2.3.2.1 The QSHE State = 2D TI Realized in HgTe/CdTe Quantum Well Structures

Graphene is a two-dimensional layer of carbon atoms exhibiting both inversion and time-reversal symmetry which leads to special spin degenerate Dirac points at the \mathbf{K} and \mathbf{K}' points in the BZ where conduction and valence band touch each other. In the close vicinity of these points electrons behave like massless Dirac fermions with a linear dispersion. In that consideration, however, spin-orbit coupling is neglected, because otherwise it introduces another mass term into the Hamiltonian and thus effectively opens up a energy gap at the \mathbf{K} points. If SOC is taken into account, this system of insulating (time-reversal invariant) graphene was predicted to be the first quantum spin Hall insulator, i.e. topological insulator, with topologically protected spin-polarized states covering the band gap [10]. Nevertheless, spin-orbit coupling scales with Z and since carbon is such a light atom, the SOC induced gap in graphene is only about $24 \mu\text{eV}$ in energy, which is outside of any experimentally feasible scale. Therefore, physicists needed to look into systems consisting of heavier atoms in order

to find feasible TI states.

Bernevig, Hughes and Zhang [3, 38] suggested to use quantum well structures made out of a thin HgTe layer sandwiched between CdTe layers, which are well studied semiconducting systems and provide high spin-orbit interaction. They predicted that depending on the HgTe thickness and the related additional confinement in the quantum well, the band structure of HgTe will have a transition from a normal semiconducting (trivial) one into a inverted (non-trivial) one and consequently, a transition from a trivial insulating state ($\nu_0 = 0$) into a topological insulating state ($\nu_0 = 1$). Thus HgTe could be the first quantum spin Hall insulator or 2D topological insulator.

Indeed, within the next year the Molenkamp group in Würzburg succeeded to measure this effect in a transport experiment [4]. Its most important result is shown in Fig. 2.7. They grew HgTe layers of different thickness sandwiched between CdTe and patterned Hall bar structures out of the entire structure. Theory predicts that below a critical thickness of $d_c = 6.5\text{ nm}$ HgTe would have a trivial insulating band gap of around 10 meV size, because confinement energy pushes the s -type band up and the p -type band down (see sample I in the figure). On the other hand above d_c , SOC leads to a band inversion and thus produces a non-trivial insulator with protected metallic states in the gap (named sample II, III and IV in the figure).

In the low-temperature transport experiment they measured the longitudinal Hall resistance as a function of an applied gate voltage tuning the Fermi level through the band structure. Fig. 2.7(b) shows the result for four different samples. For the very thin sample I ($d < d_c$) the resistance is dropping as the Fermi level cuts the valence or conduction band, but increases to infinity (in this experiment $\sim 20\text{ M}\Omega$ was the upper limit) when the Fermi level lies in the band gap, which means there are no conducting states and the sample is insulating. For the samples III and IV ($d > d_c$) the resistance/conductance in the gap region shows precisely equal values of $2 \cdot e^2/h$ which confirms the 2D topological nature of that samples and the existence of conducting channels in the gap with quantized conductance. Additionally, sample III and IV differ in length and width which also proves that this topological effect is independent on shape. The fact that sample II shows a higher fractional value of quantized conductance is due to higher temperature and finite scattering effects.

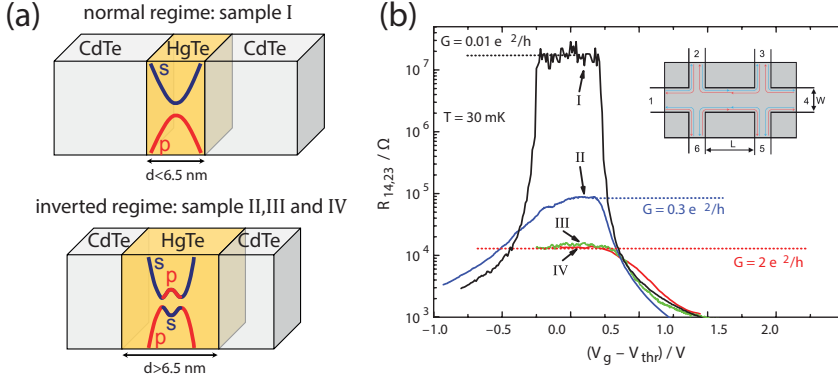


Figure 2.7: CdTe/HgTe/CdTe quantum well structures of different thicknesses of the HgTe layer. (a) Depending on the thickness the band structure in HgTe changes from a normal insulating one with finite gap into a topologically non-trivial with inverted gap. The latter state is also called the quantum spin Hall state. (b) Longitudinal Hall resistivity as a function of applied gate voltage for samples of different well thickness. In the normal band gap regime (sample I) the sample is insulating showing high resistivity in the gap, whereas in the inverted, thus topological regime (sample II, III, and IV) there exist metallic states in the gap carrying a quantized Hall conductance. The inset shows the conceptual sample design where L and W differ among the samples. (Adopted from [4, 41]).

This experiment for the first time confirmed the existence of boundary states with quantized conductance (so far only spin-integrated) in a topologically non-trivial 2D material with inverted band gap and also separated this state from a topologically trivial one with normal band gap. Nevertheless, this experiment still lacks spin resolution and higher temperature applicability.

2.3.2.2 1st Generation of Strong 3D TIs (STI)

The interpretation of electronic transport experiments is difficult in three dimensions because the signatures in conductivity are more subtle than in two dimensions and the biggest problem are contributions of bulk electronic bands and the distinction between surface and bulk transport. Therefore, for investigations of the topological properties of 3D crystals angle-resolved photoelectron spectroscopy (ARPES) has proven to be the most powerful tool as it is very surface sensitive and the surface electronic structure can be experimentally separated from bulk bands. Additionally, spinARPES allows the investigation of the spin polarization of the topological surface states.

In fact, Prof. Ando states that for confirmation of the TI nature of a material: "For 3D TIs, the simplest and most convincing is to observe the Dirac cone by ARPES experiments. To firm up the identification of a TI, one should employ spin-resolved ARPES to confirm that the Dirac cone is non-degenerate and is helically spin-polarized" [39]. Therefore, the quest was to find time-reversal and preferably also inversion symmetric materials of high spin-orbit coupling and to observe the Dirac cones with ARPES.

In 2008, only one year after the realization of the 2D TIs, the first 3D TI was experimentally found, namely the semiconducting alloy $\text{Bi}_{1-x}\text{Sb}_x$. Bi- and Sb-based alloys

have been studied already for decades due to their high thermoelectric figure of merit. Specifically in $\text{Bi}_{1-x}\text{Sb}_x$ it also has been known that depending on the stoichiometry, the band structure experiences a transition from a pure semimetal (Bi) over an insulating phase with inverted band gap ($\text{Bi}_{1-x}\text{Sb}_x$ with $0.07 < x < 0.22$) into an again semimetallic Sb phase [51] (see Fig. 2.8(b)). Using topological band theory this phase of inverted band gap was identified as a topological insulator phase and, indeed, Hsieh et al. [12, 13] measured the (111) surface band structure of $\text{Bi}_{1-x}\text{Sb}_x$ with $x = 0.1$ and confirmed the topological nature of the observed surface states. Figure 2.8 summarizes their findings. (c) and (b) show a large fraction of the Fermi surface and a respective binding energy map showing the rather complex electronic structure consisting of topological surface states which cross E_F five times. Further, these states enclose the surface TRIM $\bar{\Gamma}$ point an odd and the \bar{M} an even number of times which establishes the strong topological index to be $\nu_0 = 1$. In a later spin-resolved experiments the same group also proved the high spin polarization as well as helicity (chirality) of the surface states (see (e)).

Thus, the first three-dimensional strong topological insulator with 1;(111) configuration was found but nevertheless, its electronic structure is rather complex and the band gap rather small (few 10 meV).

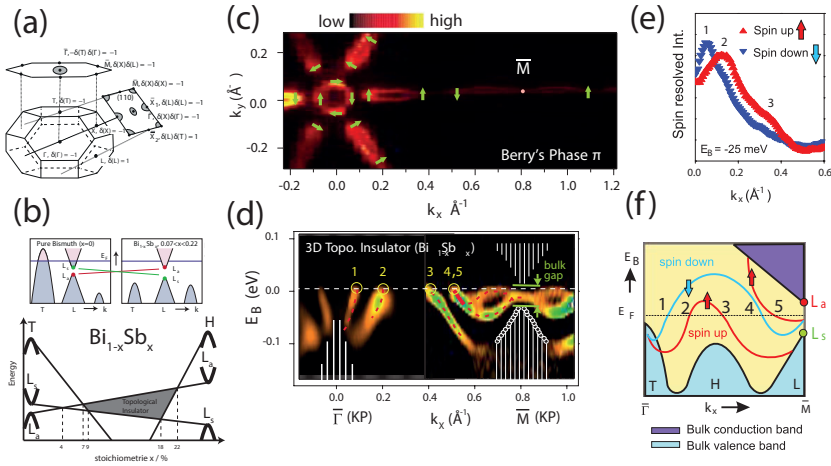


Figure 2.8: Surface electronic structure of the (111) surface of a $\text{Bi}_{0.9}\text{Sb}_{0.1}$ crystal being a 1;(111), thus strong 3D topological insulator. (a) Schematic illustration of the three-fold symmetric 3D bulk BZ and the (111) as well as (110) surface projection including an analysis of the TRIM points topology (from [52]). **(b)** Plot showing the development of the energy bands close to Fermi level for different stoichiometries of $\text{Bi}_{1-x}\text{Sb}_x$ showing a transition from semimetallic Bi over a band inverted (topologically non-trivial) insulating phase into semimetallic Sb (reproduced from [51] and [7]) **(c)** Fermi surface $k_{||,x}$ vs. $k_{||,y}$ map and **(d)** the respective E_B vs. $k_{||,x}$ map with $k_{||,y} = 0$ visualizing five surface states crossing the Fermi level. **(e)** Spin-resolved momentum distribution curve at $E_B = 25$ meV revealing spin polarization of states 1, 2 and 3. **(f)** Comic of the entire surface band-dispersion along $\bar{\Gamma}\text{M}$. (Taken from [12] and [13]).

2.3.2.3 2nd Generation of 3D TIs with a Single Dirac Cone on the Surface

Following this trend of investigating semiconducting alloys based on heavy elements like bismuth (Bi) or antimony (Sb) scientists tried to look for materials with simpler electronic structure and larger band gaps which would also allow for topological properties to show up at room temperature. These requirements are met by the second generation of 3D STIs, namely the family of X_2Y_3 alloys with $X = \text{Bi}$ or Sb and $Y = \text{Te}$ or Se . Moore [6] was the first who proposed this class of materials and Zhang et al. [16] delivered the first-principle theoretical framework which predicts Bi_2Se_3 , Bi_2Te_3 and Sb_2Te_3 to be strong 3D TIs with the strong index $\nu_0 = 1$, all weak indices zero (000), band gaps between 100 – 300 meV, and only a single linearly dispersing Dirac cone at the $\bar{\Gamma}$ on the surface (Fig. 2.9(c)). In parallel, Xia et al. [15] succeeded to observe this single Dirac cone using ARPES (Fig. 2.9(d)).

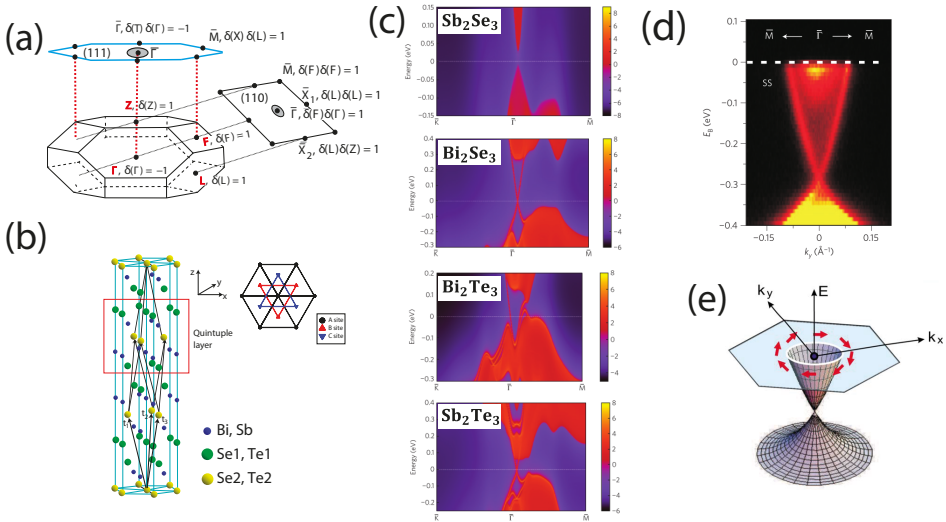


Figure 2.9: 2nd generation of 3D TIs. (a) Three-fold symmetric bulk BZ of Bi_2Se_3 with surface projections along (111) and (110) shown. The bulk TRIM points (in total eight) are shown in red and the surface TRIM points are also labeled including their topological character (from [52]). (b) Real-space tetradymite crystal structure shown as side and top view. One unit cell consists of three quintuple layers (QLs) marked by the red rectangle. The bounding among QLs is of van der Waals type. $t_{1,2,3}$ mark the primitive lattice vectors of the trigonal lattice. (c) First-principle calculation of the surface electronic structure showing topological surface states at $\bar{\Gamma}$ (except for Sb_2Se_3) (taken from [16]). (d) first ARPES measurement on Bi_2Se_3 along $\bar{\Gamma}\bar{M}$ direction showing the Dirac cone. (Taken from [15]) (e) Schematic of the spin-polarized Dirac cone. (Taken from [7]).

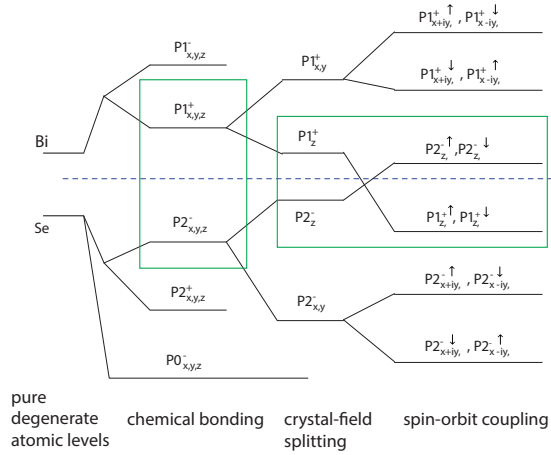
Since then, a lot of research was carried out on this class of materials [13, 53–58] including also spinARPES which nicely confirmed the helical spin-polarized nature of the Dirac cone (as indicated in Fig. 2.9(e)). The figure (a) also depicts the three-fold

symmetric 3D Brillouin zone⁹ of these materials with its time-reversal invariant momenta points marked in red (Γ , Z , $3 \cdot L$ and $3 \cdot F$) and the surface projection along (111) and (110) direction with the surface TRIM points $\bar{\Gamma}$ and \bar{M} (and \bar{X} along (110), note that \bar{K} is not a TRIM point). Different to the $\text{Bi}_{1-x}\text{Sb}_x$ case, on every surface the $\bar{\Gamma}$ point is the only TRIM point with non-zero topological index, thus creating a 1;(000) topological insulator (a table with the parity of all occupied bands at the bulk Γ point is given in [16]).

Band Inversion in 3D TIs

In this paragraph we will shortly describe how the strong spin-orbit coupling leads to the inversion of the bulk band gap and thus the topological character of the Bi_2Se_3 , Bi_2Te_3 or Sb_2Te_3 compounds. On the example of Bi_2Se_3 , the evolution of the energy levels of atomic Bi and Se orbitals under influence of different interactions can be visualized and thus the driving mechanism of this band inversion process can be understood. This was firstly described in [16] and is summarized in Fig. 2.10 (see also Fig. 2.4 for the sketch of the band structure with a non-inverted and inverted band gap). The electronic configuration of Bi is $[\text{Xe}]4f^{14}5d^{10}6s^26p^3$ and of Se $[\text{Ar}]3d^{10}4s^24p^4$ and

Figure 2.10: Illustration of the band inversion of the bulk electronic structure at the Γ point of Bi_2Se_3 . The energetic degeneracy of the atomic orbitals from Bi and Se is lifted by chemical bonding, crystal-field splitting and SOC. The blue dashed line marks the Fermi energy. (See also Fig. 2.4 which shows the band inversion in a simulated band structure). (Taken from [16]).



the valence band maximum (VBM) and the conduction band minimum (CBM) are made of p -orbitals. Chemical bonding between Bi and Se within a quintuple layer (QL) will split these p -orbitals into five hybridized p -orbitals lifting all Bi states and pushing down all Se states. Every energy level in the diagram in Fig. 2.10 is labeled with its orbital character. Additionally, the superscripts at the letters denote the bulk parity character at the Γ point. Next, the crystal field caused by the neighboring charge

⁹ Note that the here shown trigonal Brillouin zone corresponds to crystal structures with the trigonal $R\bar{3}m$ space group, as it is shown in Fig. 2.9(b) with the primitive lattice vectors $t_{1,2,3}$. Equivalently, one can also define the crystal structure and thus the Brillouin zone by a hexagonal, six-fold symmetric lattice system, as we will make use of in chapter 7 for the bulk band structure calculations of Bi_1Te_1 .

distribution will split the p -orbitals further into degenerate p_x and p_y and a shifted p_z orbital with the latter being closest to the Fermi level. In the figure those orbitals are named as the states $|P1_z^+\rangle$ and $|P2_z^-\rangle$ which means that due to parity of the bands the VBM is hole-like and the CBM electron-like. Until this point all orbitals are spin-degenerate. In the last step SOC is switched on, which means that the spin-degeneracy is lifted by mixing spin and orbital angular momentum. This leads to a repulsion of $|P1_z^+, \uparrow\rangle$ and $|P1_{x+iy}^+, \downarrow\rangle$ and similar combinations [16, 47].

If SOC is strong enough to switch the energetic positions of the lowest Bi and the highest Se p -orbital, the bulk band gap is 'inverted' and the system is driven into a topological insulator phase.

Crystal Structure

Bi_2Se_3 , Bi_2Te_3 and Sb_2Te_3 compounds belong to the family of tetradymites which exhibit a layered crystal structure with trigonal (rhombohedral) symmetry and $R\bar{3}m$ space group being a part of the larger family of hexagonal lattices [59, 60]. Figure 2.9(b) shows one unit cell of a tetradymite crystal structure which is made of the layered stacking of three so-called *quintuple layer* (QL) building blocks along the trigonal z -axis. One QL is built up by five alternating atomic planes and all atoms are bound to each other by strong covalent forces, while between adjacent quintuple layers the atoms are only weakly van der Waals bound [60]. The stacking sequence of one QL on the example of Bi_2Se_3 is: [Se(1)-Bi-Se(2)-Bi-Se(1)], where Se(1) and Se(2) mark lattice sites that differ from another by means of the distance of their next nearest-neighbors (which in the case of Se(1) are located in the next QL, and thus more far away) [47]. The weak van der Waals gaps between the QLs makes tetradymite crystals suitable for cleavage similar to the mechanical graphene exfoliation, which produces very clean and well defined surfaces exposing either Te(1) or Se(1) atomic planes. Exact atomic positions in all of the different tetradymite compounds can be found in [60].

2.3.2.4 Weak Topological Insulator

Already in section 2.3.1.4 we have seen that in 3D one has to distinguish between strong TIs with $\nu_0 = 1$ and weak TIs with $\nu_0 = 0$ and at least one non-zero weak index ν_1 or ν_2 or $\nu_3 \neq 0$. Further, we have seen how bulk band structure calculations can be employed to predict whether a material belongs to the one or the other class, i.e. predict whether a surface exhibits no, an odd, or an even number of topological surface states. In that sense, for example, the review by Ando [39] provides a table of many topological insulators that have been addressed up to that point both experimentally and theoretically, which consists mostly of 3D STIs while WTIs are only theoretically proposed [61–63].

However, only in 2013 the first weak TI with 0;(001) in form of $\text{Bi}_{14}\text{Rh}_3\text{I}_9$ crystals was synthesized and measured by Rasche et al. [64]. The crystal consists of a stacking of Bi-based honeycomb graphene-like sheets with rather weak coupling among each other. The final experimental proof that $\text{Bi}_{14}\text{Rh}_3\text{I}_9$ indeed is a weak TI was then given by Pauly et al. [41, 65] who measured topologically protected 1D electron channels at surface step edges via STS on a cleaved surface.

In general, already Fu and Kane [1, 2] understood the WTI phase as a layered 3D system, of which each layer is a 2D TI. If the coupling among the layers is sufficiently weak, the helical, topologically protected 1D edge states of the single layers become anisotropic surface states [41]. This construction is exemplarily shown in Fig. 2.11 which is adopted from [41].

Here, a 3D crystal is produced out of stacked 2D TIs (in z -direction) resulting in two topologically trivial, gapped top and bottom surfaces with no Dirac points, i.e. no surface states, marked by surface TRIMs with $\pi = +1$ (white dots) according to eq. 2.23. The other four perpendicular side surfaces are topologically non-trivial exhibiting exactly two Dirac points (black dots) and thus gapless surface states and a possible Fermi surface as indicated on the right of the figure. The topological distinction of this system would thus be $0; (001)$.

For experimental verification one could either measure the surface states of the side surfaces by ARPES (which is difficult because they are no natural cleavage planes) or measure the topological 1D edge channels of potential step edges on the top surface by STS. Since every surface shows islands or step edges, such 2D TI states will always be present (indicated by the monolayer high island in the figure).

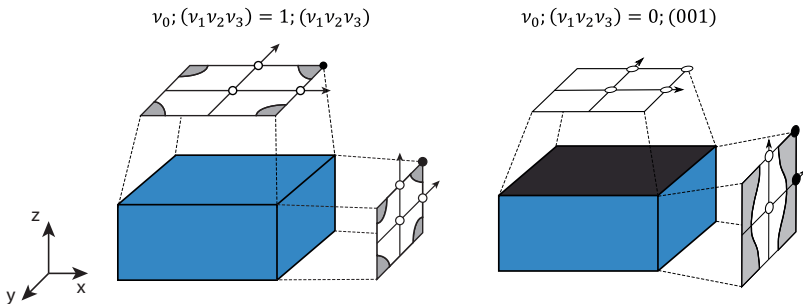


Figure 2.11: Schematic illustration of a 3D weak TI made of a stack of weakly coupled 2D TI layers. Black surfaces are gapped and topologically trivial while blue surfaces exhibit an even number of Dirac points. Potential Fermi surfaces with the topology of the surface TRIMs are depicted. (Taken from [41]).

In the later results chapter 7 more details will be presented and we will see how changes in stoichiometry between Bi and Te can drive a prototypical strong topological insulator (Bi_2Te_3 with the ratio Bi : Te = 40% : 60%) into a weak topological insulator phase (Bi_1Te_1 with Bi : Te = 50% : 50%).

2.3.3 Defect Chemistry

Because the prototypical 3D (strong) topological insulators Bi_2Se_3 , Bi_2Te_3 and Sb_2Te_3 are narrow band gap semiconductors with band gaps not larger than 0.3 eV, it is very important to have good knowledge and control over their defect chemistry. In order

to separate and minimize the effect of trivial bulk charge carrier transport from the desired non-trivial surface transport, the number of acceptor and donor defects should be balanced and minimized and the Fermi level should be in the center of the (inverted) band gap [60]. Bulk charge carrier concentrations n_{3D} should preferably not exceed values of 10^{16} to 10^{17} cm^{-3} . This issue is one of the key problems in the TI research of the recent years, because in reality, materials show bulk defect concentrations of up to 10^{20} cm^{-3} or more. Hence, this will lead to such a high electron (n -type) or hole (p -type) doping that the Fermi level is pinned to the conduction or valence band, respectively, which means that the material effectively becomes a degenerate semiconductor. Therefore, it is important to understand what kind of defects makes these materials effectively p - or n -type doped.

Man-made Bi_2Se_3 crystals are normally strongly n -type electron doped¹⁰ with typical values of $n_{3D} \sim 10^{19} \text{ cm}^{-3}$, purely due to inevitable Se vacancies $V_{\text{Se}}^{\bullet\bullet}$ or Se anti-site defects $\text{Se}_{\text{Bi}}^{\bullet}$ that have both very low formation energies¹¹ [39, 67]. Se vacancies are basically formed when in the thermodynamic equilibrium a Se atom escapes as vapor, leaving behind a doubly positively charged vacancy and two conduction electrons. Thus, in Bi_2Se_3 exist only positively charged defects which produce negative charge carriers and make the bulk of bismuth selenide highly conductive [60].

Bi_2Te_3 crystals, on the one hand behave quite similar and exhibit also positively charged $V_{\text{Te}}^{\bullet\bullet}$ vacancies, but on the other hand contain a large concentration of either negatively charged Bi'_{Te} or positively charged $\text{Te}^{\bullet}_{\text{Bi}}$ anti-site defects, depending on whether it is grown in a Te-rich or Bi-rich environment. These crystals can thus be either p -type or n -type [67–69]. In reality, bulk single crystals grown from stoichiometric melts by the Bridgman method are usually p -type, while MBE / CVD / MOVPE grown thin films are typically heavily n -type. The occurrence of both type of anti-site defects in Bi_2Te_3 , in contrast to Bi_2Se_3 , is due to the fact that the cation and anion electronegativity in Bi_2Te_3 is very similar which means that the anti-site defect less strongly prefer one site over the other [60, 70]. Nevertheless, it is still very complicated to grow crystals with low bulk carrier density.

Last but not least, in antimony telluride Sb_2Te_3 the electronegativities of Sb and Te are even more complementary, which leads to a roughly 10 times higher concentration of negatively charged Sb'_{Te} anti-site defects than in Bi_2Te_3 [60]. Hence, Sb_2Te_3 is heavily p -type doped and has never been reported differently (natively).

Consequently, to find methods to manipulate the intrinsic behavior of Bi_2Se_3 , Bi_2Te_3 or Sb_2Te_3 by different techniques, and thus to engineer their electronic band structure in a way that the Fermi level is tuned along the Dirac cone and away from bulk bands, will be the main subject of this thesis.

¹⁰ with only few exceptions as shown in [66]

¹¹ Here, the Kröger-Vink notation is used: M_S^C with:

defect type M : atoms, vacancies, interstitials, electrons e , or holes h ;

charge units C : \bullet is a single positive charge; $\bullet\bullet$ is a double positive charge; $'$ is a single negative charge; $''$ is a double negative charge;

lattice site that the defect occupies S

For example: $V_{\text{Se}}^{\bullet\bullet}$ means a selenium vacancy with double positive charge: $\text{Se}_{\text{Se}} \rightarrow V_{\text{Se}}^{\bullet\bullet} + \text{Se(g)} + 2e'$ or Bi'_{Te} is an anti-site defect with a singly negatively charged bismuth ion sitting on a tellurium lattice site: $\text{Bi}_{\text{Bi}} \rightarrow \text{Bi}'_{\text{Te}} + \text{Te(g)} + h^{\bullet}$.

2.4 Photoemission Theory

Photoemission electron spectroscopy (PES) has become one of the most frequently applied experimental techniques for studying the fundamental, physical behavior of condensed matter, such as electronic, magnetic or chemical properties. It is widely used to study both the surface and the bulk electronic structure of all types of solid state systems such as ferromagnets, superconductors, semiconductors or band insulators, adsorbates on surfaces, or purely two-dimensional systems like graphene. As already mentioned, photoemission is also outstandingly suited to study the properties of topological insulator materials, especially their spin-polarized, two-dimensional surface states.

In general, one has to differentiate between two main techniques. On the one hand, *X-ray photoelectron spectroscopy (XPS)*, which typically uses high energy photons in the X-ray regime (few 100 eV – few keV), probes the deeply bound electronic core levels that reflect the chemical state of the material. On the other hand *Ultraviolet photoelectron spectroscopy (UPS)*, which uses photon energies in the ultraviolet (UV) and vacuum-UV range (5 – 100 eV) is employed to study those electrons that are more delocalized and loosely bound and therefore form the electronic band structure of the material. This thesis will mainly focus on the latter technique.

Only a brief introduction shall be given into the common standards of fundamental photoemission theory, because this topic has been extensively studied and is well established by now. There are several excellent textbooks and review articles [71–76], as well as a countless number of theses (e.g. [35, 46, 47, 77–81]) which can be considered for a more detailed description. Nevertheless, the next chapters shall shortly summarize, based mostly on the references stated above, the basics of photoemission with the focus on its high-resolution, angle-resolved option.

2.4.1 The Photoemission Process

The first experiments on the photoelectric effect, which is the basic principle of photoemission, were carried out by H. Hertz already in 1887 [82]. In these experiments electrons were emitted from a solid when the solid was illuminated with electromagnetic radiation of a certain wavelength. However, only in the beginning of the last century Einstein was able to understand this phenomenon [83]. Einstein extended Maxwell's wave theory of light and Planck's quantum hypothesis by explaining the photoelectric effect with the absorption of discrete light quanta that lead to the excitation of electrons from the solid. He related the number and the kinetic energy of emitted photoelectrons to the intensity and the frequency of the light, and was rewarded with the Noble Prize in 1921 for this interpretation. His findings are summarized in the following equation

$$E_{kin} = h\nu - \Phi - E_B \quad (2.26)$$

where $h\nu$ is the energy of a single photon, E_{kin} is the kinetic energy of the emitted electron in vacuum, E_B is the binding energy of that electron inside the solid before it was excited, and Φ is the material-dependent work function which is a potential barrier that the electron has to overcome in order to leave the solid (in most materials typically 4 – 5 eV). In angle-integrated photoemission experiments (UV or x-ray photoelectron spectroscopy, i.e. UPS or XPS) the kinetic energy of the photoelectron is the

most important observable and one counts all photoemitted electrons as a function of their kinetic energy which results in a 1D spectrum $I(E_{kin})$ that is related to the initial electric density of states in the solid that is modulated by the photoemission process (see left side of Fig. 2.12).

Angle-Resolved Photoemission

Nowadays, one is able to precisely measure the polar (ϑ) and azimuthal (φ) emission angles of the emitted photoelectrons and, using the momentum conservation law, relate the resulting angular distribution of photoelectrons in vacuum to the initial momentum of the electrons inside the crystal. Effectively, one counts the photoelectrons as a function of their kinetic energy and emission angles, which produces multi-dimensional spectra¹². This technique, called angle-resolved photoelectron spectroscopy (ARPES), is the most direct way to investigate the electronic band structure of solids¹³. The right side of Fig. 2.12 depicts a typical modern ARPES setup. For all following considerations, it is important to distinguish between three different electron wave vectors:

- \mathbf{k}_i : the initial state wave vector of the electron in the solid before excitation
- \mathbf{k}_f : the final state wave vector in the material after excitation
- $\mathbf{K} = \mathbf{p}/\hbar$: the momentum vector of the electron emitted into vacuum

Measuring E_{kin} and the emission angles ϑ and φ is sufficient to determine the momentum vectors of the electrons in vacuum by

$$K_x = \frac{1}{\hbar} \sqrt{2mE_{kin}} \sin \vartheta \cos \varphi \quad (2.27)$$

$$K_y = \frac{1}{\hbar} \sqrt{2mE_{kin}} \sin \vartheta \sin \varphi \quad (2.28)$$

$$K_z = \frac{1}{\hbar} \sqrt{2mE_{kin}} \cos \vartheta \quad (2.29)$$

with the components related to the sample surface $\mathbf{K}_{||} = (K_x, K_y)$ and $K_{\perp} = K_z$. The goal is then, to recalculate the electronic dispersion relation $E(\mathbf{k}_i)$ inside the solid from the measured quantities, using momentum conservation and Eq. 2.26.

¹² Using two-dimensional detection systems and the energy dispersive plane in the hemispherical analyzer (compare section 3.1), a single shot measurement will result in a 2D spectrum $I(E_{kin}, k_x)$. Varying the emission angle by sample rotation adds another angular dimension $I(E_{kin}, k_x, k_y)$. Additionally, changing the photon energy can probe the third angular dimension leading to a four-dimensional data set $I(E_{kin}, k_x, k_y, k_z)$.

¹³ This, however, requires single crystalline surfaces (or at least domain sizes that are comparable to the size of the light beam spot) because only the angular distribution of photoelectrons from single crystal domains can be directly translated into the momentum distribution of electrons inside the solid. Polycrystalline samples will produce photoelectrons with all kinds of emission angles, i.e. different cuts through the electronic band structure, that overlap each other and make observation of distinct bands impossible.

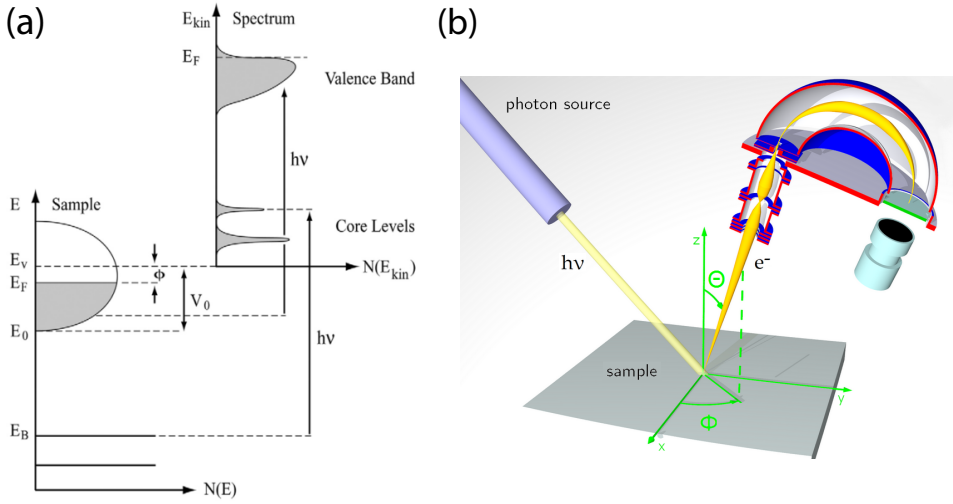


Figure 2.12: The photoemission process. (a) The initial electronic structure of electrons with the binding energy E_B in a solid (bottom left) with the element-specific core level states and the density of states at the valence band with all states occupied up to the Fermi level $E_B = 0 \equiv E_F$ (gray) is shown. Electrons are excited by light with the photon energy $h\nu$ and converted into a measured spectrum (top right) which is a function of the kinetic energy of the electrons $I(E_{kin})$. In order to be detectable, electrons have to be excited above the vacuum level $E_V = E_F + \Phi$. (Taken from [71]). (b) Sketch of a typical ARPES geometry with a photon source shining light onto a single crystalline sample surface which will lead to the emission of electrons under certain emission angles φ and θ and with a certain kinetic energy. The electron distribution $I(E_{kin}, \theta, \varphi)$ can be efficiently measured by hemispherical analyzers with 2D detection systems.

The Sudden Approximation

In general, photoemission is a very complicated many-body effect because electrons are excited from an initial state in the crystal, escape into vacuum and leave the system in a modified final state. In other words, the emission of a photoelectron from a system with N electrons comes along with the creation of a photohole in the reservoir of $N - 1$ electrons which results in complicated interactions and screening effects. In order to be able to describe such many-body processes theoretically and to relate the measured spectra to real electronic properties, the most important assumption is that the response of the system to the photoexcitation is much slower than the emission process itself, i.e. that the electrons leave the sample instantaneously before the system relaxes [71]. This assumption, called the *sudden approximation*, neglects the interaction of the photoelectron with the relaxation mechanisms of the system and allows to treat the photoemission process in a single-particle picture. This assumption becomes less appropriate for lower photon energies and thus slower photoelectrons, because their escape time will be closer to the system's response time [74]. Therefore, the sudden approximation breaks down for very low excitation energies [78].

The Phenomenological Three-Step Model of Photoemission

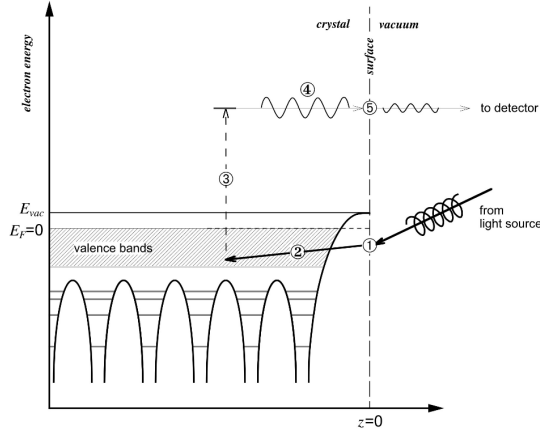


Figure 2.13: Schematic illustration of the three-step model of photoemission. Besides the original three-step model, whose individual steps are here labeled with 3 (optical excitation of the electron), 4 (travel of the electron through the material), and 5 (transmission through the surface and escape into vacuum), additionally, the steps marked with 1 and 2 denote the refraction and penetration of light in the material. (Taken from [75]).

The simplest theoretical approach to qualitatively describe photoemission in a single electron picture was given by Berglund and Spicer in 1964 [84] who divided the entire process into three independent steps, which termed this model the three-step model. The first step describes the *optical excitation* inside the solid, which leads to direct interband transitions of the electrons within the sample (step number 3 in Fig. 2.13). Secondly, the electrons have to *propagate through the material* towards the surface and experience elastic and inelastic scattering processes (step 4 in Fig. 2.13). Finally, in the third step, the electrons pass the sample surface and are *transmitted into vacuum* (step 5 in Fig. 2.13). In the following the single steps shall be examined further.

1st Step: Optical Excitation and Bulk Interband Transitions

The first step exclusively happens within the solid and its band structure. We will now consider the excitation of an electron from an initial Bloch state $|i, \mathbf{k}_i\rangle$ into a final Bloch state $|f, \mathbf{k}_f\rangle$. First of all, Eq. 2.26 holds and energy conservation requires that the initial and final state are separated by the photon energy, i.e. $E_f - E_i = \hbar\nu$. Moreover, momentum conservation has to be valid and therefore

$$\mathbf{k}_f = \begin{cases} \mathbf{k}_i & \text{reduced zone scheme} \\ \mathbf{k}_i + \mathbf{G} & \text{extended zone scheme} \end{cases} \quad (2.30)$$

which means that in the reduced scheme of the Brillouin zone the optical transitions can only be direct (vertical) and thus $\Delta\mathbf{k} = 0$, whereas in the extended scheme there can also exist transitions between k -points that are connected by the reciprocal lattice

vector \mathbf{G} provided by the bulk [74].

Note that formally, due to the particle nature of the photon there is a non-zero contribution of the photon momentum ($\mathbf{k}_{ph} = h\nu/c \neq 0$) which leads to indirect transitions $\mathbf{k}_f = \mathbf{k}_i + \mathbf{k}_{ph} + \mathbf{G}$. This term is usually neglected in UPS because it is small (0.011 Å for $h\nu = 21.2$ eV). However, it is in the same order of magnitude as the Rashba-splitting in Au(111) (≈ 0.02 Å, [85]) and therefore not negligible in times of very high angular resolution spectrometers.

Taking energy and momentum conservation laws into account, the first step of the photoemission process can be described quantum-mechanically by *Fermi's golden rule* which yields the transition probability $w_{i \rightarrow f}$ (proportional to the excited photocurrent, i.e. the PES intensity I) from an initial state $|i, \mathbf{k}_i\rangle$ to one of the possible final states $|f, \mathbf{k}_f\rangle$

$$I(E_{kin}, \mathbf{K}, h\nu) \propto \sum_{i,f} w_{i \rightarrow f} \propto \sum_{i,f} \underbrace{|\langle f | \mathcal{H}_{pert} | i \rangle|^2}_{\text{selection rules}} \times \underbrace{\delta(E_f - E_i - h\nu)}_{\text{energy conservation}} \times \underbrace{\delta(\mathbf{k}_i - \mathbf{k}_f + \mathbf{G})}_{\text{momentum cons.}} \\ \times \underbrace{\delta(\mathbf{k}_{f,\parallel} - \mathbf{K}_{\parallel}(\vartheta, \varphi))}_{\text{parallel momentum cons.}} \times \underbrace{\delta(E_{kin} - (E_f - \Phi))}_{\text{detection by analyzer}}. \quad (2.31)$$

Here, the first and second delta function warrant energy and (total) momentum conservation, respectively, whereas the third delta function represents the fact that the wave vector components parallel to the sample surface are conserved during surface transmission. Finally, the last delta function term depict the detection system by ensuring the equality of the measured kinetic energy and the final state energy inside the sample minus its workfunction¹⁴. The most important term, deciding about photoemission intensities and introducing dipole selection rules [75, 86], is the first one. This term is called the *transition matrix element* $M_{i \rightarrow f} = \langle f | \mathcal{H}_{pert} | i \rangle$ and describes the interaction of an electron with the incident photon field as a first-order perturbation given by

$$\mathcal{H}_{pert} = \frac{e}{2mc} (\mathbf{A} \cdot \mathbf{p} + \mathbf{p} \cdot \mathbf{A}) - e\phi + \frac{e^2}{2mc^2} \mathbf{A} \cdot \mathbf{A} \approx \frac{e}{mc} \mathbf{A} \cdot \mathbf{p}, \quad (2.32)$$

with the momentum operator \mathbf{p} and the electromagnetic vector potential \mathbf{A} . This equation uses the gauge of a vanishing scalar potential $\phi = 0$ of monochromatic waves in vacuum and the so-called *dipole approximation* assuming that \mathbf{A} varies only weakly over atomic distances¹⁵ (fulfilled for UV radiation) and therefore $\nabla \cdot \mathbf{A} = 0$. Further, non-linear processes due to very high photon flux are neglected ($\mathbf{A} \cdot \mathbf{p} \gg \mathbf{A}^2$).

Therefore, in the simplest picture of only optical transitions Eqs. 2.31 and 2.32 yield quantitative information about the photoemission process in terms of symmetries of the involved wave functions and restrictions such as the dipole selection rules.

¹⁴ Strictly speaking, the last two terms do not belong to the 1st step of the optical excitation but happen later and are here added just for the sake of completeness.

¹⁵ Note that this approximation might become non-valid at crystal surfaces due to strong spatial dependencies of the vector fields.

2nd Step: Propagation

The second step of the photoemission process describes the propagation of the excited photoelectron inside the material and towards the crystal surface. This step is the reason for the high surface-sensitivity or small probing depth of photoelectron spectroscopic methods, since light penetrates the material much deeper than the distance from which excited electrons are able to elastically escape.

The electrons will undergo scattering processes with other electrons, phonons or defects, which heavily reduce their undisturbed propagation range. A quantity which describes the average distance between two inelastic scattering processes is the inelastic mean free path λ (IMFP) of the electrons. The IMFP determines in an exponential damping law how the photoelectron intensity $I(d)$ of undisturbed electrons develops from its initial value I_0 as a function of a certain path length d as

$$I(d) = I_0 \exp\left(-\frac{d}{\lambda}\right). \quad (2.33)$$

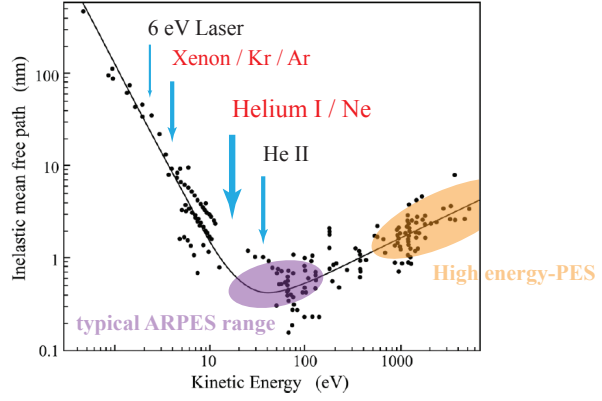
Due to the exponential nature of this law, virtually all undisturbed photoelectrons (> 95%) stem from a region within three times the IMFP, which means that the probing or information depth in photoemission is $\sim 3 \cdot \lambda$.

In a photoemission experiment only the unscattered and purely elastically scattered electrons contribute with sharp peaks or features to the spectrum, whereas inelastically scattered electrons contribute with a broad, featureless background, which is called the inelastic or secondary background. The short IMFP in solid systems in the order of 5 – 100 Å explains the high surface sensitivity of the photoelectron spectroscopy techniques (see estimation of IMFPs for different materials in Fig. 2.14). As one can see in Fig. 2.14 the general shape of the IMFP curve as a function of the kinetic energy of the excited electrons is universal for all materials with a minimum of only ≈ 5 Å. The maximum surface sensitivity can be expected at a kinetic energy of the electrons around 40 – 100 eV.

Especially the steep increase towards lower kinetic energies, where the universal curve predicts probing depths of 1 – 10 nm, is directly connected to the density of states of the occupied and unoccupied states in the vicinity of the Fermi level and the cross section of the underlying electron-electron scattering mechanisms can be described by an universally shaped loss function [78, 79]. However, this increase of the IMFP curve at lower kinetic energies is under strong debate.

Nevertheless, one can assume that for all photoemission data presented in this thesis, the surface-sensitivity is very high, which makes PES an ideal probe of surface related phenomena. On the other hand, this requires ultra-high vacuum (UHV) conditions and clean (adsorbate-free) crystal surfaces. Moreover, one can state that, according to the universal IMFP curve the often exploited Xenon excitation energy (E_{kin} of the photoelectrons $\sim 4 - 8$ eV) provides more bulk-sensitivity than spectra obtained with the Helium excitation energy ($E_{kin} = 4 - 21$ eV) or typical synchrotron VUV or soft X-ray energies, which are closer to the minimum probing depth [78].

Figure 2.14: The universal curve of the inelastic mean free path as a function of the kinetic energy of the photoexcited electrons inside the solid, reflecting the high surface sensitivity of photoelectron spectroscopy methods. The important photon energies used in this thesis and available in our ARPES laboratory are indicated. (Adopted from [87])



3rd step: Transmission and Escape into Vacuum and the Free-Electron Final State Model

The last step of the three-step model describes the transmission of the photoelectron through the crystal surface. It relates the measured emission angles and the momentum of the electron in vacuum \mathbf{K} to the initial crystal momenta \mathbf{k} . This relation is only possible (without very complicated calculations) using the very common simplification of the *free-electron final-state model* which assumes that the final Bloch eigenstates inside the sample are matched onto free-electron plane waves in vacuum [74].

The existence of the surface breaks the translational symmetry of the crystal along z -direction and introduces an abrupt but smooth change of the potential along the surface normal by matching the periodic crystal potential to the vacuum-level¹⁶, the electron wave vector component normal to the surface k_{\perp} is not conserved during the transmission.

The parallel components of the wave vector \mathbf{k}_{\parallel} , on the contrary, remain good quantum numbers and are therefore conserved in the process, assuming the symmetry of the surface potential matches that of the bulk¹⁷. Thus, the initial electron momentum

$$k_{\parallel,x} + k_{\parallel,y} = \mathbf{k}_{\parallel} = \mathbf{K}_{\parallel} = \sqrt{\frac{2m}{\hbar^2} E_{kin}} \cdot \sin \vartheta \quad (2.34)$$

can be directly derived from the measurable quantities E_{kin} and ϑ . However, in order to probe the full 3-dimensional electronic band structure $E(\mathbf{k})$, one also needs to determine the perpendicular component k_{\perp} , which is not at all trivial. Within the free-electron final-state picture and making use of $E_f = E_{kin} + \Phi$ (from Eq. 2.26),

$E_f(\mathbf{k}) = \frac{\hbar^2 (\mathbf{k}_{\parallel}^2 + k_{\perp}^2)}{2m} - E_0$, and Eq. 2.34, the perpendicular component can be approximated by

$$k_{\perp} = \sqrt{\frac{2m}{\hbar^2} (E_{kin} \cos^2 \vartheta + V_0)} \quad (2.35)$$

¹⁶ Usually approximated by a smooth potential step function along the surface normal.

¹⁷ Furthermore, reconstructed crystal surfaces can add another surface-related momentum vector $\mathbf{G}_{surf} \neq 0$ to the electron, which are so-called surface Umklapp scattering processes [88]

where E_{kin} and θ are again directly observed quantities. $V_0 = E_0 + \Phi$ is the *inner potential* corresponding to the lowest energy of the valence band E_0 with respect to the vacuum level E_V (see Fig. 2.12(a)). The model assumes that, in order to fulfill the energy conservation, only the momentum component k_{\perp} is reduced to overcome the binding energy and the surface potential, whereas the k_{\parallel} component is conserved.

The parameter V_0 makes 3D band mapping complicated, since it can only be empirically determined by (i) purely theoretical band structure calculations of all electronic states, by (ii) optimizing the agreement between measured and calculated data, or by (iii) experimental band mapping and looking for symmetries and periodicity in the measurements [71, 74]. In general, the determination of k_{\perp} in 3D band mapping, requires a tunable light source such as a synchrotron because one needs to vary the photon energy (and thus E_{kin}) smoothly, in order to select different transitions between initial and final bands for different k_{\perp} , i.e. a different cut through the 3-dimensional bulk Brillouin zone.

It has to be noted that Eq. 2.35 and the free-electron final-state approximation is only valid for either materials which exhibit a simple (free-electron-like) spherical Fermi surface topology such as alkali metals, or in general for higher exciting photon energies ($h\nu > 300$ eV). In this case the energetically higher final states become so dense in energy that they nearly form a continuum and, moreover, the crystal potential becomes only a negligible perturbation [74].

On the other hand, the free-electron final-state model describes the experimental findings often satisfactorily well. This thesis will mainly focus on the surface electronic structure of topological insulators, whose surface states can be seen as ideal 2-dimensional systems and therefore completely lack out-of-plane or k_{\perp} -dispersion (see section 2.5).

Quantum-Mechanical One-Step Model

The major drawback of the three-step model is that it can only provide a qualitative description of the photoemission process. It can serve as a reasonable approximation and it predicts which transitions are allowed and which not, but it first of all is in many cases only a rough approximation, secondly it cannot explain quantitative differences in the photoemission intensities due to photoemission-induced effects like dichroism, and more important, the influence of the sample surface is not sufficiently taken into account. For example, states that are located close to the sample surface can not be described by propagating Bloch waves and, in general, the three-step model cannot discriminate between surface and bulk electronic structure.

Therefore, a more accurate theory to quantitatively describe the photoemission process was developed by J. Pendry in terms of a one-step model approach treating photon absorption, electron removal and detection as a single, quantum-mechanical, and coherent process [72, 89]. On the basis of a realistic band structure calculation of a semi-infinite system derived by DFT (see section 2.6) this formalism is able to correctly take into account surface states, transitions into evanescent final states¹⁸, and multi-

¹⁸ If no vacuum plane wave at the final state energy can be matched to the bulk electronic Bloch state, the final state will be an exponentially decaying (Bloch) state inside the sample, called an evanescent

ple scattering effects in the final state due to strong electron-electron interactions [90]. In this respect the one-step model treats the photoemission process, in close analogy to low energy electron diffraction (LEED), in a *time-reversed LEED* formalism. Photoemission can be understood as a time-reversed version of an electron wave entering a crystal and subsequently experiencing multiple scattering events. The photocurrent in the one-step model is expressed as:

$$I \propto \sum_{\text{occupied}, i} |\langle \Psi_{LEED}^*(E_f, \mathbf{K}) | \mathbf{A}_0 \cdot \mathbf{p} | \Psi_i(\mathbf{k}) \rangle|^2 \times \delta(E_f - E_i - h\nu) \quad (2.36)$$

with the time-reversed LEED state Ψ_{LEED} as a final state which already contains the coupling to vacuum and all effects contained in the second and third step of the three-step model. Possible types of initial (right side) and final states (left side) are schematically depicted in Fig. 2.15 and shortly explained in the caption. However, the computational effort of one-step model calculations is high and only a few groups in the world are able to quantitatively simulate full photoemission spectra.

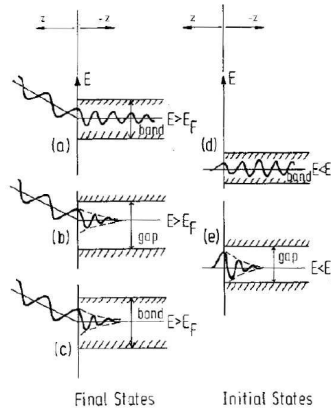


Figure 2.15: Final and initial states involved in the time-reversed LEED formalism of photoemission. In all cases, the interface between the solid and vacuum, where the electron wave functions have to match, is shown. Final states: **(a)** weakly damped Bloch wave, **(b)** and **(c)** evanescent states in a band gap or a band, respectively. Initial states: **(d)** pure bulk Bloch state, **(e)** surface state inside a forbidden gap. (Taken from [71]).

2.4.2 Single-Particle Spectral Function $A(\mathbf{k}, E)$ and Electron Self-Energy $\Sigma(\mathbf{k}, E)$

All the considerations above assume that the electronic structure can be modelled within a single-electron picture, which, however, is not sufficient to capture the influences of electronic correlations in a many-electron system. In other words, according to Fermi's golden rule (Eq. 2.31) and its delta functions, the features in an ideal photoemission spectrum should be infinitely sharp lines. However, in a real measurement

state.

every feature, both in core level as well as valence band photoemission, will have a finite spectral width (as already indicated in Fig. 2.12), which is a consequence of the quantum-mechanical nature of the photoemission process. These effects will play a major role in many-electron or strongly correlated systems such as transition metal oxides, high-temperature superconductors, or multiferroic materials.

In solid state quantum physics¹⁹ it is possible to properly implement the correlated interactions of an N electron ensemble, i.e. the excited photoelectron and the remaining $N - 1$ electron system with a single missing charge (photohole), using the Green's function formalism $G(\mathbf{k}, E)$ [72]. It is generally used to describe the behavior of quasiparticles that are 'dressed' by the electronic correlations and the electron-hole interaction [75]. In photoemission the collective Coulomb interaction of the photoelectron and the modification in the potential landscape caused by its excitation can be described as an emergent phenomenon by a quasiparticle or a collective excitation. The quantum-mechanical quantity called the *complex self-energy* $\Sigma(\mathbf{k}, E) = \text{Re}\Sigma(\mathbf{k}, E) + i \cdot \text{Im}\Sigma(\mathbf{k}, E)$ represents the energy correction of an electron with the initial energy E and the momentum \mathbf{k} moving through an interacting many-body system. Its real part $\text{Re}\Sigma$ shifts the energy of the quasiparticles and thus introduces a renormalization to the bare (single-particle) band energy ϵ , whereas the imaginary part $\text{Im}\Sigma$ reflects the finite lifetimes of these states and thus leads to a broadening of the spectral features [91].

This formalism can be connected to photoemission spectra by the *single-particle spectral function* $A(\mathbf{k}, E)$ which is proportional to the imaginary part of the Green's function. $A(\mathbf{k}, E)$ gives the probability of removing or adding a single electron of energy E and wave vector \mathbf{k} to the system. Both can be expressed in terms of the complex self-energy by

$$G(\mathbf{k}, E) = \frac{1}{E - \epsilon - \Sigma(\mathbf{k}, E)} \quad (2.37)$$

$$A(\mathbf{k}, E) = -\frac{1}{\pi} \text{Im}G(\mathbf{k}, E) = \begin{cases} \delta(E - \epsilon) & \text{noninteracting system} \\ -\frac{1}{\pi} \frac{\text{Im}\Sigma(\mathbf{k}, E)}{[E - \epsilon - \text{Re}\Sigma(\mathbf{k}, E)]^2 + [\text{Im}\Sigma(\mathbf{k}, E)]^2} & \text{interacting system.} \end{cases}$$

The spectral function $A(\mathbf{k}, E)$ replaces the energy conservation term in Eq. 2.31 for a more accurate description of the experiment.

Because of its momentum- and energy resolution, ARPES is a direct probe of the single-particle spectral function. Thus it can be used, in principle, to determine real and imaginary part of the electrons self-energy. Therefore, ARPES is well-suited to study effects induced by many-body interactions, such as energy shifts or lifetime broadening due to the described energy renormalization, because the photoemission linewidths contain information about the lifetimes of both photohole and photoelectron [92, 93]. Figure 2.16 depicts these effects by an illustration of hypothetical experimental ARPES spectra of a non-interacting electron system revealing ideally sharp peaks (b) and the same shifted and broadened spectral features from a real measurement of a correlated material (c).

¹⁹ and in the limit of the sudden approximation.

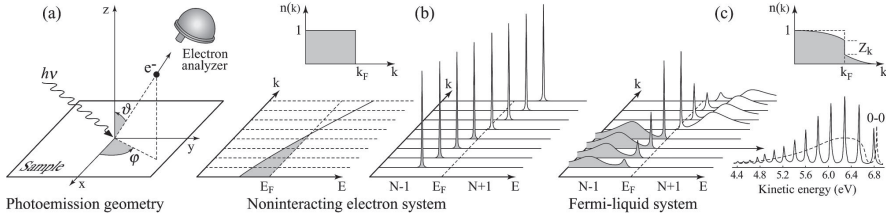


Figure 2.16: Relation of the photoemission signal to initial states. (a) Geometry of an ARPES experiment. (b) Energy distribution curves (right) for different points in k -space for a non-interacting electron system with a single band dispersing across the Fermi level E_F (left). Here the spectral features are a perfect delta functions. (c) The same spectra for a realistic case of an interacting Fermi-liquid. One can see that the peaks are shifted in their energetic position by $\text{Re}\Sigma$ and gain a finite width due to $\text{Im}\Sigma$, if many-body quasiparticle interactions are considered. Additionally, the corresponding ground state ($T = 0$ K) momentum distribution function $n(\mathbf{k})$ is shown. Renormalization of the electronic dispersion smears the ideal step function. (Taken from [93]).

As mentioned above, ARPES can be used to directly probe the spectral function and extract information about the physics of the quasiparticle many-body correlations in the solid. Modern multichannel electron spectrometers acquire 2D images that simultaneously contain information about energy and angle (momentum) within a single measurement (section 3.1 provides detailed information). However, a typical ARPES dataset can be separated for analysis into energy distribution curves (EDCs) and momentum distribution curves (MDCs) which are cuts through the data set at certain constant k or constant binding energy E_B , respectively. Since both MDCs and EDCs contain all the information necessary to determine $\Sigma(\mathbf{k}, E)$, both can be used to extract quasiparticle peak positions and lineshapes, which are related to their lifetimes. However, usually MDCs have much simpler lineshapes, because the inelastic background and the low-energy cutoff caused by the Fermi-Dirac function depend strongly on energy but only weakly on momentum and thus have to be taken into account in EDC but not in MDC analysis. Also the self-energy itself depends weakly enough on the momentum that it can be assumed constant along the MDCs. Thus, simple Lorentzian centroids fitted to the MDCs determine the band dispersion of the renormalized quasiparticle state (the real part of the self-energy $\text{Re}\Sigma$), while EDCs are usually better suited to extract the lifetime of the states (the imaginary part $\text{Im}\Sigma$) [78].

Especially in low-dimensional systems, such as electronic surface states, the lack of k_\perp dispersion additionally simplifies the situation because the width of the photoemission peaks is directly related to the lifetime of the photohole, as the contribution of the final state to the lifetime broadening vanishes [92, 93]. Moreover, topological surface states are typically considered as weakly interacting states [94–96] and, more importantly, can be assumed as linearly dispersing in small energy windows. Hence, in this thesis quasiparticle lifetimes τ and thus scattering rates Γ of the TSS electrons will be extracted (section 4.2.2) from the half width at half maxima (HWHM) of Lorentzian

peaks $\Delta\mathbf{k}(E)/2$ fitted to the MDCs. For this, the direct relation

$$1/\tau = \Gamma = 2 \cdot \text{Im}\Sigma = v_g \Delta\mathbf{k}(E) \quad (2.38)$$

can be used, assuming a constant group velocity $v_g = \frac{\partial E}{\hbar \partial k}$, i.e. a linear dispersion of the TSS [92, 97].

2.4.3 Spin-Resolved Photoemission

In this section the basic concept of spin-resolved photoelectron spectroscopy (spin-ARPES) shall be very briefly depicted. In section 2.3.2.1 we have seen that spin-ARPES can provide very strong experimental evidence for answering the question, whether a surface state is topologically trivial or non-trivial, since a necessary condition for a TSS is its strong helical spin polarization. This will be important, because as we will see in chapter 7, there are surface states without spin polarization that can easily be confused with typical TI Dirac cone-like surface states. In this matter, only spinARPES can provide experimental answers.

In order to measure the spin polarization of the excited photoelectrons, one can employ the spin dependence in a scattering experiment (see Fig. 2.17). We consider a spin-polarized beam of electrons that has been filtered for the energy E and the wave vector \mathbf{k} by an angle-resolving spectrometer. This polarized beam impinges now under normal incidence onto a W(001) single crystal and the electrons experience a low energy electron diffraction (LEED) process. Due spin-orbit coupling and differing scattering probabilities of spin up and spin down electron, the electron scattering process at a target with high atomic number Z is highly spin-dependent. Therefore, this spin-polarized LEED (SPLEED) process causes a left-right asymmetry A_x of the backscattered electron beam (along P_x direction in Fig. 2.17). Exploiting this asymmetry between left and right scattered electrons I_L and I_R , respectively²⁰, the spin polarization P_x of the beam of electrons can be determined by

$$P_x(E, \mathbf{k}) = \frac{A_x(E, \mathbf{k})}{S} = \frac{1}{S} \cdot \frac{I_L(E, \mathbf{k}) - I_R(E, \mathbf{k})}{I_L(E, \mathbf{k}) + I_R(E, \mathbf{k})} \quad (2.39)$$

with the measured intensities I_L and I_R , which are related to the spin-resolved partial intensities $I_{\uparrow, \downarrow}$ for spin up and spin down electrons and a given spin quantization axis defined by the scattering geometry [32]. The quantity $S = [0, \dots, 1]$ is called *Sherman function*²¹ and reflects the efficiency of the detector to separate the two spin directions, taking into account the details of the scattering process. Typically, for SPLEED detector schemes the Sherman function can be approximated by $S \approx 0.27$ [58]. For comparison of the efficiency of different spin detection principles, a figure of merit was introduced:

²⁰ Note that 'left' and 'right' relate to specific LEED diffraction spots ($I_L = I_{20}$ and $I_R = I_{\bar{2}0}$) and the nomenclature depends on the particular geometry. In our geometry, left and right scattered electrons are used to determine the in-plane spin polarization of the sample. The SPLEED detection scheme, however, allows the simultaneous detection of the samples out-of-plane spin polarization P_y by the 'up-down asymmetry', according to Fig. 2.17.

²¹ Strictly, the term Sherman function was induced for the Mott scattering process solely, and the more general term *asymmetry function* could be used instead.

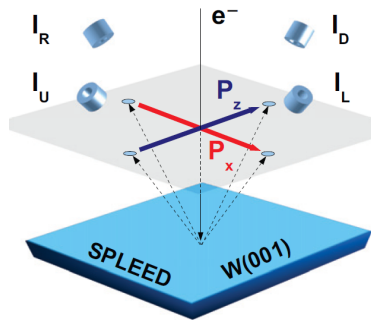
FoM = $\frac{I}{I_0} \cdot S^2$. It depends on the efficiency of the spin-dependent selection process, represented by S , and the reflectivity $\frac{I}{I_0}$ of all incoming electrons I_0 that reach the detector [88].

However, knowing the spin polarization value $P_x(E, \mathbf{k})$ and the spin-integrated total intensity $I_{\text{total}}(E, \mathbf{k}) = I_L(E, \mathbf{k}) + I_R(E, \mathbf{k})$, the spin-resolved partial intensities of spin up and spin down electron beam can be recovered respectively by

$$I_{\uparrow, \downarrow} = \frac{1}{2} \cdot I_{\text{total}}(E, \mathbf{k}) \cdot (1 \pm P_x(E, \mathbf{k})). \quad (2.40)$$

A nice comparison of different spin detection schemes and polarimeters is given in [58] and [98].

Figure 2.17: Description of the SPLEED detection scheme. An incoming beam of spin-polarized electrons scatters under normal incidence at a W(001) crystal surface. Four independent channeltrons positioned in the four LEED spots allow the detection of in-plane and out-of-plane (P_z and P_x) spin polarization by the scattered asymmetry, simultaneously. (Taken from [47]).



2.5 Surface Electronic Structure

In general, the existence of the surface transforms an infinite, periodic bulk crystal into a semi-infinite one. The breaking of the symmetry alone has a severe impact on the electronic structure. On top of that, one usually finds that instead of an ideal sharp truncation of the bulk structure, the atomic lattice tries to minimize the potential step at the surface by rearrangement of the topmost atomic lattice sites (e.g. by the creation of surface reconstructions). Thus, atomic positions and consequently the electronic configuration in the first few layers at the surface relax and differ from the bulk which gives rise to new two-dimensionally localized surface electronic bands. These surface bands are called *surface states*, if they are located in a gap of the projected bulk band structure, or *surface resonances*, if they occur within the projection of the bulk bands onto a specific surface.

Historically, one distinguishes between Tamm [99] and Shockley [100] surface states, for the case of *d*-like, tightly bound or *sp*-like, nearly free electrons in the ideal surface region, respectively. However, there is no real physical distinction between the two different terms [101]. The latter arise as the solution of the Schrödinger equation in the framework of the nearly free electron approximation for clean and ideal surfaces, which is suited for the description of metals and narrow gap semiconductors (such as topological insulators).

Pendry and Gurman [102] formulated general criteria for the existence of surface states: For example, if two bands can be approximated as nearly free electron plane waves and have the same symmetry, they will hybridize and open up a band gap in which a surface state will be localized [103]. Moreover, if spin-orbit interaction induces a band gap that is located between two high-symmetry points, this band gap will always host a surface state [102].

Additionally to these general criteria for metals and semiconductors, the topological band theory has taught us that metallic (topological) surface states have to be present at every interface of two materials where the topological character changes from trivial to non-trivial (see section 2.3). Trivial surface states, which heavily depend on the electronic configuration of the surface atoms and which are very sensitive to contaminations saturating the dangling bonds, require very clean vacuum conditions and usually show a time-dependent deterioration. Topologically non-trivial surface states, on the other hand, are caused by the change in topology, being a bulk parameter, and are thus very robust under disorder or contamination.

In any case, one always has to distinguish between the 3D bulk electronic structure $E(\mathbf{k})$, yielding nearly a continuum of bands when projected onto a certain surface, and the additional distinct 2D surface electronic structure $E(\mathbf{k}_{\parallel})$. Figure 2.18 illustrates this on the example of a band structure calculation of a 100 QL slab²² of Bi_2Se_3 . Note also, that the dispersion is shown along surface high-symmetry directions $\bar{\Gamma}\text{M}$ and $\bar{\Gamma}\text{K}$ in the 2D surface BZ. The color code reveals the surface localization. The deeper lying bulk states (violet-dark) are projected onto the (111)-surface and form a quasi-continuum²³, while the localized surface states (yellow) show distinct and sharp features in the projected bulk band gaps. In the figure, the upper yellow surface state is the topological state, closing the band gap, while the lower one is an ordinary surface state in a SOC induced band gap as predicted by Pendry and Gurman [102], which is, however, additionally spin-split due to the Rashba-effect at the surface.

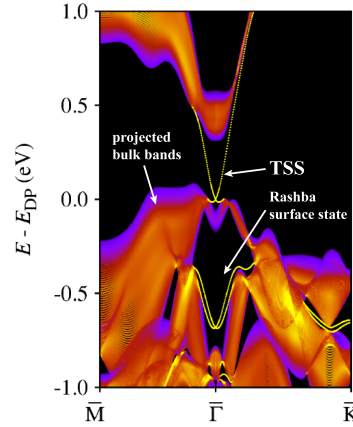


Figure 2.18: Surface electronic DFT slab calculation $E(\mathbf{k}_{\parallel})$ of a 100 QL slab of Bi_2Se_3 along (111) direction using the local density approximation. Color coded is the contribution of the first QL (1 nm): yellow = surface state, violet = bulk. (Calculated by I. Aguilera, PGI-1).

²² In DFT calculation of larger systems one has to model the periodic crystal by multiplication of smaller ‘unit cells’, called slabs, that have surfaces on both sides and are separated by vacuum. Here e.g. one QL of the 3D TI Bi_2Se_3 .

²³ Every single band of the projected band structure represents a different cut through the 3D Brillouin zone, i.e. a different k_{\perp} .

The surface breaks the translational symmetry of the crystal perpendicular to the surface. Therefore, only the electron wave vector \mathbf{k}_{\parallel} parallel to the surface remains a good quantum number and is conserved while k_{\perp} is not a good quantum number anymore, and the surface mixes states with the same E and \mathbf{k}_{\parallel} but different k_{\perp} [102]. In other words, surface related electronic states have a vanishing or negligible out-of-plane dispersion $E(k_{\perp})$, which makes them optimally suited for ARPES investigations. Moreover, as we have seen above, photoemission is a very surface sensitive technique. And, since this thesis will mainly present results obtained with very high resolution and photoelectrons of kinetic energies close to the minimum of the universal curve (Fig. 2.14), “the volume contained in the first surface layer can be responsible for roughly half the PE signal” [71]. This is the reason for the facts that photoemission is so sensitive to surface contaminations, surface roughness or reconstructions but it is also ideally suited to study distinct surface states.

2.6 Density Functional Theory

Since many of the experimental ARPES results shown in this thesis will be compared to ab-initio band structure calculations performed by our colleagues from PGI-1, this section shall introduce the basic ideas of *density functional theory* (DFT) calculations.

In order to precisely describe the state of a many-body system consisting of a huge number of interacting particles, one would need to calculate a many-body wave function that reflects the position of every single particle in the system. Already for small systems of crystalline solids this becomes numerically enormously demanding and cannot be managed even by highest power computers. Therefore, the first approximation that is always employed is the Born-Oppenheimer approximation that neglects the motion of the atomic nuclei compared to that of the electrons in the system. This implies that the electronic structure can only be simulated for a certain given atomic geometry and that, especially at the surface of the solid, the atomic positions need to be relaxed according to classical mechanics and energy minimization principles before the band structure can be calculated.

Next, in order to reduce the complexity of the problem, DFT makes use of the Hohenberg-Kohn-Sham theorem [104, 105] which states that the total energy of a atomistic many-particle system E can be expressed as a functional of its electron density $\varrho(\mathbf{r})$, i.e. $E = E[\varrho(\mathbf{r})]$, and that E is minimal for the system’s ground-state electron density $\varrho_0(\mathbf{r})$ [106] and thus

$$E[\varrho_0(\mathbf{r})] \leq E[\varrho(\mathbf{r})] = T_e[\varrho(\mathbf{r})] + E_{N-e}[\varrho(\mathbf{r})] + E_{e-e}[\varrho(\mathbf{r})], \quad (2.41)$$

where T_e gives the kinetic energy of the electrons and E_{N-e} and E_{e-e} are terms describing the nuclei-electron and electron-electron interaction, respectively, and are all also functionals of the electron distribution. Using this theorem the many-body problem can be transferred into an effective single-particle problem where the classical

Schrödinger equation needs to be solved with an effective Hamiltonian

$$\begin{aligned}
 \mathcal{H}_{eff} = & \underbrace{\frac{-\hbar}{2m}\nabla^2}_{\text{kinetic energy}} - \underbrace{e^2 \sum_i \frac{Z_i}{|\mathbf{r} - \mathbf{R}_i|}}_{N-e \text{ Coulomb attraction}} \\
 & + \underbrace{e^2 \int \frac{\rho(\mathbf{r}')}{|\mathbf{r} - \mathbf{r}'|} d\mathbf{r}'}_{e-e \text{ Coulomb repulsion}} + \underbrace{V_{ext}(\mathbf{r})}_{\text{external potential}} + V_{xc}(\mathbf{r}). \quad (2.42)
 \end{aligned}$$

The only non-classical term without a simple physical meaning or analogon here is the last one V_{xc} , known as the exchange-correlation potential capturing all the electron-electron interactions and correlations, and it is the main quest in DFT to find successful approximations for this term.

DFT-LDA

The first, very successful and widely used approximation is the *local-density approximation* (DFT-LDA), which assumes a homogeneous electron gas and the fact that the exchange-correlation energy depends only on the local electron density of each volume element $d\mathbf{r}$

$$E_{xc}^{LDA}[\rho(\mathbf{r})] \approx \int \rho(\mathbf{r}) \epsilon_{xc}^{LDA}[\rho(\mathbf{r})] d\mathbf{r} \quad (2.43)$$

with the exchange-correlation energy per particle $\epsilon_{xc}[\rho]$ which can be split into an exchange and a correlation energy contribution $\epsilon_{xc}[\rho] = \epsilon_x[\rho] + \epsilon_c[\rho]$. The former exchange energy is given by $\epsilon_x[\rho] \propto \int \rho(\mathbf{r})^{4/3} d\mathbf{r}$, while the latter correlation energy can only be numerically estimated by Monte Carlo simulations [107]. For spin-resolved density-functional theory calculations, the spin-degenerate charge density is replaced by a spin densities $\rho(\mathbf{r}) \rightarrow \rho(\mathbf{r}) = \rho_{\uparrow}(\mathbf{r}) + \rho_{\downarrow}(\mathbf{r})$ with the spin up and spin down configurations ρ_{\uparrow} and ρ_{\downarrow} , respectively. Hence, the LDA extends to a *local spin density approximation* (LSDA).

DFT-GGA

The second common approach to evaluate the exchange-correlation energy, is the *generalized gradient approximation* (DFT-GGA), which is in recent years considered to generally improve the description of total energies, ionization energies, electron affinities of atoms or other solid state properties especially in strongly inhomogeneous systems [106]. Here, the exchange-correlation energy may be written as

$$E_{xc}^{GGA}[\rho(\mathbf{r})] \approx \int \rho(\mathbf{r}) \epsilon_{xc}^{GGA}(\rho(\mathbf{r}), \nabla \rho(\mathbf{r})) d\mathbf{r} \quad (2.44)$$

meaning that it locally depends on the electronic density ρ and its gradient $\nabla \rho$ which makes it much more suitable to describe spatially inhomogeneous systems

FLAPW

In order to actually calculate the electron wave functions and thus the electronic band structure, one needs to make further assumptions for the construction of suitable basis functions. All DFT ground state calculations shown in this thesis have been calculated using the FLEUR code package (see [108]) which is based on the self-consistent *full-potential linearized augmented-plane-wave method* (FLAPW). It has its origin in the augmented-plane-wave method (APW) introduced by Slater [109], who separated the real space in a periodical crystal into spherical regions around the atoms ('muffin-tins') and interstitial regions between the spheres and assumed energy dependent (augmented) basis functions (plane waves) as the eigenfunction of this problem. The next step of linearized APW (LAPW) replaces the energy-dependence of the eigenfunctions by selecting a fixed set of muffin-tin radial functions and their energy derivatives [106]. Finally, the full-potential LAPW method treats all electrons as well as charge density and the potential in a fully relativistic, self-consistent way without any assumptions about the potential shape. This makes the FLAPW method the most successful and accurate one amongst DFT approaches for the calculation of the electronic structure and the correct prediction of effects due to spin-orbit coupling.

However, next to all advantages and achievements of DFT, one should not forget that it is based on the electronic charge density in the equilibrium ground state of the system and can thus only predict the initial, undisturbed electronic structure of solids. DFT can by definition not accurately simulate excited states and is known to systematically underestimate the sizes of the band gaps in semiconductors and insulators, because they are a ground-state property and DFT suffers from the correct treatment of quasiparticle self-interaction and many-body effects [110]. Especially for topological insulators the size of the band gap is of crucial importance because it may decide whether the gap is able to invert or not which means whether a material is topologically trivial or not. Therefore, more complicated methods based on the GW approximation, which includes many-body correlation effects in the complex self-energy $\Sigma(E)$, can be used for the more accurate description of correlated materials [110, 111]. Due to the better reproduction of experimental band gap sizes and its direct or indirect nature, we will later also use GW calculations performed by I. Aguilera from PGI-1 to interpret the ARPES data.

On top of these intrinsic and material-specific many-body correlation effects, the photoemission process induces further complication and a modification of the electronic structure. In order to correctly model photoemission spectra with all the special allowed and forbidden optical transitions, (spin-dependent) intensity modulations due to light-induced coupling effects, such as magnetic dichroism, surface effects or correct final states, more complicated photoemission calculations exploiting the one-step model of photoemission (see section 2.4.1) have to be used [90]. Here, DFT band structure calculations serve as input files for the initial states and the whole photoemission process has to be simulated subsequently.

Nevertheless, due to the lower computational efforts and the higher availability of DFT-LDA or -GGA band structure calculations, they are commonly used to compare and interpret photoemission and ARPES results and to study the initial band structure of complex materials.

CHAPTER 3

Experimental Setup

This chapter will introduce the details of the angle-resolved photoelectron spectroscopy experiments. Most of the results presented in this thesis have been obtained with the laboratory-based high energy and angular resolution ARPES machine. The ARPES setup was upgraded with new analysis and preparation chambers, which will be introduced in this chapter in detail. The last section will explain how spin-polarized ARPES measurements (in chapter 7) have been carried out at our synchrotron-based ARPES apparatus at the beamline 5 of the DELTA synchrotron in Dortmund.

Additionally, other *ex situ* experimental methods like core-level X-ray photoelectron spectroscopy (XPS), X-ray diffraction techniques (XRD), scanning tunneling microscopy (STM) and scanning transmission electron microscopy (STEM) have been exploited for characterization of the samples, but shall only be briefly introduced in the individual results sections.

Standard experiments were carried out with MBE-grown thin film samples that were either previously exposed to air or samples that were transferred from the MBE system into the ARPES apparatus by means of a vacuum transfer suitcase under UHV conditions (see appendix). In the first case the sample surfaces needed to be cleaned using additional preparation procedures in the ARPES preparation chamber. The vacuum transfer method is definitely preferable, because it prevents the sample surfaces from oxidizing and getting contaminated and thus saves irreversible cleaning steps, but it is much more time consuming. Additionally, all samples have been characterized *ex situ* later.

3.1 The High-Resolution ARPES apparatus at PGI-6

Since photoelectron spectroscopy is such a surface sensitive technique, it requires atomically clean, adsorbate free sample surfaces. Furthermore, the excited electrons that leave the sample need to travel on an undisturbed path to the electron detector which can be a few m away from the sample and only unscattered electrons carry the information about the electronic structure of the sample. Therefore, PES experiments need to be carried out in ultra-high vacuum conditions with very a low density of resid-

ual gas atoms or molecules (pressure of $p < 5 \cdot 10^{-9}$ mbar). The base pressure in our ARPES setup is typically $5 - 10 \cdot 10^{-11}$ mbar. Under such conditions the gas density, i.e. residual molecules per unit volume, is around $10^{12} \frac{1}{\text{m}^3}$, which leads to an average distance that a particle, e.g. an electron, can travel before it experiences a collision with another particle, is around 10^4 m. This is sufficiently long to reach the detector unscattered. More importantly, based on the ideal gas equations, one can estimate the average time until a clean surface becomes covered by a complete monolayer of residual gas adsorbates. Under atmospheric conditions the surface of a sample will be covered completely within 1 ns but at 10^{-10} mbar it takes around $10^4 \text{ s} \approx 3 \text{ h}$ until the sample will be covered with one monolayer. This value will of course depend on the exact composition of the residual gas and the material specific sticking coefficient, which is a measure of the probability that incident molecules adsorb on the surface. The sticking coefficient depends on the temperature such that low sample temperatures will drastically decrease the time span until the surface is covered. These facts should be kept in mind, because for PES experiments the cleanliness of the sample surface is crucial and its temporal evolution defines the timeframe of a typical experiment. In chapter 5.1 a clear time dependence of the ARPES signal due to contamination of the sample surface will be presented.

UHV conditions in the system described here are achieved by several turbomolecular pumps and titanium sublimation pumps (TSPs). The turbomolecular pumps are prepumped by another stage of turbomolecular pumps, themselves prepumped by oil-free scroll pumps. Thus, by achieving best possible prevacuum conditions, the final base pressure in the system can be pushed to $< 1 \cdot 10^{-10}$ mbar. In our system, any kinds of strong electric or magnetic fields are intentionally relinquished. This is the reason why no ion getter pumps, which are commonly used to achieve lowest pressures, are employed.

Figure 3.1 depicts a CAD drawing of the entire laboratory-based ARPES apparatus. The setup consists of one 4-axis manipulator that vertically transfers the sample from the preparation chamber into the main chamber, where the large hemispherical electron analyzer and the different light sources are located. The following subsection will describe both preparation and analysis chambers in detail.

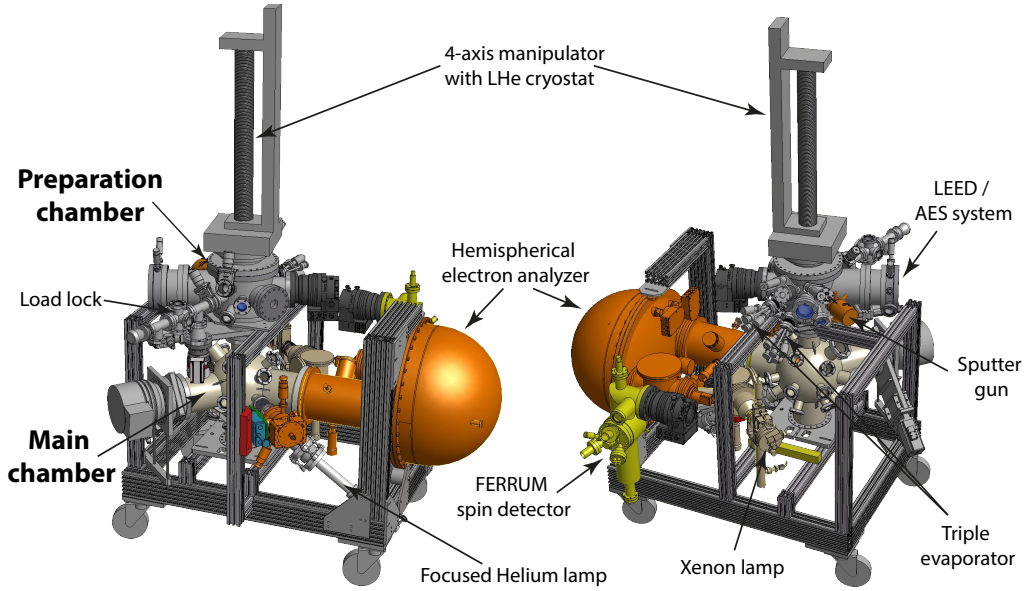


Figure 3.1: Schematic front and back view of the laboratory-based HR ARPES system in PGI-6, Research Center Jülich. The geometry of preparation and main chamber was chosen to be vertical in order to provide most stable sample positioning and rotation. (Courtesy of B. Küpper).

Preparation Chamber

MBE-grown thin films are mounted onto standard Omicron sample holders where they are usually mechanically fixed with a frame assuring good thermal contact for efficient cooling to low temperatures. The sample holder is then transferred via a small load lock chamber onto the four-axis manipulator in the preparation chamber. Figure 3.2 highlights the preparation chamber with all attached devices for sample preparation and analysis.

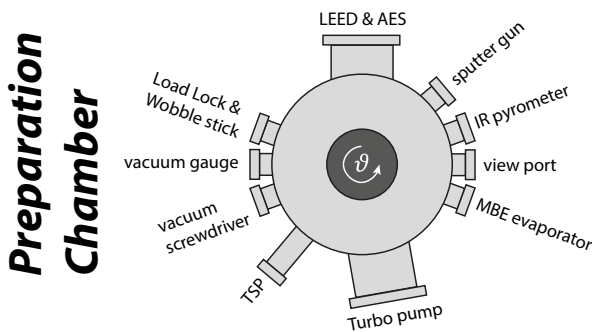


Figure 3.2: Simplified scheme of the upper preparation chamber.

Four-Axis Manipulator with Liquid He Cryostat

The system is equipped with one universal manipulator that can move in all three spatial directions. It allows a full rotation around the azimuthal θ angle, which is enabled by a differentially pumped rotary seal (head of the manipulator is shown in Fig. 3.3). The manipulator hosts a liquid helium flow cryostat, which can be cooled by additional rough pumping to 4.1 K. The temperature is controlled by a special, low-temperature Si diode at the end of the cryostat. However, this readout as well as the coldest spot are few cm away from the sample position. The lowest possible sample temperatures in our system, as determined by analysis of the metallic Fermi-Dirac distribution, are about 15 K. To achieve a good thermal contact between sample and manipulator, one can mechanically press the sample holder to the manipulator by two additional screws. These screws are tightened by a custom-made vacuum screwdriver. Figure 3.3 illustrates the estimated temperature gradient along the manipulator head.

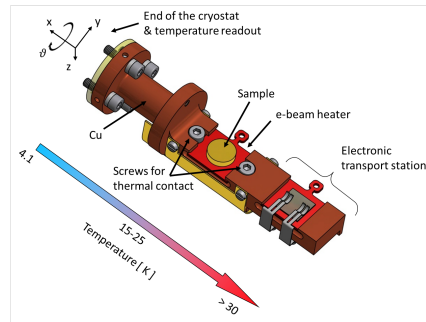


Figure 3.3: 3D sketch of our sample holder setup with indicated cooling efficiency. (Courtesy of B. Küpper).

Additionally, the sample stage features a second stage, which allows for simple two-point electronic transport measurements such as $R(T)$ or $U(I)$. Using this stage, observed transport properties shall be related to the directly probed electronic band structure *in situ*. However, such measurements were so far only preliminary and will not be shown within this thesis.

Annealing

PES experiments require atomically clean surfaces, since only unscattered electrons carry the desired information about the electronic structure. Therefore, all sample surfaces have to be cleaned prior to the ARPES measurements. The easiest and commonly used sample preparation treatment in surface science is annealing. Therefore, the sample holder hosts a tungsten filament behind the back side of the sample plate. Heat is produced by making use of the Edison effect, where electrons are emitted from the filament when electric current is applied. These electrons can be directed with a strong electric field to bombard the back plate of the sample holder. In this way temperatures up to 500 – 600°C can easily be reached. For the precise control of the sample temperature, the surface is observed using infrared pyrometers. We can apply a standard pyrometer operating $> 300^\circ\text{C}$ and a normal visible light viewport as well as a pyrometer operating between $-20 - 500^\circ\text{C}$ requiring a special ZnSe vacuum viewport for low-wavelength IR transmission. Knowing the material specific thermal emissivity

factor ε from literature values, the temperature can be measured with sufficiently high accuracy ($\pm 20^\circ\text{C}$).

For materials, which are in general rather non-reactive and inert, it can be enough to only anneal the sample under vacuum to $100 - 200^\circ\text{C}$ in order to desorb water and loosely bound adsorbates, such as carbon-hydrates or -oxides, from the surface. However, most of the samples that have been exposed to air will be oxidized. A perfect surface of a topological insulator, for example, would terminate with a saturated quintuple layer which should not form any bonds to adsorbates on the surface and is thus rather inert. In reality, however, vacancies in the crystal structure can be filled by oxygen and small carbon-complexes can intercalate in between the QLs e.g. at step edges due to the large van-der-Waals gaps. These contaminations deteriorate the crystal structure and thus have to be removed before one can probe the band structure by ARPES.

If the oxidized layer is not too large¹, a simple annealing step suffices to clean the surface, as it can be the case for Sb_2Te_3 thin films. Normally, however, 3D TI samples tend to oxidize severely and more 'aggressive' cleaning needs to be applied. In general, for the 3D TI thin films the annealing temperature needs to be kept below the MBE-growth temperatures ($T_{\text{Bi}} \approx 460^\circ\text{C}$; $T_{\text{Sb}} \approx 420^\circ\text{C}$; $T_{\text{Te}} \approx 330^\circ\text{C}$; $T_{\text{Se}} \approx 110^\circ\text{C}$) in order to avoid degradation or interdiffusion of the films and desorption of the metallic elements.

Sputtering

If annealing to elevated temperatures fails to remove the surface contaminations or strongly bound adsorbates, one can employ an irreversible method of noble ion bombardment, which is called sputtering and is based on the energy and momentum conserving process of ion collisions with the sample surface. In the system presented here, an UHV sputter gun is used which accelerates argon (Ar) ions to high kinetic energies ($500 - 1200\text{ eV}$; much higher than lattice bonding) towards the sample. The ions bombard the sample surface and remove the upper layers. Those ions that reach the sample generate a current which can be detected. This sample current I_s , the ion kinetic energy E , the argon partial pressure p_{Ar} and the sputtering time t are the important parameters during sputtering from which by further *ex situ* characterization and experience, sputtering rates and proper cleaning procedures can be developed. An example of the determination of the sputtering rate by Auger depth profiling will be presented in section 6.2.2.

Since sputtering can be quite rough and not necessarily homogeneous, the surface has to be healed by annealing afterwards. Thus, thermal energy is input into the sample, which mobilizes the surface atoms, in order to recrystallize the lattice. Nevertheless, since sputtering is an irreversible method based on the removal of atoms, one has to be very careful not to irretrievably destroy the thin film samples. Moreover, we will later see that the manipulation of the top atomic layers and the surface termination by sputtering, will also influence the surface electronic structure (section 7.3.4).

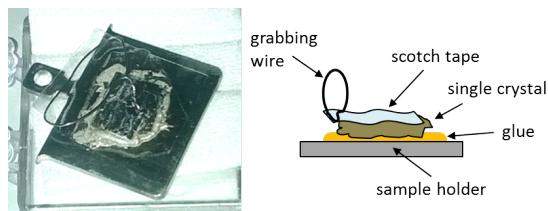
¹ Figure 7.5 in section 7.3.3 depicts a nice example of a topological insulator sample (investigated by TEM), where we can observe the size of the oxidized layer below the sample surface.

Cleavage of Single Crystals

The best way to create clean sample surfaces for photoemission is to use a mechanical force to truncate the crystal along a certain crystallographic direction where the atomic binding forces are lowest. This procedure, called cleavage, can result in macroscopically large and atomically flat and clean terraces of highest quality which are optimal for photoemission experiments. Especially for layered crystals, such as transition metal dichalcogenides (see Ref. A.4) or 3D TI bulk single crystals, the simplest way of cleavage by the 'scotch tape method' can be employed, due to the weak van-der-Waals binding between adjacent QLs.

The photograph and sketch below show how mechanical cleavage by scotch tape was employed on a bulk Sb_2Te_3 single crystal. When the scotch tape is removed from the crystal under UHV conditions using a wobble stick, the top layers of the material are removed. ARPES spectra of cleaved crystals compared to MBE grown thin films typically reveal sharper spectral features and less non-crystalline background signal. However, the disadvantages of bulk single crystals are the facts that cleavage typically results in atomically flat areas of only small size and that only thin film growth of TIs provides possibilities for future applications.

Figure 3.4: Photo and sketch of a mounted TI single crystal with attached scotch tape for in situ cleavage.



Low-Energy Electron Diffraction (LEED)

LEED is the most widely used technique to judge the crystalline quality and cleanliness of a sample in surface science experiments [71, 89]. LEED can not only determine the crystallographic orientation of a surface, but also tells about size and rotational alignment of specific surface reconstructions or adsorbate layers on clean surfaces. After preparation of the sample, the sample is placed in front of our combined LEED & AES system, which is equipped with an electron gun, several electrostatic lenses and a fluorescent phosphorous screen to image the diffracted electrons.

Electrons of kinetic energies between 20 and 200 eV are emitted from a LaB_6 cathode and accelerated and collimated under normal incidence onto the sample surface. Due to their low kinetic energy, electrons penetrate only few Å into the material (see Fig. 2.14) before they interact with the periodic 2D crystal structure, which acts as a diffraction grating, and are elastically backscattered onto the imaging screen. Thus, LEED is also a very surface sensitive technique. On the imaging screen distinct spots form characteristic LEED diffraction patterns that reflect the crystallographic orientation of the two-dimensional sample surface. The size, shape, and intensity as well as the signal-to-noise ratio of the LEED spots are directly related to the homogeneity and roughness

of the crystal surface. Further, from the observed patterns the in-plane lattice constants can be determined.

Auger Electron Spectroscopy (AES)

For a chemical analysis of our samples and for chemical depth profiling (see section 6.2.2) Auger electron spectroscopy can be employed using the combined LEED & AES system. This chemical analysis is mandatory because the MBE-grown samples have not been characterized in terms of their stoichiometries.

The AES process is based on the element-characteristic ionization of three different adjacent electronic core levels involved. Figure 3.5 depicts the process, schematically. The deepest atomic core level is excited by a high energy photon or electron beam (in this case a $1s$ electron) and the created hole is unstable and filled by an electron from the next $2s$ shell. When transitioning to the lower level, the electron loses a characteristic amount of energy which corresponds to the difference in orbital energies. Next, this transition energy can be coupled by a virtual photon into a third electron from the next $2p$ level, which can be emitted from the atom, if the energy is large enough. This last electron is then called the Auger electron and may also be detected with a spectrometer. Thus, the Auger process is a complicated multi-electron process but is widely used to identify characteristic elemental peaks and it does not require access to high energy photon sources. In a spectroscopic notation the Auger processes are labeled *KLL*, *LMM* or *MNN* depending on the electrons involved ($n = 1 \equiv K$, $n = 2 \equiv L$, $n = 3 \equiv M$, ...). The process in Fig. 3.5 thus is an Auger *KLL* process.

The electrons from the LaB_6 cathode are accelerated typically to 3 keV and are collimated to the sample surface. Here, they excite Auger electrons which are emitted towards the screen. Due to an additional multiple grid optics, the screen also serves as a retarding field electron analyzer. Ramping the retarding fields in these grids results in a filtering of the electrons according to their kinetic energy. The energy resolution of such analyzers is, due to the rather simple design, in the order of few eV which is sufficient for rough chemical analysis, however, determination of precise stoichiometric compositions by AES is challenging.

AES characterization experiments were usually performed at the end of a measurement cycle, because the impinging high energy electrons are known to break carbonic bonds at the surface, leading to increased contamination.

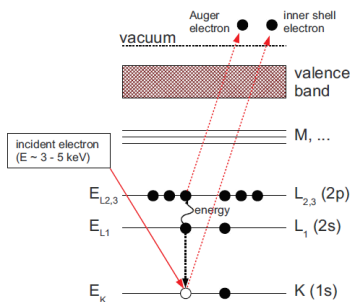


Figure 3.5: Sketch of the Auger electron emission process (taken from [47]).

Main ARPES Analysis Chamber

After the sample surfaces have been prepared, cleaned and characterized in terms of chemistry and crystallographic ordering, they are transferred into our main ARPES analysis chamber and photoemission experiments can be performed. The main chamber as well as our different light sources shall be shortly introduced in this section. Figure 3.6 depicts a full scheme of the chamber with all components.

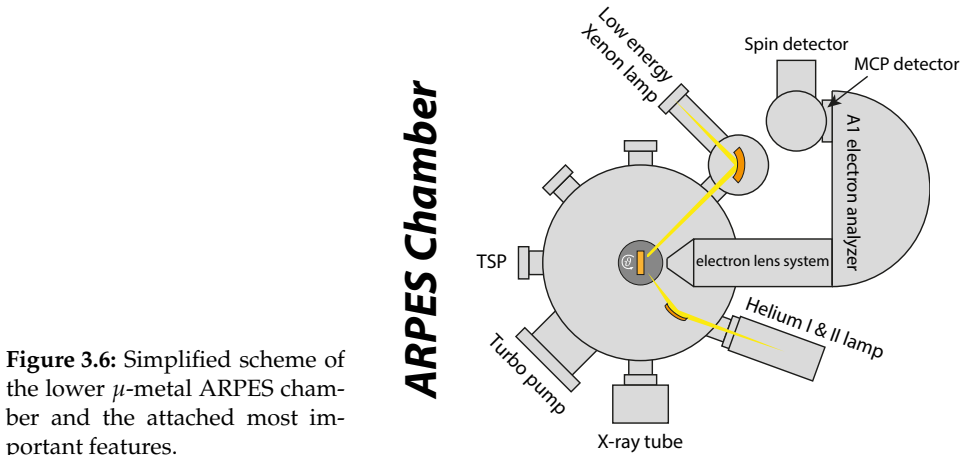


Figure 3.6: Simplified scheme of the lower μ -metal ARPES chamber and the attached most important features.

μ -Metal Shielding

Since this thesis deals with electrons of very low kinetic energy in the order of only few eV², it is very important to shield and minimize all possible external or remanent electric and magnetic fields in order to prohibit any distortions on the electron trajectories and to assure high angular resolution. Already the geomagnetic field of the earth $\approx 25 - 40 \mu\text{T}$ would cause a Lorentz force on the electrons that will deflect them from their path to the detector. This is why the entire main chamber was made out of special μ -metal material consisting of an alloy of approximately 75% nickel, 15% iron and other copper and molybdenum composites, which exhibits a very high magnetic permeability and is thus well-suited to keep the inside of the chamber field-free. Using this shielding, a remaining external magnetic field of only $\approx 10 - 20 \text{ nT}$ could be achieved at the position of the sample and can therefore be neglected.

Hemispherical Electron Energy Analyzer

The heart of the ARPES main chamber is the hemispherical MBS A1 electron analyzer which consists of a lens system of four electrostatic transfer lenses and the hemispherical capacitor analyzer (see Fig. 3.7(a)). The first electron-optical element of the system is the sample which is on ground potential. Depending on the voltages applied to the

² Using the microwave-driven xenon lamp as an excitation source, the measured electrons exhibit kinetic energies of $E_{kin} = h\nu - \phi - E_B \approx 8.44 \text{ eV} - 4.5 \text{ eV} - E_B \in [0 - 3.94 \text{ eV}]$, as an example for a material with workfunction of $\phi = 4.5 \text{ eV}$. This number varies typically between $3 - 5.5 \text{ eV}$.

lens system, the electrons are projected onto the entrance slit of the hemisphere either by conserving their spatial (Fig. 3.7(b)) or angular distribution (Fig. 3.7(c)), respectively (green, blue and red are electron trajectories in Fig. 3.7). The angular resolution of this imaging system depends strongly on the used lens voltage tables and can vary with kinetic energy. Especially for low photon energies these lens tables have to be carefully calibrated. Typically, angular modes with acceptance angles of 15° or 30° for all different photon energies can be employed. A detailed characterization of the angular resolution of the system will be given below.

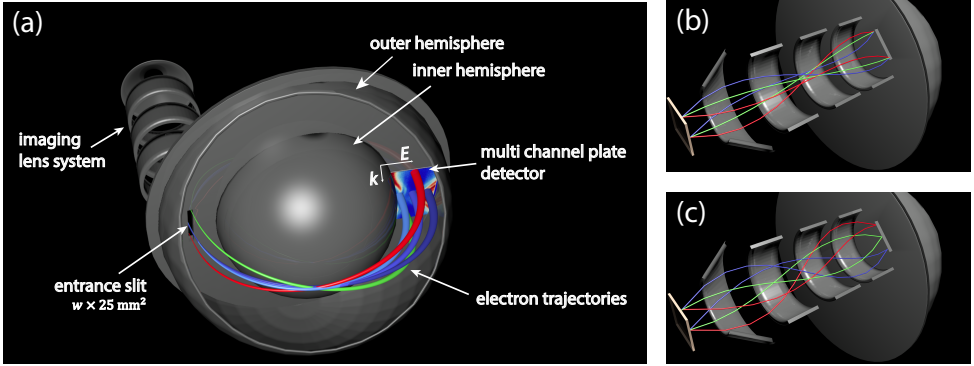


Figure 3.7: Scheme of our hemispherical electron energy analyzer. (a) The MCP detector instantaneously measures a two dimensional image of kinetic energy and angular, i.e. momentum distribution of the photoelectrons. Here, green, blue, and red trajectories illustrate electrons with differing incoming angle, while the different blue shadings vary in energy. (b) and (c) show schematically the electron trajectories in the lens system in spatial (b) and angular (c) imaging mode, respectively, where either separate points on the sample or distinct emission angles are imaged onto individual points on the detector. Here the green, blue, and red trajectories stem from different points on the sample and either they are imaged spatially (b) or filtered by their angular distribution (c).

When the electrons have reached the entrance slit of the energy analyzer, where the inner and outer hemisphere form a concentric capacitor arrangement and a constant voltage is applied, due to energy-dependent deflection, the electrons are filtered according to their kinetic energy. Only electrons within a kinetic energy window equal to $\approx 10\%$ of the pass energy E_p will be transmitted through the analyzer (trajectories in Fig. 3.7 with different blue shading), whereas electrons with higher or lower energy will be absorbed on the outer or inner hemisphere, respectively. Finally, a two-dimensional multichannel plate (MCP) detector system will detect, multiply and visualize the electrons. Therefore, the analyzer simultaneously detects a 2D image of kinetic energy vs. emission angle. For certain voltages between the sample and the entrance slit of the analyzer, emitted electrons of specific initial kinetic energy will be retarded or accelerated such that their energy matches the pass energy and they can pass the analyzer. Thereby, by scanning these voltages it is possible to measure the entire initial kinetic energy spectrum of the photoelectrons.

The energy resolution of the analyzer ΔE_A is defined as

$$\Delta E_A = E_p \cdot \left(\frac{w}{2R_0} + \frac{\alpha^2}{2} \right) \approx \frac{E_p[\text{eV}] \cdot w[\text{mm}]}{R_0[\text{mm}]}, \quad (3.1)$$

so it basically depends on the pass energy E_p , the width of the entrance slit w , the mean radius of the two hemispheres $R_0 = \frac{R_1+R_2}{2}$ (200 mm for MBS A1) and the angular acceptance α of the entrance slit. The latter is in typical spectrometers confined by another angular aperture in front of the entrance slit such that $\frac{\alpha^2}{2} \approx \frac{w}{2R_0}$. The resolution of the spectrometer should be always adjusted to the measurement case and one has to take the intrinsic energetic broadening due to Fermi-Dirac statistics into account, which is directly related to the sample temperature. At room temperature, for example, the physical limit of energy resolution is roughly $4k_B T \approx 100$ meV, while at low temperatures it is in the range of a few meV. For HR-ARPES at low temperatures the typical measurement settings would be a slit width of $w = 0.4$ mm and pass energy $E_p = 5$ eV which results in $\Delta E_A = 10$ meV or better. An estimation of the performance of our system will be shown below.

Focused Helium Lamp

The standard photon sources for laboratory-based ARPES experiments are helium discharge lamps as described in [112]. In these systems, a certain partial pressure of helium is put into the discharge chamber, where the gas is ionized in a high electric field, a plasma is ignited, and excited and recombining electrons emit light of certain characteristic wavelengths. Every noble gas element has a special emission spectrum and the single spectral lines are very sharp. However, often additional monochromators are used to separate the different emission lines by diffraction at a grating or an aperture or absorption at certain filters. For photoemission experiments the photon energy is at least in the vacuum ultraviolet regime (VUV, $\lambda < 200$ nm), which means that the light will be absorbed by air and which is why the lamps have to be connected to the UHV system and the light is created under vacuum conditions.

For the results presented in this thesis two different helium lamps have been used, which are both non-monochromatized. Helium is more or less the only noble gas which can be employed in photoemission experiments without monochromator because it has only few and well separated emission lines allowing for the recording of the entire valence band³. The first lamp is the very intense filament-driven lamp (UVS300) and the other one a standard electrical arc discharge lamp (HIS13). The latter is less intense but employs a special toroidal mirror for improved focusing of the light. Both lamps are connected to the chamber and two stages of differential pumping decrease the He partial pressure in the chamber during operation of the lamps to around $p \approx 5 \cdot 10^{-9}$ mbar.

Since the beam spot size on the sample surface defines the area from which the photoelectrons are emitted and imaged by the lens system, it will also directly affect the angular resolution in ARPES. Specifically, in first approximation it will scale inversely with the beam spot size, since the chance that only homogeneous areas of the surface

³ He I α : 58.43 nm = 21.22 eV and He II α : 30.38 nm = 40.81 eV; the additional β lines are already more than 100 times less intense and therefore nearly negligible.

are excited is increased and possible error sources are minimized. The following Fig. 3.8 shows how the size of the beam spot could be deduced experimentally using photoemission. For this, the spatial imaging mode of the spectrometer is used and a deflector voltage in the lens system is scanned in order to move the electron beam across the detector (x -axis of the images). Fig. 3.8 (c) was used to calibrate detector pixel (y -axis) and deflector voltage (x -axis) into mm by imaging a known structure, in this case the head of a screw with a diameter of 3 mm. Using this calibration, one is able to approximately deduce the dimensions of the beam profiles both horizontally and vertically. Indeed, one can see that the UVS300 (a) has the larger FWHM beam spot of roughly $1.5 \times 1 \text{ mm}^2$, whereas the focused HIS 13 (b) has a spot size of $0.39 \times 0.72 \text{ mm}^2$ making it more favorable for ARPES investigations. Due to the experimental geometry and the incidence angles, the spot size in (a) [(b)] is increased in the horizontal [vertical] direction.

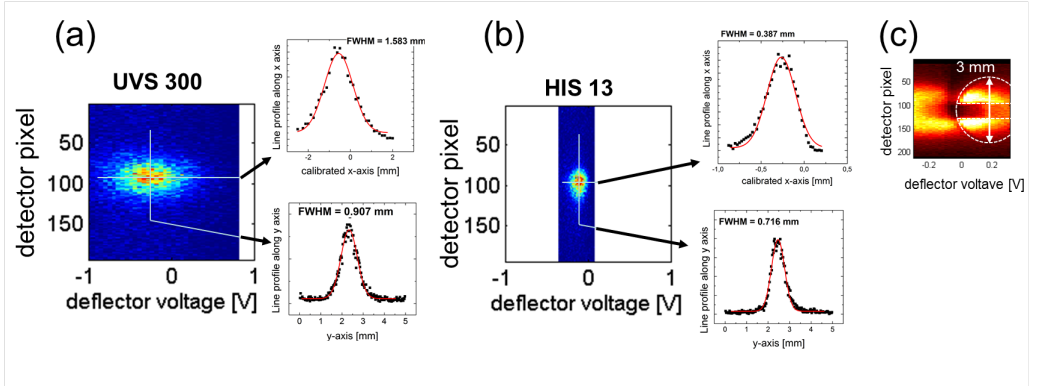


Figure 3.8: Determination of the beam spot size of the two different He lamps used in this thesis. (a) and (b) Images of the beam spots made by scanning a deflector voltage and recording spectra in the spatial mode of the spectrometer. Thereby, horizontal and vertical profiles of the beam could be extracted. (c) Image of a screw on our manipulator for calibration of detector pixel and deflector voltage into mm.

Monochromatized Xenon Lamp

Additionally to standard helium discharge lamps, the system is equipped with a microwave-excited noble gas lamp, which can be operated using different noble gases like xenon (Xe), krypton (Kr), or argon (Ar) and producing photons with energies of $h\nu = 8.44, 10.0$, or 11.6 eV , respectively. The details of the development and characterization of this modern photoemission laboratory source are presented in [113]. First, the strong benefit of this source is the fact that it is completely vacuum-separated from the measurement chamber by a LiF window which enables perfect ultra high vacuum conditions during all experiments. The second advantage is that it is equipped with three different ionic crystal filters (sapphire, CaF_2 and LiF for the use of Xe, Kr, or Ar, respectively) in order to absorb higher photon energies from undesired emission lines and thus to provide monochromatic light. Due to the monochromaticity of the light and due to the low photon energies, this source allows the study of the electronic structure with

high energy and angular resolution. Additionally, according to the universal curve of photoemission (see Fig. 2.14), low photon energy may provide a more bulk-sensitive access to the electronic bandstructure.

The beam spot diameter of this lamp is in the order of 2 – 3 mm which allows high-resolution ARPES investigations only on macroscopically flat and homogeneous samples. Nevertheless, many of the results presented later are obtained using this source.

UV Laser System

During the time of this thesis, the system was also upgraded with a commercial mode-locked Ti:sapphire laser system producing ultra-short pulses of IR light between 760 – 840 nm wavelength. Making use of strong non-linear processes the frequency of light can be quadrupled when focused into two special non-linear BBO crystals to reach $\lambda_{final} \approx 206 \text{ nm} = 6.02 \text{ eV}$. This enables the use of this light source in photoemission experiments. A scheme of the recently added setup for laser-ARPES is shown in Fig. 3.9. The advantage of this light source is the easy handling of this light, since 200 nm is above the absorption edge of air and the setup can be adjusted and manipulated under ambient conditions, a quite high photon flux, very small beam spot sizes down to $\approx 100 \mu\text{m}$ depending on the focusing and most importantly, the full control of the polarization of the light, which allows access to all linear and circular polarizations. The latter immediately opens up new possibilities to study photoemission effects, such as dipole selection rules or dichroism, in detail. The details on the characterization of the new source as well as on first measurements on topological insulators can be read in [114].

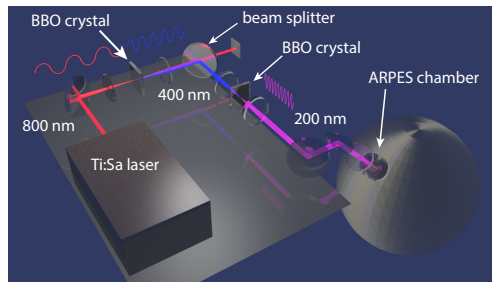


Figure 3.9: Schematic illustration of the recently added laser setup for laser-ARPES investigations.

ARPES Measurement Geometry

This paragraph shall briefly explain the geometry of the ARPES experiments presented here and define the coordinates that are used to describe real or reciprocal space results. For this, Fig. 3.10(a) depicts a 3-dimensional sketch of a typical ARPES geometry. The sample is mounted on the manipulator such that the sample surface is the xy -plane, whereas the z -direction is defined by the distance to the entrance of the spectrometer. This means the z -coordinate is the first parameter that influences the electrostatic lens system imaging the photoelectrons onto the entrance slit, because all lens voltages are

carefully adjusted to a certain sample-analyzer distance (35 mm to the entrance lens). The sample is exposed to photons impinging under 45° horizontally (along the red shaded yz -plane) when Xe excitation is used, or under 24° vertically (along the green shaded xz -plane) when the He lamp is employed. These planes, defined by the light pointing vector and the sample surface normal, are called light incidence planes (red and green shaded planes in Fig. 3.10(a)). The incidence angles are given with respect to the plane of the sample surface. In our setup the long axis $L = 25$ mm of the spectrometer entrance slit ($w \times L = w \times 25 \text{ mm}^2$), which defines the electron emission plane (equivalent to the green shaded plane), is aligned vertically along the x -axis which means that the surface electronic structure E_B along $k_{||,x}$ is imaged at a certain fixed value of $k_{||,y}$ within one shot. The range of $k_{||,x}$ is given by the angular mode of the lens system, and the acceptance angle of the analyzer (30° or 15° typically), and the used photon energy because of equation 2.34. This means that low photon energy will by definition reveal a smaller fraction of the k space, but with a higher k -resolution.

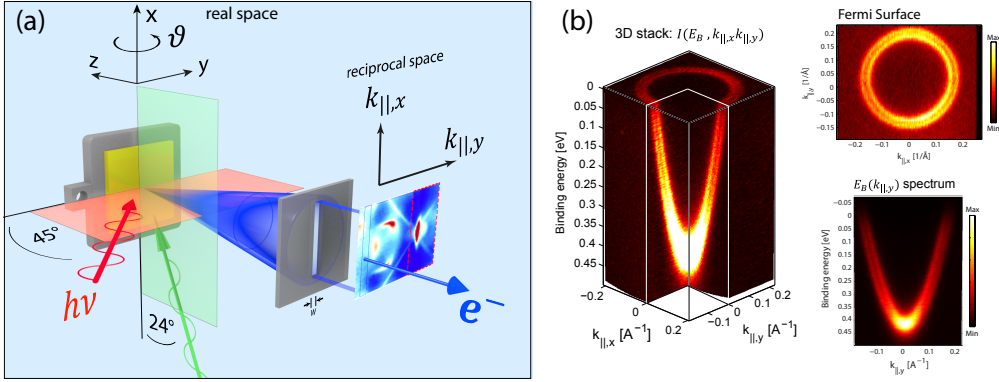


Figure 3.10: Sketch of the ARPES measurement geometry and a typical data set. (a) Note the definition of the real space and reciprocal space coordinates in our laboratory reference frame. Two different light incidence planes for He or Xe excitation are shown (blue and red shaded plane and green and red arrow, respectively) as well as the photoelectron emission plane (blue shaded plane). The electron emission cone is imaged onto the analyzer entrance slit (dimension: $w \times 25 \text{ mm}^2$). The result can be transformed into the reciprocal space. Here, the Fermi surface of a 32 ML thick Fe(001) film deposited on a Au single crystal is shown, exemplary. (b) Typical 3D data stack $I(E_B, k_{||,x}, k_{||,y})$ obtained from Fermi surface mapping on the Au(111) surface state from which slices along desired directions such as constant energy cuts or binding energy maps can be produced.

By rotating the sample by the angle ϑ about the x axis, the second angle and consequently $k_{||,y}$, is varied and thus mapped. Thereby a three-dimensional data stack $I(E_B, k_{||,x}, k_{||,y})$ of the surface electronic structure is created. This is exemplarily shown in Fig. 3.10(b) for the parabolic, Rashba-split surface state of a Au(111) single crystal surface. The third dimension in k space is defined by the photon energy by equation 2.35. This stack of data can be cut at any value in order to create two-dimensional constant energy cuts $k_{||,x}$ vs. $k_{||,y}$ at given E_B , such as the Fermi surface ($E_B = E_F$), or

binding energy maps $E(k_{||,x})$ or $E(k_{||,y})$ at fixed values of $k_{||,y}$ or $k_{||,x}$, respectively. Along $k_{||,y}$ direction one can rotate full 180°, which is sufficient to map the entire surface Brillouin zone for all typical materials and commonly employed photon energies. Due to the fact that our manipulator allows only one polar rotational axis, one is restricted to only one slice along the $k_{||,x}$ direction, always. However, for most of the materials and especially strong topological insulators this is absolutely sufficient.

Performance of the System

Here, we will shortly demonstrate the standard performance of our system concerning the two most important quantities in ARPES experiment, energy and angular resolution.

Energy Resolution

For the detailed investigation of the electronic bandstructure it is necessary to push the energy resolution in ARPES experiments to values that are as small as possible and below typical energy scales of SOC-related effects. Due to the progress in modern spectrometer technology, the energy resolution ΔE_A (Eq. 3.1) can be theoretically pushed well below 1 meV, considering of course the compromise of decreasing count rates. However, besides the physical limit of the electron analyzer, two other limiting factors will influence the photoemission signal: (1) monochromacy, i.e. spectral bandwidth, of the used light source ΔE_{hv} , and (2) the intrinsic thermal broadening of the electronic structure ΔE_{FD} due to the Fermi-Dirac statistics of the electrons itself. The measured spectrum (close to the Fermi level) in a real experiment will always contain all these three effects and will thus be a convolution as described by

$$I_{PES} = f_{FD} * f_A * f_{hv} = \underbrace{\left(\exp \left(\frac{E - E_F}{k_B T} \right) + 1 \right)^{-1}}_{\text{Fermi-Dirac distribution}} * \underbrace{\exp \left(-\frac{E^2}{2w_A^2} \right)}_{\text{analyzer resolution}} * \underbrace{\exp \left(-\frac{E^2}{2w_{hv}^2} \right)}_{\text{light bandwidth}}. \quad (3.2)$$

Here, the broadening due to the finite sample temperature T is taken into account in the Fermi-Dirac distribution f_{FD} with the Boltzmann constant $k_B = 8.617 \cdot 10^{-5} \frac{\text{eV}}{\text{K}}$, and the two Gaussian distributions describe the broadening due to the settings of the electron analyzer and the spectral bandwidth of the light. The parameters w_A and w_{hv} relate to the full width at half maximum (FWHM= ΔE) as $w_{A/hv} = \frac{\Delta E_{A/hv}}{2\sqrt{2\ln 2}}$, whereas the energy resolution of the Fermi-Dirac function can be expressed as $\Delta E_{FD} \approx 4 \cdot k_B T$ [115].

Typically, both analyzer and light broadening can be set or optimized to small values (in the order of meV) and the limiting factor of the total energy resolution is the finite temperature of the sample. In Fig. 3.11 the typical total energy resolution ΔE_{total} , which follows from the separate contributions by $\Delta E_{total} = \sqrt{\Delta E_{FD}^2 + \Delta E_A^2 + \Delta E_{hv}^2}$, will be estimated for the three different laboratory sources available in our system. In each of the spectra, the sp -like highest occupied states were measured close to the Fermi edge of the polycrystalline Cu manipulator, which was cooled to low temperatures and did not show additional spectral features besides the sp states. The finite

energetic broadening at the Fermi level contains all the information from Eq. 3.2. Since we cannot measure the actual temperature at the position of the sample, this method of evaluating the width of the Fermi level can also be used to determine the sample temperature.

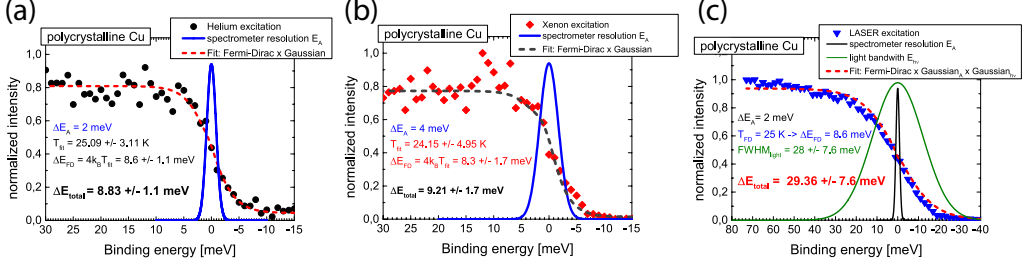


Figure 3.11: Determination of the experimental energy resolution. PES spectra near the Fermi level of the polycrystalline Cu block measured at low temperature and with three different light sources, (a) He lamp $h\nu = 21.2$ eV, (b) Xe lamp $h\nu = 8.4$ eV, and (c) the UV laser $h\nu = 6$ eV. The raw data was fitted with a convolution of the Fermi-Dirac distribution with a Gaussian of fixed width according to the setting of the analyzer (a) and (b) and an additional Gaussian representing the spectral broadening of the light (c).

In Fig. 3.11(a) and (b), which were measured with the He $h\nu = 21.2$ eV and the Xe $h\nu = 8.4$ eV lamp, respectively, the broadening of the light source was neglected because the emission lines of these lamps are known to be very sharp ($\Delta E_{hv} \approx 600 \mu\text{eV}$ for Xe excitation and $\Delta E_{hv} \approx 1$ meV for He excitation [113]) and thus much smaller compared to the analyzer resolution. The only major difference between the spectra in (a) and (b) is that in the Xe excitation case the photoelectron signal above the Fermi level really vanishes to zero, because the lamp is monochromatic. The spectra were fitted with a convolution of the Fermi-Dirac distribution and a Gaussian with a fixed width ($\Delta E_A = 2$ meV in (a) and $\Delta E_A = 4$ meV in (b) derived from Eq. 3.1 and given analyzer settings). From this fit one is able to extract the actual sample temperature as $T^{\text{He}} = 25.09 \pm 3.11$ K and $T^{\text{Xe}} = 24.15 \pm 4.95$ K and therefore a total energy resolution of

$$\Delta E_{\text{total}}^{\text{He}} = \sqrt{(4k_B T^{\text{He}})^2 + (2 \text{ meV})^2} \approx 8.83 \pm 1.1 \text{ meV} \quad (3.3)$$

$$\Delta E_{\text{total}}^{\text{Xe}} = \sqrt{(4k_B T^{\text{Xe}})^2 + (4 \text{ meV})^2} \approx 9.21 \pm 1.7 \text{ meV} \quad (3.4)$$

showing a nice agreement to each other. However, the statistics in both spectra is not very high and the spectrometer was not set to achieve highest possible resolution, but instead a typical setting and condition of the spectrometer should be demonstrated.

In Fig. 3.11(c), the spectrum was obtained using our newly installed laser setup and the first thing one notices is that the Fermi edge is much more broadened although settings of the spectrometer and sample conditions are comparable to (a) and (b). The reason is the non-negligible spectral broadening of the laser light source due to the fact that the generation of the 6 eV light is based on non-linear frequency doubling using ultra short light pulses in the fs regime. In contrast to a continuous wave light source, which can

be assumed to have infinitesimally narrow emission lines, theoretically, pulsed light sources will experience a fundamental limit known as the time-bandwidth product predicting the lowest possible duration of a light pulse $\Delta\tau$ for a given spectral bandwidth $\Delta h\nu$ and vice versa as $\frac{\Delta\tau \cdot \Delta h\nu}{h} \geq 0.441$, for a Gaussian shaped light pulse. Since the actual pulse length of the 6 eV light is unknown and it is not trivial to measure, this method can also be used to get an estimate of it. Therefore, the Fermi edge in Fig. 3.11(c) was fitted by a convolution according to Eq. 3.2, but this time the width of the Gaussian due to the spectrometer was assumed to be $\Delta E_A = 2$ meV and it was further assumed that the sample temperature will again be around 25 K, fixing the width of the Fermi-Dirac distribution. Thereby, one gets a reasonable fit for a second Gaussian with $\Delta E_{hv} = 28.0 \pm 7.6$ meV which leads to a total energy resolution of

$$\Delta E_{total}^{LASER} = \sqrt{(4k_B \cdot 25 \text{ K})^2 + (2 \text{ meV})^2 + \Delta E_{hv}^2} \approx 29.36 \pm 7.6 \text{ meV}. \quad (3.5)$$

Moreover, one can now estimate the lower limit of the pulse duration of the 6 eV light as $\Delta\tau \geq 62.1 \pm 2.4$ fs, which is physically the lowest possible limit the beam pulse can exhibit. Using the laser light source, the achievable resolution will thus be limited. However, its very high photon flux, the possible small beam spot sizes and the full control over the light polarization compensates this compromise for future spin-polarized measurements.

Angular Resolution

The quantification of the angular distribution is less trivial. In first approximation, it will increase as the size of the beam spot decreases. Moreover, the k -space resolution strongly depends on the photon energy used, since the accessible fraction of the k -space depends on the kinetic energy of the photoelectrons (Eq. 2.34). All angular lens modes of the spectrometer are calibrated by imaging a well defined pattern of e.g. a special angular test device, for the different photon energies (compare [114] for a more detailed example).

In order to estimate the ultimate angular resolution and to prove that our standard light sources can be used for high-resolution ARPES experiments, a Au(111) single crystal was employed as a test sample. As presented in section 2.2, the special electronic configuration at the surface reconstruction of noble metal (111)-surfaces hosts free-electron-like parabolic surface states at the Fermi level whose spin-degeneracy is split by the SOC-induced Rashba-effect [85, 91] (as visualized in Fig. 3.10(b)). This effect makes the Au(111) surface an ideal ARPES calibration sample due to its simple, but nonetheless spin-polarized band structure close to the Fermi level with a splitting that is in the same order of magnitude as the resolution of modern spectrometers, when VUV photon sources are employed. For Au(111) the Rashba-induced splitting of the parabolic surface state near the Fermi level is known to be $\Delta k_{Rashba}(\text{Au}) = 0.023 \text{ \AA}^{-1}$ and $\Delta E = 110$ meV [85]. The top panels of Fig. 3.12 show the ARPES $E(k_{||,x})$ maps of the Au(111) surface state measured at low temperature with both He and Xe excitation. Underneath, the MDCs, integrated along the white dashed area, are plotted. In both spectra the Rashba-splitting is clearly visible down to the spin-degenerate point at $\bar{\Gamma}$. From fits to the peaks in the MDCs at the Fermi level the Rashba splitting was determined as $\Delta k_{Rashba} = 0.0224 \pm 0.0013 \text{ \AA}^{-1}$ for both excitations (average of the two values

at $\pm k$ of the He spectra), which is in good agreement to the literature value. From this data one can fairly state that both light sources provide an angular resolution of better than $\Delta k < 0.0224 \text{ \AA}^{-1} \simeq 0.6^\circ$.

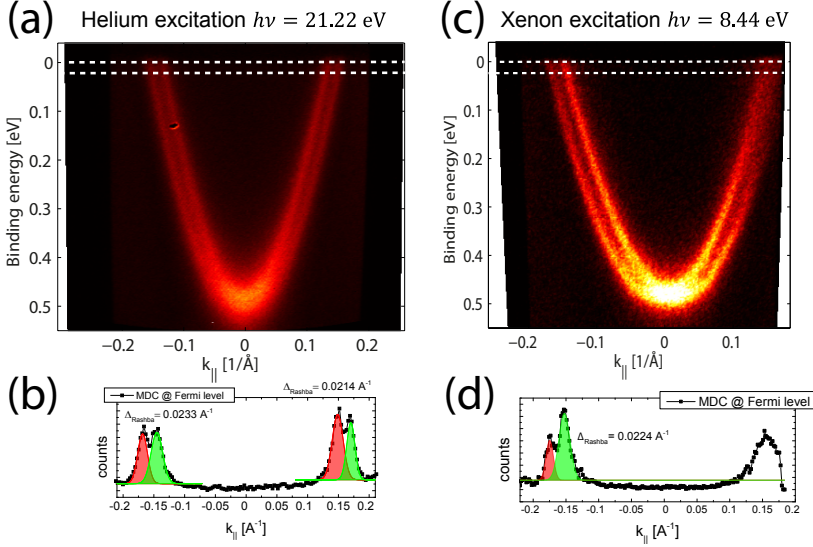


Figure 3.12: Determination of the experimental angular resolution. (a) and (c) $E(k_{||,x})$ maps of the Rashba-split Shockley surface state measured on the surface of a Au(111) single crystal which was cooled to low temperatures ($\approx 25 \text{ K}$) with two different photon energies, He $h\nu = 21.2 \text{ eV}$ (a) and Xe $h\nu = 8.4 \text{ eV}$ (c). (b) and (d) MDCs integrated over the white dashed area with fitted peaks. From the fits the Rashba-splitting at the Fermi level was deduced.

3.2 Spin-Resolved Photoelectron Spectroscopy

Spin-resolved photoelectron spectroscopy can be used to achieve strong experimental evidence about the topological character of an electronic surface state, i.e. for the classification of a new material type as strong or weak topological insulator (see chapter 7). The ARPES apparatus in Jülich was only recently upgraded with a modern, efficient spin polarimeter, which is based on the exchange scattering at an oxidized magnetic iron film. Before, however, a spin-polarized low energy electron diffraction (SPLEED) polarimeter at the beamline 5 of the DELTA synchrotron facility in Dortmund could be employed [116]. In the SPLEED detector the intensity imbalance or spin asymmetry according to Eq. 2.39 and Fig. 2.17 is achieved by spin-dependent scattering of electrons with $\approx 100 \text{ eV}$ kinetic energy on a W(001) single crystal and the simultaneous detection using four different channeltrons which are placed in the (2,0), (0,2), $(\bar{2},0)$ and $(0,\bar{2})$ diffraction direction. This spin-dependent scattering is caused by spin-orbit coupling and the figure of merit of such type of detectors is around $\text{FoM} \approx 1.6 \cdot 10^{-4}$ [58]. The angular resolution that is achieved by the hemisphere is relinquished and only angle-

integrated but spin-resolved energy distribution curves at a given azimuthal angle ϑ of the sample, i.e. a certain $k_{\parallel,y}$ value, can be measured. A detailed description of the setup at BL5 can be found in [47].

The strength of this system is its bright light source and the fact that this spin detector allows the simultaneous measurement of one in-plane and the out-of-plane spin direction by four independent channeltron detectors. However, the latter is also a strong disadvantage because the different electron detectors are prone to intrinsic instrumental asymmetries which are complicated to cancel out when measuring non-magnetic sample systems, such as topological insulators. One way to overcome this problem is to always measure the same point in the BZ for positive $+k$ and negative $-k$ values and to check for a reversal of the spin signal, which should be present in helical spin textures as they are expected in topological surface states. Moreover, the scattering process with 100 eV electrons makes this spin detection process extremely surface sensitive. It is known that in order to keep a W(001) surface clean from adsorbates or intrinsic contaminations, even under UHV, frequent preparation cycles (every 1.5 – 3 h) are mandatory [58].

CHAPTER 4

Prototypical Binary 3D Topological Insulators

Since most of the results presented in this thesis are obtained on MBE-grown thin films of 3D TIs and many of the samples have been measured after they have been exposed to air and consequently oxidized, a standard cleaning procedure in UHV will be shortly introduced (4.1). After this, a general description of the electronic structure of the main prototypical 'parental' 3D STIs Bi_2Te_3 , Bi_2Se_3 and Sb_2Te_3 will be presented, including a short comparison between ARPES on single crystals and thin films (4.2).

4.1 Cleaning of MBE-Grown 3D TI Thin Films

First, a brief description of the standard thin film cleaning and analysis methods will be introduced, since they have been employed for obtaining most of the later results. The general preparation procedures have been introduced in section 3.1, as either cleavage, sputter-anneal cycles or vacuum transfer of the samples. In each case, the quality of the sample surfaces prior or post to the main ARPES measurements needed to be verified either by AES, LEED (see section 3.1) or PES itself.

Figure 4.1 summarizes a typical analysis of the surface quality of TI thin film samples, introduced from ambient conditions.

Auger Electron Spectroscopy

Figure 4.1(a) exemplarily depicts the development of the Auger spectra of a 50 nm thick Sb_2Te_3 film during preparation. The relevant Auger transitions in this case are: the *KLL* transition of carbon and oxygen at 271 and 511 eV, and the *MNN* transitions of antimony and tellurium that occur as double peaks at 455 and 463 eV and at 484 and 489 eV, respectively. The black curve shows the AES spectra of the untreated sample after insertion into the chamber. Besides the peaks of metallic Sb and Te, the spectrum reveals the heavy oxidation by O and contamination with C of the sample. Additionally, the metallic peaks are slightly shifted to lower kinetic energies due to the modified chemical surrounding in the upper oxidized layer. After one cycle of sputtering with a 6 – 8 μA current of Ar ions of 500 eV kinetic energy for several minutes and annealing at $\approx 270^\circ\text{C}$ for 5 min, the spectrum developed into the blue curve. The

oxygen peak already vanished completely, and the Sb and Te peaks are both shifted to their correct metallic-state positions and further start to have a sharp and undisturbed shape, which is an indication of a removal of the first oxidized layers. The carbon peak, however, remains nearly unchanged and another sputter-anneal cycle is needed to remove it (red curve). Now, the surface of the sample can be assumed as free of contaminations and suitable for PES measurements.

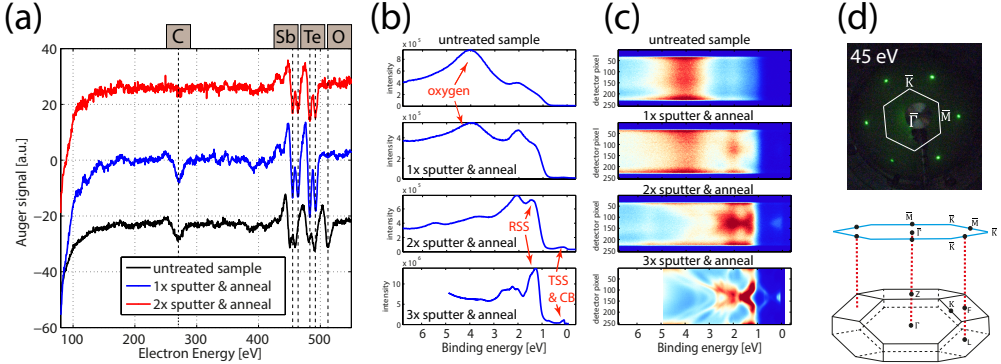


Figure 4.1: Analysis of a typical thin film cleaning process. (a) AES spectra of an untreated (black), once (blue) and twice (red) sputtered and annealed Sb_2Te_3 sample. (b) Angle-integrated EDCs of the ARPES maps in (c) showing a comparable cleaning procedure with 3 sputtering and annealing steps performed on a Bi_2Se_3 sample ($h\nu = 21.2$ eV). The spectra show the development of an oxygen related peak and the appearance of the Rashba-split and topological surface state (RSS and TSS). (d) Respective LEED pattern obtained at 45 eV kinetic energy of the clean Bi_2Se_3 sample and a schematic sketch of the trigonal bulk BZ (black) with its 2D surface projection along the (111) direction (blue).

Photoelectron Spectroscopy

Another way to tell the quality of the sample surface that is similarly efficient as checking AES, is to analyze the valence band electronic structure by measuring (AR-) PES. In this case, the development of the valence band spectra is summarized in Fig. 4.1(b) and (c). Here, exemplary, 1D PES (b) and 2D ARPES (c) spectra of a 107 nm thick Bi_2Se_3 film are shown. Besides the differing sputtering rates on Sb or Te compared to Bi or Se, the materials are assumed and observed to behave very similar.

The upper spectrum shows the signal from the untreated surface and neither any dispersing features nor a metallic Fermi edge can be identified. The only common very prominent non-dispersive feature is an oxygen-related state around 4 eV binding energy and a constantly decreasing photoemission signal. After one and two cycles of sputtering and annealing (similar parameters as above) the oxide state starts to decrease and other strongly dispersive features start to appear, the most intense one can be related to the well-known Rashba-split surface state (RSS) around $E_B = 1.3$ eV (more details on this feature will follow).

After a third cycle of sputtering and annealing, a clear, nearly undisturbed valence band structure with relatively low background signal can be revealed and the topologically protected surface state (TSS) starts to be visible close to E_F .

Low-Energy Electron Diffraction

Figure 4.1(d) shows a LEED pattern of the sample in the last state of (b) and (c) obtained with electrons of 45 eV kinetic energy. Again a very high signal-to-noise ratio and rather sharp LEED spots are revealed which also confirms the high crystalline quality of the surface. Further, by measuring LEED, the orientation of the surface BZ (marked by the white hexagon) and thus the predefined ARPES measurement $k_{||,x}$ direction can be identified. Additionally, the three-fold symmetric bulk and surface Brillouin zones are shown (compare Fig. 2.9).

4.2 Comparison of the Binary Compounds Bi_2Se_3 , Bi_2Te_3 , and Sb_2Te_3

4.2.1 Cleaved Single Crystals Compared to MBE-Grown Thin Films

Before going into the main results, some general remarks on the qualitative agreement between measurements on topological insulator thin films and bulk single crystals are in order. In general, the quality of ARPES spectra measured on MBE-grown thin film samples is not comparable to those achieved on cleaved bulk single crystal surfaces. Most of the fundamental studies on TI properties were carried out on such bulk single crystals [12, 15, 53, 55, 97]. Due to the layered crystal structure of the TIs (see section 2.3.2.3) a bulk crystal will cleave easily along the van der Waals gaps which leads to terraces of atomically flat and clean surfaces [60]. Such kind of quality and flatness is hard to achieve with MBE-grown films, because already the substrate can induce different kinds of strain, stacking faults, or dislocation defects.

On the other hand, it is emphasized that only thin film growth opens up a manifold of interesting possibilities, like nano-structuring and processing, the easy control of doping, or the creation of heterostructures or superlattices. In terms of applications and device oriented research, one has to pursue this approach and many groups have achieved great results with thin films in recent years as presented for example in [117–121] or the excellent review [122]. Therefore, the comparison to single crystals can be used in order to assure that the physical properties of the thin films are in agreement with the bulk crystals.

4.2.1.1 Single Crystal vs. Theory

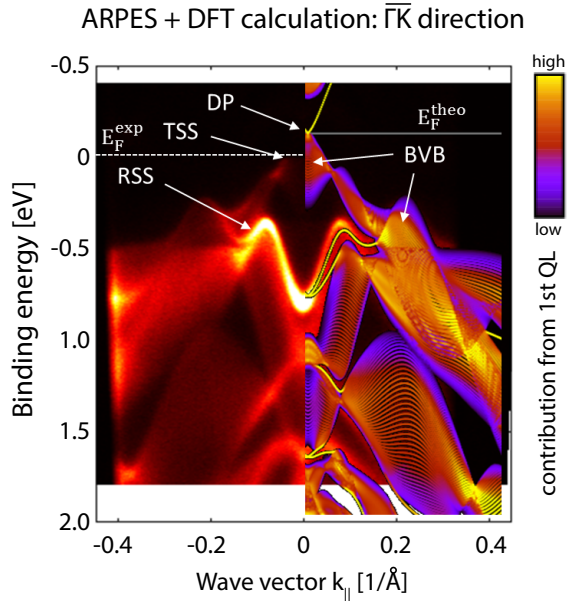
Figure 4.2(a) shows the ARPES map of a Sb_2Te_3 single crystal that was cleaved under UHV conditions using the method described in section 3.1. The cleavage resulted in several small areas of metallic shiny flakes that were clean but too small to reliably position the beam spot on. The latter complicates Fermi surface mapping on such samples immensely, and in our laboratory only the focused He lamp is suitable in this case (21.2 eV) to measure ARPES.

However, the obtained ARPES spectra are of very high quality and individual sharp bands as well as continua of projected bulk (valence) bands (BVBs) can be clearly revealed and separated from the low background signal. Furthermore, the agreement to the calculation, which is superimposed on one half of the image, is astonishingly high. The calculations used here are based on the GW quasiparticle approach which

results in improved relative energy positions between the spectral features [123]. In this case, every single spectral feature can be matched between experiment and theory. Still, the Fermi level in the calculations E_F^{theo} is about 175 meV shifted compared to the experimental one E_F^{exp} . As we will see in the next subsection in more detail, Sb_2Te_3 is a p -type TI with the Fermi level cutting the lower Dirac cone (topological surface state TSS), which means that the Dirac point (DP) is above E_F . The second most prominent spectral feature in Sb_2Te_3 (especially for this photon energy) is a Rashba-split surface state (RSS) located at a spin-orbit induced gap at $\bar{\Gamma}$ and between 0.4 – 0.8 eV binding energy [41, 56]. The Rashba-splitting at $k_{\parallel} \approx 0.18 \text{ \AA}^{-1}$ as well as the dispersion of the split states into different bulk bands can clearly be resolved [56, 124]. The fact, that the spectral weight of the TSS is quite low at this photon energy is known [41, 125], but the small size of the flat cleaved terraces makes it impossible to use any of the other photon sources in our lab. Here, the lateral size of the sample is of importance, which is why on larger thin film samples the TSS can be investigated more extensively (see next section).

Furthermore, Fig. 4.2 contains information about the localization of the states in the color code. This calculation shows the contribution from the first QL, which means that high intensity (yellow) encodes that the state is localized mostly within the first QL, and is thus a surface state, whilst low intensity (violet, black) corresponds to deeper localized, bulk states. From this, one can nicely identify the surface-related features which are mainly the uppermost TSS and the RSS.

Figure 4.2: Comparison ARPES data vs. theory. ARPES $E(k_{\parallel,x})$ map from the cleaved surface of a Sb_2Te_3 single crystal obtained with $h\nu = 21.2 \text{ eV}$ in comparison with improved band structure calculations for a 50 QL slab of Sb_2Te_3 . Several spectral features are indicated by arrows. Additionally, experimental E_F^{exp} and theoretical Fermi levels E_F^{theo} are shown. Color-coded is the contribution from the first QL of the material, i.e. high-intensity (yellow) states stem from within the 1st QL, while low-intensity (dark) states originate from the bulk. (Calculations by I. Aguilera, PGI-1).



4.2.1.2 Single Crystal vs. Thin Film

Next, a qualitative comparison between the cleaved single crystal and an MBE-grown thin film will be presented. For this, the two ARPES maps in Fig. 4.3 obtained using $h\nu = 21.2$ eV are compared. The Sb_2Te_3 thin film (right) was exposed to air after growth and needed to be prepared in the ARPES chamber by a combined sputtering and annealing process. In this case, a single sputtering cycle with 500 eV Ar ions followed by an annealing step at 250 °C for 5 min was sufficient.

Comparison of the two spectra in Fig. 4.3 reveals some qualitative differences. The spectrum obtained from the thin film shows significantly higher background signal and spectral features that are broadened both in the angular as well as the energy dimension. This comparison is a clear proof that the angular and energy resolution of ARPES spectra can be often limited by the sample quality rather than experimental setup properties. On the other hand, quantitatively, one can identify and retrieve nearly every single spectral feature and moreover, match their energetic positions, which can be observed as the good agreement of the EDCs spectra. Here, again the film has less sharp peaks, but their positions match well.

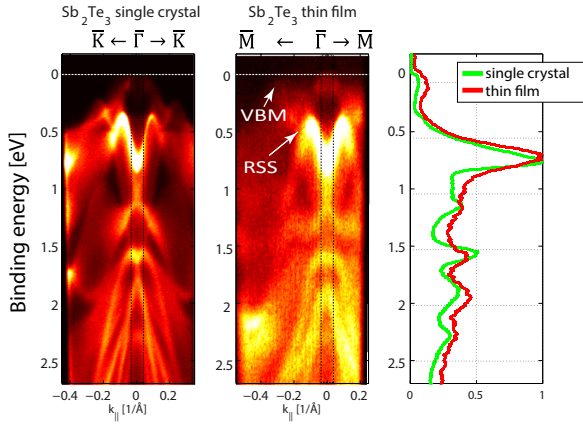
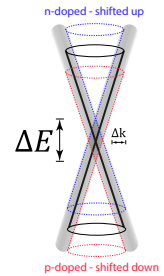


Figure 4.3: Comparison of Sb_2Te_3 single crystal and MBE-grown thin film. Wide energy ARPES $E(k_{||,x})$ maps as well as EDCs along $\bar{\Gamma}$ (integrated over the black dashed region) from the same cleaved Sb_2Te_3 single crystal and a MBE-grown Sb_2Te_3 thin film which needed to be annealed prior to measurement. Both spectra were obtained using $h\nu = 21.2$ eV at room temperature. Note, however, that the cut direction through the SBZ is not the same.

The measured spectral features in ARPES will be broadened due to multiple effects. First, by the intrinsic line broadening caused by many-body quasiparticle interactions (explained in section 2.4.2), then, by the finite angular and energetic resolution of the experiment, and last, by inhomogeneities and imperfections at the sample surface that lead to a superposition of several spectral features. Moreover, it was also reported recently that the formation of twin boundaries at the surface of 3D TIs can lead to an effective self-doping of up to a few hundred meV [126]. The sketch aside illustrates how the revealed Dirac cone spectra of a few inhomogeneous regions at the surface that are differently doped would affect and effectively broaden the observed energy and angular resolution ΔE and Δk .



In summary, it was demonstrated that MBE-grown thin films in general exhibit the

same properties as bulk single crystals, but exhibit a lower intrinsic quality due to their higher impurity concentrations, substrate-induced strain, stacking faults, dislocations, or larger surface roughness. All this can lead to distortions and broadening of the spectra features in ARPES. Nevertheless, the flexibility and advantages of MBE-growth while recovering the interesting physical properties prevail the qualitative spectroscopic drawbacks.

4.2.2 Comparison of the Surface Electronic Structure

This section reveals the major differences and similarities between the three parental binary STIs Bi_2Se_3 , Bi_2Te_3 and Sb_2Te_3 .

4.2.2.1 Preparation

As we have seen in the beginning of this chapter and before, the crystal structure of these materials is the same and their electronic configurations are very similar and therefore also the growth parameters and the preparation procedures are comparable. Thus, their electronic structure measured by ARPES is expected to be very similar, too. Nevertheless, the films that are presented here have been prepared using different techniques. The Bi_2Se_3 film was capped with a thick amorphous layer of Se that could be flashed off (see more in chapter 5.1), similarly the Sb_2Te_3 film was prepared by annealing only, as described in the previous section, whereas the Bi_2Te_3 sample was vacuum transferred from the MBE making any preparation procedure unnecessary.

Figure 4.4(a) shows AES spectra of all three parental TI materials after they have been measured with ARPES and proves the cleanliness of the surface. The spectra reveal all relevant Auger transitions of the occurring elements and a rather low contamination level (note, that the blue and red spectra show also contributions from the sample holder and thus also a slight carbon contamination). Unfortunately, the Se *LMM* peak at 1310 eV kinetic energy in Bi_2Se_3 cannot be detected since our AES spectrometer is very inaccurate at such high energies.

4.2.2.2 Wide-Energy ARPES

For the analysis of the electronic structure, the wide energy overview ARPES spectra of the full valence band is compared. Therefore, Fig. 4.4(b) depicts the wide range $E(k_{||,x})$ maps close to $\bar{\Gamma}$ obtained with He I excitation on thin films of all three materials and their corresponding EDCs along normal emission on the right. All three samples reveal a comparable quality of the spectra, many spectral features can be identified and matched and in general, the electronic structure is very similar, indeed. Slight variations can be explained by the different cut directions through the SBZ. Again, the most prominent feature with the largest spectral weight is the Rashba-split surface state (RSS) that is present in each of the materials. In Bi_2Se_3 its peak is at 1.43 eV, in Bi_2Te_3 at 0.98 eV and in Sb_2Te_3 around 0.65 eV binding energy. The peak of this feature will often serve as a reference for observed energetic shifts since it is the strongest peak in the EDCs.

Furthermore, the most important difference between the three materials is their intrinsic charge carrier (doping) type which can be inferred from these spectra. As we have seen in section 2.3.3 the materials defect chemistry of the Te or Se vacancies and

anti-site defects defines the natively dominating charge carrier type, which is of ***n*-type (electron-like)** in Bi_2Se_3 and Bi_2Te_3 and of ***p*-type (hole-like)** in Sb_2Te_3 for most of the man made crystals. In other words, their intrinsic defect type will either pin the Fermi level in the bulk conduction band minimum (CBM) or bulk valence band maximum (VBM). And indeed, the observation that was described in section 2.3.3 is in line with what one finds in the overview spectra in Fig. 4.4, because in both Bi_2Se_3 and Bi_2Te_3 the Fermi level cuts through the CBM and the band gap is only occupied by the TSS, whereas in Sb_2Te_3 E_F truncates the VBM clearly (see also Fig. 4.5).

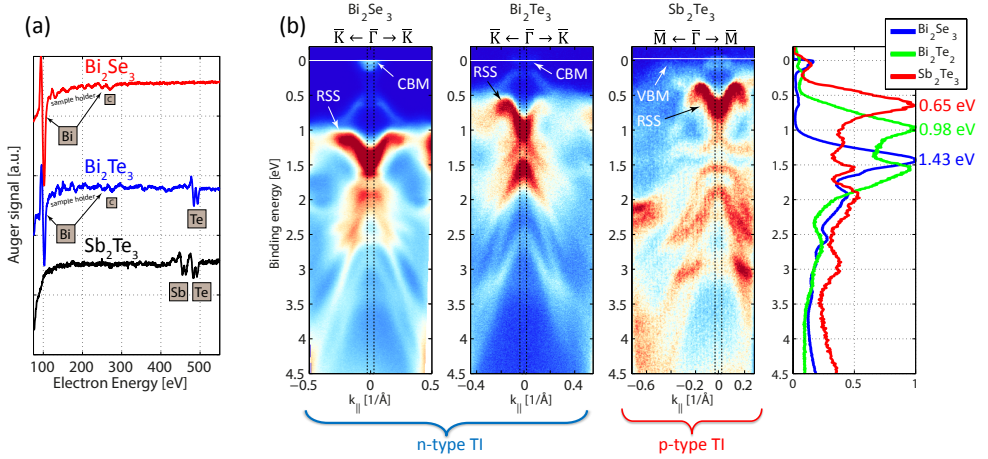


Figure 4.4: Spectroscopic comparison of the three parental binary TIs. (a) AES spectra of Bi_2Se_3 , Bi_2Te_3 and Sb_2Te_3 thin films. (b) Full valence band ARPES $E(k_{||,x})$ maps along indicated crystallographic directions, measured on thin films of Bi_2Se_3 , Bi_2Te_3 and Sb_2Te_3 , respectively, under room temperature conditions and using $h\nu = 21.2$ eV. The corresponding EDCs along normal emission quantify the energetic shift of the otherwise similar electronic structure. Additionally, the blue and red spectra depict some contribution from the Mo sample holder between 100 and 200 eV, due to not perfect alignment of the electron beam.

4.2.2.3 HR-ARPES and MDC Analysis

Next, the more interesting region close to the Fermi level, hosting the topological Dirac cone, is investigated in detail in Fig. 4.5. Here, a thorough analysis of the high-resolution ARPES spectra from MBE-grown thin films is presented.

The figure depicts the ARPES $E(k_{||,x})$ maps of all three materials close to the Fermi level in panels (a), where the topological surface state can be unambiguously identified. In the case of the *n*-type Bi_2Se_3 and Bi_2Te_3 samples¹ only the upper cone can be seen, since the lower cone is buried in the VBM as it has been investigated in [47]. The Fermi level cuts the CBM confirming the materials *n*-type nature². For *p*-type Sb_2Te_3 , on the other hand, only parts of the lower cone are occupied and the Fermi level truncates well through the VBM. In this case, the TSS can be probed much better using lower

¹ The details of the development of the Bi_2Se_3 spectrum will be explained in section 5.1.

² Here, He I excitation was used, since it results in reasonable spectral weight from the TSS for both Bi-based TIs.

(or higher) photon energies, due to better matching matrix element effects, which is in line with previous studies [56, 125]. All three materials reveal comparably sharp spectral features, i.e. a comparable quality of the samples, which makes a quantitative and comparative analysis possible. Moreover, Bi_2Te_3 and Sb_2Te_3 show nearly unperturbed Dirac states close to the Fermi level, while Bi_2Se_3 hosts a lot of conduction band states at E_F impeding the analysis here. However, it is typically complicated to compare results from different samples which are moreover measured at different times and conditions, such as slightly different temperatures.

Nevertheless, the following will attempt a detailed analysis of the TSS spectral features using the MDCs extracted from the ARPES maps in Fig. 4.5(a), which follows a method presented in several studies [94, 96, 97, 127]. It is only valid under the assumption that the TSS are states that interact with, for example, bulk states only weakly [97]. Hence, panels (b) in Fig. 4.5 show the respective MDCs (as red lines) from the areas indicated by the white dashed rectangles. The MDCs were fitted (black lines) by a self-determined fixed number of Voigt profiles, being a convolution of a Gaussian profile with fixed width w_G , which represents the finite angular resolution of the setup and sample-related deterioration, and a Lorentzian of variable width w_L , directly relating to the lifetime broadening and scattering rates of the quasiparticles in this low-dimensional system (see section 2.4.2). The width of the Gaussian peak w_G , i.e. the experimental resolution, was assumed to be $w_G = 0.02 \text{ \AA}^{-1}$ (as estimated in section 3.1). Then, equation 5b from Ref. [128] ($w_L \approx w_V - \frac{w_G^2}{0.9 \cdot w_V + 0.1 \cdot w_G}$) was used to determine the width of the Lorentzian peak w_L from the assumed Gaussian w_G and the measured (pseudo-) Voigt profile w_V .

Figure 10.2 in the appendix exemplary shows the fits to the MDCs at E_F for all three spectra. From those fits to all MDCs the energy-dependent lifetime property of the Dirac cone surface electrons is extracted and these numbers are compared for the different materials. The fact, that a different photon energy is used for Sb_2Te_3 should not matter, since [97] proves the photon energy independence of such analysis.

Therefore, panels (c) and (d) depict the energy-dependent positions of the fitted peaks, i.e. the $k_{||}(E)$ dispersion, and the half-width at half-maxima of the Lorentzian peaks ($\text{HWHM} = \Delta k(E)/2$) from the two branches of the TSS, respectively (blue [red] symbols = left [right] branch of the cone). The dispersion of the Dirac cone $k_{||}(E)$ can be determined reasonably showing only a slightly deviated linear behavior. This is supported by panels (e), where the group velocity \mathbf{v}_g , which is calculated as $\mathbf{v}_g = \partial E / \hbar \partial \mathbf{k}$ ($\hbar \frac{m}{s} \equiv \text{eV\AA}$) from the reciprocal values of the dispersion, is plotted versus binding energy. Here, all three spectra show rather constant and very similar values for v_g along the first few 100 meVs with deviation for binding energies where the linear fit gets less accurate.

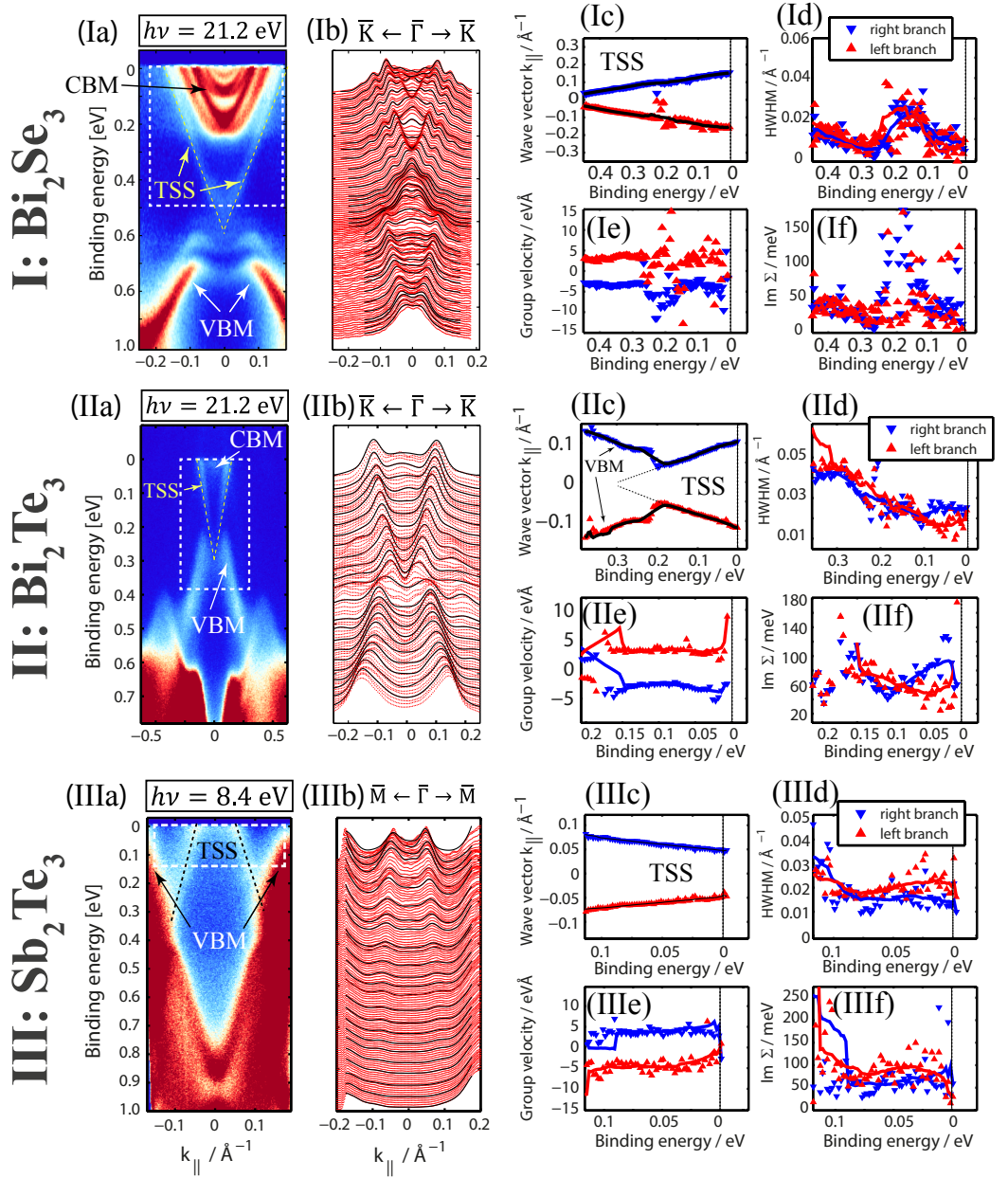


Figure 4.5: (I,II,III a) HR-ARPES maps of the TSS measured on thin films of Bi_2Se_3 (I), Bi_2Te_3 (II) and Sb_2Te_3 (III) using either 21.2 eV or 8.4 eV as indicated. All samples were cooled to low temperatures. The Dirac cone-like TSS is marked by dashed lines. (b) The corresponding MDCs (red lines) from the regions indicated by white rectangles were fitted by a varying number of Lorentzian-peaks (black lines). From the fits the peak positions, i.e. $k_{||}(E)$ (c), and peak widths, i.e. $\text{HWHM}(E)$ (d), of both left and right branches of the TSS were extracted. (e) The group velocity $v_g(E) = \partial E / \hbar \partial k$ of the surface state electrons was also extracted from the peak positions. (f) Multiplication of v_g and HWHM results in the imaginary part of the self-energy $\text{Im} \Sigma(E)$.

The fitted peak widths in panel (d) exhibit higher noise signal and are less accurate. Especially, in the case of the Bi_2Se_3 surface band structure, several conduction bands contribute with high intensity between the upper Dirac cone branches and impede an accurate fitting. But also here, the energy region $E_B = 250 - 450$ meV of free TSS delivers good results. The last panels (f) depict the respective energy-dependent complex part of the quasiparticle self-energy $\text{Im}\Sigma$ of the Dirac cone electrons, obtained by the relation $\text{Im}\Sigma(E) = v_g(E) \cdot \Delta k(E)/2$ (see Eq. 2.38). Obviously, the result is spoiled by the high noise in the HWHM-spectra, especially from Bi_2Se_3 , but nevertheless, a slowly decaying trend towards the Fermi level can be seen and all materials reveal similar values.

Table 4.1 summarizes the results from Fig. 4.5 at the Fermi level E_F and additionally states the energetic position of the Dirac point being extracted from the intersection of interpolated linearly dispersing lines³. As one can see, the results for the Fermi velocities v_F and imaginary part of the self-energy $\text{Im}\Sigma$ are very similar and in the same order of magnitude as it has been reported earlier [96, 97]. Due to the rather poor statistics in the determination of the HWHM, the statistical error by the standard deviation on $\text{Im}\Sigma(E_F)$ is very large (nearly 100% of the averaged value). Therefore, these numbers have to be treated with care. Only in Bi_2Se_3 the $\text{Im}\Sigma(E_F)$ is about a factor of 2 smaller than in the other materials, which is probably due to the higher quality of the film and thus sharper spectral features, as it will be pointed out in section 5.1. Unfortunately, in that case unfavorable final state transitions with huge contribution from the CBM are excited, due to the constraints in photon energy.

	Bi_2Se_3	Bi_2Te_3	Sb_2Te_3
carrier type	<i>n</i> -type	<i>n</i> -type	<i>p</i> -type
$E(\text{DP})$	550 ± 10 meV	300 ± 10 meV	-120 ± 10 meV
$v_g(E_F)$	$3.24 \text{ eV}\text{\AA} \equiv 4.92 \cdot 10^5 \text{ m/s}$	$2.95 \text{ eV}\text{\AA} \equiv 4.48 \cdot 10^5 \text{ m/s}$	$3.01 \text{ eV}\text{\AA} \equiv 4.58 \cdot 10^5 \text{ m/s}$
$\text{Im}\Sigma(E_F)$	~ 31.9 meV	~ 68.3 meV	~ 69.5 meV

Table 4.1: Summary of Fig. 4.5 showing the comparison of the parental 3D TIs with the extracted Dirac point position $E(\text{DP})$. The values for the (absolute) Fermi velocity $v_g(E_F) = v_F$ and $\text{Im}\Sigma(E_F)$ are averaged numbers from panels (e) and (f) close to E_F . The statistical errors are approximately $\Delta v_g \approx 50\% \bar{v}_g$ and $\Delta \text{Im}\Sigma \approx 100\% \bar{\text{Im}\Sigma}$.

For a more comprehensive analysis of the self-energy constituents, i.e. a detailed discrimination of the individual effects that lead to lifetime-broadening, which are the different scattering mechanisms such as electron-electron, electron-disorder ($\text{Im}\Sigma_{e-d} \sim 10 - 30$ meV [96]) or electron-phonon scattering, the experimental resolution is not sufficient. Electron-phonon interaction, for example, manifests itself as tiny kinks in the dispersion of states close to E_F , as it is reported e.g. in [127] or the review [129]. Those effects, however, are more pronounced in highly-correlated materials such as superconductors. Topological insulators and their TSSs, on the other hand, do not belong to strongly interacting, correlated systems, which is why there are no kinks observed and electron-phonon scattering has been reported to be ‘exceptionally weak’

³ Here, a constant error is assumed, due to the set energy resolution of $\Delta E_A = 10$ meV. Note, that the position of DP will be discussed in chapter 6 for Sb_2Te_3 because comparison to DFT delivers more accurate results.

[95] ($\text{Im}\Sigma_{e-ph} < 2 \text{ meV}$ [97]).

The observed broadening is probably mostly due to sample-related broadening, which means that the electron-disorder scattering may be much increased in the thin film samples presented here, compared to what was reported earlier. Nevertheless, it should be pointed out that we are not aware of any of such analysis performed on thin film TIs up to date, but instead, only on cleaved single crystals. In summary, we believe that these samples do allow a quantitative comparison and that we found and reproduced, for all three different materials, values for the Dirac fermions self-energy which are of the correct order of magnitude. This again underlines the quality of our thin film TI samples.

Band Structure Engineering by Doping

This chapter will summarize our findings on the manipulation of the electronic structure by 'conventional' and more simple means of surface doping by adsorbates and impurities (compare upper and central left panel in Fig. 1.1) and bulk alloying of the different TI materials (lower left panel in Fig. 1.1).

5.1 Unintentional Surface Doping or the 'Aging' Effect in Bi_2Se_3

Bi_2Se_3 is probably the most widely studied 3D TI due to the largest bulk band gap and the location of the Dirac point in the gap (free of any bulk bands). Thin films of this material have been grown in the University Würzburg by our collaborators Steffen Schreyeck et al. in the group of Prof. L.W. Molenkamp.

In this section, observations of the well-known 'aging' effect of the Bi_2Se_3 surface are presented, where adsorption/contamination of various (residual gas) elements leads to charge accumulation on the surface. The latter strongly increases the intrinsic n-doping of Bi_2Se_3 , which is observed as a time-dependent variation of the surface electronic structure. This charge accumulation is accompanied by a downward band bending of conduction and valence bands and a consequent occurrence of a two-dimensional electron gas (2DEG). This is due to the confinement at the surface resulting in a quantization of both conduction and valence band states. Moreover, these quantized 2DEG states are subject to a strong surface-confined SOC leading to a pronounced Rashba-splitting of the new conduction states. This phenomenon was extensively studied experimentally [94, 130–135] as well as theoretically [136–138], but the exact underlying mechanisms are still under debate, as it will be discussed later. What is new here is that a full reversibility of this 'aging' effect will be demonstrated, meaning that the time (and temperature)-dependent energy shift can be reversed completely. Unfortunately, we will not be able to chemically identify the surface adsorbates, since our setup was at this point still lacking the *in situ* XPS capability, necessary for a proper chemical analysis. However, the precise knowledge about the adsorbate is not necessary, because similar effects have been shown for many different adsorbed or deposited

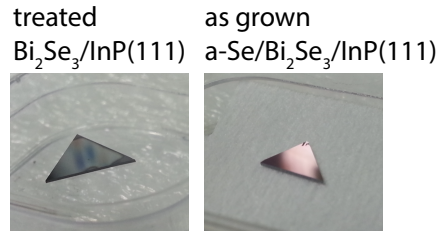
elements or molecules.

It should be noted that such effects have only been reported for Bi_2Se_3 . Likewise, we do not observe time- or temperature-dependent energetic shifts in any other 3D TI that would be of similar order of magnitude as in Bi_2Se_3 .

5.1.1 Sample Design and Preparation

Films of Bi_2Se_3 have been grown by MBE on $\text{InP}(111)$ substrates and the quality and properties of this growth are discussed in detail in [121, 139, 140]. In contrast to $\text{Si}(111)$ substrates, the $\text{InP}(111)$ substrate exhibits a much reduced lattice mismatch of $\sim 0.2\%$ (instead of $\sim 7.8\%$ for $\text{Si}(111)$). This is in general expected to lead to higher-quality films and less defect concentrations. However, using $\text{Si}(111)$ as substrate promises a higher impact for conventional electronics and semiconductor industry. The thickness of the Bi_2Se_3 layer, which is grown at elevated substrate temperatures, is $\sim 107\text{ nm}$. After the sample has been cooled down to room temperature for 4 hours, an approximately 100 nm thick film of amorphous Se was put on the samples in order to protect against oxidation. Finally, the large wafer is cut into small samples along the crystallographic directions resulting in triangular or trapezoidal sample shapes. The photos in Fig. 5.1 show one sample after the Se capping layer has been flashed off (left) and one sample in its original state (right).

Figure 5.1: Photograph of two 107 nm Bi_2Se_3 thin films grown on $\text{InP}(111)$ substrates. The as grown sample has an additional 100 nm thick capping layer of amorphous Se that produces a reddish color, while the treated sample obtains a metallic grayish color after annealing.



After transfer into the ARPES chamber, the samples just needed to be annealed to $\sim 150^\circ\text{C}$ for few minutes, which is enough to completely desorb the loosely bound amorphous Se capping layer from the surface. By looking at the sample during annealing with the eye, one can identify a color transition of the sample from reddish, caused by the thick amorphous Se layer, to metallic, as soon as the Bi_2Se_3 layer is exposed (as shown in the photo in Fig. 5.1). Then, the sample is ready for ARPES measurements which is also proven by the sharp LEED pattern in Fig. 5.2.

5.1.2 Pristine and Aged Bi_2Se_3

Figure 5.2 summarizes the main findings of the ARPES investigations on fresh, ‘pristine’ Bi_2Se_3 films obtained immediately after flashing off the Se capping layer, and the very same sample two days later after it ‘aged’ in the UHV system and got into a stable / saturated state. The figure depicts the ARPES $E(k_{||,x})$ maps along $\overline{\Gamma K}$ direction obtained with $h\nu = 21.2\text{ eV}$ photon energy for both sample states, as well as the very

same two data sets using another approach to visualize dispersive features by the concept of the mathematical curvature¹ (as introduced in [141]). This method sometimes enhances the visibility of certain spectral features, but can also introduce additional noise. In principle, it contains the same information as the spectra above. Additionally, the figure depicts representative constant energy cuts at various binding energies in a three-dimensional plot for the purpose of better identification of certain bands and their symmetries.

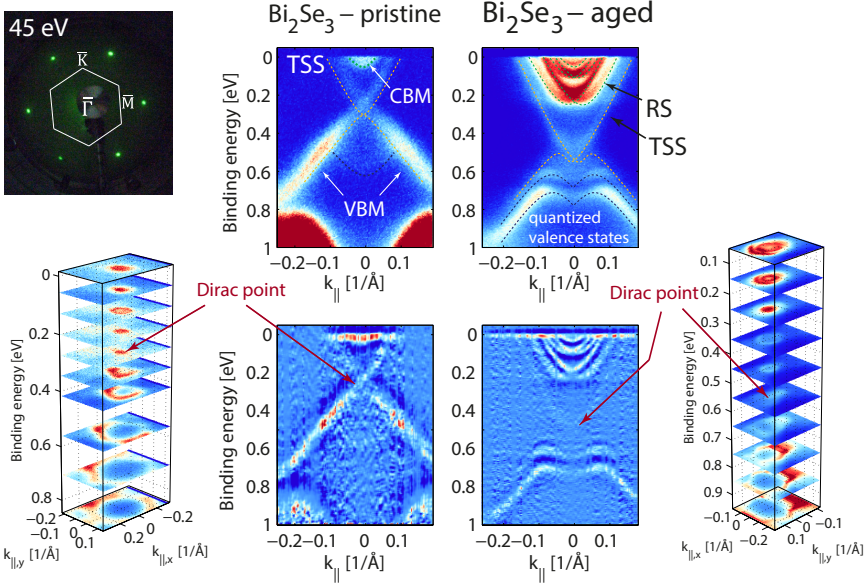


Figure 5.2: Surface electronic structure of a 107 nm film of Bi_2Se_3 immediately after flashing off the capping layer and after two days in the UHV system. Most important spectral features are marked. The ARPES $E(k_{\parallel,x})$ maps were taken along $\bar{\Gamma}\bar{K}$ direction and using $h\nu = 21.2\text{ eV}$ at low temperatures ($T \sim 30 - 50\text{ K}$). Additionally, the respective 1D curvature plots of the MDCs and a three-dimensional view of different constant energy contours are shown. A LEED pattern of the sample is obtained with 45 eV electrons after finishing the ARPES investigation (top left).

First of all, it shall be emphasized how remarkable and dramatic the time-dependent change of the surface electronic structure in this material is. To the best of our knowledge and experience, none of the other parental or advanced 3D TIs shows such a behavior or time-dependent shifts of a comparable magnitude. As mentioned above, in Bi_2Se_3 this effect was observed several times [94, 130–135]. Multiple conclusions can be drawn from Fig. 5.2:

¹ The approach quantitatively determines 'how much a curve is not straight' [141] and is very similar to the often used method of visualizing the second derivative of ARPES data. The curvature function is given by $C(x) = \frac{f''(x)}{(1+f'(x)^2)^{3/2}}$. We will only use 1D curvature plots along the MDC direction which is known to introduce fake artifacts at the Fermi level.

- The Fermi level shifts upwards, i.e. the entire electronic structure shifts towards higher binding energies by about 250 meV, enhancing the *n*-type behavior of Bi₂Se₃ with a larger fraction of the conduction band being occupied.
- The topological surface state is visible in both cases and the Dirac point shifts from $E_B = 300$ meV to $E_B = 550$ meV. Mostly the upper part of the Dirac cone is visible and the DP is very close to the VBM and later even buried in the VBM pockets.
- The shape of the Dirac cone changes from circular to hexagonal at the Fermi surface when the distance to the DP is increased as seen in the constant energy contours. This warping of the Dirac cone is caused by out-of-plane spin components of the Dirac electrons and was reported several times [39, 142] (it is even more pronounced in Bi₂Te₃ [47])
- The bulk VBM, reflecting the trigonal symmetry of the lattice, is shifted and transformed into M-shaped bands which are additionally quantized into several states (at least three).
- Similarly, the bulk CBM, keeping a trivial, free-electron like shape, is quantized into three different CB states which are moreover subject to a strong surface Rashba-effect (Rashba-surface states RSS) that splits the parabolas in *k*. Quantitatively, this splitting is much larger than in Au(111) for example, since Bi atoms are much heavier than Au atoms.

Most of this interesting and rich physics that is happening in Bi₂Se₃ can be understood by surface adsorbate induced charge accumulation and consequent band bending in the surface electronic structure. It should be emphasized that since ARPES is such a surface-sensitive technique, its results will be always prone to surface band bending effects, especially when probing semiconducting samples. Even under good UHV conditions, residual gas atoms or molecules such as CO, K, H₂ or also H₂O will, as a function of time and depending on other parameters such as temperature and the sample sticking coefficient, form a closed layer on the surface of each sample. Those adsorbing atoms will either donate or take away electrons from the surface. The situation is then similar to a metal-semiconductor junction or Schottky contact, where this charge transfer in equilibrium leads to an upwards or downwards band bending in the semiconductor near-surface band structure.

Figure 5.3 visualizes the band bending effect on the example of Bi₂Se₃. The central panel depicts a schematic energy diagram of conduction and valence band as a function of space across the bulk of the TI sample (gray). The scheme is supported by GW band structure calculations of a 100 QL slab of Bi₂Se₃ (left) by our coworkers. In this calculation the yellow bands are surface states and orange and violet states are bulk bands projected onto the (111) surface (see also section 2.5). Therefore, the energy diagram in the center represents the bulk electronic structure along the $\bar{\Gamma}$ direction with conduction band states in orange, followed by the fundamental band gap, the upmost valence band states in violet and, finally, another spin-orbit induced gap. In the bulk electronic structure the Fermi level (dashed line) may even be below the CBM.

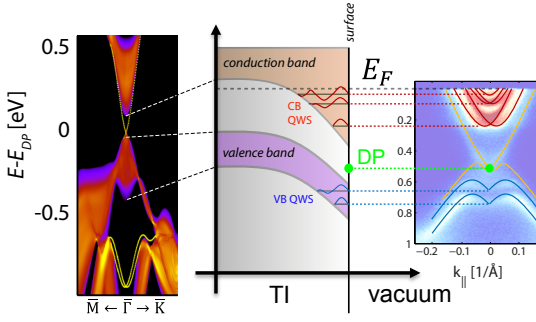


Figure 5.3: Sketch explaining the observed quantum confinement of the 'aged' sample caused by strong band bending on the surface of the sample. The sketch of the band diagram in the TI is interpreted by GW band structure calculations. (Calculated by I. Aguilera).

If the surface of the TI gets covered by adsorbates, the direction of charge transfer will determine the direction of band alignment. For Bi_2Se_3 , the adsorption of typical residual gases like CO, K, H_2O or alkali metals has been shown ([94, 131, 132]) to induce a substantial downwards band bending, pushing the CBM well below E_F , as illustrated in the figure when approaching an interface to the vacuum. As a consequence these conduction band electrons are confined in a two-dimensional potential well on the surface, i.e. a 2DEG is formed, which leads to a confinement and thus quantization of the possible energetic states which an electron can occupy [143]. Those quantum well states (QWS) are shown in Fig. 5.3 (right) by discrete energy lines with electronic wavefunctions that can be analytically calculated. Indeed, the lowest three of those QWS can be identified in the ARPES spectrum of the aged Bi_2Se_3 sample, both in the conduction band (CB QWS) where the states have a trivial, 2DEG-like, parabolic shape, as well as in the valence band (VB QWS) where the shape of the bands is more complex and M-shaped.

Additionally, the parabolic CB QWS are strongly spin-split by the Rashba-effect due to the strong potential gradient at the surface, and one can clearly identify the splitting in the lowest two CB QWS. From Fig. 10.2 in the appendix one can estimate the Rashba-splitting to be $\Delta k_{\text{Rashba}} \approx 0.030 \pm 0.006 \text{ \AA}^{-1}$ which is 1.35 times larger than the splitting observed in Au(111).

5.1.3 Evolution of the Surface Electronic Structure

Next, the aging effect will be systematically analyzed. Therefore, another sample was prepared by flashing-off the Se capping layer and cooling it down to low temperatures. Meanwhile, ARPES spectra were recorded with short exposure times over a total time frame of few hours. It should be noted that similar time-dependent studies have been performed under the systematic dosing of typical residual gas molecules and aging on the time scale of minutes and few hours has been observed [94, 131, 132]. In our study, we did not purposely dose adsorbates into the chamber and the UHV conditions were rather good (base pressure $< 1 \cdot 10^{-10}$ mbar). Nevertheless, the cooling of the sample, which effectively corresponds to an increase of the sticking coefficient, and the fact

that the opening of the He lamp was only 2 mm away from the sample², lead to an enhanced aging speed of the surface.

Figure 5.4 summarizes our findings about the time-dependence of the aging. Panels (e) and (f) show ARPES $E(k_{||,x})$ maps of the main features close to E_F obtained with low exposure times and respective 1D curvature plots of the MDCs. Measuring such spectra every few minutes produces a 3D stack of time-dependent data and panels (a) [b] and (c) [d] depict the raw data [curvature plotted data] of cuts through the center of the spectra (along $\bar{\Gamma}$), i.e. binding energy vs. time pictures during the cooling of the sample (a) [(b)] and during the warming up and annealing of the sample (c) [(d)]. Additionally, (a) and (b) depict one of the first spectra, where the observed spectral features can be clearly identified. The upper two bands are the CB QWS, followed by the Dirac point and the VB QWS at lower binding energies. The lowest feature is the oversaturated Rashba surface state. The spectra in panels (e) and (f) correspond to the instants in time that are marked by the orange arrows

Indeed, the evolution with time of all these states can be clearly followed. The general observation from the spectra taken during the cooling is that the bands shift in energy towards higher E_B by about 250 meV. The strong shift in the beginning is accompanied by the emergence of the 2DEG and the Rashba-splitting. What follows is a saturation of the effect and a smearing of the spectral features. Longer measuring at low temperatures would just increase the broadening of the spectral features until the sample is fully covered with 'dirt'. This is in good agreement to what was reported earlier [131, 132].

Our main finding is that this effect is completely reversible, as Fig. 5.4(c) and (d) prove. After about 1.5 hours the spectra got smeared out. Then, the cooling was stopped and the sample was annealed with small power in order to increase the warming-up speed. Interestingly, a shift of the features towards lower E_B could be observed in the measured spectra (see Fig. 4.3.2(c) and (d)). In the end the sample was annealed to higher temperatures than room temperature, which led to another steep shift to even lower values of E_B than at the beginning³. Besides this shift, the spectral features also recover, which is a strong indication that the effect is caused by surface adsorbates and not by intercalation into the van der Waals gaps. This is because intercalated contaminants could probably not be removed as easy as surface adsorbates. To get an idea of the real sample temperature, Fig. 5.4(g) depicts a number that was extracted from the Fermi-Dirac distribution of each of the obtained spectra by $T \approx \frac{\Delta E_{FD}}{4k_B}$.

Further means of chemical analysis (like XPS) would be necessary to unambiguously identify the contaminants, unfortunately, it has not been available at the time of the experiment.

² The lamp is differentially pumped twice but the operating He partial pressure in the chamber is $2 \cdot 10^{-9}$ mbar, which means that some small portions of residual gases and impurities from the He gas bottle can and will in principle access the chamber and will immediately stick to the sample. This effect could additionally be decreased freezing the inlet line and thus purifying the gas.

³ Also it should be noted that several minutes passed after flashing of the Se cap and the first spectrum, which means that point $t = 0$ does not mark the 'perfectly clean' sample, unfortunately.

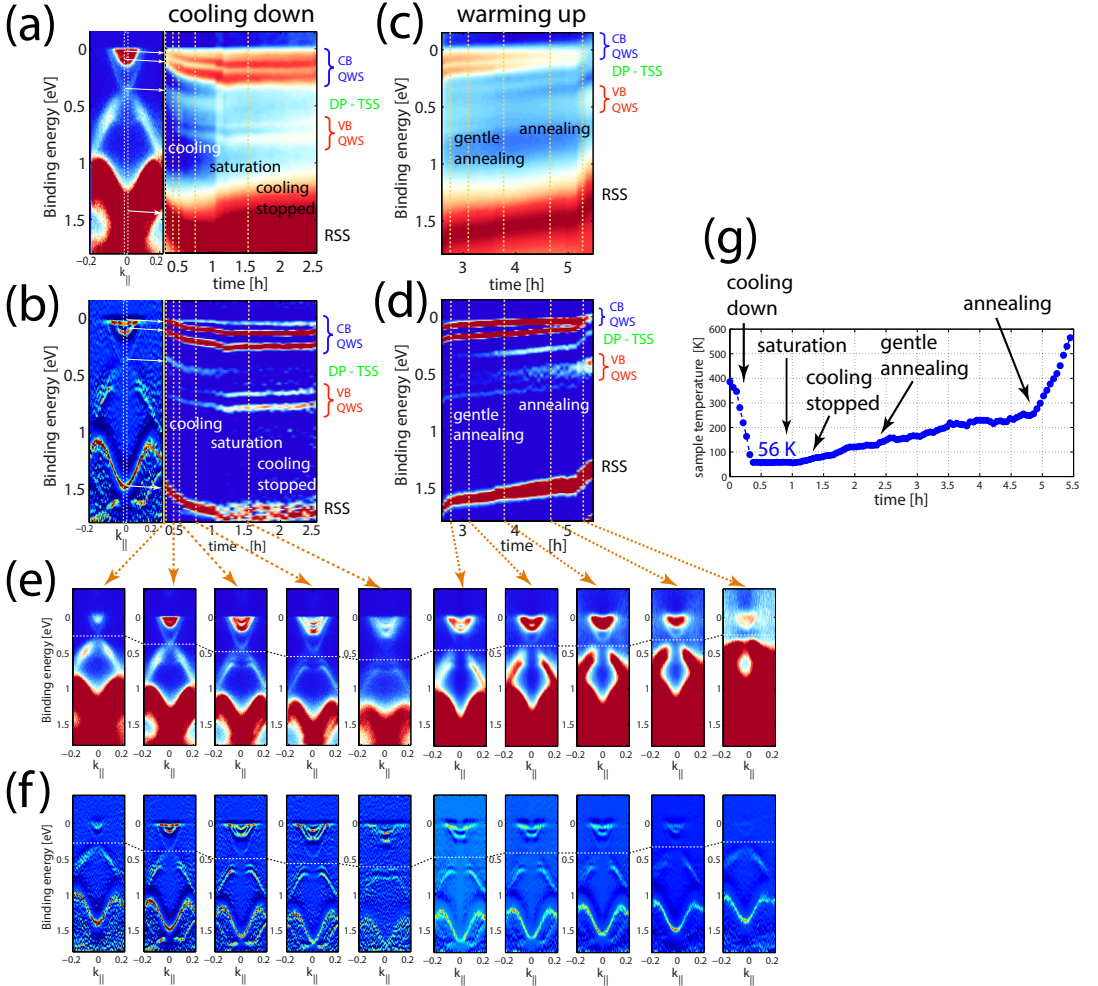


Figure 5.4: Systematic time-dependent investigation of the aging evolution of a Bi_2Se_3 thin film obtained with $h\nu = 21.2\text{ eV}$. (a) [b] and (c) [d] depict cuts at $\bar{\Gamma}$ (white dashed region) through the 3D stack of time-dependent ARPES spectra [1D curvature plots; method from [141]] during cooling and warming up / annealing, respectively. Development of several spectral features can be obtained. (e) and (f) show respective spectra at temporal positions marked by the orange arrows. (g) Temperature of the sample versus time, extracted from fits to the Fermi distribution of the spectra.

5.1.4 Conclusion

The debate about the underlying mechanism driving that substantial energetic shift in Bi_2Se_3 single crystals as well as thin films is still ongoing. Some groups are convinced that purely surface-near band bending caused by (electron) charge transfer from adsorbates is the reason for the observed effect ([94, 131–133, 138]). On the other hand,

other researchers claim that the causes are rather intercalation effects, where lighter elements or molecules diffuse into the comparably large van der Waals gaps between the QLs, leading to an effective spatial expansion of the QLs, which in turn manipulates the surface electronic band structure ([133, 136, 137]). For experimental investigations like this, one would need tools for very high-resolution structural analysis (STM, surface XRD, etc).

Our findings point more towards the first interpretation, because the temperature-dependent reversibility of the effect clearly states that the cause can be removed again, which would be rather difficult if material intercalates into the crystal. Therefore, we infer that probably surface adsorbates from common UHV residual gases introduce the observed energetic shift, which can be reversed by desorption upon annealing. We think that the reason that we observe this effect only in Bi_2Se_3 (within these time-frames) is due to the very high concentration of positively charged Se vacancies $V_{\text{Se}}^{\bullet\bullet}$ and Se anti-site defects $\text{Se}_{\text{Bi}}^{\bullet}$, which is by far larger in Bi_2Se_3 than in any other of the 3D TI materials (see section 2.3.3). These defects probably favor the charge transfer from common residual gas adsorbates compared to the other TI materials.

The observed quantization of the M-shaped VBM close to the DP could be confused with a gap opening of the TSS possibly due to the breaking of the time-reversal symmetry. However, closer studies, also employing magnetic impurities, showed that this is not the case [94]. Magnetic impurities / adatoms in low concentrations do not resemble a collective magnetic moment and thus lead only to charge doping, which we will also discuss in the next chapter.

5.2 Active Surface Doping of 3D TIs with Sub-ML Impurities

After the last chapter presented the possible effects caused by unintentional surface contamination, this chapter will discuss the influences of surface doping by a controlled deposition of ultrathin layers of magnetic as well as non-magnetic impurities. In this way it is possible to alter the surface band structure or to shift the Dirac point into the fundamental band gap or as close as possible towards the Fermi level. First it shall be demonstrated how a *p*-type Sb_2Te_3 film can be electron doped (shifting E_F towards the conduction band) by magnetic Fe adatoms, followed by the results on hole doping (shifting E_F towards the valence band) in *n*-type Bi_2Te_3 by MgO .

Furthermore, by introduction of magnetic order into a TI, time-reversal symmetry and thus the robust protection of the TSS is expected to get broken, i.e. a band gap is supposed to open up in the TSS which destroys the TIs surface metallicity [144]. However, there have been controversial findings on a band gap opening in the Dirac cone, depending on whether or not surface or bulk dopants really form a magnetic ordering [145–148].

5.2.1 Sample Preparation and *in situ* Deposition

All results presented from now on have been obtained from high-quality thin films that have been grown on Si(111) by our coworkers from PGI-9 exploiting an MBE machine and their experience with Si substrates [117, 119, 125, 149]. The high lattice mismatch between Si and the Sb_2Te_3 in-plane lattice constants is compensated for by an additional Te layer at the interface to Si which saturates the dangling bonds of the Si surface atoms. Due to this Te layer and the fact that the separate QLs are only weakly van der Waals bound, the growth is nearly strain-free and production of high quality crystals is possible.

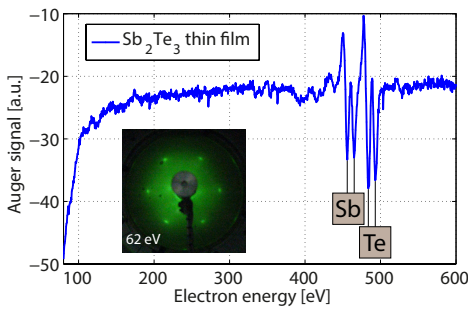


Figure 5.5: Auger spectrum and LEED pattern of a 50 nm thick film of Sb_2Te_3 after two cycles of sputtering and annealing.

After growth the samples were exposed to air and subsequently introduced into the chamber and, therefore, needed to be cleaned by repeated sputtering and annealing cycles (see section 4.1). Figure 5.5 shows the Auger spectrum after two such cleaning cycles from a 50 nm thick film of Sb_2Te_3 grown on Si(111). As one can see, there are only two clear double-feature peaks at 456 eV and 464 eV originating from Sb and at 485 eV

and 493 eV from Te. The spectrum shows no contaminations or oxide contributions, indicating a clean Sb_2Te_3 sample. The inset additionally depicts the LEED pattern obtained using 62 eV electrons, revealing high crystalline quality of the surface.

For the deposition of ultrathin films of Fe or MgO onto the surface an *in situ* molecular beam evaporator was employed, which is equipped with a high-purity Fe rod and a tungsten crucible filled with pieces of stoichiometric MgO single crystals. In this evaporator the materials are heated above the evaporation temperature by electron-beam bombardment. Monitoring the emission current and the materials ion flux, very small amounts can be controllably deposited onto the surface.

5.2.2 Electron Doping of the p -type TI Sb_2Te_3 with Magnetic Fe

First, we start with the adsorption of small amounts of Fe onto the surface of p -type Sb_2Te_3 . Since Fe exhibits 3*d*- and *sp*-electrons in its outer shell close to the Fermi level and its electronegativity is with 1.83 on the Pauling scale lower than any Sb-Te compound (> 2) [150], Fe is expected to dope electrons to the surface of the TI. Thereby, one could imagine Sb_2Te_3 to get counter-doped and to compensate and suppress the p -type bulk carriers.

The deposition rate at certain fixed evaporator parameters has been determined by depositing a thick Fe reference film and measuring its thickness *ex situ* by X-ray reflectivity to be about $\sim 1.54 \text{ \AA}/\text{min} \approx 1 \text{ ML}/\text{min}$. This number should, however, be treated only as a rough estimate, because for example the thickness of the oxidized Fe layer is unknown and will influence the reflectivity measurement.

The clean Sb_2Te_3 was repeatedly deposited with sub-ML of Fe and ARPES spectra were recorded for each deposition step. Figure 5.6 depicts the near-Fermi level ARPES $E(k_{\parallel,x})$ maps along $\overline{\Gamma\text{K}}$ obtained with $h\nu = 8.4 \text{ eV}$ for pure Sb_2Te_3 and surfaces that have been exposed to an Fe beam for 20 s, 40 s, and 60 s, respectively.

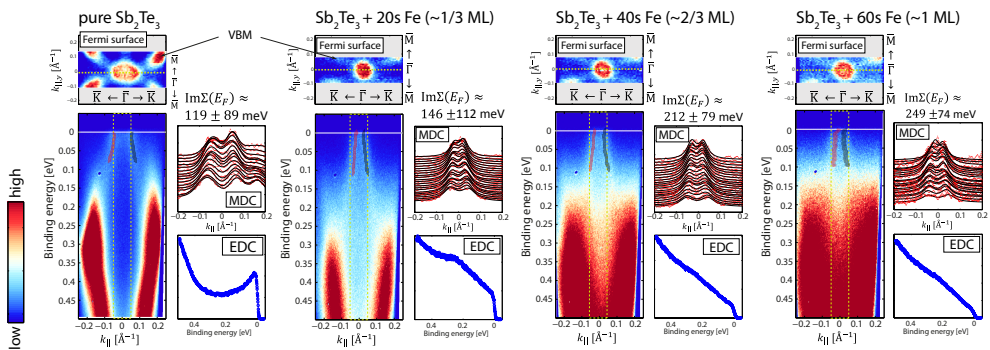


Figure 5.6: Surface doping of Sb_2Te_3 with sub-ML Fe impurities. HR-ARPES obtained using $h\nu = 8.4 \text{ eV}$ on pure Sb_2Te_3 surface and 20 s, 40 s, and 60 s Fe exposed surfaces, measured at $T \approx 25 \text{ K}$. Respectively shown are $E(k_{\parallel,x})$ maps along $k_{\parallel,y} = 0$ (center left), Fermi surfaces (top), MDCs between $E = 0 - 100 \text{ meV}$ (right upper panel; red dots = data; black line = fits) and EDCs integrated over the yellow square (right lower panel).

Additionally, the corresponding Fermi surfaces, the MDCs between $E = 0 - 100$ meV (red = data, black = fit), and the EDCs integrated along the yellow, dashed square are shown. The TSS, observed as the lower Dirac cone, can be clearly identified at this photon energy and the peak positions obtained from fits to the MDCs are superimposed in the spectra (red and black symbols for the left and right branch, respectively). Indeed, as one can nicely see, Fe adsorption leads to an electron doping of Sb_2Te_3 , resulting in a considerable downshift of the entire band structure, i.e. an upshift of the Fermi level along the lower Dirac cone, already after the first deposition of about $1/3\text{ML}$. This can also be clearly observed in the Fermi surfaces, where the area of the Dirac cone contour strongly decreases and its shape changes from hexagonal to more circular. Moreover, the strong intensity contribution from the valence band maximum decreases significantly, but does not vanish. The position of the Dirac point can be again estimated from the linear fits to the MDC peak positions and their intersections⁴. It shifts from $E(\text{DP, pure}) \approx -110$ meV to $E(\text{DP, 20 s Fe}) \approx -35$ meV upon the first deposition. Further adsorption of Fe up to 1 ML did not result in a further shift or appearance of the DP in the spectra, but only in a deterioration of the signal, i.e. a saturation of the effect. It seems that the Fermi level is somehow pinned to the valence band and it is not easy to tune it into the fundamental gap. Since the observed shift is not enough to see the DP, one cannot suppose a possible band gap opening due to time-reversal symmetry breaking.

The observed effect is very similar to the one reported for sub-ML adsorption of the alkali metal Cs in [151], where the shift of the Fermi level is also saturated already after a fraction of a ML. From the widths of the fitted peaks (black curves in the MDC plots) and the group velocity, calculated as described in section 4.2.2, one can again extract the imaginary part of the self-energy which is related to the scattering rate of the TSS electrons following Eq. 2.38. The resulting numbers close to E_F are depicted above the MDC plots in Fig. 5.6. One can see that, indeed, Fe deposition leads to an increase of the self-energy. This is solely due to the fact that new defects and thus scattering centers are introduced into the system. However, there is again a rather large statistical error due to the intrinsic broadening of the spectra. Nevertheless, a clear trend can be revealed.

5.2.3 Hole Doping of the n -type TI Bi_2Te_3 with Non-Magnetic MgO

In a similar manner, a second surface doping experiment was designed and performed. This time, we want to dope holes, i.e. extract electrons from the surface of an n -type 3D TI Bi_2Te_3 in order to shift the Fermi level downwards along the upper Dirac cone. Therefore, sub-ML amounts of MgO were co-evaporated readily from pieces of stoichiometric MgO single crystals filled into a W crucible at very slow deposition rates of $\sim 0.4 \text{ ML/min}$. Oxygen is the element with the second highest electronegativity (3.44 on the Pauling scale [150]) and is thus a very good electron acceptor and different groups have already reported a p -type surface doping of TIs using oxygen adsorbates

⁴ Note that the estimation of the DP by linear fits is known to be not totally accurate, because the Dirac cones are only dispersing linearly in the vicinity of DP. Precise comparison to band structure calculations are known to result in different, more accurate numbers for $E_B(\text{DP})$ [125]. This will be discussed more detailed in section 6.3. However, the linear fit method is the easiest and for relative comparison of energetic shifts this method is well-suited.

[152, 153]. In stoichiometric MgO, however, one would not expect any surface doping of the TI, because all oxygen bonds are saturated by Mg. However, thin layers of MgO could be potentially interesting as protecting capping layers or as tunnel contacts, which is why we are interested in the effect of MgO on the electronic structure. Figure 5.7 shows the summary of this experiment, in the same fashion as in the previous section, for the pure (and sputtered) Bi_2Te_3 film and the $\text{MgO}/\text{Bi}_2\text{Te}_3$ sample after 5 s, 10 s and 30 s of deposition. Here, $h\nu = 21.2$ eV was used for excitation, since the TSS in Bi_2Te_3 is known to reveal a more favorable photoemission crosssection for this photon energy. Note that the $E(k_{||,x})$ maps are shown with two different intensity scales in order to properly illustrate the upper TSS and the strong lower RSS. The spectra of pure Bi_2Te_3 clearly show the contribution from the CBM and the strong hexagonal warping of the cone in the Fermi surface. Here, the DP is about 520 meV below E_F ⁵. Upon deposition of sub-ML of MgO, again clear energetic shifts are observed. The entire band structure is shifted significantly upwards, i.e. the Fermi level shifts downwards along the upper cone, the size of the Fermi surface contour considerably shrinks, the contribution of the valence band decreases (as seen in the EDCs) and, in general, the spectra get distorted and the effect seems to be saturated after a fraction of a ML of MgO. Again the widths of the TSS can be extracted from the fits to the MDCs and the near-Fermi imaginary part of the self-energy $\text{Im}\Sigma(E_F)$ can be extracted and is given above the MDC plots. Again, the deposition of adatoms results in enhanced surface electron-defect scattering as one can see by the increase of $\text{Im}\Sigma(E_F)$. The position of the Dirac point shifts from 520 meV over 340 meV to 280 meV and 240 meV for the individual deposition steps. Unfortunately, the DP remains buried in the VBM and is too far away from E_F to make any claims about possible gap openings.

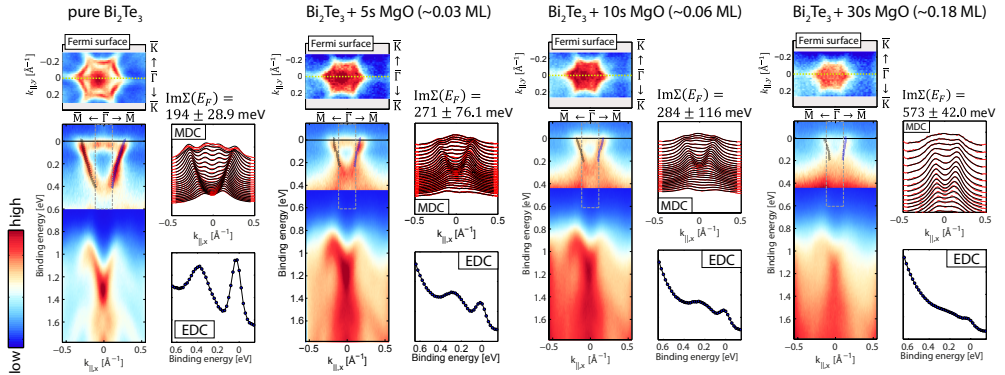


Figure 5.7: Surface doping of Bi_2Te_3 with sub-ML MgO impurities. ARPES obtained using $h\nu = 21.2$ eV on pure, 5 s, 10 s and 30 s exposed surfaces measured at room temperature. Respectively, $E(k_{||,x})$ maps along $k_{||,y} = 0$ (center left), Fermi surfaces (top), MDCs between $E = 0 - 200$ meV (right upper panel; red dots = data; black line = fits) and EDCs integrated over the yellow square (right lower panel) are shown.

⁵ Note that sputtered Bi_2Te_3 shows a slightly different spectra than clean, vacuum transferred Bi_2Te_3 , as it will be discussed in detail in chapter 7.

The fact that we observe p -type surface doping upon deposition of MgO points towards the conclusion that the MgO is not evaporated in a stoichiometric way. Already slight excesses of oxygen, however, may explain the observed hole doping which is similar as it was reported in [152] or [153] for pure oxygen dosing. Nevertheless, the similarity of MgO with respect to pure oxygen doping on the surface electronic structure promise the possibility of simultaneous doping and protection of the surface by an inert MgO capping layer.

5.2.4 Conclusion

In this chapter a considerable tunability of the surface electronic structure and the topological surface states has been presented by controlled adsorption of impurities. By a proper choice of the surface dopants one can either donate electrons or holes (accept electrons) to the surface and thus tune the chemical potential of a p -type or n -type TI either towards the conduction or valence band. However, it seems that it is not easy to unpin the Fermi level from the strongly degenerate bulk bands, i.e. to suppress the strong bulk carrier contribution, and to tune E_F into the band gap. At least for the parental TIs Bi_2Te_3 and Sb_2Te_3 this seems unlikely, but they probably exhibit too large bulk degeneration and their DP is > 100 meV away from the Fermi level. In case of a more advanced intrinsic band structure with the DP close to E_F , the precise sub-ML surface doping could be the last tool to properly align the DP to the desired energetic position.

5.3 Bulk Doping in Ternary Topological Insulators (Bi_{1-x}Sb_x)₂Te₃

The approach that is by far the most widely used to manipulate the surface electronic structure of TIs and to suppress their bulk conductivity is to tailor their structural properties in ternary or quaternary alloys of the common, parental TI elements, such as (Bi_{1-x}Sb_x)₂Te₃ [21–23] or Bi_{2-x}Sb_xTe_{3-y}Se_y [24, 25]. The crystallographic and topological properties remain the same as in the parental TIs, while it has been shown that the Fermi level and the DP position can be tuned by varying the composition (x or y) and the bulk conductivity can be reduced.

This topic was studied extensively by other groups in the last couple of years. Only for the sake of completeness and since we also pursued this approach to band-structure-engineer TIs (see references A.5 and A.6), some results on the surface electronic structure of such ternary TI alloys shall be presented here.

Results and Discussion

The ternary TI thin films have been grown by MBE and are characterized by various methods in reference A.6. The chemical composition, for example, has been estimated by *ex situ* performed XPS. For the samples investigated here the nominal compositions were $x = 100\%$, 93% , 82% , 48% . For ARPES investigations the samples have been inserted from the air into the ARPES chamber and needed to be prepared by sputtering and annealing cycles. Although a rather homogeneous bulk crystal structure and composition can be assumed, the annealing of such alloys might lead to strong elemental interdiffusion and thus modify the surface composition and electronic structure.

In order to get a rough estimate of the chemical composition of the samples, they have been measured by Auger electron spectroscopy after the ARPES analysis. The composition of the samples shall be assumed to be homogeneous throughout the film and at the surfaces, which is why the surface sensitive AES method can be used to estimate the overall composition. Figure 5.8 shows the series of AES spectra from the three ternary TIs as well as two reference spectra from Sb₂Te₃ ($x = 100\%$) and Bi₂Te₃ ($x = 0\%$) films. As one can clearly see, the Sb MNN lines clearly vanish from top to bottom, while Te MNN roughly stays the same and the Bi NOO line at $E = 103$ eV increases strongly.

For a quantitative analysis of AES spectra one can, considering the characteristic sensitivity factors of the individual Auger transitions for certain primary electron beam energies, estimate the atomic percent concentrations C_i of the occurring element i using the following equation (after [154])

$$C_i = \frac{\Delta_i / S_i d_i}{\sum_{\alpha} \Delta_{\alpha} / S_{\alpha} d_{\alpha}}. \quad (5.1)$$

Here Δ_i is the peak-to-peak intensity of the Auger signal, S_i is the sensitivity factor that can be found in literature [154] and d_i is a lock-in amplifier setting of the specific element i . The latter will be canceled out from the equation. Therefore, extracting the

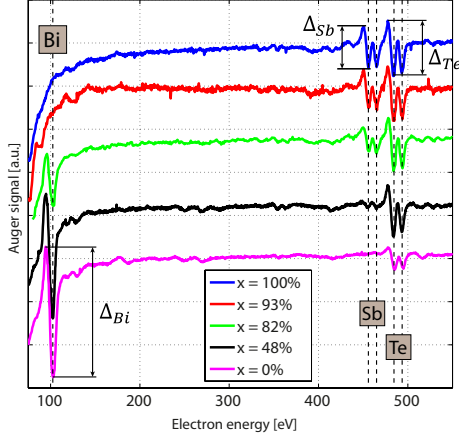


Figure 5.8: Auger spectra of a series of ternary $(\text{Bi}_{1-x}\text{Sb}_x)_2\text{Te}_3$ TI alloys obtained after the samples have been sputtered and annealed. Peak-to-peak intensities Δ_i are marked for the individual elements i . The nominal value for x is given in the legend but will be discussed in the text.

peak-to-peak intensities of the Auger lines, the following element concentrations have been found for the five samples:

nominal	Sb_2Te_3 , $x = 100\%$	$x = 93\%$	$x = 82\%$	$x = 48\%$	Bi_2Te_3 , $x = 0\%$
C_{Sb}	39.0%	37.9%	25.6%	8.2%	0%
C_{Bi}	0%	0.6%	7.5%	19.9%	39.9%
C_{Te}	61.0%	61.6%	66.9%	71.9%	60.1%
$x = \frac{C_{\text{Sb}}}{C_{\text{Sb}} + C_{\text{Bi}}}$	100%	98.6%	77.4%	29.3%	0%

Table 5.1: Elemental composition of the ternary TI films, extracted from Auger spectra in Fig. 5.8 and using Eq. 5.1.

It should be noted that this method is prone to a rather large error, which is caused among other reasons by the uncertainty of the sensitivity factor. These numbers therefore only serve as a rough estimate also due to the fact that they stem only from the sample surfaces, but they agree to the nominal numbers reasonably.

Finally, Fig. 5.9 depicts the full summary of the ARPES measurements on the three ternary TI films ($x = 48\%$, 82% , and 93%) as well as another binary Sb_2Te_3 reference sample. The figure shows the Fermi surfaces and the corresponding $E(k_{||,x})$ maps at $k_{||,y} = 0$ close to the Fermi level and additionally, a 3D illustration of the full data set for each sample is plotted. The spectral features in each of the spectra are rather unsharp and blurred, which is most probably due to the surface quality and roughness as well as to strong inhomogeneities in the surface chemical composition. Similar observations of Sb-rich and Sb-poor regions on the surface, which are identified by shifts in Raman modes and scanning force microscopy, are shown in Ref. A.6. Such variations in the composition directly lead to spectral blurring as explained above (section 4.2). The preparation procedure very likely enhances this effect, since the spectra obtained from vacuum transferred ternary TI films exhibit much higher spectral quality as shown in Ref. A.5.

Nevertheless, in each of the spectra a Dirac cone-like TSS can be identified and the electronic structure clearly shifts by more than 300 meV. In the case of an Sb content of 48% (or probably less) the electronic structure reveals an n -type character with the Fermi level close to the conduction band. This is followed by an intermediate state in the 82% and 93% Sb content samples, where the Dirac point seems to be close to or smeared out around the Fermi level. Furthermore, the Fermi surface maps reveal that for the 93% and 100% Sb content samples the Fermi level clearly truncates the valence band, thus p -type bulk transport can be expected.

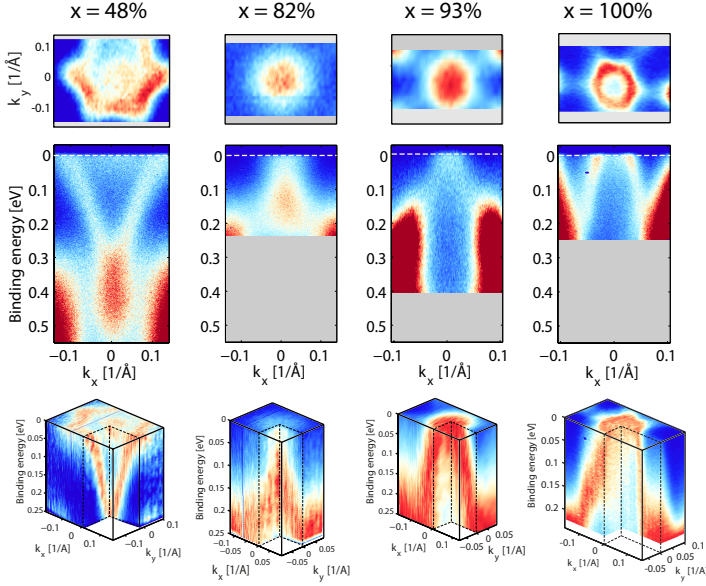


Figure 5.9: Comparison of the surface electronic structure of the ternary TI alloys $(\text{Bi}_{1-x}\text{Sb}_x)_2\text{Te}_3$ with $x = 48\%$, 82% , 93% and 100% , i.e. pure Sb_2Te_3 , measured with $h\nu = 8.4 \text{ eV}$ at low temperature. Shown are the Fermi surfaces $k_{||,x}$ vs. $k_{||,y}$ at $E_B = E_F$, the $E(k_{||,x})$ maps at $k_{||,y} = 0$ as well as a three-dimensional illustration of the data stack.

Interestingly, electrical transport measurements reveal that the 48% ternary sample is the most intrinsic semiconductor with lowest bulk charge carrier concentration which means that the Fermi level is expected to lie in the band gap. However, the ARPES investigations show a different picture since the 48% sample shows a strong n -type character while the 93% sample seems to be potentially closest to an insulating state. This controversy between more bulk-sensitive transport and very surface-sensitive ARPES measurements is also discussed in reference A.6. We believe that due to surface band banding effects, similar to the ones illustrated in Fig. 5.3, the electronic structure, and thus the position of the Dirac point $E_B(DP)$, can be very different in the bulk than at the surface. This fact should be kept in mind always, although also for applications the properties of the surface electronic structure will be determining.

Realization of a Topological p-n Junction in $\text{Sb}_2\text{Te}_3/\text{Bi}_2\text{Te}_3$ Heterostructures

The following chapter presents our findings on the more complicated approach to engineer the band structure of 3D topological insulators by the creation of a heterostructure of two binary compounds (see upper right panel in Fig. 1.1). The chapter consists of parts that appeared in *Nature Communications* as Ref. [A.3].

As we have seen in subsection 2.3.3 (and [60, 67]) Bi_2Te_3 films are known to exhibit mostly *n*-type charge carriers due to Te vacancies and ionized Bi_{Te} antisite defects. In contrast, in Sb_2Te_3 the major defects are Sb_{Te} antisite defects which impose *p*-type charge carriers. Therefore, alloying leads to an effective compensation of charge carriers and thus to a shift of the chemical potential, tunable surface states and, eventually, also to a suppression of the bulk conductivity in TIs. Similarly, bringing two binary TI films of opposite carrier character in contact, they are expected to exhibit a separation of carriers making them a natural p-n junction system. The creation of such a horizontal or vertical (parallel or perpendicular to the surface plane) topological p-n junction should also lead to a compensation of charge within the depletion layer formed at their interface. The latter should be accompanied by a built-in electric field, which in turn can affect the chemical potential and potentially bend the bands in the TIs. However, the effect of such a topological p-n junction on the topologically protected surface states or the surface electronic structure in general has not been reported so far.

This chapter will present the direct observation of thickness-dependent electronic shifts of the chemical potential in vertical topological p-n junctions, which we explain by surface band bending caused by the built-in interfacial electric field at the interface between the *p*- and *n*-type material. The vertical junctions were created in $\text{Sb}_2\text{Te}_3/\text{Bi}_2\text{Te}_3$ heterostructures of variable layer thickness, grown by molecular beam epitaxy which assures high crystalline quality and high accuracy of the thickness and composition of the thin films. While the bottom Bi_2Te_3 layer thickness was kept constant, modifications of the top Sb_2Te_3 layer thickness resulted in a varying influence from the built-in electric field on the interfacial depletion layer on the probed upper surface. Thereby,

the energetic position of the Dirac point is shifted by about 200 meV with respect to the Fermi level. In this way it is possible to alter the Sb_2Te_3 surface from being of p -type charge carrier character to n -type by reducing its thickness above the Bi_2Te_3 layer.

We believe that our findings add a fundamentally new approach to the conventional ones, such as doping or biasing, of engineering the band structure in TIs, and especially their Dirac cone, by intrinsic interfacial effects.

Moreover, structures that exhibit a spatial separation of variable Dirac cone structures opens up new possibilities to study exotic quantum phenomena. For example, Wang et al. [155] proposed to study the effect of the lateral variation of the chemical potential on the spin-locked transport and its control by external electric fields in horizontal topological p - n junctions. In a similar way, the vertical separation of the Dirac cones might enable the observation of the so-called topological exciton condensate, which is proposed to exhibit fractionally charged excitations (similar to Majorana fermions) in its vortices without any additional interface [156]. The only prerequisites are separated electron- and hole-type Dirac fermions on opposite surfaces which interact electrostatically. This will be briefly outlined at the end of this chapter.

6.1 Sample Design and Preparation

A set of epitaxial $\text{Sb}_2\text{Te}_3/\text{Bi}_2\text{Te}_3$ bilayers was grown by means of molecular beam epitaxy on high ohmic n -type doped Si:P(111) substrates of $10 \times 10 \text{ mm}^2$ size (doping level $\sim 10^{13} \text{ cm}^{-3}$) under ultra-high vacuum conditions. Bi_2Te_3 is known to grow epitaxially on Si:P(111) , forming films of high structural quality [117]. Since Bi_2Te_3 and Sb_2Te_3 have very similar lattice constants (Bi_2Te_3 : $a = 4.385 \text{ \AA}$, $c = 30.49 \text{ \AA}$; Sb_2Te_3 : $a = 4.264 \text{ \AA}$, $c = 30.458 \text{ \AA}$), Sb_2Te_3 grows epitaxially on Bi_2Te_3 as well. The thickness of the underlying Bi_2Te_3 layer was kept constant for all samples as ~ 6 QLs, whereas the Sb_2Te_3 layer thickness t was varied $t = 25, 15, 7, 6$ QLs (Fig. 6.1(a)). Further, the growth rates were kept constant at $v_{\text{Bi}_2\text{Te}_3} = 11 \text{ nm/h}$ and $v_{\text{Sb}_2\text{Te}_3} = 9 \text{ nm/h}$.

In addition to the set of $\text{Sb}_2\text{Te}_3/\text{Bi}_2\text{Te}_3$ bilayers, a 10 QL thick Sb_2Te_3 film was prepared to serve as a reference sample. In those thickness regimes the coupling and hybridization of adjacent surface states through the layers can be neglected [157, 158]. The detailed growth parameters, structural analysis and characterization of the system have been presented in earlier publications [117, 149].

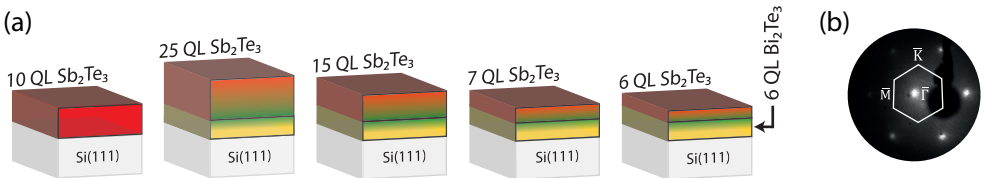


Figure 6.1: The set of epitaxial $\text{Sb}_2\text{Te}_3/\text{Bi}_2\text{Te}_3$ heterostructures grown by MBE (a) Sketch of the sample set. (b) Low-energy electron diffraction pattern of the 15 QL Sb_2Te_3 sample showing the hexagonal symmetry and the high crystalline quality of the trigonal (111) surface.

For the electronic structure investigations, the samples have been transferred into the ARPES apparatus under ambient conditions after growth. Subsequently, they needed to be annealed up to 220-250°C for a few minutes, in order to desorb surface contaminations and the top oxide layer, until the hexagonal LEED pattern could be observed (see Fig. 6.1(b)).

6.2 Experimental Characterization

This subsection presents the results of the sample characterization with a particular focus on the interface between the Sb_2Te_3 and the Bi_2Te_3 layer. In the ideal case, this is the region where, in equilibrium, the opposite charge carriers repel each other and diffuse into the other material, and form a space charge or depletion region with a built-in electric field. For conventional semiconductors the size of the depletion layer can typically vary between 10 nm and 1000 nm for charge carrier concentrations of $10^{14} - 10^{18} \text{ cm}^{-3}$ [143]. Thus, the quality and sharpness of the interface is of crucial importance for the p-n junction-induced effects.

6.2.1 Structural Analysis by HR-STEM

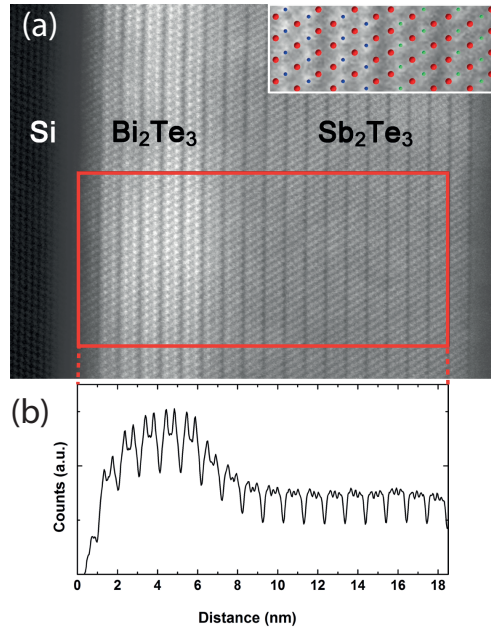
The technique that is most powerful to investigate the structural properties of the entire sample and the interface between two layers is scanning transmission electron microscopy (STEM). Here, a focused electron beam is passed through a sufficiently thin specimen and transmitted and scattered electrons are image. The size of the scanning electron beam determines the spatial resolution of the technique, which was 0.8 Å in the study presented here, and thus allowed structural investigations on the atomic scale. An aberration corrected scanning transmission electron microscope (FEI Titan 80-300) was used on cross-sectional, specially prepared specimens. The samples have been prepared by focused ion beam (FIB) etching using first 30 keV Ga ions followed by a 5 keV final treatment in order to thin the samples down. Additional Ar ion milling, using 900 eV and subsequently 500 eV Ar ions, was employed to reduce the surface damage introduced by FIB. The STEM was operated in the high-angular annular dark field mode (HAADF), which means that an annular detector measures electrons that are incoherently scattered in the specimen. This scattering strongly scales with the atomic number Z^2 of scattering atoms in the sample, which means that HAADF images contain Z contrast. Thereby, one is able to distinguish between elements of large difference in atomic number, such as Sb and Bi.

Figure 6.2(a) displays a high-angular annular dark field (HAADF) image of a 15 QL Sb_2Te_3 / 6 QL Bi_2Te_3 sample. According to the difference in atomic number, Bi atomic columns appear brightest, while Sb and Te are not distinguishable. First of all, the crystalline quality and the degree of structural order of the individual quintuple layers, which are clearly separated by van der Waals gaps, are very high. Only at the interface to the Si substrate (left), the contrast is slightly deteriorated due to amorphisation during preparation of the sample for STEM or the additional Te bilayer at the Si interface which was reported by Borisova et al. [149]. Nonetheless, the individual atomic columns are clearly revealed, which is highlighted in the inset displaying four

quintuple layers across the interface at higher magnification with a structural model as overlay.

In Fig. 6.2(b) the intensity averaged within the red frame (in (a)) is plotted versus distance, which also serves as scale of the STEM image in (a). Towards the Si substrate a decrease in counts is observed indicating a reduction in specimen thickness, which is in line with the observed amorphisation. At the $\text{Sb}_2\text{Te}_3 / \text{Bi}_2\text{Te}_3$ interface the intensity is observed to decrease over a region of only two quintuple layers, i.e. 2 nm. Since the contrast within the Sb_2Te_3 remains constant, one can assume a constant thickness across the interface as well. Hence, the intensity gradient across the small interface region implies intermixing of Bi and Sb.

Figure 6.2: Structural analysis of the 15 QL Sb_2Te_3 / 6 QL Bi_2Te_3 sample via STEM. (a) HAADF image of atomic resolution. The large overview image reveals the high quality of the crystal. Van der Waals separated quintuple layers can be observed. The contrast in the image is related to the size of the atoms on which electrons are scattered, i.e. chemical contrast is obtained. To estimate the size of the intermixed interface region a line profile is plotted in (b), integrated over the red rectangle in (a). This line profile also serves as a scale bar for (a). The inset in (a) shows a magnified region across the interface of the two layers with a structural model superimposed (blue atoms = Bi; green atoms = Sb and red atoms = Te). (Data obtained with the help of M. Luysberg and M. Lanius, PGI-5 and PGI-9).



6.2.2 Depth Profiling by AES

Since STEM is a very local probe and it should be verified that the intermixing region does not dramatically increase after the annealing step that is necessary for ARPES investigations, an additional structural characterization step by Auger electron spectroscopy depth profiling was employed *in situ*.

Therefore, selected samples have been investigated by repeated gentle 500 eV Ar^+ ion sputtering and subsequent Auger electron spectroscopy cycles in order to determine the composition profile by thinning the sample down. Due to the unfocused Ar ion beam, this technique is a fully destructive method. Figure 6.3 shows the result of such AES depth profiling for a 15 QL Sb_2Te_3 / 6 QL Bi_2Te_3 sample. In Fig. 6.3(a) the

AES spectrum after each sputtering cycle is plotted (from untreated, thick sample = blue curve to fully etched, thin sample = red curve). From the single AES spectra the relevant peaks can be identified and the relative amount of Bi, Te, Sb and Si can be determined by extracting the peak-to-peak signals, respectively. Hence, the composition can be plotted against the sputtering cycle and, by knowing the real sample thickness from STEM (see Fig. 6.2), this can be recalculated into film thickness, as done in Fig. 6.3(b).

Again, separated regions of Sb_2Te_3 (blue curve) and Bi_2Te_3 (red curve) can be clearly distinguished. Moreover, a sizable interdiffusion of Sb and Bi at the $\text{Sb}_2\text{Te}_3/\text{Bi}_2\text{Te}_3$ interface is found which might have been slightly enhanced by the additional annealing step. To be more precise, firstly, Sb diffuses to the $\text{Bi}_2\text{Te}_3/\text{Si}$ interface and, secondly, Bi shows a non-vanishing signal throughout the entire heterostructure. However, at the surface to vacuum the characteristic low energy 103 eV NOO peak of Bi was found to be small in all samples.

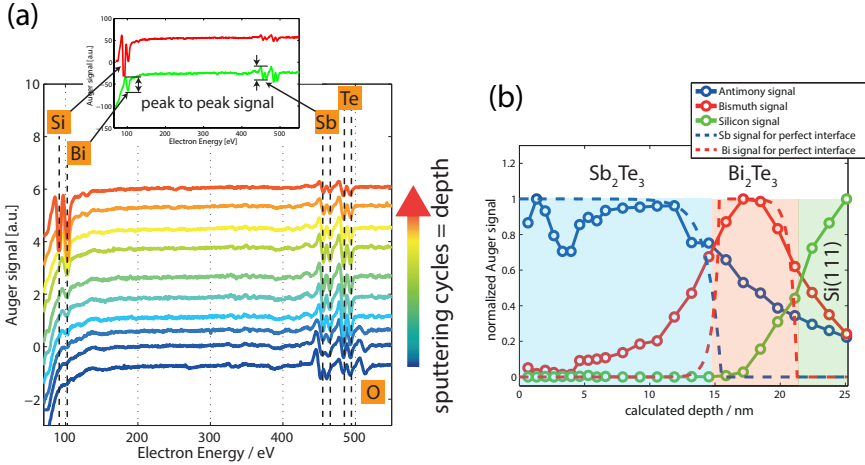


Figure 6.3: Structural analysis of the 15 QL Sb_2Te_3 / 6 QL Bi_2Te_3 sample via AES depth profiling. (a) Single AES spectra obtained after repeated cycles of ion sputtering (from blue = untreated to red). Peaks belonging to different elements are marked. The inset shows how the peak-to-peak signal was obtained. (b) The peak-to-peak signal from Bi (red), Sb (blue) and Si (green) is plotted against sputtering time which is recalculated into sample thickness by calibration via the STEM measurements. The dashed lines mark the lower limit of accuracy which this method can provide assuming an ideal sharp interface between the two materials.

This depth profile confirms the existence of an intermixed interface region between the two TI layers of roughly 5 nm width. However, the real extension of this region will be smaller than the red or blue profiles because one has to take several broadening effects into account. Firstly, the measured AES signal is a convolution of the true profile and an exponentially decaying, thickness-dependent function that includes the inelas-

tic mean free paths of the Auger electrons (simulated by the dashed lines in Fig. 6.3(b)). Such a function gives an upper limit of the accuracy of the AES profiling method, assuming that the sputtering process proceeds homogeneously, i.e. in the 'layer-by-layer' mode. Secondly, the measured profile is convoluted with the depth resolution function [159], taking into account sputtering-induced changes in the composition and surface roughness. This means that the true profile is expected to be steeper than derived here, i.e. the intermixed region is $< 5 \text{ nm}$, which is in good agreement with the presented STEM data and also means that the cleaning procedure did not significantly influence the quality of the interface.

6.2.3 Transport Properties

To prove the existence of different regimes of (bulk) charge carrier types in the heterostructures, magnetic field-dependent transport measurements were performed at 1.4 K in standard Hall-bar geometry (a sketch of the processed Hall-bars is shown in Fig. 6.4(a)). The sample widths varied between $w = 20$ and $40 \mu\text{m}$, which did not influence the results. The resulting Hall resistances are shown in Fig. 6.4(b).

A transition from n - to p -type regime could be observed for increasing top Sb_2Te_3 layer thickness. The slope of the transversal Hall resistivity R_{xy} changes from negative to positive between a sample thickness of 6 QL (green curve) and 17 QL Sb_2Te_3 (red curve). This implies that the electronic transport is mostly dominated by hole (p -type) and electron (n -type) transport, respectively. The non-linearity of the Hall resistance at lower fields is interpreted as an effect due to the coexistence of both p - and n -type charge carriers in the samples. However, it is neither as strong nor does it change its slope as it was reported for certain gate voltages previously in similar heterostructures [160]. Furthermore, the slight change of the slope between the 6 QL sample (green curve) and the 3 QL sample (black curve), which is opposite to the general trend, is due to the limited accuracy of this measurement.

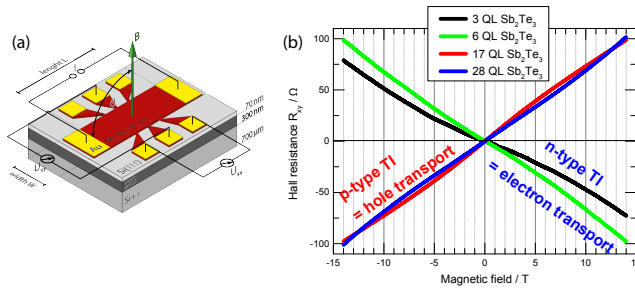


Figure 6.4: Field-dependent transport measurements. (a) Sketch of the standard Hall-bar structures, which are created by electron beam lithography from the p - n heterostructures. (b) Hall resistance R_{xy} of 4 different samples with varying top Sb_2Te_3 layer thickness investigated at fixed gate voltages and low temperature. For thinner top layer thickness of 3 QL (black curve) and 6 QL (green curve) the heterostructure is in an n -type (electron) transport regime, whereas for thicker films of 17 QL (red curve) and 28 QL (blue curve) p -type (hole) transport is dominant. (Data obtained by C. Weyrich, PGI-9).

6.3 Engineering of the Surface States by the Built-In Electric Field

The detailed surface electronic structure of the studied heterostructures was mapped using high-resolution ARPES. Figure 6.5(a)-(d) displays wide-range binding energy E_B vs. wavevector $k_{||,x}$ ARPES maps along trajectories traversing the $\bar{\Gamma}$ -point of the surface Brillouin zone for the four different heterostructures. The spectra were recorded with $h\nu = 21.2$ eV, since this allows access to the entire valence band. The exact cut directions in k -space were deduced by Fermi surface mapping and are highlighted in the insets of Fig. 6.6(b)-(e). The plotted overview spectra all show dispersing bulk bands at relatively low background intensity, which signals the high crystalline quality of the samples. Typical features of the Sb_2Te_3 band structure are revealed (compare section 4.2.1 or ref. [58]), such as the prominent Rashba-split surface state located between $E_B = 0.4 - 0.8$ eV and $k_{||} = \pm 0.28 \text{ \AA}^{-1}$ in a spin-orbit induced gap within the projected band structure [56]. This feature is identified for all heterostructures and has the largest spectral weight. As highlighted by the respective energy distribution curves in Fig. 6.5, the bottom of this Rashba-split surface state shifts by about 250 meV from the 25 QL to the 6 QL Sb_2Te_3 sample. Furthermore, indications of the topologically protected Dirac cone states near the Fermi level are found in each spectrum. The photoemission cross section for these states is small at 21.2 eV, however, they can be analyzed in detail at lower photon energy (see next paragraph).

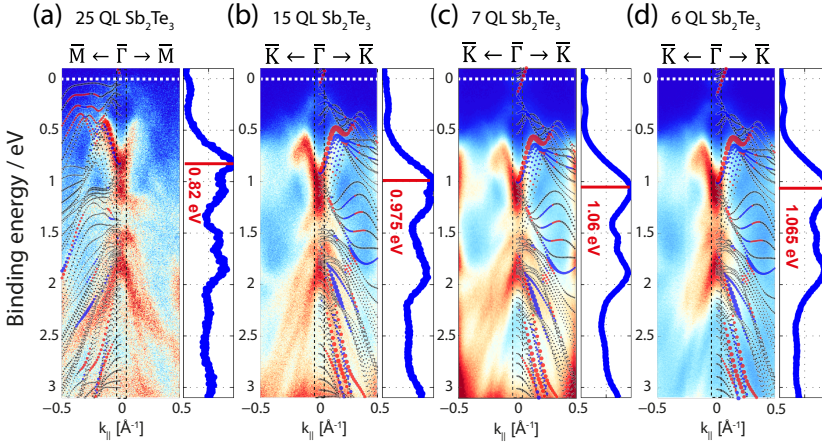


Figure 6.5: Wide energy E_B vs. $k_{||}$ ARPES maps. 25 QL (a), 15 QL (b), 7 QL (c) and 6 QL (d) Sb_2Te_3 samples measured along indicated crystallographic directions using $h\nu = 21.2$ eV. The samples were cooled to ≈ 25 K. The electronic structure of a 6 QL thick Sb_2Te_3 slab calculated by DFT along the corresponding crystallographic direction is superimposed. Red and blue dots in this calculation refer to opposite in-plane spin orientations. The Fermi level is indicated by the white dashed line. The EDCs which are integrated over the black dashed rectangles are shown on the right of each ARPES map and mark the energetic position of the most prominent features. The main feature being the bottom of the lower Rashba-split surface state serves as a gauge for the observed energetic shift.

An *ab initio* calculated (spin-polarized) electronic structure of a 6 QL thick Sb_2Te_3 slab along the corresponding crystallographic direction was superimposed on each spectrum to confirm the origin of the spectral features [58]. And indeed, in every spectrum most of the spectral features can be identified to originate from pure Sb_2Te_3 , which illustrates that the decreasing Sb_2Te_3 layer thickness leads to an energetic shift of the entire band structure towards higher binding energies. The theoretical band structures were calculated by full-relativistic density functional theory using the generalized gradient approximation and a full-potential linearized augmented plane wave (FLAPW) method which is implemented in the FLEUR code (see ref. [108]).

The same effect of a shifting band structure is observed for the Dirac cone-like topological surface band near the Fermi level. Figures 6.6(a)-(e) present the Fermi surface $k_{||,x}$ vs. $k_{||,y}$ maps, the E_B vs. $k_{||,x}$ spectra at $k_{||,y} = 0$ from a region close to the Fermi level and corresponding MDCs from the pure Sb_2Te_3 film and the set of heterostructures (25 QL, 15 QL, 7 QL, and 6 QL, respectively) measured with $h\nu = 8.4$ eV. The magnified calculated electronic structure is superimposed in each spectrum. The insets in the Fermi surfaces in Fig. 6.6 illustrate the exact cut direction through the surface Brillouin zone.

In each of these high-resolution ARPES spectra the Dirac cone can be observed. The spectra reveal that for decreasing Sb_2Te_3 top layer thickness the chemical potential of the sample surface is shifted from within the valence band through the forbidden band gap and towards the conduction band. Thereby, the Dirac point crosses the Fermi level at about 15 QL Sb_2Te_3 . The samples consisting of pure Sb_2Te_3 (a) and the heterostructures with 25 QL (b) and 15 QL (c) Sb_2Te_3 top layer exhibit a Fermi level which still cuts the valence band. This is visible as a sizable spectral weight from bulk bands with hexagonal symmetry within the Fermi surfaces. On the contrary, for the two thin films with 7 QL (d) and 6 QL (e) top layer thickness the Fermi level is well above the valence band and apparently inside the fundamental band gap with a Dirac point below E_F . This is in perfect agreement with the transport data shown in Fig. 6.4.

From the superimposed calculated electronic structure, whose Fermi level needed to be adjusted for each sample separately, the position of the Dirac point with respect to the Fermi level is determined with an accuracy of ± 20 meV. This method is known to be more precise than determining the intersection of two regression lines fitted to the Dirac cone [58]. The extracted binding energy positions of the Dirac points $E_B(\text{DP})$ are listed in Table 6.1. The total energetic shift deduced from the shifting Dirac point from the thickest to the thinnest heterostructure sample is about 200 meV, albeit slightly lower than the number derived from the wide energy spectra in Fig. 6.5. Furthermore, the Fermi velocity v_F , derived from linear fits to the topological surface states close to the Fermi level according to $E_B = \hbar v_F |k_{||}|$, is given in Table 6.1. Similar values have been obtained for pure Sb_2Te_3 and Bi_2Te_3 thin films in previous works [21, 155]. The observed energetic shifts of the electronic structure in ARPES and transport are highly reproducible and in accordance with the expected charge carrier character of the sample surface which is of p -type or n -type depending on the distance to the Bi_2Te_3 layer.

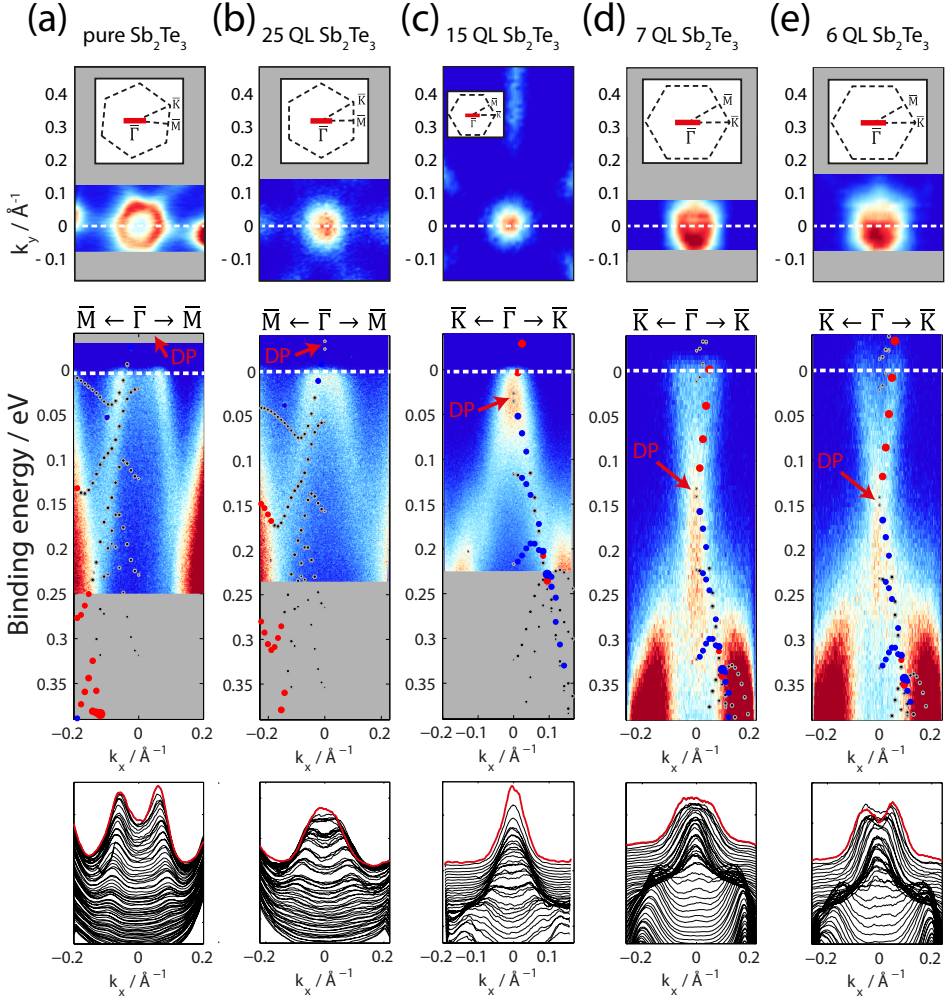


Figure 6.6: High-resolution ARPES close to the Fermi level using $h\nu = 8.4$ eV. (a) present the results obtained for the reference binary Sb_2Te_3 film. For the heterostructures the Sb_2Te_3 top layer thickness is marked on top. The upper panels depict the measured Fermi surfaces $k_{||,y}$ vs. $k_{||,x}$ for $E_B = E_F$. The black dashed lines in the insets depict the hexagonal shape of the surface Brillouin zone. This symmetry character is also conserved for the shape of the surface state as one departs from the Dirac point. The white dashed lines (= red line in the inset) indicate the cut direction where the corresponding normal emission spectra were recorded. The Dirac point is marked by red arrows and the band structure calculations from DFT with adopted Fermi energy are superimposed in each spectrum. Again, red and blue dots here represent opposite in-plane spin polarization of the states. Below, the respective MDCs at binding energies from $E_B = 0.2$ eV (bottom) to $E_B = E_F = 0$ eV (top, marked by the red line) are shown.

sample	$E_B(DP)$ [meV]	v_F [10^5 m/s]
pure Sb_2Te_3	-65	4.4
25 QL	-35	2.5
15 QL	+30	2.2
7 QL	+140	5.2
6 QL	+145	4.8

Table 6.1: Dirac point binding energies and Fermi velocities of the different samples. Binding energy position of the Dirac point is extracted from the superimposed calculations. Negative (positive) binding energy refers to the unoccupied (occupied) band structure above (below) the Fermi level. The third column shows the Fermi velocities derived from linear fits to the surface states close to the Fermi level.

6.3.1 1D Schrödinger-Poisson Model

The fundamental challenge in interpreting the presented results is to establish whether the observed energetic shifts are due to built-in electrostatic fields at the interface of the TI heterostructures and thereby caused band bending at the surface, or whether they are caused by other effects, like the segregation of Bi to the surface and thus simple surface alloying.

In order to estimate the effect of p - n junction-induced band bending, the system was modeled in 1D and the conventional 1D Poisson and 1D Schrödinger equations were solved self-consistently¹. Thus, a simple band diagram through the entire system was simulated [161]. The system consists of a semi-infinite Si-substrate, a 6 nm thick layer of n -type doped Bi_2Te_3 and a layer of variable thickness of p -type doped Sb_2Te_3 (Fig. 6.7, inset). The electron and hole effective masses as well as the band gaps were taken from the results of ab-initio calculations [162, 163]. To our knowledge, the band offset between Si and Bi_2Te_3 has so far not been determined and was assumed to be equal to the difference between the electron affinities of Si (4.05 eV from ref. [164]) and Bi_2Te_3 . The Bi_2Te_3 electron affinity ranges from 4.125 to 4.525 eV (ref. [165]), thus the band offset value of 0.3 eV between Si and Bi_2Te_3 seems acceptable. Values for the dielectric constant for both materials were found in literature to be $\epsilon_{\text{Bi}_2\text{Te}_3} = 75$ [166] and $\epsilon_{\text{Sb}_2\text{Te}_3} = 36.5$ [167]. Several numbers for the bulk native defects and surface states density were computed, i.e. tested, and the resulting band diagrams were compared to the experimental spectra. The values with best agreement were found to be for donor-type native defects in Bi_2Te_3 : $N_d = 2 \cdot 10^{19} \text{ cm}^{-3}$ and acceptor-type native defects in Sb_2Te_3 : $N_a = 2 \cdot 10^{18} \text{ cm}^{-3}$. Additionally, two layers of negative surface charge with a density of $1 \cdot 10^{12} \text{ cm}^{-2}$ were assumed at the interfaces between topologically trivial to non-trivial materials (at the interface of Bi_2Te_3 to the Si substrate and at the Sb_2Te_3 surface to vacuum). All these charge densities are within experimentally confirmed uncertainty limits. The simulations were performed assuming $T = 20 \text{ K}$. Moreover, to account for our knowledge of the slight intermixing at the interface, instead of a

¹ The Schrödinger equation was written for the envelope function using the effective mass approximation and both equations were iteratively, numerically solved and the solution was altered until the charge neutrality of the structure was fulfilled.

step-like charge carrier distribution, an intermixed interface region of 5 nm width, following the experimentally deduced profile from Fig. 6.3(b), was included in the model. The band gap of the two materials has been linearly changed from 0.12 eV for Bi_2Te_3 to 0.16 eV for Sb_2Te_3 within this region.

Finally, the model simulates the band diagram through the entire sample and two examples for 10 and 35 nm Sb_2Te_3 layer thickness are shown in Fig. 6.7(b) and (c). In the thin top layer regime (c), one can see that the sample surfaces are in an insulating state with the conduction band minimum close to the Fermi level, whereas for the thick top layers (b) the Fermi level cuts well through the valence band. Figure 6.7(a) summarizes the results of the model by plotting the position of the VBM for various top layer Sb_2Te_3 thicknesses and comparing it to the experimental ARPES data (red dots with errors explained in the caption). The dashed black line marks the Fermi level. The conduction band edge is not shown but would follow the same slope. Experimentally, a shift of the entire electronic structure of about 200 meV was observed, while the simulations even overestimate the effect and predict a shift of about 350 meV. We are aware of the physical shortcomings and oversimplifications of this model, such as the very rough inclusion of intermixing effects, which will be shortly discussed below (section 6.4). Nevertheless, the general trend of the observation can be reproduced and thus, the feasible agreement between the model and the ARPES data suggests that indeed a topological p-n junction was created and the resulting electrostatical effect of surface band bending could be probed.

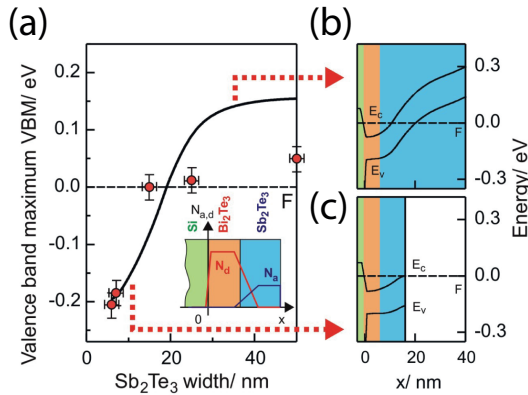
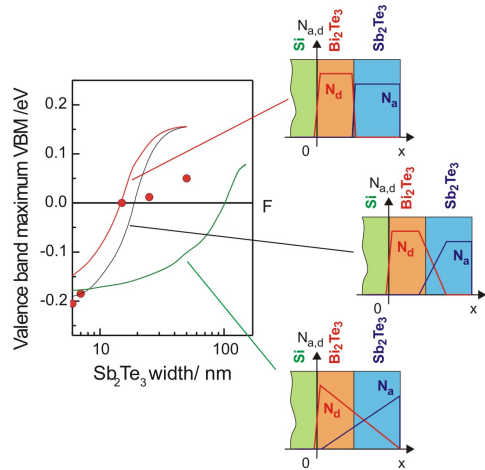


Figure 6.7: Result of the 1D model simulations using Schrödinger-Poisson equation. (a) Calculated energetic position of the valence band maximum with respect to the Fermi level at the surface to vacuum for different Sb_2Te_3 layer thicknesses (black line) and experimentally derived values of the VBM from ARPES (red dots). A large error of ± 25 meV was estimated on the position of the VBM because determination from ARPES is difficult. An error of ± 2 nm was assumed on the accuracy of the film thickness from combined XRR and STEM investigations. (b) and (c) show the band diagram of both valence and conduction band throughout the entire system for top layer thicknesses of 35 nm and 10 nm, respectively (connected by red dashed arrows to the curve in a). (Simulations performed by N. Demarina, PGI-2).

6.3.1.1 Estimations for Extreme Limits of the Model

In order to further evaluate the effect of intermixing on the position of the bands, two extreme cases of negligible and very strong intermixing have been additionally modeled. Figure 6.8 shows a similar illustration of the position of the VBM vs. Sb_2Te_3 top layer thickness. The red dots and the black curve are the same as in Fig. 6.7(a) for a charge carrier distribution based on the measured profile in Fig. 6.3(b). Additionally, the red curve depicts the results of the model for a perfectly sharp interface, i.e. no intermixing at all, and the green curve for strong gradual intermixing of the charge carrier distribution through the entire structure (the sketches on the right depict the situation for each curve). As one can see, the green curve is quite different from the experimental results, whereas the red and black curves are quite similar and resemble the experimental data pretty well. This means that strong gradual intermixing does not match our findings, whereas the above modeled assumptions describe them well.

Figure 6.8: Estimation of the limits of the 1D model. Similar plot like in Fig. 8.7(a). This time the shape of the impurity (charge carrier) distribution is modified. Red curve shows result for a perfectly sharp interface between the two Bi_2Te_3 and Sb_2Te_3 layers and the green curve, respectively, for a very strong gradual intermixing. The black curve assumes a light composition profile on the basis of the experimentally deduced profile (from Fig. 6.3(b)). In the sketches, red and blue lines represent donor- and acceptor-type carrier distribution, respectively. (Simulations performed by N. Demarina, PGI-2).



6.4 Discussion and Outlook

As we have seen, similar shifts of the chemical potential can arise from electron doping caused by slight variations in the chemical composition of ternary TIs (chapter 5.3 and refs. [21–23]). However, the following important arguments have to be taken into account:

1. The here presented ARPES scans are highly reproducible on different samples which debilitates the suspicion that the preparation process modifies the structural properties and the size of the intermixed interface layer.
2. The AES depth profiling reveals a considerable diffusion of Bi into the Sb_2Te_3 layer but the Bi NOO peak at $E = 103$ eV is negligibly small at the surface of each

heterostructure. Unfortunately, our system was still lacking the XPS capability for a proper surface chemistry analysis at the time of the experiments.

3. The Fermi level is shifted from p-doped to n-doped regime with decreasing Sb_2Te_3 thickness, which is in perfect agreement with the transport data (Fig. 6.4).
4. The order of magnitude and the relative trend of the observed energetic shifts is in very good agreement to our theoretical model (see Fig. 6.7). This strongly indicates that, indeed, purely electrostatic band bending due to the creation of a depletion layer can lead to such an effect.

On the other hand, the facts that none of the investigated topological insulators are actual intrinsic insulators and that they suffer from significant bulk charge carrier densities, declares it questionable whether they can be depleted at all. Moreover, there exist theoretical models, which treat 3D TIs as highly doped narrow-band gap semiconductors and question their ultimate bulk resistivity due to poorly screened random potential fluctuations [19, 168]. Such models would make an interpretation in the sense of an extended depletion region and electrostatic band bending in the samples questionable and drastically increase the computational complexity.

However, these theories assume a full charge compensation, which is also unrealistic, because experimentally TIs are always either over- or undercompensated. Further, recent experiments indicated that the bulk carrier limitations can indeed be overcome in certain TI compounds [25] or by the use of dual-gating of thin films [169, 170]. Finally, Brahlek et al. [18] show that band bending effects between bulk and surface Fermi level can lead to a metal-to-insulator transition and that the Fermi level can become unpinned from the bulk conduction/valence band and fall into the band gap. Hence, the use of the electrostatic Poisson equation becomes valid also in topological insulators and the creation of an extended depletion layer is possible.

6.4.1 Topological Exciton Condensate

In conclusion, we presented a completely new approach to band structure engineer the TSS in 3D TIs, purely by intrinsic interfacial effects and without the introduction of impurities or external fields. Moreover, such p-n heterostructures offer spatially (vertically) separated Dirac cone structures, which first of all can be used to electrically control spin currents and second of all, open up opportunities to study novel exotic quantum phenomena. The latter shall be briefly mentioned here.

One big research goal in today's condensed matter physics is the study of Majorana fermions, which are predicted to occur due to proximity effects at the interface between a TI and a s-wave superconductor, if the Dirac point is adjusted precisely at the Fermi level [171, 172].

Another fundamentally interesting novel state in condensed matter research was proposed by Seradjeh et al. [156], which they called topological exciton condensate (TEC). They predict its appearance in a dual-biased STI film with vertically separated Dirac fermions with small electron Fermi surface on the one surface and a small hole Fermi surface on the opposite surface (see Fig. 6.9).

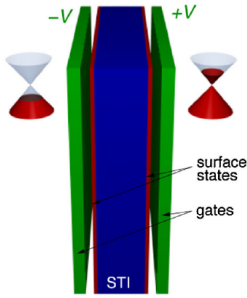


Figure 6.9: Sketch of a theoretically proposed device for the creation of a topological exciton condensate in a dual-biased STI film. (Figure taken from [156]).

A mathematical formalism was presented which describes how the opposing n - and p -type Dirac fermions couple to each other electrostatically via the Coulomb interaction and form an exciton condensate. This means, the electrons do not behave as fermions any more but couple to each other and become a bosonic, coherent liquid of electron-hole pairs, residing in opposing layers [156]. Due to their bosonic nature, they are able to condensate to the same ground state. This state hosts some interesting excitations, such as a stable vortex-like zero-energy mode which carries fractional charge of $\pm e/2$ and is protected by topology. Seradjeh et al. suggest to verify the existence of the TEC as a zero-bias peak in a transport experiment or by optical methods.

However, the TEC is so far a purely theoretical prediction, but the here presented topological p - n junctions may provide a reasonable playground for such investigations. Dirac electrons which reside in the (n -type) topological state at the interface between Bi_2Te_3 and silicon (which cannot be probed by ARPES) could couple to the (p -type) surface Dirac electrons so that a TEC is formed. In this way, compared to dual-gating of a single TI layer, our approach of combining two binary TI layers has the advantage of linearly dispersing Dirac states on both sides of the heterostructure, which enables the existence of two identical electron and hole Fermi surfaces. By a careful adjustment of the structural parameters it might be possible to set the desired conditions. Consequently, the built-in spatial asymmetry of the Dirac bands and the reliable tunability of the chemical potential in the $\text{Sb}_2\text{Te}_3/\text{Bi}_2\text{Te}_3$ heterostructures paves the way for studying exciting novel phenomena, such as the TEC, as well as potential applications in spintronics.

Natural Superlattice and Weak Topological Insulator Bi_1Te_1

Analogue to the development in semiconductor physics and according to the lower right panel in Fig. 1.1, this chapter discusses our results on the manipulation of the electronic properties by the creation of complicated superlattice structures. A thorough investigation of the crystal- and electronic structure of the stoichiometric natural superlattice $[\text{Bi}_2]_x[\text{Bi}_2\text{Te}_3]_y$ with $x = 1$ and $y = 2$, i.e. Bi_1Te_1 , is presented. Compared to the prototypical 3D strong TI Bi_2Te_3 ($x = 0, y = 3$), very minor attention in terms of topological properties was paid to the closely related compounds in the Bi-Te family and we are not aware of any study of their electronic structure.

As we have seen in section 2.3.1.4 the quantum spin Hall effect can be generalized into three dimensions and materials are classified by topological \mathbb{Z}_2 invariants $(\nu_0; \nu_1\nu_2\nu_3)$ [1, 173]. In the topologically non-trivial class one distinguishes between weak (WTI; $\nu_0 = 0$ but ν_1, ν_2 or $\nu_3 \neq 0$) and strong (STI; $\nu_0 \neq 0$) 3D topological insulators (see 2.3.2.4). A WTI exhibits an even number of topologically protected surface states on distinct surfaces, whereas the STI has an odd number of Dirac points on any surface. The WTI phase can exist in a material that consists of stacked two-dimensional quantum spin Hall systems, i.e. 2D TIs. Its existence has very recently been experimentally proven by Pauly et al. (Ref. [A.2]) by measuring the topologically protected 1D electron channels at surface step edges via STS on the cleaved surface of a $\text{Bi}_{14}\text{Rh}_3\text{I}_9$ single crystal [64].

Interestingly, it has been theoretically predicted that ultrathin two-dimensional Bi(111) bilayers (BL) will form a quantum spin Hall, i.e. a 2D TI phase [174, 175]. Indeed, quite recently this 2D TI phase has been experimentally realized by Bi(111) bilayers grown on top of bulk Bi_2Te_3 , which creates a model system to study the interaction of 2D and 3D TIs [176–179]. Moreover, also Bi_2Te_3 quintuple layers become a 2D TI system in the low thickness limit [180–183]. Consequently, a stacked superlattice of Bi BLs and ultrathin Bi_2Te_3 layers would potentially result in a weak topological insulating state and would enable the study of combined 3D and 2D TI materials exhibiting both electronic 2D surface states as well as 1D QSH edge states [94, 184–187]. Fortunately, the

so called ‘infinitely adaptive series’ of $[\text{Bi}_2]_x[\text{Bi}_2\text{Te}_3]_y$ offers a natural, stable form of such well-ordered superlattices for a broad range of x and y values [60, 188, 189] (see Fig. 7.1). While structural properties of such superlattices have been studied in detail, because of their relevance as thermoelectric materials [190], their electronic structure has very rarely been addressed.

7.1 Crystal Structure of the Natural Superlattice Series $[\text{Bi}_2]_x[\text{Bi}_2\text{Te}_3]_y$

The following figure 7.1(a) shows all (known) members of the infinitely adaptive series¹ of the $[\text{Bi}_2]_x[\text{Bi}_2\text{Te}_3]_y$ alloy family between elemental metallic Bi (right side) and ionic, semiconducting Bi_2Te_3 (left side). The relative amount of Bi atoms in the unit cell increases from 40% on the left to 100% on the right. Each of the individual alloys is derived from a stacking of the hexagonal Bi_2 bilayers and Bi_2Te_3 quintuple layers building blocks [60, 188, 189]. The x and y values give the number of the individual building blocks per unit cell, respectively, and they are separated by van der Waals gaps. The main difference between the various stable compounds is the size of the unit cell along the stacking direction c , which can vary quite a lot.

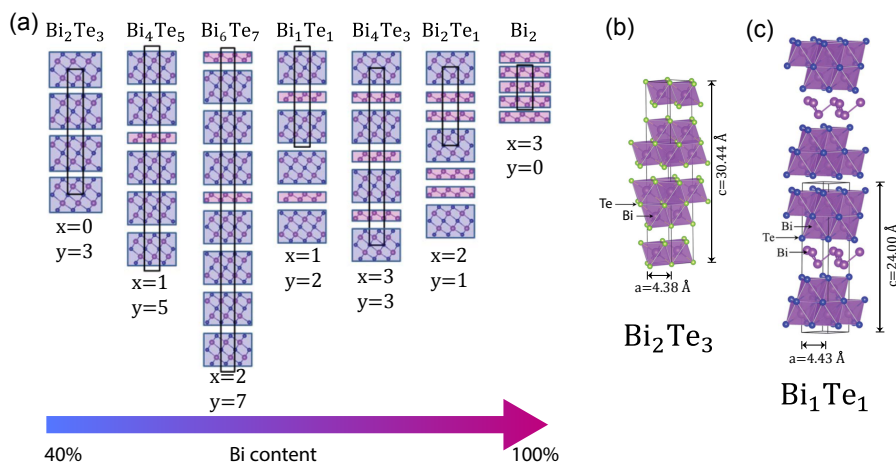


Figure 7.1: (a) Stable compounds of the natural superlattice family $[\text{Bi}_2]_x[\text{Bi}_2\text{Te}_3]_y$ with growing Bi concentration from left to right. (b) and (c) Crystallographic sketch of Bi_2Te_3 and Bi_1Te_1 with indicated unit cell and lattice constants. The main difference is the size of the unit cell in stacking direction c , and the additional Bi bilayers between two QLs. (Figures adapted from [60]; values for lattice constants from [189]).

Figure 7.1(b) and (c) depict the crystal structures of the main examples, i.e. Bi_2Te_3 and Bi_1Te_1 , respectively. As one can see, the difference in the c constant is quite severe as

¹ This is a crystallographic concept in which different very stable structural components can be stacked on top of each other in arbitrary integer ratios [60].

it decreases from $c_{\text{Bi}_2\text{Te}_3} = 30.44 \text{ \AA}$ to $c_{\text{Bi}_1\text{Te}_1} = 24.00 \text{ \AA}$, whereas the lattice constant a is very similar in all of the phases. Nevertheless, the value of c is easily accessible in diffraction experiments. This is an important point because, as one can imagine, to control the growth of these thermodynamically similar phases is not trivial, since the amount of Bi is only increased by 10%.

Growth, Surface Termination and Preparation

All samples for this study are grown as thin films on Si(111) substrates via MBE. For the evaporation of Te and Bi, standard effusion cells were heated to $T_{\text{Te}} = 260^\circ\text{C}$ and $T_{\text{Bi}} = 460^\circ\text{C}$, resulting in an extremely low growth velocity of $v = 2.5 \text{ nm/h}$. The Te shutter was opened several seconds in advance to terminate the silicon surface by Te, which saturates the dangling bonds. While Bi_2Te_3 is grown in a Te overpressure regime, resulting in a closed multilayer growth with mound formation on top of the film [149], Bi_1Te_1 requires equal vapor pressures of Te and Bi. This 1 : 1 ratio between Bi and Te changes the structure from solely quintuple layers in Bi_2Te_3 to the implanting of additional Bi bilayers between every two QLs in Bi_1Te_1 .

The surface termination, which will later be an important issue, can vary in Bi_1Te_1 between 1 Bi BL, 1 QL and 2 QLs, whereas Bi_2Te_3 is always QL-terminated.

After growth, the samples were transferred without breaking the vacuum from the MBE chamber into the ARPES apparatus by our UHV shuttle with a base pressure $< 1 \cdot 10^{-9} \text{ mbar}$, which means that no additional UHV preparation was needed. On top of that, we will later distinguish between thin films that were then measured ‘as grown’ (and vacuum-transferred) and such that were conventionally prepared by sputtering and annealing (later named ‘sputtered’ samples). For this, samples have been altered by gentle Ar sputtering with 750 eV ions and annealing up to 200°C for 15 min. This is mandatory, because spinARPES investigations at the synchrotron require a sample cleaning procedure by sputtering. Therefore, the effect of sputtering on the surface electronic structure was also studied. We will conclude that, since the sputtering yield ratio between Te and Bi is $5.7/3.3 \approx 1.7$ [191], a Te deficiency results in favorably Bi-rich, i.e. Bi BL-terminated surfaces, while the ‘as grown’ samples are due to the growth mode expected to exhibit Bi-poor, i.e. QL-terminated surfaces. However, the complexity of the crystal structure will easily result in non-homogeneously terminated surfaces that exhibit terraces and islands of different terminations [184].

7.2 Topological Invariants Revealed by DFT

This section will describe our most interesting finding. In contrast to what is claimed in Ref. [60], where the authors imply (but do not show) to have measured topological surface states in Bi_1Te_1 (and they argue with studies on the similar but still different compound Bi_4Se_3), the DFT calculations performed by our colleagues from PGI-1 reveal that the \mathbb{Z}_2 topological invariants of Bi_1Te_1 are $\nu_0; (\nu_1\nu_2\nu_3) = 0; (001)$, which means that this material is not a strong but a weak topological insulator².

² In contrast, Bi_2Te_3 is characterized by $\nu_0; (\nu_1\nu_2\nu_3) = 1; (000)$.

DFT calculations of Bi₁Te₁ were performed both for the bulk phase and thin films with three different surface terminations. To simulate a Bi BL terminated surface, a symmetric 26 layer film with BL-QL-QL-BL-QL-QL-BL stacking was used. For the single and double QL termination, symmetric 24 and 34 layer films were set up. The full-potential linearized augmented plane wave (FLAPW) method as implemented in the FLEUR code [108] was employed with the relaxed lattice parameters from the Vienna *ab-initio* simulation package (VASP) [192, 193]. Further, the generalized gradient approximation (GGA) in the Perdew-Burke-Ernzerhof (PBE) form [194] was used for the exchange correlation potential, and spin-orbit coupling is included self-consistently in the calculations.

From the DFT calculations one obtains structural parameters that are in good agreement with the experimental data presented below. The size of the bulk unit cell in *c*-direction is 25.0 Å. It consists of two QLs of 7.48 Å thickness each and a Bi BL of 1.68 Å. The BL-QL separation is 2.66 Å and the distance between the QLs is 3.04 Å. At the surfaces, these distances contract slightly, e.g. the QL-QL distance decreases by 0.06 Å at the 2 QL-terminated surface, while the QL-BL distance is reduced only by 0.04 Å for the 1 QL termination. For BL termination, the interlayer distance changes even less. The step-height between a BL-terminated and a 2 QL-terminated surface is thus 1.68 + 2.66 = 4.34 Å.

7.2.1 Bulk Band Structure and Topology

Figure 7.2(a) depicts the bulk band structure of Bi₁Te₁ in the relaxed structural geometry according to DFT calculations (distance of the upper Bi bilayer $d = 2.66$ Å). There are no states at the Fermi level E_F , reflecting the insulating character of this material. Note that the states around the Fermi level alternate between BL- (green lines) and QL-related (red lines), where the highest occupied levels at Γ and A stem from QLs (red), while the lowest unoccupied states originate from BLs (green), and vice versa for the M and L points.

Figure 7.2(c) depicts the Brillouin zone of the hexagonal lattice that was used in this calculations. The directions along which the band structure was calculated are shown by orange lines and all high-symmetry points are marked. Additionally, the bulk TRIM points are labeled according to their parity invariants $\delta(\text{TRIM})$ with a blue ‘-’ or a red ‘+’. The latter is calculated by DFT as the product of the parity eigenvalues of all occupied states as +1 (‘+’) at the Γ - and A-points and -1 (‘-’) at the M- and L-points (blue circles). As explained in section 2.3.1.4 and Refs. [1, 2], one can calculate the topological invariants of an inversion-symmetric material from the parity eigenvalues of the eight bulk TRIM points, i.e. Γ , A, $3 \times \text{M}$, and $3 \times \text{L}$. For an easier illustration, Fig. 7.2(d) depicts an equivalent view of the bulk BZ in reduced internal coordinates, using the reciprocal-lattice vector $\mathbf{G}_\nu = \nu_1 \mathbf{a}^* + \nu_2 \mathbf{b}^* + \nu_3 \mathbf{c}^*$, with the unit vectors ($\mathbf{a}^*, \mathbf{b}^*, \mathbf{c}^*$) connecting adjacent TRIM points and unambiguously identifying them. Using this simplification and eqs. 2.24 and 2.25, one can deduce all four topological \mathbb{Z}_2 invariants

as:

$$\begin{aligned}
 (-1)^{\nu_0} &= \delta(\Gamma)\delta(A)\delta(M_1)\delta(M_2)\delta(M_3)\delta(L_1)\delta(L_2)\delta(L_3) \\
 &= \delta(0,0,0)\delta\left(0,0,\frac{1}{2}\right)\delta\left(\frac{1}{2},0,0\right)\delta\left(\frac{1}{2},\frac{1}{2},0\right) \cdot \dots \\
 &\quad \dots \cdot \delta\left(0,\frac{1}{2},0\right)\delta\left(\frac{1}{2},0,\frac{1}{2}\right)\delta\left(\frac{1}{2},\frac{1}{2},\frac{1}{2}\right)\delta\left(0,\frac{1}{2},\frac{1}{2}\right) \\
 &= (+1)(+1)(-1)(-1)(-1)(-1)(-1)(-1) = +1 \\
 \Rightarrow \nu_0 &= 0
 \end{aligned}$$

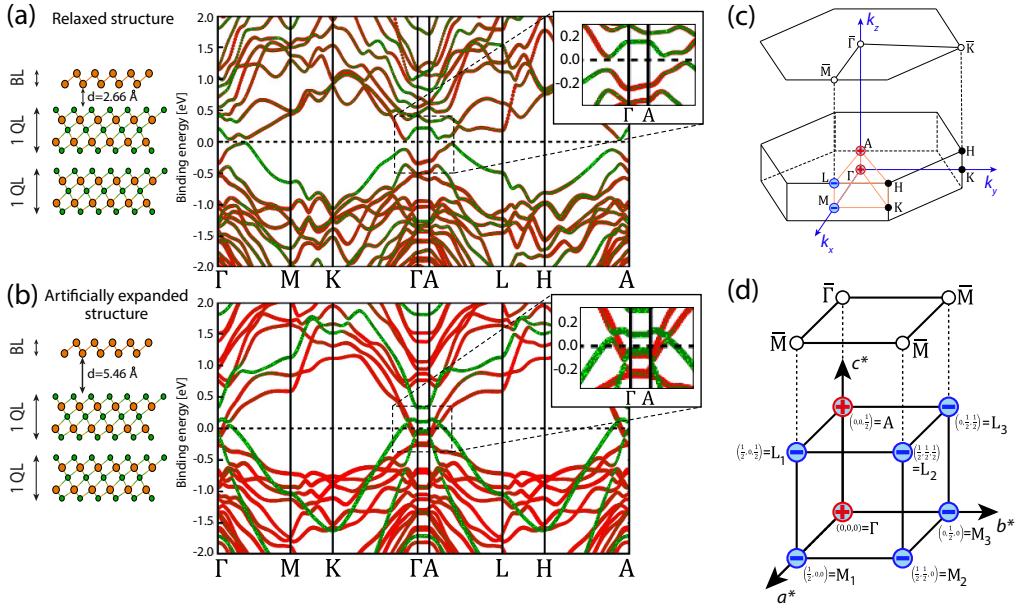


Figure 7.2: Bulk band structure calculation of Bi₁Te₁ in the relaxed geometry **(a)** and with artificially expanded distances between the BL and the QLs **(b)**. Electronic states that are localized mostly in the BL are marked in green, while the states localized mostly in the QLs are shown in red. In **(b)**, the band structure of the BL shows an (inverted) gap about 0.2 eV [195] above the Fermi level E_F (marked with a dashed line). **(c)** Bulk and surface projected Brillouin zones of the hexagonal lattice with high-symmetry points labeled. The bulk TRIM points are Γ , A , $3 \times L$ and $3 \times M$ (with parity character ‘+1’ [‘-1’] marked by red ‘+’ [blue ‘-’], respectively). Orange lines mark the directions along which the band structure is calculated in **(a)**. **(d)** Illustration of the bulk BZ in internal coordinates $(\mathbf{a}^*, \mathbf{b}^*, \mathbf{c}^*)$ with $\mathbf{G}_v = \nu_1 \mathbf{a}^* + \nu_2 \mathbf{b}^* + \nu_3 \mathbf{c}^*$ for the determination of the topological invariants ν_0 ; $(\nu_1 \nu_2 \nu_3)$. The parity eigenvalues of the eight TRIM points are again labeled in red and blue. (Calculations by C. Niu and G. Bihlmayer, PGI-1).

and further the weak indices as:

$$\begin{aligned} (-1)^{\nu_1} &= \delta(M_1)\delta(M_2)\delta(L_1)\delta(L_2) = (-1)(-1)(-1)(-1) \Rightarrow \nu_1 = 0 \\ (-1)^{\nu_2} &= \delta(M_2)\delta(M_3)\delta(L_2)\delta(L_3) = (-1)(-1)(-1)(-1) \Rightarrow \nu_2 = 0 \\ (-1)^{\nu_3} &= \delta(A)\delta(L_1)\delta(L_2)\delta(L_3) = (+1)(-1)(-1)(-1) \Rightarrow \nu_3 = 1. \end{aligned}$$

In summary, the topological \mathbb{Z}_2 invariants turn out to be $\nu_0; (\nu_1\nu_2\nu_3) = 0; (001)$. This means that Bi₁Te₁ is a weak topological insulator (WTI) with surfaces perpendicular to the (001) direction in internal coordinates, which corresponds to the stacking direction c , being so-called 'dark' surfaces and free of topological surface states. Since this surface is also the natural cleavage plane of the crystal and the easiest to probe in a photoemission experiment, this statement shall be verified in the following using (spin-) ARPES.

It is tempting to relate the WTI property to the fact that both, the Bi BL and the 2 QLs Bi₂Te₃ are 2D TIs (see [180, 183] and [175]) and that the WTI results from a simple stacking of 2D TIs in the c -direction. However, the band structure calculations in Fig. 7.2(b) show a more complex scenario, when introducing artificially expanded atomic distances at the surface (QL-BL separation increased to $d = 5.46 \text{ \AA}$):

If the BL is sufficiently separated from the 2 QLs, the states can be decomposed in contributions from the two components (green = Bi BL and red = 2 QLs, respectively). But, due to a charge transfer, the inverted gap of the BL is shifted above the Fermi level and, accordingly, some of the 2 QL Bi₂Te₃ conduction band states are below E_F . Only the hybridization of the BL states with the QL states opens up the gap that leads to the insulating bulk structure in Fig. 7.2(a), as can be nicely deduced from the changing color of the bands along the k -directions (note the difference in the magnified region at Γ and A point). Nevertheless, the topological character of the stacked film remains non-trivial. A similar complexity is also found for the first confirmed, stacked weak TI Bi₁₄Rh₃I₉ [41, 64].

7.2.2 Surface Band Structure and Termination

Next, the surface electronic structure will be investigated. For this, the bulk electronic structure is projected onto the (111) surface (in trigonal primitive coordinates) which corresponds to cleavage planes perpendicular to the stacking direction and which is the accessible surface for ARPES investigations. Since surface states are localized at the last few atomic lattice sites, here the surface termination of the crystal is of crucial importance. As mentioned above, the Bi₁Te₁ crystal can exhibit three different surface terminations which are 1 QL, 2 QLs, and 1 Bi BL. Therefore, Fig. 7.3 depicts respective spin-resolved DFT surface electronic structure calculations along \overline{MTK} of a slab of Bi₁Te₁ terminated by either a single QL, two QLs, or a Bi BL (Note that the position of E_F is not adjusted). The calculations reveal the spin polarization of the states near the film surface (blue=spin up, red=spin down). Here, the size of the symbols corresponds to the degree of polarization. The bands of strong helical spin polarization are mostly surface-related states, such as the states close to E_F or the M-shaped band around $E_B = 1 \text{ eV}$. The surface features originating from the QL terminations (left and center panel) are rather parabolic and electron-like, while the Bi BL terminated surface (right panel) produces hole-like crossing states close to E_F which are similar to what

was observed in different systems [178, 184].

Interestingly, the insulating bulk band gap that was found in Fig. 7.2 is recovered in this surface electronic structure calculation only in the left panel, i.e. the 1 QL-terminated scenario and, moreover, only along the $\overline{\Gamma K}$ direction. Already along the $\overline{\Gamma M}$ direction, the band gap is closed by surface states, not to mention the variety of surface states in the two other termination scenarios. Effectively, the different surface-related states minimize the band gap significantly or even make the system metallic by cutting the Fermi level.

This rich variety of surface-related and spin-polarized states and the complexity of the different terminations suggest that a detailed discrimination will be complicated, since our ARPES technique lacks lateral resolution and will always probe a superposition of several differently terminated surfaces.

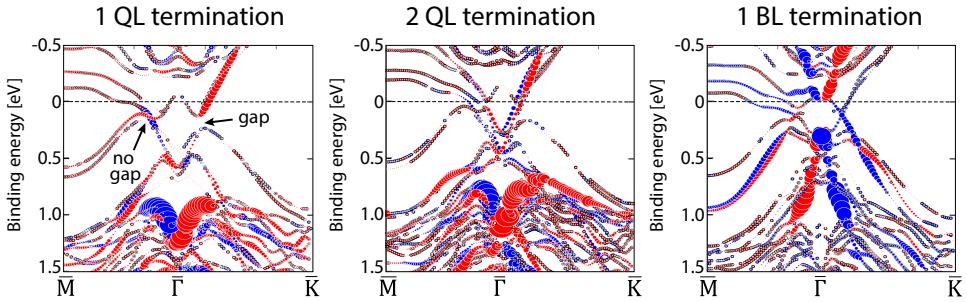


Figure 7.3: DFT surface electronic structure calculations along \overline{MK} of slabs of Bi_1Te_1 terminated by a single QL (left), two QLs (center) and a Bi BL (right). (a) Spin-integrated projected band structure with bulk projected bands in black and surface bands in red. (b) Spin-resolved surface electronic structure with spin up (down) electrons marked by blue (red) symbols. Size of the symbols corresponds to the degree of polarization. (Calculations by C. Niu and G. Bihlmayer, PGI-1).

7.3 Experimental Characterization

After the theoretical introduction and the classification of Bi_1Te_1 as a WTI, it is necessary to assure that the correct stoichiometric phase is investigated by a thorough structural characterization.

7.3.1 Stoichiometry by RBS

One of the most powerful and non-destructive techniques to determine the stoichiometry of thin films is Rutherford backscattering spectrometry (RBS) [196]. It is based on the highly mass-dependent elastic (back-) scattering and the consequent energy gain or loss of high-energy ions at the surface or the bulk of a thin sample. While in standard methods like XPS an uncertainty of up to 20% has to be assumed on atomic composition values (at%), RBS can deliver sensitivities $< 1\%$ [197]. The technique works best for heavy elements on light substrates, which makes it well-suited for this study [196]. Therefore, selected Bi_1Te_1 samples were analyzed by RBS / ion channeling using

1.4 MeV He⁺ ions and a backscattering angle of 170°. A peak integration of the separated Te and Bi scattering peaks resulted in a Bi : Te ratio of 1 : 1, i.e. 50% : 50%, within the experimental accuracy which in this case was estimated to be 1%.

7.3.2 Bulk Crystal Structure by XRD

As stated above, the best way to distinguish the individual phases along the homologous series of [Bi₂]_x[Bi₂Te₃]_y is to determine the size of the out-of-plane lattice constant c along the stacking direction. Therefore, a high-resolution Bruker D8 diffractometer for XRD measurements was employed.

Figure 7.4(a) comparatively shows the $\omega/2\theta$ scans from both Bi₂Te₃ (top) and Bi₁Te₁ (bottom) samples. From these 1D curves, the crystal phase can be determined by comparing the observed peak positions with calculated Bragg reflections. For the determination of both, the in-plane and out-of-plane lattice constants a and c , two-dimensional reciprocal space mapping needs to be employed. For this, one has to scan both, the incoming and the diffracted X-ray beam by rotating sample (ω) and analyzer (2θ), i.e. to obtain multiple 1D curves as in Fig. 7.4(a) for different sample rotations ω [198]. This results in 2D reciprocal space maps, as shown in Fig. 7.4(b). If asymmetrical crystal reflections, such as the (1,0,-1,16) reflection for Bi₁Te₁ and the (1,0,-1,20) reflection for Bi₂Te₃ are analyzed, both a and c can be extracted. They were found as: $a = 4.37 \text{ \AA}$ and $c = 30.51 \text{ \AA}$ for Bi₂Te₃ and $a = 4.45 \text{ \AA}$ and $c = 24.0 \text{ \AA}$ for Bi₁Te₁. Thus, a clear difference in the c constant is revealed for the two samples.

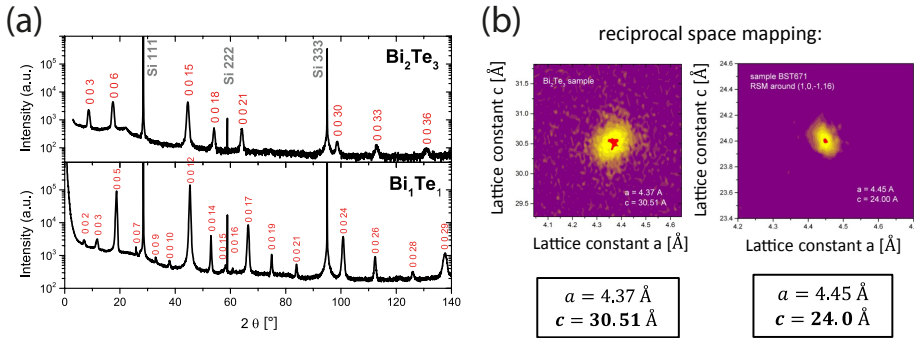


Figure 7.4: X-ray diffraction analysis. (a) Comparative XRD $\omega/2\theta$ scans for both Bi₂Te₃ and Bi₁Te₁ films averaged over the entire crystal with identified Bragg reflexes. (b) 2D reciprocal space maps of the (1,0,-1,20) reflection of Bi₂Te₃(left) and the (1,0,-1,16) reflection of Bi₁Te₁ (right) film. Extracted lattice constants a and c are highlighted below. (Data taken by G. Musler, PGI-9).

7.3.3 Unit Cell by STEM

For the ultimate proof of the different bulk crystal structure of the here presented Bi₁Te₁ films, high-resolution STEM was performed. Therefore, cross-sectional specimen were prepared using the similar procedure as described in section 6.2.1 and STEM images of atomic resolution were taken in high-angular annular dark field mode, leading to

chemical contrast between Bi and Te atoms. Figure 7.5 depicts a HAADF image of the entire cross-sectional sample (left) and a representative zoomed section (right) of a 35 nm thick Bi_1Te_1 film. A clear contrast between the occurring atoms in general and specifically Bi and Te can be observed (heavy elemental columns appear bright, light elements dark). In the left image, clearly the Si substrate followed by the Bi_1Te_1 layer can be seen. The uppermost layer suddenly appears much darker, which we can relate to a heavy oxidation of the top Bi_1Te_1 layers³. The last layer is a polycrystalline Pt layer, which needed to be deposited for the processing and preparation of the sample. The oxidation of the upper Bi_1Te_1 layer was expected, but the sharpness of the transition between oxidized and pure Bi_1Te_1 as well as the depth of oxidation is an interesting finding by itself. However, we will here focus on the precise crystal structure of the otherwise very homogenous and qualitative Bi_1Te_1 film. Therefore, the right image depicts a magnified region of the deeper layers (Note that the yellow frame is only illustrative).

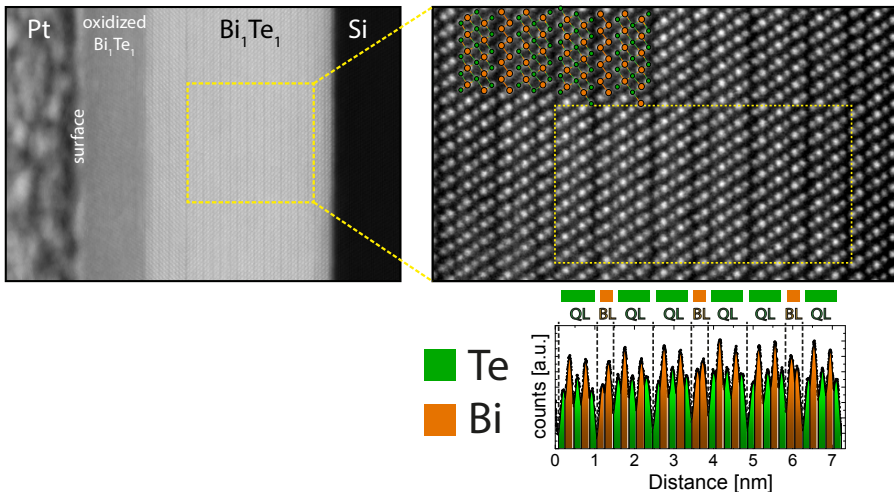


Figure 7.5: STEM analysis of a 35 nm thick Bi_1Te_1 film confirming the high bulk crystalline quality. The contrast in the image scales with the Z^2 number (bright = Bi, darker = Te). **Left:** The entire crosssectional specimen with deposited polycrystalline Pt layer, necessary for preparation. The depth of oxidized top layer due to exposure to air is clearly revealed. Otherwise, the sample is highly homogeneous. The right image depicts a zoom into the unoxidized layer (yellow square may not correspond precisely). **Right:** Quintuple layers and Bi bilayers separated by van der Waals gaps can be identified. The yellow frame marks the region over which the line profile below is measured while averaging in vertical direction. QLs and BLs are denoted and Bi and Te atoms are displayed by orange and green columns, respectively. (Data obtained with the help of M. Luysberg and M. Lanius, PGI-5 and PGI-9).

³ Oxygen atoms increase the contrast here and could also be confirmed by additional energy-dispersive X-ray spectroscopic (EDX) analysis

Here, distinct van der Waals gaps, separating quintuple layers from Bi bilayers are visible and the arrangement of BL and QL nicely matches the expected 1 : 2 composition ratio, which can also be seen by the superimposed schematic model of the Bi_1Te_1 structure. Furthermore, by extracting a line profile (yellow frame) and fitting Gaussians to the peaks (green = Te; red = Bi) the atomic positions can be determined very precisely. Hence, the size of the bulk unit cell was determined to be $c = 24.003 \text{ \AA}$, which is in excellent agreement with the result from XRD.

However, since the superlattice character of Bi_1Te_1 implies that there is more than one possible surface termination, and neither XRD nor STEM probe the surface, more surface-sensitive techniques needed to be applied. Therefore, in order to characterize the chemical composition of the surface of Bi_1Te_1 , XPS measurements were performed.

7.3.4 Surface Chemistry by XPS and the Influence of Sputtering

Figure 7.6(a) shows high-resolution XPS spectra on the Bi 5d shallow core level of a Bi_2Te_3 reference film (blue symbols), and a Bi_1Te_1 film (black symbols). This data was taken on sputtered samples at the BL5 of the DELTA synchrotron using $h\nu = 100 \text{ eV}$ synchrotron light and a Scienta SES-2002 spectrometer with high energy resolution which was limited by room temperature ($\Delta E \approx 100 \text{ meV}$; beamline is described in [116]). This shall firstly only illustrate the ability to detect the Bi BL also at the surface of Bi_1Te_1 by spectroscopic methods. A peak splitting in the Bi_1Te_1 sample by $\Delta \approx 890 \text{ meV}$ is observed in each of the Bi 5d spin-orbit doublets, which is not present in the Bi_2Te_3 reference sample and which proves the existence of the Bi BL close to the surface. It indicates that Bi exists in two distinct chemical environments. Comparison with the literature data confirms that the high-binding energy component originates from Bi bound in a metallic bilayer, while the low-binding energy component is related to Bi located inside the semiconducting quintuple layer [94, 184].

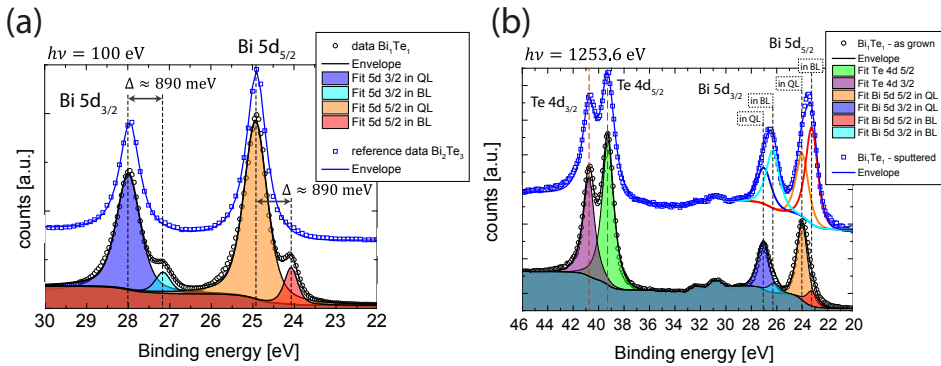


Figure 7.6: (a) High-resolution XPS spectra of the Bi 5d shallow core level for both Bi_2Te_3 and Bi_1Te_1 thin films taken with $h\nu = 100 \text{ eV}$ at BL5. Individual components of the peaks are determined and highlighted separately. (b) *In situ* laboratory-based XPS study on Bi_1Te_1 after growth and after sputtering using $h\nu = 1253.6 \text{ eV}$ at Te 4d and Bi 5d core levels. The Bi : Te ratio can be determined by extracting the peak areas.

Next, the effect of sputtering on the surface chemistry will be studied, since (as mentioned above) one expects an influence due to the strong deviation on sputtering yield. Therefore, a lab-based XPS study on a vacuum transferred and a subsequently sputtered and annealed Bi_1Te_1 sample was performed. Here, a standard non-monochromatized Mg K_α X-ray tube and an Omicron spectrometer was used, resulting in an energy resolution of ≈ 700 meV.

In order to show that sputtering removes Te more efficiently and, thus, produces Bi-rich surfaces, Fig. 7.6(b) depicts the Bi and Te core level spectra of Bi_1Te_1 immediately after growth and after subsequent sputtering and annealing (black symbols = Bi_1Te_1 as grown; blue symbols = Bi_1Te_1 sputtered). As compared to the results presented in Fig. 7.6(a), the energy resolution is worse, since a non-monochromatized Mg K_α source is used, and, consequently, the features are broadened. Nevertheless, the peaks were fitted with two components for Te $4d$ and four components for Bi $5d$, using the splitting as defined from Fig. 7.6(a). The total Bi signal with respect to the Te signal has significantly increased upon sputtering. Using the same fitting parameters for both curves and constraining SOC induced peak ratios of $3d$ levels and the peak positions to the values deduced from Fig. 7.6(a), Bi : Te ratios as well as the Bi QL : BL ratios can be extracted from the filled peak areas, respectively. The total Bi signal has increased by a factor of 2.0 and the QL : BL ratio has dramatically decreased from 5.2 to 0.7 upon sputtering. This effect also appears directly as an energetic shift of the Bi peak in the blue curve with respect to the black curve, while the Te peaks are not shifted at all. One can conclude that the amount of Bi BL in Bi_1Te_1 can be dramatically increased by sputtering and annealing and the Bi_1Te_1 thin film surface can be altered from a Bi-poor into a Bi-rich termination. However, we will later see that the electronic structure remains mostly unchanged.

7.4 Surface Electronic Structure of Bi_1Te_1 vs. Bi_2Te_3

This section will describe the differences in the electronic structure between the two compounds in detail.

The comparative results of our ARPES investigations on untreated and vacuum transferred Bi_2Te_3 and Bi_1Te_1 thin films are summarized in Fig. 7.7. As mentioned and confirmed above, the as grown Bi_1Te_1 surface can be considered as Bi-poor. In the case of the prototypical STI Bi_2Te_3 the results presented here nicely reproduce earlier findings [57].

In general, the spectra exhibit sharp features and a very good signal to noise ratio revealing the high crystalline quality of the thin films. Figures 7.7(a) and (e) depict wide range binding energy E_B vs. wavevector $k_{||}$ maps of Bi_2Te_3 and Bi_1Te_1 , respectively, along trajectories in the $\overline{\Gamma K}$ direction which traverse the $\overline{\Gamma}$ point of the surface BZ recorded with $h\nu = 21.2$ eV. Already at first glance, the spectra of the two samples show a lot of similarities but also some major differences (e.g. marked by the white arrows). Both samples are of n -type nature with the conduction band minimum being cut by the Fermi level, but in Bi_1Te_1 there seems to be an even stronger downshift of the entire valence bands, due to a possible electron donation of the Bi bilayers to the QLs [94]. The downshift as well as the spectral changes are clearly revealed by

the energy distribution curves (EDCs) in (i), which are obtained along normal emission, i.e. $k_{||,x} = 0 \text{ \AA}^{-1}$ (left) and $k_{||,x} = -0.4 \text{ \AA}^{-1}$ (right). Here, black arrows mark the spectral changes that can be attributed to new bands appearing in (e). Additionally, in the spectra the spin-polarized surface electronic structure slab-calculations from Fig. 7.3 are superimposed (for 1 QL surface termination in the case of Bi₁Te₁). Here, red and blue dots mark oppositely oriented in-plane spin channels and the size of the dots corresponds to the spin-polarization. The Fermi level in the calculation needed to be shifted upwards by 250 meV [100 meV] to better fit to the experimental data of Bi₁Te₁ [Bi₂Te₃]. As one can see, the agreement between ARPES data and DFT simulation is very high and nearly every feature can be matched. Only the gap-opening that is predicted in the uppermost prominent band, which is labeled β , along $\overline{\Gamma K}$ direction, is not reproduced in the experimental spectra. This will be discussed below. Panels (b) and (f) depict magnified near-Fermi level spectra along both $\overline{\Gamma M}$ and $\overline{\Gamma K}$ direction obtained with both $h\nu = 21.2 \text{ eV}$ and $h\nu = 8.4 \text{ eV}$. The two different photon energies are used to probe a different cut in the 3D Brillouin zone, i.e. a different k_{\perp} , and thus to prove the surface state character of a band. Indeed, for Bi₂Te₃ the Dirac cone-like topologically protected surface state, which is well-known in literature, is revealed and the Dirac point, which has a very little photoemission signal when excited with $h\nu = 21.2 \text{ eV}$, is located around $E_B \approx 300 \text{ meV}$ and buried in bulk valence band pockets.

On the other hand, the prominent and interesting β feature seems to disperse strongly linearly and could, at the first glance, also be confused with a topologically non-trivial Dirac cone state. Indeed, the lack of k_{\perp} -dispersion of the TSS in Bi₂Te₃ and the β band in Bi₁Te₁ is quantified in Fig. 7.7(c) and (g), where the wave vector $k_{||,x}$ of the right branch of the TSS and the β state is plotted against the binding energy for the two different photon energies. The data points were extracted out of Voigt peak fits to the momentum distribution curves (MDCs) of both spectra in Fig. 7.7(b) and (f). For the first 200 meV below E_F , the fit is very good but it gets worse when the states start to hybridize with other bands at higher energies. The fact that the dispersion of those states is exactly the same for both 21.2 eV and 8.4 eV is a strong indication for their surface state character. Moreover, from this the Fermi velocity v_F can be determined by linear fits as $v_F = \frac{E}{k_{||} \cdot \hbar}$ to be $v_F \approx 2.38 \text{ eV \AA} = 3.61 \cdot 10^5 \frac{\text{m}}{\text{s}}$ for Bi₁Te₁ and $v_F \approx 3.15 \text{ eV \AA} = 4.79 \cdot 10^5 \frac{\text{m}}{\text{s}}$ for Bi₂Te₃.

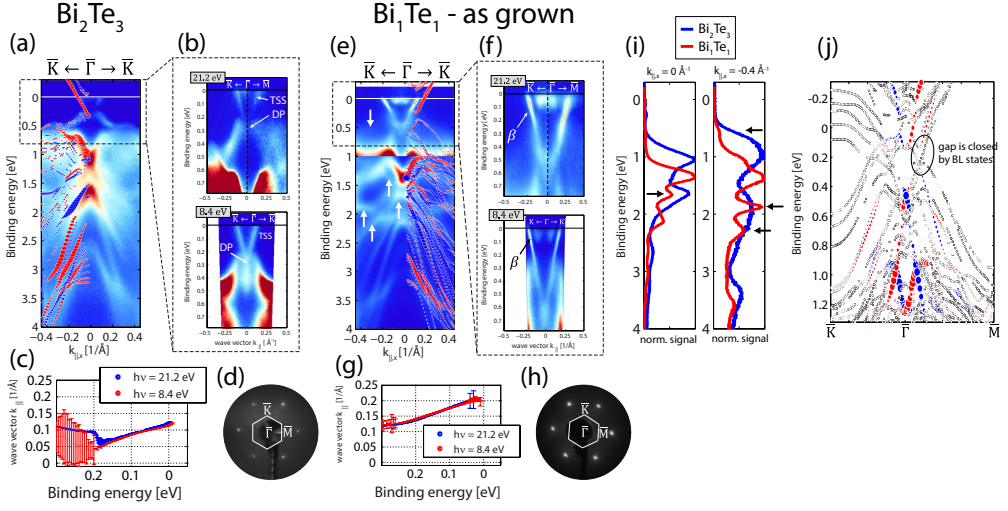


Figure 7.7: Comparative ARPES investigation on thin films of Bi_2Te_3 and Bi_1Te_1 at low temperatures $T \approx 25\text{ K}$. (a) [e] Wide energy range E_B vs. k_{\parallel} spectra along $\overline{\Gamma K}$ direction of a 19 nm Bi_2Te_3 film [a 45 nm *in situ* transferred Bi_1Te_1 film, exhibiting a Bi-poor surface] measured with $h\nu = 21.2\text{ eV}$ with superimposed spin-polarized DFT calculations (red and blue dots are opposite in-plane spin channels; 1 QL termination is used in (e)). White arrows in (e) mark prominent changes compared to (a). Note that the contrast in the spectra close to the Fermi level has been scaled up to improve visibility of the upmost bands. (b) [f] Magnified electronic structure close to the Fermi level for two different photon energies $h\nu = 21.2\text{ eV}$ and 8.4 eV along indicated crystallographic directions. (c) [g] Plot of the inverse energy dispersion $k(E_B)$ of the right branch of the prominent surface state for both photon energies as determined by Voigt fits to the momentum distribution curves (MDCs) in (b) [f]. (d) [h] Low-energy electron diffraction pattern from both samples for identification of the orientation of the surface Brillouin zone. (i) Energy distribution curves (EDCs) obtained from the spectra shown in (a) (red curve) and (f) (blue curve) along $k_{\parallel,x} = 0\text{ \AA}^{-1}$ (left) and -0.4 \AA^{-1} (right). Black arrows mark spectral changes corresponding to white arrows in (e). (j) Superposition of the surface electronic structure calculation for 1 QL and 1 BL terminations in Bi_1Te_1 (see Fig. 7.3(b)). The gap that opens up along $\overline{\Gamma M}$ in the QL-terminated case may be closed by additional BL-related states.

The low-energy electron diffraction patterns in (d) and (h) are shown to underline the high crystalline surface quality and the orientation of the surface Brillouin zones. The reason why one does not observe a gap-opening in the ARPES data, neither along $\overline{\Gamma M}$ nor $\overline{\Gamma K}$ direction, may be due to the lack of lateral resolution of the technique. Since the beam spot size in these experiments is $400\text{ }\mu\text{m}$ or even 1 mm , and one expects differently terminated surface terraces to be in the order of $1 - 10\text{ }\mu\text{m}$ size [94, 184], the method will always probe a superposition of several signals. Figure 7.7(j) exemplarily depicts the superposition of the spin-resolved DFT calculations for 1 QL and BL terminated surfaces as they are shown in Fig. 7.3. The vast variety of different surface bands may easily hybridize and potentially close the gap. Such hybridization of two different surface states, which is another clear difference to Bi_2Te_3 , is presented in the next subsection.

However, the strongest argument why the β state is not a TSS will be presented in 7.4.3 and is based on spinARPES investigations.

7.4.1 Off-Normal Emission and the Appearance of New Dirac Cones?

Another strong and interesting difference between Bi_1Te_1 and Bi_2Te_3 was observed at off-normal emission angles. Figure 7.8 depicts the Fermi surfaces of the two materials and multiple $E_B(k_{||,x})$ spectra along the indicated cut directions, i.e. differing values of $k_{||,y}$. Along normal emission ($k_{||,y} = 0$; spectra 1) one most clearly observes the TSS and the prominent β feature. Additional features can only be vaguely guessed. Going away from normal emission (spectra 2 and 3), the TSS starts to detach itself from the VBM and a gap starts to open, and no other features are notable in the Bi_2Te_3 data. On the other hand, the spectra of Bi_1Te_1 reveal a growing spectral weight next to the β feature and in spectrum 3 one can see how this feature splits into two separate features. This means that the β band may consist of a hybridization of (at least) two states, which may be the reason that one cannot observe the predicted gap opening. Next, spectrum 4 depicts a very interesting point, because the additional feature starts to form some Dirac cone-like structure, while the TSS in Bi_2Te_3 is clearly gapped from the valence band.

This interesting behavior is definitely in strong contrast to Bi_2Te_3 and unusual for standard STIs. However, we are still in the progress of investigating the possibilities of such Dirac cones located away from the main surface TRIM points. A possible explanation may be an additional symmetry protection by mirror symmetry as it can appear in topological crystalline insulators (TCI), where double-Dirac cone features have been recently observed at non-TRIM points [199, 200].

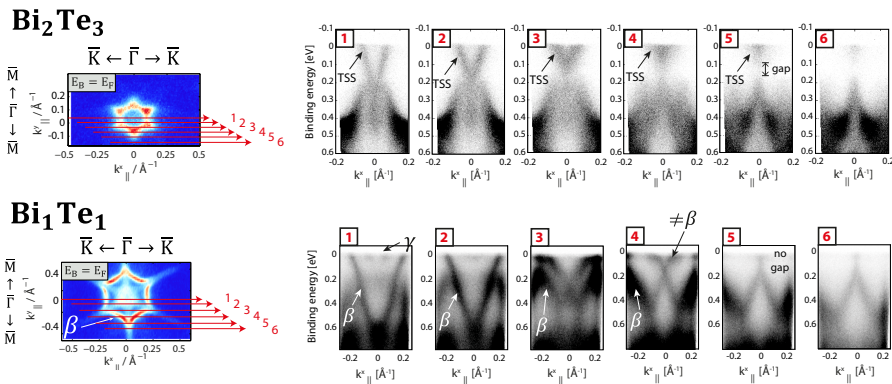


Figure 7.8: Comparison of the off-normal emission spectra of Bi_2Te_3 and Bi_1Te_1 obtained with $h\nu = 8.4\text{ eV}$ at low temperature. Fermi surfaces and $E_B(k_{||,x})$ spectra for several values of $k_{||,y}$. The numbers at the spectra correspond to the lines in the Fermi surface indicating the cut directions.

7.4.2 The Influence of Sputtering on the Surface Electronic Structure

In order to perform spinARPES measurements at the synchrotron-based beamline at DELTA, samples needed to be prepared by sputtering and annealing. Therefore, we investigate and discuss the effect of sputtering on the electronic structure and the results are summarized in Fig. 7.9. Here, panels (a) and (c) show near-Fermi level E_B vs. $k_{||,x}$ spectra along $\bar{\Gamma}\bar{K}$ direction for the as grown, i.e. Bi-poor, surface and the sputtered, i.e. Bi-rich surface of a Bi₁Te₁ thin film, respectively. Panels (b) and (d) display corresponding $k_{||,x}$ vs. $k_{||,y}$ constant energy contours at $E_B = E_F$, 70 meV, 320 meV and 570 meV.

First of all, it is important to note that the changes in the crystal quality and ARPES spectra are not dramatic and the general structure remains unaltered. Upon sputtering, which produces a Bi-rich surface (see Fig. 7.6), the most prominent β band does not change at all (Figs. 7.9(a) and (c)) but the material gets even further n-doped, which can be seen by a slightly larger area within the β band in the Fermi surface. The strongest difference between the as grown and the sputtered Bi₁Te₁ samples are the vanishing parabolic electron-like γ bands, having six-fold symmetric shapes in the constant energy cut closely below the Fermi level, and the appearance of the hole-like, more linearly dispersing δ and ζ bands which have a circular shape close to the Fermi surface and appear as strong six-fold symmetric bands around 320 meV below the Fermi level.

The γ bands can be interpreted as being created by domains of 2 QL termination, whereas the latter δ and ζ states originate from Bi BLs, as the good agreement to the calculations in Figs. 7.3 indicates, respectively. Hence, in Bi₁Te₁ it is possible to slightly modify the electronic structure by manipulating the surface termination by sputtering. In other words, one is able to 'switch' on and off certain bands, while other features as well as the general structure remains constant.

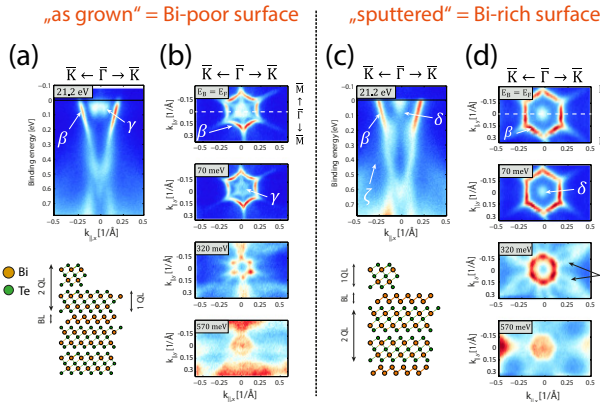


Figure 7.9: Effect of sputtering and annealing on the surface electronic structure of Bi₁Te₁. (a) [c] E_B vs. $k_{||,x}$ spectra along $\bar{\Gamma}\bar{K}$ direction of the as grown Bi₁Te₁ surface [after sputtering and annealing], recorded using $h\nu = 21.2$ eV at low temperatures. A simplified scheme of the surface crystal structure is shown below (orange = Bi atoms; green = Te atoms). (b) [d] Corresponding constant energy contours at indicated binding energies.

7.4.3 Spin-Resolved ARPES

Finally, a strong experimental argument for the topological nature of a surface state is the measurement of its helical spin polarization [39]. Thus, Fig. 7.10 summarizes our findings on the spin polarization of the β state of sputtered, i.e. Bi-rich Bi₁Te₁ (a-d). As seen above, the β state was shown to be independent of the surface termination. Again the data from Bi₁Te₁ is compared to measurements on Bi₂Te₃ and the spin polarization of the prototypical TSS (e-h).

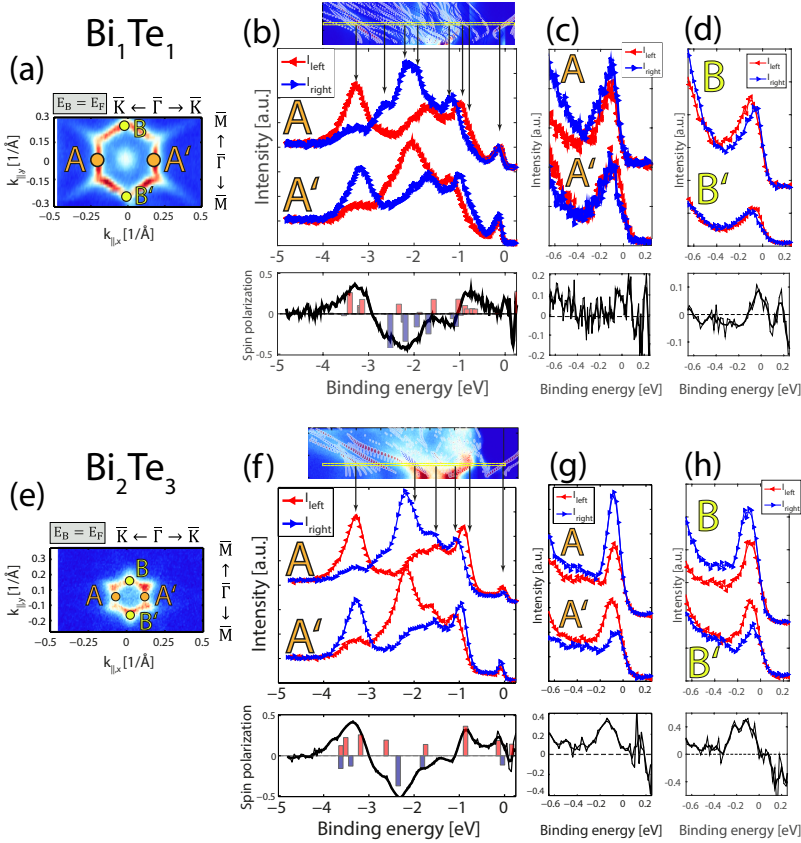


Figure 7.10: SpinARPES investigations recorded with $h\nu = 22$ eV and a SPLEED polarimeter. (a) [e] Fermi surface of Bi₁Te₁ [Bi₂Te₃] to illustrate the four k -points A, A', ($k_{||,x} = \pm 0.21 \text{ \AA}^{-1}$ [$k_{||,x} = \pm 0.12 \text{ \AA}^{-1}$]) B and B' ($k_{||,y} = \pm 0.25 \text{ \AA}^{-1}$ [$k_{||,y} = \pm 0.13 \text{ \AA}^{-1}$]) along which the spin polarization is measured. (b) [f] Wide energy spin-polarized EDCs along A and A' with ARPES spectra and superimposed spin-polarized DFT calculation above and effective net spin polarization below. The latter has the calculated spin polarization superimposed as a bar graph. (c) [g] Magnified spectra along A and A' close to the Fermi level. (d) [h] Respective spectra and spin polarization along B and B'.

Figures 7.10(a) and (e) show the Fermi surfaces of Bi_1Te_1 and Bi_2Te_3 , respectively, illustrating the k -points marked by A, A', B and B' along which the spin polarization was measured. Then, Figs. 7.10(b)-(d) and (f)-(h) depict the wide range and close-Fermi level (in-plane) spin-resolved partial intensities I_{left} and I_{right} along the highlighted regions, which were corrected by the asymmetry Sherman function $S = 0.27$ and the net spin polarization underneath. Additionally, above panels (b) and (f) the corresponding ARPES maps with superimposed spin-polarized DFT calculations are shown for the assignment of the peaks to the individual bands. Both samples show quite similar and rather high in-plane spin polarization of 40-50% in the bands at higher binding energies, around $E_B \sim 3.2$ eV, $E_B \sim 2.1$ eV and $E_B \sim 1.1$ eV in panels (b) and (f). The full reversal of the spin polarization between regions A and A' confirms the helical nature of these states. Further, the TSS of Bi_2Te_3 shows a helical spin polarization of up to 40% in panels (g) and (h), which nicely confirms its topological nature and is in agreement with what was reported earlier [57].

In contrast, panels (b) and (c) reveal that the most interesting β state at the Fermi level exhibits only very little (though non-vanishing) in-plane spin polarization (max. 10%) without a clear reversal at the opposite k -points. Such weak spin polarization can be induced by SOC in topologically trivial surface states, as most of the states in the superimposed calculation in panel (b) show some non-zero spin polarization. Our spinARPES findings agree well with the DFT calculations and further show the rich spin structure of Bi_1Te_1 but also indicate the topologically trivial nature of the β state.

7.5 Conclusion and Outlook

In summary, a thorough investigation of the electronic structure of the stoichiometric natural superlattice phase Bi_1Te_1 , i.e. $(\text{Bi}_2)_1(\text{Bi}_2\text{Te}_3)_2$ was presented. The *ab initio* DFT calculations find a gapped bulk band structure and classify this material as a weak topological insulator with $\mathbb{Z}_2 = (0;001)$ and the surface perpendicular to the stacking direction as being free of topological surface states (Fig. 7.2). Surface electronic structure calculations further reveal the rich variety of surface-related states depending on the surface termination (Fig. 7.3).

It was shown that high-quality thin films of Bi_1Te_1 on Si(111) have been grown successfully by MBE and their bulk crystal structure has been characterized by XRD and STEM (Figs. 7.4 and 7.5) as well as their surface chemistry by XPS (Fig. 7.6). For the first time, the rich surface electronic (spin) structure of Bi_1Te_1 has been analyzed in detail by high-resolution ARPES (Fig. 7.7) and spinARPES (Fig. 7.10) and has been compared to findings on the prototypical 3D STI Bi_2Te_3 . Certain electronic states have been found and identified as being surface related. Depending on different possible surface terminations, certain bands can be “switched” on and off by sputtering. Unfortunately, the here employed experimental setups are lacking spatial resolution and thus average over differently terminated surface terraces. Nevertheless, one can unambiguously distinguish between Bi-rich and Bi-poor surfaces of Bi_1Te_1 .

Most importantly, it was demonstrated that the very prominent β feature in Bi_1Te_1 , which could easily be mistaken for a topologically protected surface state, exhibits negligible spin polarization. We conclude that it is very likely topologically trivial and only induced by SOC. However, the spin polarization was measured only using one

single photon energy of $h\nu = 22\text{ eV}$. By chance, unfavorable final state effects or photoemission induced dichroism effects due to the linear polarization of the light, may also lead to a reduction of the detected spin polarization [201]. The strong difference to the spin polarization in Bi_2Te_3 , however, indeed points towards the topologically different characters of the materials.

Assuming that Bi_1Te_1 is a WTI, it should exhibit topologically protected surface states only on distinct surfaces, whereas it is expected to host topologically non-trivial one-dimensional electron channels at certain step edges of the Bi bilayers being a 2D TI. The latter can be probed in a careful STS study, similar to what was reported in [41], and we plan to perform such experiments in the near future. This would give, combined with our spin-ARPES findings, the ultimate experimental answer about the topological properties of Bi_1Te_1 .

Furthermore, we have found indications of an additional classification of Bi_1Te_1 as a topological crystalline insulator by both theory and experiment (Fig. 7.8), which needs to be investigated further. Our newly installed, highly efficient FeO-based FERRUM spin detector would allow for a detailed and high-resolution study of the additional and hybridized states close to the Fermi level. The experimental confirmation of a new combined WTI and TCI phase among the BiTe family by spin-ARPES seems to be accessible in the nearest future.

Summary and Outlook

The first excitement among scientist, after the topological band theory has been developed and introduced and the first topological insulators have been experimentally realized, was followed by a mild frustration about the low resistivity of these supposed-to-be semiconducting materials due to strong contributions from bulk carriers to the total conduction. The problem is that the Fermi level in these materials does not lie in the middle of the forbidden band gap as in intrinsic semiconductors, but is located very close to or in the bulk conduction or valence band, making these materials degenerate or highly-doped semiconductors. This is why the next task for the scientific community was, or still is, to find ways to suppress the bulk conductivity and tune the Fermi level into the band gap.

Within this thesis various well-established as well as novel approaches to engineer or tune the electronic band structure of 3D topological insulators are presented and described, which is an important step towards future spintronic device application. Further, this thesis has shown it is possible to produce thin films of all three prototypical 3D TI materials, Bi_2Se_3 , Bi_2Te_3 , and Sb_2Te_3 , by molecular beam epitaxy with a quality that is comparable to commonly investigated bulk single crystals in terms of their structural, electronic and topological properties. A thorough investigation of their electronic band structure by angle-resolved photoemission spectroscopy was presented. The establishment of high-quality MBE growth on Si(111) or similar widespread substrates and the tunability of the Fermi level within the topologically protected Dirac cone states of these samples paves the way for industrial applications of these materials.

We have shown that the widely studied, so-called 'aging' effect of the surface electronic structure of Bi_2Se_3 is fully reversible by annealing which means that the effect is purely induced by (an unintentional) charge transfer followed by surface band bending due to surface adsorbates. The adsorption of residual gas molecules or atoms can be enhanced by cooling down the sample, which increases the surface sticking coefficient. A full reversibility of the shifting electronic band structure was shown by heating up the sample subsequently. More complex effects, like intercalation of molecules between adjacent quintuple layers, could not be explained by this observation.

Furthermore, it has been shown that the Fermi level of the p -type TI Sb_2Te_3 and the n -type TI Bi_2Te_3 can be tailored towards the Dirac point by deposition of sub-ML amounts of Fe or MgO, respectively. Also it was shown that increasing the surface defect concentration by these adsorbates enhances the complex self-energy of the Dirac surface electrons, which is related among others to electron-defect scattering.

The most important finding of this thesis was the realization of a vertical topological p - n junction in $\text{Sb}_2\text{Te}_3/\text{Bi}_2\text{Te}_3$ heterostructures, which resulted in the possibility to manipulate the surface electronic structure by a completely internal structural parameter, i.e. the thickness of the Sb_2Te_3 layer, without introducing disorder or external fields. Varying the thickness of the top layer, tailors the distance or the influence of the built-in potential at the interface due to the p - n junction on the probed upper surface. Thereby, we were able to drive the p -type Sb_2Te_3 surface into an n -type regime, meanwhile passing a situation where the Fermi level is closely adjusted to the Dirac point. Technologically, this approach offers new possibilities next to the well-established ternary or quaternary alloying. Moreover, we believe that it delivers a new route to the realization of the fundamentally interesting topological exciton condensate.

In the last chapter, a thorough investigation of the less studied but closely related Bi_1Te_1 compound, forming a stable natural superlattice, was presented and compared to Bi_2Te_3 . While the latter is among the prototypical strong topological insulators, Bi_1Te_1 has been shown to be a weak TI by density functional theory. After detailed structural confirmations about the differences in the unit cell size, we also find strong differences in the surface electronic structure. Most importantly, spin-resolved ARPES reveals that the prominent surface states in Bi_1Te_1 , which could easily be confused with topological Dirac cones, exhibit only very weak and not helical spin polarization which is a strong evidence for their topologically trivial nature. We plan to perform more experimental studies by STS in order to proof the existence of topologically protected 1D edge channels which could provide the last and ultimate conclusion regarding the weak topological nature of Bi_1Te_1 .

In the near future two interesting and important plans will be pursued. First of all, we want to connect ARPES measurements of the surface electronic structure with actual electric transport properties. This can be achieved by a recently upgraded in situ contact stage with which we can measure $R(T)$ or $U(I)$ dependencies of the TI samples in situ and while measuring ARPES. Here, first tries have successfully been performed, but until now we could only confirm metallic behavior of the simple binary 3D TIs. Performing such kind of experiments on more complicated heterostructures or Fermi level adjusted TIs, we expect to be able to prove the two-dimensional surface transport properties.

Furthermore, the system was recently upgraded with a very efficient FeO-based spin detector, which, for the first time, allows full spin-resolved band mapping, because the measuring times of a spin-polarized spectrum has been decreased dramatically as compared to the formerly used SPLEED detectors.

This new instrumental opportunities open up many novel ways to study the interesting spin-polarized band structures and transport properties of these fascinating spintronic materials.

Appendix

A.1 The Dirac equation

We start from the relativistic Dirac equation for an electron of charge e in a scalar potential V

$$\mathcal{H}_D \Psi = i\hbar \frac{\partial}{\partial t} \Psi = E\Psi; \quad \mathcal{H}_D = eV(\mathbf{r}) + \beta mc^2 + \underbrace{\begin{pmatrix} 0 & \boldsymbol{\sigma} \\ \boldsymbol{\sigma} & 0 \end{pmatrix}}_{\boldsymbol{\alpha}} \cdot (c\mathbf{p} + e\mathbf{A}(\mathbf{r}))$$

with $\boldsymbol{\sigma}$ being the Pauli matrices (see eq. 2.4) and β a matrix of unit matrices I_2 of the same rank than $\boldsymbol{\alpha}$, i.e. $\beta = \begin{pmatrix} I_2 & 0 \\ 0 & -I_2 \end{pmatrix}$. Letting this Dirac Hamiltonian \mathcal{H}_D act on a four-component wavefunction Ψ that can be split into a two-vector of a so-called large and small components ψ and χ , i.e. $\Psi = \begin{pmatrix} \psi \\ \chi \end{pmatrix}$ results in

$$\begin{aligned} \mathcal{H}_D \Psi &= E\Psi = \left(eV(\mathbf{r}) + \beta mc^2 + \underbrace{\begin{pmatrix} 0 & \boldsymbol{\sigma} \\ \boldsymbol{\sigma} & 0 \end{pmatrix}}_{\boldsymbol{\alpha}} \cdot (c\mathbf{p} + e\mathbf{A}(\mathbf{r})) \right) \Psi \\ &\Rightarrow \begin{pmatrix} mc^2 + eV(\mathbf{r}) & \boldsymbol{\sigma} \cdot (c\mathbf{p} + e\mathbf{A}(\mathbf{r})) \\ \boldsymbol{\sigma} \cdot (c\mathbf{p} + e\mathbf{A}(\mathbf{r})) & mc^2 + eV(\mathbf{r}) \end{pmatrix} \cdot \begin{pmatrix} \psi \\ \chi \end{pmatrix} = \begin{pmatrix} E & 0 \\ 0 & E \end{pmatrix} \cdot \begin{pmatrix} \psi \\ \chi \end{pmatrix} \\ &\Rightarrow \begin{pmatrix} E - mc^2 - eV(\mathbf{r}) & -\boldsymbol{\sigma} \cdot (c\mathbf{p} + e\mathbf{A}(\mathbf{r})) \\ -\boldsymbol{\sigma} \cdot (c\mathbf{p} + e\mathbf{A}(\mathbf{r})) & E + mc^2 - eV(\mathbf{r}) \end{pmatrix} \cdot \begin{pmatrix} \psi \\ \chi \end{pmatrix} = \begin{pmatrix} 0 \\ 0 \end{pmatrix} \\ &\Rightarrow \begin{array}{ll} \text{I:} & (E - mc^2 - eV(\mathbf{r})) \cdot \psi = \boldsymbol{\sigma} \cdot (c\mathbf{p} + e\mathbf{A}(\mathbf{r})) \cdot \chi \\ \text{II:} & (E + mc^2 - eV(\mathbf{r})) \cdot \chi = \boldsymbol{\sigma} \cdot (c\mathbf{p} + e\mathbf{A}(\mathbf{r})) \cdot \psi \end{array} \quad (10.1) \\ &\Leftrightarrow \text{II: } \chi = \frac{\boldsymbol{\sigma} \cdot (c\mathbf{p} + e\mathbf{A}(\mathbf{r}))}{(E + mc^2 - eV(\mathbf{r}))} \cdot \psi \end{aligned}$$

substituting II into I of line 10.1 leads to

$$\left(E - mc^2 - eV(\mathbf{r}) \right) \cdot \psi - \boldsymbol{\sigma} \cdot (c\mathbf{p} + e\mathbf{A}(\mathbf{r})) \cdot \frac{\boldsymbol{\sigma} \cdot (c\mathbf{p} + e\mathbf{A}(\mathbf{r}))}{(E + mc^2 - eV(\mathbf{r}))} \cdot \psi = 0. \quad (10.2)$$

With a Taylor expansion of the term

$$\frac{c^2}{E + mc^2 - eV} = \frac{1}{2m} \left[\frac{2mc^2}{E + mc^2 - eV} \right] = \frac{1}{2m} \left[\frac{1}{1 + \frac{E - eV}{2mc^2}} \right] \approx \frac{1}{2m} \left(1 - \frac{E - eV}{2mc^2} + (\dots)^2 + \dots \right)$$

eq. 10.2 becomes

$$\left(E - mc^2 - eV(\mathbf{r})\right) \cdot \psi - \boldsymbol{\sigma} \cdot (c\mathbf{p} + e\mathbf{A}(\mathbf{r})) \cdot \frac{1}{2m} \left(1 - \frac{E - eV}{2mc^2}\right) \cdot \psi = 0.$$

Rewriting this equation basically results in the sometimes called Pauli equation which is given in eq. 2.6 where all terms of the equation are explained.

A.2 Rashba-splitting

We start with the Hamiltonian for electrons in a 2DEG which is confined in the (x, y) plane and which are subject to an electric field normal to this plane, i.e. along $e_z = (0, 0, 1)$ direction

$$\mathcal{H} = \mathcal{H}_K + \mathcal{H}_R = \frac{\mathbf{p}^2}{2m^*} + \alpha_R(\boldsymbol{\sigma} \times \mathbf{p})_z = \frac{\mathbf{p}^2}{2m} + \alpha_R(\sigma_x p_y - \sigma_y p_x)$$

with the Rashba Hamiltonian that is rewritten from eq. 2.10 and the Pauli matrices

$\sigma_x = \begin{pmatrix} 0 & 1 \\ 1 & 0 \end{pmatrix}$ and $\sigma_y = \begin{pmatrix} 0 & -i \\ i & 0 \end{pmatrix}$ the equation can be written as

$$\mathcal{H} = \frac{\mathbf{p}^2}{2m} + \alpha_R \begin{pmatrix} 0 & p_x - ip_y \\ p_x + ip_y & 0 \end{pmatrix}.$$

Substituting the wavevector k for the momentum operator $\mathbf{p} = \hbar \mathbf{k}_{||} = \hbar \begin{pmatrix} k_x \\ k_y \\ 0 \end{pmatrix}$

$$\mathcal{H} = \frac{\hbar^2 k^2}{2m} + \alpha_R \hbar \begin{pmatrix} 0 & k_x - ik_y \\ k_x + ik_y & 0 \end{pmatrix}.$$

The Schrödinger equation of this problem can be solved analytically

$$\begin{aligned} \mathcal{H}\Psi &= E\Psi \\ \Leftrightarrow \det|\mathcal{H}\Psi - E\Psi| &= 0 \\ \Leftrightarrow \left| \begin{pmatrix} -\frac{\hbar^2}{2m}(k_x^2 + k_y^2) - E & \alpha_R \hbar(k_x - ik_y) \\ \alpha_R \hbar(k_x + ik_y) & \frac{\hbar^2}{2m}(k_x^2 + k_y^2) - E \end{pmatrix} \right| &= 0 \\ \Leftrightarrow \left(\frac{\hbar^2}{2m}(k_x^2 + k_y^2) - E \right)^2 - \alpha_R^2 \hbar^2 (k_x^2 + k_y^2) &= 0 \\ \Leftrightarrow \left(\frac{\hbar^2}{2m}(k_x^2 + k_y^2) - E \right)^2 &= \alpha_R^2 \hbar^2 (k_x^2 + k_y^2) \\ \Leftrightarrow \left(\frac{\hbar^2}{2m}(k_x^2 + k_y^2) - E \right) &= \pm \alpha_R \hbar \sqrt{k_x^2 + k_y^2} \\ \Leftrightarrow E(k) &= \frac{\hbar^2}{2m} \underbrace{(k_x^2 + k_y^2)}_{k_{||}^2} \pm \alpha_R \hbar \underbrace{\sqrt{k_x^2 + k_y^2}}_{|k_{||}|} \end{aligned}$$

The last equation explains the splitting of the free electron parabola depending on the spin of the electron (\pm denote spin up and spin down states). Note that the Rashba splitting is linear in $k_{||}$.

A.3 Vacuum shuttle by II. Physikalisches Institut in Aachen

In order to prevent MBE grown TI films from oxidizing and surface contaminations, we started to employ a self-made vacuum suitcase for transferring the samples from the MBE into the ARPES system without breaking the vacuum. Fig. 10.1 shows the CAD scheme of this device. A small UHV chamber which is initially pumped down by a turbo pump will be kept in UHV by a small ion getter pump supplied by either mains voltage or during transport by rechargeable car batteries. Thus, the whole chamber can stay in 10^{-10} mbar for several hours. The surrounding frame makes it easily attachable to various UHV setups.

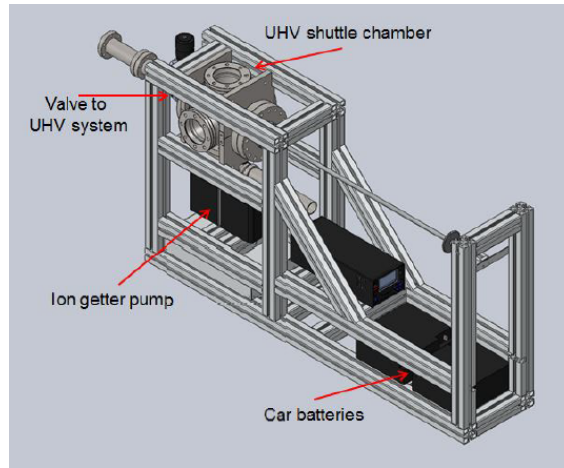


Figure 10.1: Scheme of the UHV vacuum shuttle

A.4 MDC analysis of ARPES spectra

For the quantitative comparison of the ARPES spectra of the three prototypical parental 3D STIs Sb_2Te_3 , Bi_2Te_3 and Bi_2Se_3 , as it is described in section 4.2.2, the momentum distribution curves obtained by ARPES have been analyzed. Figure 10.2 depicts the MDCs at the Fermi level from the respective ARPES spectra presented in Fig. 4.5, where the number of states at the Fermi level could be determined by counting. Only in the case of Bi_2Se_3 a more complicated situation with several states is found, but also here one can precisely distinguish and count the states, as they are 10, i.e. two due to the upper Dirac cone, and two parabolic conduction band states which are both split by the Rashba effect leading to eight states at E_F . The peaks have then be fitted by Voigt profiles consisting of a Gaussian with fixed width, which represents experimental and sample-related broadening, and a Lorentzian which exhibits the broadening caused by many-body interactions and the lifetime of the probed quasiparticles. Positions and widths of the Voigt peaks could then be extracted and quantitatively compared. Doing

this for all of the MDCs at different binding energies, an energy-dependence could be obtained.

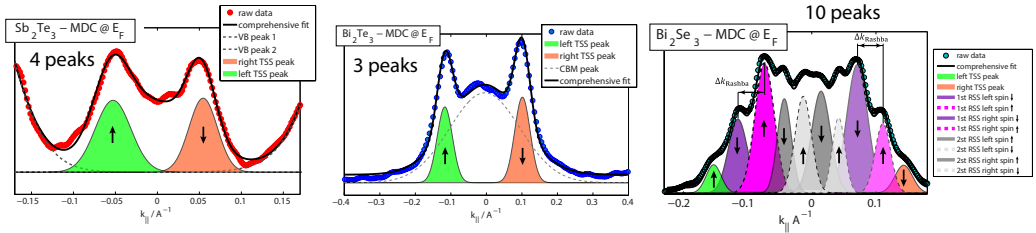


Figure 10.2: Momentum distribution curves at the Fermi energy E_F extracted from the ARPES spectra shown in Fig. 4.5 for thin films of the three main 3D TIs. The number of states at the Fermi level can be determined from the spectra.

Bibliography

- [1] L. Fu and C.L. Kane. Topological insulators with inversion symmetry. *Physical Review B*, 76:045302, 2007.
- [2] L. Fu, C.L. Kane, and E.J. Mele. Topological insulators in three dimensions. *Physical Review Letters*, 98:106803, 2007.
- [3] B.A. Bernevig and S.-C. Zhang. Quantum spin hall effect. *Physical Review Letters*, 96:106802, 2006.
- [4] M. König, S. Wiedmann, C. Brühne, A. Roth, H. Buhmann, L. W. Molenkamp, X.-L. Qi, and S.-C. Zhang. Quantum spin hall insulator state in hgte quantum wells. *Science*, 318:766, 2007.
- [5] J.E. Moore and L. Balents. Topological invariants of time-reversal-invariant band structures. *Physical Review B*, 75:121306, 2007.
- [6] J.E. Moore. Topological insulators: The next generation. *Nature Physics*, 5:378, 2009.
- [7] M.Z. Hasan and C.L. Kane. Colloquium: Topological insulators. *Reviews of Modern Physics*, 82:3045–3067, 2010.
- [8] X.L. Qi. Topological insulators and superconductors. *Reviews of Modern Physics*, 83:1057–1110, 2011.
- [9] C.L. Kane and E.J. Mele. z_2 topological order and the quantum spin hall effect. *Physical Review Letters*, 95:146802, 2005.
- [10] C.L. Kane and E.J. Mele. Quantum spin hall effect in graphene. *Physical Review Letters*, 95:226801, 2005.
- [11] C.L. Kane and E.J. Mele. A new spin on the insulating state. *Science*, 314:1692–1693, 2006.
- [12] D. Hsieh, D. Qian, L. Wray, Y. Xia, Y.S. Hor, R.J. Cava, and M.Z. Hasan. A topological dirac insulator in a quantum spin hall phase. *Nature*, 452:970–974, 2008.
- [13] D. Hsieh, Y. Xia, L. Wray, D. Qian, A. Pal, J.H. Dil, J. Osterwalder, F. Meier, G. Bihlmayer, C.L. Kane, Y.S. Hor, R.J. Cava, and M.Z. Hasan. Observation of unconventional quantum spin textures in topological insulators. *Science*, 323:919–922, 2009.

- [14] C. Day. Exotic spin textures show up in diverse materials. *Physics Today*, April 2009.
- [15] Y. Xia, D. Qian, D. Hsieh, L. Wray, A. Pal, H. Lin, A. Bansil, D. Grauer, Y. Hor, R.J. Cava, and M.Z. Hasan. Observation of a large-gap topological-insulator class with a single dirac cone on the surface. *Nature Physics*, 5:398–402, 2009.
- [16] H. Zhang, C.-X. Liu, X.-L. Qi, X. Dai, Z. Fang, and S.-C. Zhang. Topological insulators in Bi_2Se_3 , Bi_2Te_3 and Sb_2Te_3 with a single dirac cone on the surface. *Nature Physics*, 5:438–442, 2009.
- [17] D. Hsieh, Y. Xia, D. Qian, L. Wray, J.H. Dil, F. Meier, J. Osterwalder, L. Patthey, J.G. Checkelsky, N.P. Ong, A.V. Fedorov, H. Lin, A. Bansil, D. Grauer, Y.S. Hor, R.J. Cava, and M. Z. Hasan. A tunable topological insulator in the spin helical dirac transport regime. *Nature*, 460:1101–1105, 2009.
- [18] M. Brahlek, N. Koirala, N. Bansal, and S. Oh. Transport properties of topological insulators: Band bending, bulk metal-to-insulator transition, and weak anti-localization. *Solid State Communications*, 2014. arXiv:1408.1614v1 [cond-mat.mtrl-sci].
- [19] B. Skinner, T. Chen, and B.I. Shklovskii. Why is the bulk resistivity of topological insulators so small ? *Physical Review Letters*, 109:176801, 2012.
- [20] T. Zhang, N. Levy, J. Ha, Y. Kuk, and J.A. Stroscio. Scanning tunneling microscopy of gate tunable topological insulator Bi_2Se_3 thin film. *Physical Review B*, 87:115410, 2013.
- [21] J. Zhang, C.-Z. Chang, Z. Zhang, J. Wen, X. Feng, K. Li, M. Liu, K. He, L. Wang, X. Chen, Q.-K. Xue, X. Ma, and Y. Wang. Band structure engineering in $(\text{Bi}_{1-x}\text{Sb}_x)_2\text{Te}_3$ ternary topological insulators. *Nature communications*, 2:574, 2011.
- [22] D. Kong, Y. Chen, J.J. Cha, Q. Zhang, J.G. Analytis, K. Lai, Z. Liu, S.S. Hong, K.J. Kostie, J. Koski, S.-K. Mo, Z. Hussain, I.R. Fisher, Z.-X. Shen, and Y. Cui. Ambipolar field effect in the ternary topological insulator $(\text{Bi}_{1-x}\text{Sb}_x)_2\text{Te}_3$ by composition tuning. *Nature Nanotechnology*, 6:705–709, 2011.
- [23] M. Neupane, S.-Y. Xu, L. Wray, A. Petersen, R. Shankar, N. Alidoust, C. Liu, A. Fedorov, H. Ji, J.M. Allred, Y.S. Hor, T.-R. Chang, H.-T. Jeng, H. Lin, A. Bansil, R.J. Cava, and M.Z. Hasan. Topological surface states and dirac point tuning in ternary topological insulators. *Physical Review B*, 85:235406, 2012.
- [24] T. Arkane, T. Sato, S. Souma, K. Kosaka, K. Nakayama, M. Komatsu, T. Takahashi, Z. Ren, K. Segawa, and Y. Ando. Tunable dirac cone in the topological insulator $\text{Bi}_{2-x}\text{Sb}_x\text{Te}_{3-y}\text{Se}_y$. *Nature Communications*, 3:636, 2012.
- [25] Y. Pan, D. Wu, J. R. Angevaere, H. Luigjes, E. Frantzeskakis, N. de Jong, E. van Heumen, T. V. Bay, B. Zwartsenberg, Y. K. Huang, M. Snelder, A. Brinkman, M. S. Golden, and A. de Visser. Low carrier concentration crystals of the topological insulator $\text{Bi}_{2-x}\text{Sb}_x\text{Te}_{3-y}\text{Se}_y$: a magnetotransport study. *New Journal of Physics*, 16:123035, 2014.

-
- [26] F. Bloch. Über die quantenmechanik der elektronen in kristallgittern. *Zeitschrift für Physik*, 52:555–600, 1928.
- [27] S.-C. Zhang. Topological insulators. *Scholarpedia*, 10:30275, 2015.
- [28] H. Ibach and H. Lüth. *Festkörperphysik*, volume 7. Springer-Verlag Berlin, 2009.
- [29] W. Pauli. Zur quantenmechanik des magnetischen elektrons. *Zeitschrift für Physik A Hadrons and Nuclei*, 43:601, 1927.
- [30] G. Bihlmayer. *Electronic States in Solids*, chapter A1. Forschungszentrum Jülich GmbH, 40th IFF Spring School, 2009.
- [31] G. Bihlmayer. *Relativistic effects in solids*, chapter A10. Forschungszentrum Jülich GmbH, 45th IFF Spring School, 2014.
- [32] J. Kessler. *Polarized Electrons*. Springer Verlag Berlin Heidelberg, 1985.
- [33] P.A. Dirac. The quantum theory of the electron. *Proc. R. Soc. London Ser.*, 118:351, 1928.
- [34] H.A. Beethe and E.E. Salpeter. *Quantum Mechanics of One- and Two-Electron Systems*. Plenum, New York, 1977.
- [35] M. Ellguth. *A spin- and momentum-resolved photoemission study of strong electron correlation in Co/Cu(001)*. PhD thesis, Martin-Luther Universität Halle-Wittenberg, 2014.
- [36] Y.A. Bychkov and E.I. Rashba. Properties of a 2d electron gas with lifted spectral degeneracy. *JETP Letters*, 39:78–81, 1984.
- [37] G. Bihlmayer, Y.M. Koroteev, P.M. Echenique, E.V. Chulkov, and S. Blügel. The rashba-effect at metallic surfaces. *Surface Science*, 600:3888–3891, 2006.
- [38] B.A. Bernevig, T.L. Hughes, and S.-C. Zhang. Quantum spin hall effect and topological phase transition in hgte quantum wells. *Science*, 314:1757–1761, 2006.
- [39] Y. Ando. Topological insulator materials. *arXiv: 1304.5693v1 [cond-mat.mtrl-sci]*, 2013.
- [40] S.-Q. Shen. *Topological Insulators: Dirac Equation in Condensed Matter*. Springer, 2012.
- [41] Christian Pauly. *Strong and weak topology probed by surface science: A combined scanning tunneling and photoemission spectroscopy study on the topology of phase change materials and bismuth-based graphene-like sheet systems*. PhD thesis, RWTH Aachen, 2015.
- [42] K. von Klitzing, G. Dorda, and M. Pepper. New method for high-accuracy determination of the fine-structure constant based on quantized hall resistance. *Physical Review Letters*, 45:494–497.

- [43] D.J. Thouless, M. Kohmoto, M.P. Nightingale, and M. den Nijs. Quantized hall conductance in a two-dimensional periodic potential. *Physical Review Letters*, 49:405–408, 1982.
- [44] M.C. Chang. *Berry phase in solid state physics*, chapter A7. Forschungszentrum Jülich GmbH, 40th IFF Spring school, 2009.
- [45] A. Altland and L. Fritz. Lecture notes: Primer on topological insulators.
- [46] Y. Xia. *Photoemission studies of a new topological insulator class: experimental discovery of the Bi₂X₃ topological insulator class*. PhD thesis, Princeton University, 2010.
- [47] A. Herdt. *Exploring the electronic properties of novel spintronic materials by photoelectron spectroscopy*. PhD thesis, Universität Duisburg-Essen, 2012.
- [48] L. Fu and C.L. Kane. Time reversal polarization and a z_2 adiabatic spin pump. *Physical Review B*, 74:195312, 2006.
- [49] R.S.K. Mong, J.H. Bardarson, and J.E. Moore. Quantum transport and two-parameter scaling at the surface of a weak topological insulator. *Physical Review Letters*, 108:076804, 2012.
- [50] K. Kobayashi, T. Ohtsuki, and K.-I. Imura. Disordered weak and strong topological insulators. *Physical Review Letters*, 110:236803, 2013.
- [51] B. Lenoir, M. Cassart, J.-P. Michenaud, H. Scherrer, and S. Scherrer. Transport properties of bi-rich bi-sb alloys. *J. Phys. Chem. Solids*, 57:89–99, 1996.
- [52] Frank Ortman, Stephan Roche, and Sergio O. Valenzuela. *Topological Insulators: Fundamentals and Perspectives*. Wiley - VCH, 2015.
- [53] D. Hsieh, Y. Xia, D. Qian, L. Wray, F. Meier, J. Dil, J. Osterwalder, L. Patthey, A. Fedorov, H. Lin, A. Bansil, D. Grauer, Y. Hor, R.J. Cava, and M.Z. Hasan. Observation of time-reversal-protected single-dirac-cone topological-insulator states in Bi₂Te₃ and Sb₂Te₃. *Physical Review Letters*, 103:146401, 2009.
- [54] S.R. Park, W.S. Jung, Chul Kim, D.J. Song, C. Kim, S. Kimura, K.D. Lee, and N. Hur. Quasiparticle scattering and the protected nature of the topological states in a parent topological insulator Bi₂Se₃. *Physical Review B*, 81:041405, 2010.
- [55] Y.L. Chen, J.G. Analytis, J.-H. Chu, Z.K. Liu, S.-K. Mo, X.L. Qi, H.J. Zhang, D.H. Lu, X. Dai, Z. Fang, S.C. Zhang, I.R. Fisher, Z. Hussain, and Z.-X. Shen. Experimental realization of a three-dimensional topological insulator Bi₂Te₃. *Science*, 325:178–181, 2009.
- [56] C. Pauly, G. Bihlmayer, M. Liebmann, M. Grob, A. Georgi, D. Subramaniam, A. Varykhalov, O. Rader, and M. Morgenstern. Probing two topological surface bands of Sb₂Te₃ by spin-polarized photoemission spectroscopy. *Phys. Rev. B*, 86:235106, 2012.

-
- [57] A. Herdt, L. Plucinski, G. Bihlmayer, G. Mussler, S. Döring, J. Krumrain, D. Grützmacher, S. Blügel, and C.M. Schneider. Spin-polarization limit in Bi_2Te_3 dirac cone studied by angle- and spin-resolved photoemission experiments and ab initio calculations. *Physical Review B*, 87:035127, 2013.
- [58] L. Plucinski and C.M. Schneider. The electronic structure of spintronic materials as seen by spin-polarized angle-resolved photoemission. *Journal of Electron Spectroscopy and Related Phenomena*, 2013.
- [59] O. Madelung, U. Roessler, and M. Schulz. The landoldt-boernstein database 41c, 1998.
- [60] R.J. Cava, H. Ji, M.K. Fuccillo, Q.D. Gibson, and Y.S. Hor. Crystal structure and chemistry of topological insulators. *Journal of Materials Chemistry C*, 1:3176, 2013.
- [61] B. Yan, L. Muehler, and C. Felser. Prediction of weak topological insulator in layered semiconductors. *Physical Review Letters*, 109:116406, 2012.
- [62] Z. Ringel, Y.E. Kraus, and A. Stern. Strong side of weak topological insulators. *Physical Review B*, 86:045102, 2012.
- [63] P. Tang, B. Yan, W. Cao, S.-C. Wu, and C. FelC. Felser. Duan. Weak topological insulators induced by the interlayer coupling: A first-principles study of stacked Bi_2TeI . *Physical Review B*, 89:041409, 2014.
- [64] B. Rasche, A. Isaeva, M. Ruck, S. Borisenko, V. Zabolotnyy, B. Büchner, K. Koepernik, C. Ortix, M. Richter, and J. van den Brink. Stacked topological insulator built from bismuth-based graphene sheet analogues. *Nature Materials*, 12, 2013.
- [65] C. Pauly, B. Rasche, K. Koepernik, M. Liebmann, M. Pratzer, M. Richter, J. Kellner, M. Eschbach, B. Kaufmann, L. Plucinski, C.M. Schneider, M. Ruck, J. van den Brink, and M. Morgenstern. Subnanometre-wide electron channels protected by topology. *Nature Physics*, 11, 2015.
- [66] Y.S. Hor, A. Richardella, P. Roushan, Y. Xia, J.G. Checkelsky, A. Yazdani, M.Z. Hasan, N.P. Ong, and R. J. Cava. p-type Bi_2Se_3 for topological insulator and low-temperature thermoelectric applications. *Physical Review B*, 79:195208, 2009.
- [67] D.O. Scanlon, P.D.C. King, R.P. Singh, A. de la Torre, S. McKeown Walker, G. Balakrishnan, F. Baumberger, and C.R.A. Catlow. Controlling bulk conductivity in topological insulators: key role of anti-site defects. *Advanced Materials*, 24:2154–8, 2012.
- [68] D.-X. Qu, Y.S. Hor, J. Xiong, R.J. Cava, and N.P. Ong. Quantum oscillations and hall anomaly of surface states in the topological insulator Bi_2Te_3 . *Science*, 329:821–823, 2010.
- [69] J.-L. Mi, M. Bremholm, M. Bianchi, K. Borup, S. Johnsen, M. Søndergaard, D. Guan, R.C. Hatch, P. Hofmann, and B.B. Iversen. Phase separation and bulk

- p-n transition in single crystals of $\text{Bi}_2\text{Te}_2\text{Se}$ topological insulator. *Advanced Materials*, 25:889–893, 2013.
- [70] L.-L. Wang, M. Huang, S. Thimmaiah, A. Alam, S.L. Bud’ko, A. Kaminski, T.A. Lograsso, P. Canfield, and D.D. Johnson. Native defects in tetradymite $\text{Bi}_2(\text{Te}_x\text{Se}_{3-x})$ topological insulators. *Physical Review B*, 87:125303, 2013.
 - [71] S. Hüfner. *Photoelectron Spectroscopy*. Springer-Verlag, Berlin, 2003.
 - [72] W. Schattke and M.A. van Hove. *Solid-State Photoemission and Related Methods*. Wiley-VCH, Manheim, 2003.
 - [73] E.W. Plummer and W. Eberhardt. *Angle-Resolved Photoemission as a Tool for the Study of Surfaces*.
 - [74] A. Damascelli. Probing the electronic structure of complex systems by arpes. *Physica Scripta*, T109:61–74, 2004.
 - [75] C.M. Schneider. *Photoelectron Emission Spectroscopy*, chapter F3. Forschungszentrum Jülich GmbH, 43rd IFF Spring School, 2012.
 - [76] S. Hüfner. *Very High Resolution Photoelectron Spectroscopy*. Springer, Berlin, 2007.
 - [77] L. Plucinski. *Bulk and Surface Electronic Structure of Gallium Nitride and Zinc Selenide*. PhD thesis, Universität Hamburg, 2002.
 - [78] J. Koralek. *Laser Based Angle-Resolved Photoemission Spectroscopy and High Tc Superconductivity*. PhD thesis, University of Colorado, 2006.
 - [79] K. Hild. *Femtosecond Laser-based Investigations of Magnetic Circular Dichroism in Near-Threshold Photoemission*. PhD thesis, Johannes Gutenberg University Mainz, 2011.
 - [80] Y. Wang. *Laser-Based Angle-Resolved Photoemission Spectroscopy of Topological Insulators*. PhD thesis, Harvard University, 2012.
 - [81] M. Eschbach. Magnetic circular dichroism in laser-induced threshold photoemission microscopy. Master’s thesis, RWTH Aachen, 2012.
 - [82] H. Hertz. Über einen einfluss des ultravioletten lichtes auf die elektrische entladung. *Annalen der Physik*, 267, 1887.
 - [83] A. Einstein. Zur elektrodynamik bewegter körper. *Annalen der Physik*, 322(132), 1905.
 - [84] C.N. Burglund and W.E. Spicer. Photoemission studies of copper and silver: Theory. *Physical Review*, 136:A1030, 1964.
 - [85] S. LaShell, B.A. McDougall, and E. Jensen. Spin splitting of an $\text{Au}(111)$ surface state band observed with angle resolved photoelectron spectroscopy. *Physical Review Letters*, 77:3419, 1996.

-
- [86] W. Eberhardt and F.J. Himpsel. Dipole selection rules for optical transitions in the fcc and bcc lattices. *Physical Review B*, 21:5572, 1980.
- [87] M.P. Seah and W.A. Dench. Quantitative electron spectroscopy of surfaces. *Surf. Interface Anal.*, 1:2, 1979.
- [88] J. Osterwalder. Spin-polarized photoemission, lecture notes universität zürich, switzerland. Springer-Verlag Berlin Heidelberg, 2006.
- [89] J. Pendry. Theory of photoemission. *Surface Science*, 57:679, 1976.
- [90] Jan Minar. *Theoretical Description of ARPES: The One-Step Model*, chapter 13. Forschungszentrum Jülich, 2014.
- [91] J. Henk. *Habilitationsschrift: Beiträge zur Theorie der Elektronenspektroskopie: Anwendungen der relativistischen Vielfachstreuungstheorie*. Martin-Luther Universität, 2004.
- [92] N.V. Smith, P. Thiry, and Y. Petroff. Photoemission linewidths and quasiparticle lifetimes. *Physical Review B*, 47, 1993.
- [93] A. Damascelli, Z. Hussain, and Z.-X. Shen. Angle-resolved photoemission studies of the cuprate superconductors. *Review of Modern Physics*, 75, 2003.
- [94] T. Valla, Z.-H. Pan, D. Gardner, Y.S. Lee, and S. Chu. Photoemission spectroscopy of magnetic and nonmagnetic impurities on the surface of the Bi_2Se_3 topological insulator. *Physical Review Letters*, 108:117601, 2012.
- [95] Z.-H. Pan, A.V. Fedorov, D. Gardner, Y.S. Lee, S. Chu, and T. Valla. Measurement of an exceptionally weak electron-phonon coupling on the surface of the topological insulator Bi_2Se_3 using angle-resolved photoemission spectroscopy. *Physical Review Letters*, 108:187001, 2012.
- [96] C. Chen, Z. Xie, Y. Feng, H. Yi, A. Liang, S. He, D. Mou, J. He, Y. Peng, X. Liu, Y. Liu, L. Zhao, G. Liu, X. Dong, J. Zhang, L. Yu, X. Wang, Q. Peng, Z. Wang, S. Zhang, F. Yang, C. Chen, Z. Xu, and X.J. Zhou. Tunable dirac fermion dynamics in topological insulators. *Scientific Reports*, 3:2411, 2013.
- [97] J. Sanchez-Barriga, M.R. Scholz, E. Golias, E. Rienks, D. Marchenko, A. Varykhalov, L. V. Yashina, and O. Rader. Anisotropic effect of warping on the lifetime broadening of topological surface states in angle-resolved photoemission from Bi_2Te_3 . *Physical Review B*, 90:195413, 2014.
- [98] S. Suga and C. Tusche. Photoelectron spectroscopy in a wide $h\nu$ region from 6 eV to 8 keV with full momentum and spin resolution. *Journal of Electron Spectroscopy and Related Phenomena*, 2015.
- [99] I. Tamm. Über eine mögliche art der elektronenbindung an kristalloberflächen. *Phys. Z. Soviet Union*, 1:733, 1932.

- [100] W. Shockley. On the surface states associated with a periodic potential. *Physical Review*, 56:317, 1939.
- [101] H. Lüth. *Surfaces and Interfaces of Solids*. Springer-Verlag, Berlin Heidelberg, 1993.
- [102] J.B. Pendry and S.J. Gurman. Theory of surface states: General criteria for their existence. *Surface Science*, 49:87–105, 1975.
- [103] F. Forstmann and J.B. Pendry. Surface states on d-band metals. *Z. Physik*, 235:75–84, 1970.
- [104] P. Hohenberg and W. Kohn. Inhomogeneous electron gas. *Physical Review*, 136, 1964.
- [105] W. Kohn and L.J. Sham. Self-consistent equations including exchange and correlation effects. *Physical Review*, 140(A1133), 1965.
- [106] W. Schattke. *Solid-State Photoemission and Related Methods: Theory and Experiment*. John Wiley & Sons, 2003.
- [107] K. Capelle. A bird’s eye view of density-functional theory. *Brazilian Journal of Physics*, 36(1318).
- [108] see <http://www.flapw.de> for a discription of the code.
- [109] J.C. Slater. Wave functions in a periodic potential. *Physical Review*, 51, 1937.
- [110] I. Aguilera. *Topological Insulators: Fundamentals and Perspectives*, chapter 7: Many-Body Effects in the Electronic Structure of Topological Insulators, pages 161–189. Wiley-VCH, 2015.
- [111] C. Friedrich, S. Blügel, and A. Schindlmayr. Efficient implementation of the *gw* approximation within the all-electron flapw method. *Physical Review B*, 81:125102, 2010.
- [112] G. Schönhense and U. Heinzmann. A capillary discharge tube for the production of intense vuv resonance radiation. *J. Phys. E: Sci. Instrum.*, 16:74–82, 1983.
- [113] S. Suga, A. Sekiyama, G. Funabashi, J. Yamaguchi, M. Kimura, M. Tsujibayashi, T. Uyama, H. Sugiyama, Y. Tomida, G. Kuwahara, S. Kitayama, K. Fukushima, K. Kimura, T. Yokoi, K. Murakami, H. Fujiwara, Y. Saitoh, L. Plucinski, and C. M. Schneider. High resolution, low *hν* photoelectron spectroscopy with the use of a microwave excited rare gas lamp and ionic crystal filters. *Review of Scientific Instruments*, 81:105111, 2010.
- [114] Pika Gospodaric. Laser-based angle-resolved photoemission spectroscopy study of spin-orbit coupling effects on solid state surfaces. Master’s thesis, University of Cologne, 2015.
- [115] S. Suga and A. Sekiyama. *Photoelectron Spectroscopy: Bulk and Surface Electronic Structures*. Springer-Verlag Berlin Heidelberg, 2014.

-
- [116] L. Plucinski, A. Oelsner, F. Matthes, and C.M. Schneider. A hemispherical photoelectron spectrometer with 2-dimensional delay-line detector and integrated spin-polarization analysis. *Journal of Electron Spectroscopy and Related Phenomena*, 181:215–219, 2010.
- [117] J. Krumrain, G. Mussler, S. Borisova, T. Stoica, L. Plucinski, C.M. Schneider, and D. Grützmacher. Mbe growth optimization of topological insulator Bi_2Te_3 films. *Journal of Crystal Growth*, 324:115–118, 2011.
- [118] P. Gehring, B.F. Gao, M. Burghard, and K. Kern. Growth of high-mobility $\text{Bi}_2\text{Te}_2\text{Se}$ nanoplatelets on hbn sheets by van der waals epitaxy. *Nano Letters*, 12:5137–5142, 2012.
- [119] S. Borisova, J. Kampmeier, M. Luysberg, G. Mussler, and D. Grützmacher. Domain formation due to surface steps in topological insulator Bi_2Te_3 thin films grown on si (111) by molecular beam epitaxy. *Applied Physics Letters*, 103:081902, 2013.
- [120] G. Bendt, S. Zastrow, K. Nielsch, P.S. Mandal, J. Sanchez-Barriga, O. Raderc, and S. Schulz. Deposition of topological insulator Sb_2Te_3 films by an mocvd process. *Journal of Materials Chemistry A*, 2:8215, 2014.
- [121] N.V. Tarakina, S. Schreyeck, M. Luysberg, S. Grauer, C. Schumacher, G. Karczewski, K. Brunner, C. Gould, H. Buhmann, R.E. Dunin-Borkowski, and L. W. Molenkamp. Suppressing twin formation in Bi_2Se_3 thin films. *Advanced Materials Interfaces*, 1:1400134, 2014.
- [122] Y. Guo, Z. Liu, and Hailin Peng. A roadmap for controlled production of topological insulator nanostructures and thin films. *Small*, 11:3290–3305, 2015.
- [123] I. Aguilera, C. Friedrich, G. Bihlmayer, and S. Blügel. Gw study of topological insulators Bi_2Se_3 , Bi_2Te_3 , and Sb_2Te_3 : Beyond the perturbative one-shot approach. *Physical Review B*, 88:045206, 2013.
- [124] C. Seibel, H. Bentmann, J. Braun, J. Minár, H. Maaß, K. Sakamoto, M. Arita, K. Shimada, H. Ebert, and F. Reinert. Connection of a topological surface state with the bulk continuum in $\text{Sb}_2\text{Te}_3(0001)$. *Physical Review Letters*, 114:066802, 2015.
- [125] L. Plucinski, A. Herdt, S. Fahrenndorf, G. Bihlmayer, G. Mussler, S. Döhring, J. Kampmeier, F. Matthes, D.E. Bürgler, D. Grützmacher, S. Blügel, and C.M. Schneider. Electronic structure, surface morphology, and topologically protected surface states of Sb_2Te_3 thin films grown on si(111). *Journal of Applied Physics*, 113:053706, 2013.
- [126] H. Aramberri, J.I. Cerda, and M.C. Munoz. Tunable dirac electron and hole self-doping of topological insulators induced by stacking defects. *Nano Letters*, 15:3840–3844, 2015.

- [127] T. Valla, A.V. Fedorov, P.D. Johnson, and S.L. Hulbert. Many-body effects in angle-resolved photoemission: Quasiparticle energy and lifetime of a $\text{mo}(110)$ surface state. *Physical Review Letters*, 83:2085, 1999.
- [128] T. Váczi. A new, simple approximation for the deconvolution of instrumental broadening in spectroscopic band profiles. *Applied Spectroscopy*, 68:1274–1278, 2014.
- [129] T. Cuk, D.H. Lu, X.J. Zhou, Z.-X. Shen, T.P. Devereaux, and N. Nagaosa. A review of electron-phonon coupling seen in the high- T_c superconductors by angle-resolved photoemission studies (arpes). *Physica Status Solidi (b)*, 242:11–29, 2005.
- [130] M. Bianchi, D. Guan, S. Bao, J. Mi, B.B. Iversen, P.D.C. King, and P. Hofmann. Coexistence of the topological state and a two-dimensional electron gas on the surface of Bi_2Se_3 . *Nature Communications*, 1:128, 2010.
- [131] M. Bianchi, R.C. Hatch, J. Mi, B.B. Iversen, and Ph. Hofmann. Simultaneous quantization of bulk conduction and valence states through adsorption of non-magnetic impurities on Bi_2Se_3 . *Physical Review Letters*, 107:086802, 2011.
- [132] P.D.C. King, R.C. Hatch, M. Bianchi, R. Ovsyannikov, C. Lupulescu, G. Landolt, B. Slomski, J.H. Dil, D. Guan, J.L. Mi, E.D.L. Rienks, J. Fink, A. Lindblad, S. Svensson, S. Bao, G. Balakrishnan, B.B. Iversen, J. Osterwalder, W. Eberhardt, F. Baumberger, and Ph. Hofmann. Large tunable rashba spin splitting of a two-dimensional electron gas in Bi_2Se_3 . *Physical Review Letters*, 107:096802, 2011.
- [133] M. Ye, S.V. Eremeev, K. Kuroda, M. Nakatake, S. Kim, Y. Yamada, E.E. Krasovskii, E.V. Chulkov, M. Arita, H. Miyahara, T. Maegawa, K. Okamoto, K. Miyamoto, T. Okuda, K. Shimada, H. Namatame, M. Taniguchi, Y. Ueda, and A. Kimura. Relocation of the topological surface state of Bi_2Se_3 beneath the surface by ag intercalation. arXiv:1112.5869, Dec 2011.
- [134] Z.-H. Zhu, G.. Levy, B. Ludbrook, C.N. Veenstra, J.A. Rosen, R. Comin, D. Wong, P. Dosanjh, A. Ubaldini, P. Syers, N.P. Butch, J. Paglione, I.S. Elfimov, and A. Damascelli. Rashba spin-splitting control at the surface of the topological insulator Bi_2Se_3 . *Physical Review Letters*, 107:186405, 2011.
- [135] M.S. Bahrany, P.D.C. King, A. de la Torre, J. Chang, M. Shi, L. Patthey, G. Balakrishnan, Ph. Hofmann, R. Arita, N. Nagaosa, and F. Baumberger. Emergent quantum confinement at topological insulator surfaces. *Nature Communications*, 3:1159, 2012.
- [136] S.V. Eremeev, T.V. Menshchikova, M.G. Vergniory, and E.V. Chulkov. New interpretation of the origin of 2deg states at the surface of layered topological insulators. arXiv:1107.3208, July 2011.
- [137] T.V. Menshchikovaa, S.V. Eremeeva, and E.V. Chulkov. On the origin of two-dimensional electron gas states at the surface of topological insulators. *JETP Letters*, 94:106–111, 2011.

-
- [138] K. Park, C. De Beule, and B. Partoens. The ageing effect in topological insulators: evolution of the surface electronic structure of Bi_2Se_3 upon k adsorption. *New Journal of Physics*, 15:113031, 2013.
 - [139] N.V. Tarakina, S. Schreyeck, T. Borozenko, C. Schumacher, G. Karyzewski, K. Brunner, C. Gould, H. Buhmann, and L.W. Molenkamp. Comparative study of the microstructure of Bi_2Se_3 thin films grown on si(111) and inp(111) substrates. *Crystal Growth and Design*, 12:1913–1918, 2012.
 - [140] S. Schreyeck, N.V. Tarakina, G. Karczewski, C. Schumacher, T. Borzenko, C. Brüne, H. Buhmann, C. Gould, K. Brunner, and L.W. Molenkamp. Molecular beam epitaxy of high structural quality Bi_2Se_3 on lattice matched inp(111) substrates. *Applied Physics Letters*, 102:041914, 2013.
 - [141] P. Zhang, P. Richard, T. Qian, Y.-M. Xu, X. Dai, , and H. Ding. A precise method for visualizing dispersive features in image plots. *Review of Scientific Instruments*, 82:043712, 2011.
 - [142] L. Fu. Hexagonal warping effects in the surface states of the topological insulator Bi_2Te_3 . *Physical Review Letters*, 103:266801, 2009.
 - [143] Prof. Dr. Rudolf Gross and Dr. Achim Marx. Vorlesungsskript zur vorlesung ‘festkörperphysik’ im ws 1998/1999.
 - [144] Y.L. Chen, J.-H. Chu, J.G. Analytis, Z.K. Liu, K. Igarashi, H.-H. Kuo, X.L. Qi, S.K. Mo, R.G. Moore, D.H. Lu, M. Hashimoto, T. Sasagawa, S.C. Zhang, I.R. Fisher, Z. Hussain, and Z.X. Shen. Massive dirac fermion on the surface of a magnetically doped topological insulator. *Science*, 329:659–662, 2010.
 - [145] M.R. Scholz, J. Sánchez-Barriga, D. Marchenko, A. Varykhalov, A. Volykhov, L.V. Yashina, and O. Rader. Intact dirac cone of Bi_2Te_3 covered with a monolayer fe. *Phys. Status Solidi RRL*, 7:139–141, 2013.
 - [146] Y.S. Hor, P. Roushan, H. Beidenkopf, J. Seo, D. Qu, J.G. Checkelsky, L.A. Wray, D. Hsieh, Y. Xia, S.-Y. Xu, D. Qian, M.Z. Hasan, N.P. Ong, A. Yazdani, and R.J. Cava. Development of ferromagnetism in the doped topological insulator $\text{Bi}_{2-x}\text{Mn}_x\text{Te}_3$. *Physical Review B*, 81:195203, 2010.
 - [147] S.-Y. Xu, M. Neupane, C. Liu, D. Zhang, A. Richardella, L.A. Wray, N. Alidoust, M. Leandersson, T. Balasubramanian, J. Sánchez-Barriga, O. Rader, G. Landolt, B. Slomski, J.H. Dil, J. Osterwalder, T.-R. Chang, H.-T. Jeng, H. Lin, A. Bansil, N. Samarth, and M.Z. Hasan. Hedgehog spin texture and berry’s phase tuning in a magnetic topological insulator. *Nature Physics*, 8:616–622, 2012.
 - [148] J.G. Checkelsky, J. Ye, Y. Onose, Y. Iwasa, and Y. Tokura. Dirac-fermion-mediated ferromagnetism in a topological insulator. *Nature Physics*, 8:729–733, 2012.
 - [149] S. Borisova, J. Krumrain, M. Luysberg, G. Mussler, and D. Grützmacher. Mode of growth of ultrathin topological insulator Bi_2Te_3 films on si(111) substrates. *Crystal Growth & Design*, 12:6098–6103, 2012.

- [150] L. Pauling. *The Nature of the Chemical Bond*, volume 3rd. Cornell University, 1960.
- [151] Ch. Seibel, H. Maaß, M. Ohtaka, S. Fiedler, C.Jünger, C.-H. Min, H. Bentmann, K. Sakamoto, and F. Reinert. Single dirac cone on the cs-covered topological insulator surface Sb_2Te_3 (0001). *Physical Review B*, 86:161105, 2012.
- [152] B. Zhou, Z.K. Liu, J.G. Analytis, K. Igarashi, S.K. Mo, D.H. Lu, R.G. Moore, I.R. Fischer, T. Sasagawa, Z.X. Shen, Z. Hussain, and Y.L. Chen. Controlling the carriers of topological insulators by bulk and surface doping. *Semicond. Sci. Technol.*, 27:124002, 2012.
- [153] L.V. Yashina, J. Sanchez-Barriga, M.R. Scholz, A.A. Volykhov, A.P. Sirotnina, V.S. Neudachina, M.E. Tamm, A. Varykhalov, D. Marchenko, G. Springholz, G. Bauer, A. Knop-Gericke, and O. Rader. Negligible surface reactivity of topological insulators Bi_2Se_3 and Bi_2Te_3 towards oxygen and water. *ACS Nano*, 7:5181–5191, 2013.
- [154] S. Mroczkowski and D. Lichtman. Calculated auger yields and sensitivity factors for *kll* – *noo* transitions with 1-10 kv primary beams. *Journal of Vacuum Science and Technology A*, 3:1860–1865, 1985.
- [155] J. Wang, X. Chen, B.-F. Zhu, and S.-C. Zhang. Topological p-n junction. *Physical Review B*, 85:235131, 2012.
- [156] B. Seradjeh, J. Moore, and M. Franz. Exciton condensation and charge fractionalization in a topological insulator film. *Physical Review Letters*, 103:066402, 2009.
- [157] J. Linder, T. Yokoyama, and A. Sudbø. Anomalous finite size effects on surface states in the topological insulator Bi_2Se_3 . *Phys. Rev. B*, 80:205401, 2009.
- [158] Y. Zhang, K. He, C.-Z. Chang, C.-L. Song, L.-L. Wang, X. Chen, J.-F. Jia, Z. Fang, X. Dai, W.-Y. Shan, S.-Q. Shen, Q. Niu, X.-L. Qi, S.-C. Zhang, X.-C. Ma, and Q.-K. Xue. Crossover of the three-dimensional topological insulator Bi_2Se_3 to the two-dimensional limit. *Nature Physics*, 6:584–588, 2010.
- [159] D. Briggs and M.P. Seah. *Practical Surface Analysis, Auger and X-ray Photoelectron Spectroscopy*. Wiley, 1990.
- [160] Z. Zhang, X. Feng, M. Guo, Y. Ou, J. Zhang, K. Li, L. Wang, X. Chen, Q. Xue, X. Ma, K. He, and Y. Wang. Transport properties of $\text{Sb}_2\text{Te}_3/\text{Bi}_2\text{Te}_3$ topological insulator heterostructures. *physica status solidi (RRL) - Rapid Research Letters*, 7:142–144, 2013.
- [161] F. Stern. Iteration methods for calculating self-consistent fields in semiconductor inversion layers. *Journal of Computational Physics*, 6:56–67, 1970.
- [162] I.A. Nechaev and E.V. Chulkov. Quasiparticle band gap in the topological insulator Bi_2Te_3 . *Phys. Rev. B*, 88:165135, 2013.
- [163] B.Yu. Yavorsky, N.F. Hinsche, I. Mertig, and P. Zahn. Electronic structure and transport anisotropy of Bi_2Te_3 and Sb_2Te_3 . *Phys. Rev. B*, 84:165208, 2011.

- [164] data base at www.ioffe.ru.
- [165] J. Nagao, E. Hatta, and K. Mukasa. Evaluation of metal – Bi_2Te_3 contacts by electron tunneling spectroscopy. *Proceedings of the XV International Conference on Thermoelectrics. Pasadena, CA , USA*, page 404, 1996.
- [166] W. Richter, H. Köhler, and C. Becker. A raman and far-infrared investigation of phonons in the rhombohedral v2-vi3 compounds Bi_2Te_3 , Bi_2Se_3 , Sb_2Te_3 and $\text{Bi}_2(\text{Te}_{1-x}\text{Se}_x)_3$ ($0 < x < 1$), $(\text{Bi}_{1-y}\text{Sb}_y)_2\text{Te}_3$ ($0 < y < 1$). *Phys. Status Solidi (b)*, 84:619, 1977.
- [167] R. Drope. PhD thesis, RWTH Aachen University, 1975.
- [168] B. Skinner and Brian B.I. Shklovskii. Theory of the random potential and conductivity at the surface of a topological insulator. *Physical Review B*, 87:075454, 2013.
- [169] C.-Z. Chang, Z. Zhang, K. Li, X. Feng, J. Zhang, M. Guo, Y. Feng, J. Wang, L.-L. Wang, X.-C. Ma, X. Chen, Y. Wang, K. He, and Q.-K. Xue. Simultaneous electrical-field-effect modulation of both top and bottom dirac surface states of epitaxial thin films of three-dimensional topological insulators. *Nano Letters*, 15:1090–1094, 2015.
- [170] V. Fatemi, B Hunt, H. Steinberg, S. L. Eltinge, F. Mahmood, N. P. Butch, K. Watanabe, T. Taniguchi, N. Gedik, R. C. Ashoori, and P. Jarillo-Herrero. Electrostatic coupling between two surfaces of a topological insulator nanodevice. *Physical Review Letters*, 113:206801, 2014.
- [171] L. Fu and C. Kane. Superconducting proximity effect and majorana fermions at the surfaces of a topological insulator. *Phys. Rev. Lett*, 100, 2008.
- [172] J.-P. Xu, C. Liu, M.-X. Wang, J. Ge, Z.-L. Liu, X. Yang, Y. Chen, Y. Liu, Z.-A. Xu, C.-L. Gao, D. Qian, F.-C. Zhang, and J.-F. Jia. Artificial topological superconductor by the proximity effect. *Physical Review Letters*, 112(217001), 2014.
- [173] L. Fu, C.L. Kane, and E.J. Mele. Topological insulators in three dimensions. *Physical Review Letters*, 98:106803, 2007.
- [174] S. Murakami. Quantum spin hall effect and enhanced magnetic response by spin-orbit coupling. *Physical Review Letters*, 97:236805, 2006.
- [175] M. Wada, S. Murakami, F. Freimuth, and G. Bihlmayer. Localized edge states in two-dimensional topological insulators: Ultrathin bi films. *Physical Review B*, 83:121310, 2011.
- [176] T. Hirahara, G. Bihlmayer, Y. Sakamoto, M. Yamada, H. Miyazaki, S. ichi Kimura, S. Blügel, and S. Hasegawa. Interfacing 2d and 3d topological insulators: $\text{Bi}(111)$ bilayer on Bi_2Te_3 . *Physical Review Letters*, 107:166801, 2011.

- [177] F. Yang, L. Miao, Z. F. Wang, M.-Y. Yao, F. Zhu, Y. R. Song, M.-X. Wang, J.-P. Xu, A. V. Fedorov, Z. Sun, G. B. Zhang, C. Liu, F. Liu, D. Qian, C. L. Gao, and J.-F. Jia. Spatial and energy distribution of topological edge states in single bi(111) bilayer. *Physical Review Letters*, 109:016801, 2012.
- [178] L. Miao, Z. F. Wang, W. Ming, M.-Y. Yao, M. Wang, F. Yang, Y. R. Song, F. Zhu, A. V. Fedorov, Z. Sun, C. L. Gao, C. Liu, Q.-K. Xue, C.-X. Liu, F. Liu, D. Qian, and J.-F. Jia. Quasiparticle dynamics in reshaped helical dirac cone of topological insulators. *PNAS*, 110:2758–2762, 2013.
- [179] H. W. Yeom, S. H. Kim, W. J. Shin, K.-H. Jin, J. Park, T.-H. Kim, J. S. Kim, H. Ishikawa, K. Sakamoto, and S.-H. Jhi. Transforming a surface state of a topological insulator by a bi capping layer. *Physical Review B*, 90:235401, 2014.
- [180] C.-X. Liu, H. Zhang, B. Yan, X.-L. Qi, T. Frauenheim, X. Dai, Z. Fang, and S.-C. Zhang. Oscillatory crossover from two-dimensional to three-dimensional topological insulators. *Physical Review B*, 81:041307, 2010.
- [181] Y.-Y. Li, G. Wang, X.-G. Zhu, M.-H. Liu, C. Ye, X. Chen, Y.-Y. Wang, K. He, L.-L. Wang, X.-C. Ma, H.-J. Zhang, X. Dai, Z. Fang, X.-C. Xie, Y. Liu, X.-L. Qi, J.-F. Jia, S.-C. Zhang, and Q.-K. Xue. Intrinsic topological insulator Bi_2Te_3 thin films on si and their thickness limit. *Advanced Materials*, 22:4002–4007, 2010.
- [182] Y. Sakamoto, T. Hirahara, H. Miyazaki, S. Kimura, and S. Hasegawa. Spectroscopic evidence of a topological quantum phase transition in ultrathin Bi_2Se_3 films. *Physical Review B*, 81:165432, 2010.
- [183] Yang Liu, Guang Bian, T. Miller, M. Bissen, and T.-C. Chiang. Topological limit of ultrathin quasi-free-standing Bi_2Te_3 films grown on si(111). *Physical Review B*, 85:195442, 2012.
- [184] Q. D. Gibson, L. M. Schoop, A. P. Weber, H. Ji, S. Nadj-Perge, I. K. Drozdov, H. Beidenkopf, J. T. Sadowski, A. Fedorov, A. Yazdani, T. Valla, and R. J. Cava. Termination-dependent topological surface states of the natural superlattice phase Bi_4Se_3 . *Physical Review B*, 88:081108, 2013.
- [185] J. C. Johannsen, G. Autes, A. Crepaldi, S. Moser, B. Casarin, F. Cilento, M. Zaccagna, H. Berger, A. Magrez, Ph. Bugnon, J. Avila, M. C. Asensio, F. Parmigiani, O. V. Yazyev, and M. Grioni. Engineering the topological surface states in the $(\text{Sb}_2)_m - \text{Sb}_2\text{Te}_3$ superlattice series. *Physical Review B*, 91:201101, 2015.
- [186] M.S. Christian, S.R. Whittleton, A. Otero de-la Roza, and E. Johnson. Chemical bonding and surface interactions in Bi_2Se_3 and Bi_4Se_3 . *Computational and Theoretical Chemistry*, 1053:238–244, 2015.
- [187] A. Isaeva, B. Rasche, and M. Ruck. Bismuth-based candidates for topological insulators: Chemistry beyond Bi_2Te_3 . *Physical Status Solidi PRL*, 7:39–49, 2013.
- [188] H. Lind and S. Lidin. A general structure model for bi-se phases using a super-space formalism. *Solid State Sciences*, 5:47–57, 2003.

-
- [189] J.W.G. Bos, H.W. Zandbergen, M.-H. Lee, N.P. Ong, and R.J. Cava. Structures and thermoelectric properties of the infinitely adaptive series $(\text{Bi}_2)_m(\text{Bi}_2\text{Te}_3)_n$. *Physical Review B*, 75:195203, 2007.
- [190] P. Bayliss. Crystal chemistry and crystallography of some minerals in the tetradymite group. *Am. Mineral*, 76:257–265, 1991.
- [191] National Physical Laboratory. Database of sputtering yields.
- [192] G. Kresse and J. Furthmüller. *Comput. Mater. Sci.*, 6:15, 1996.
- [193] G. Kresse and J. Furthmüller. *Physical Review B*, 54:11169, 1996.
- [194] J.P. Perdew, K. Burke, and M. Ernzerhof. Generalized gradient approximation made simple. *Physical Review Letters*, 77:3865, 1996.
- [195] Y.M. Koroteev, G. Bihlmayer, E.V. Chulkov, and S. Blügel. *Physical Review B*, 77:045428, First-principle investigation of structural and electronic properties of ultrathin Bi films 2008.
- [196] B. Schmidt and K. Wetzig. *Ion Beams in Materials Processing and Analysis*. Springer Science & Business Media, 2012.
- [197] C. Jeynes, N.P. Barradas, and E. Szilágyi. Accurate determination of quantity of material in thin films by rutherford backscattering spectrometry. *Analytical Chemistry*, 84:6061–6069, 2012.
- [198] G. Mussler. Vorlesungsskript röntgendiffraktometrie.
- [199] Y. Tanaka, Z. Ren, T. Sato, K. Nakayama, S. Souma, T. Takahashi, K. Segawa, and Y. Ando. Experimental realization of a topological crystalline insulator in snTe. *Nature Physics*, 8(800), 2012.
- [200] Y. Ando and L. Fu. Topological cryscystal insulators and topological superconductors: From concepts to materials. *ArXiv:1501.00531v1*, 2015.
- [201] M.R. Scholz, J. Sanchez-Barriga, J. Braun, D. Marchenko, A. Varykhalov, M. Lindroos, Y.J. Wang, H. Lin, A. Bansil, J. Minar, H. Ebert, A. Volykhov, L.V. Yashina, and O. Rader. Reversal of the circular dichroism in angle-resolved photoemission from Bi_2Te_3 . *Physical Review Letters*, 110:216801, 2013.

List of publications (in chronological order)

Articles

- A.1 P. Olbrich, L.E. Golub, T. Herrmann, S.N. Danilov, H. Plank, V.V. Bel'kov, G. Mussler, Ch. Weyrich, C.M. Schneider, J. Kampmeier, D. Grützmacher, L. Plucinski, **M. Eschbach**, & S.D. Ganichev. Room-Temperature High-Frequency Transport of Dirac Fermions in Epitaxially Grown Sb₂Te₃- and Bi₂Te₃-Based Topological Insulators. *Physical Review Letters* **113**, 096601 (2014)
- A.2 C. Pauly, B. Rasche, K. Koepernik, M. Liebmann, M. Pratzer, M. Richter, J. Kellner, **M. Eschbach**, B. Kaufmann, L. Plucinski, C.M. Schneider, M. Ruck, J. van den Brink, & M. Morgenstern. Subnanometre-wide electron channels protected by topology. *Nature Physics* **11**, 338-343 (2015)
- A.3 **M. Eschbach**, E. Młyńczak, J. Kellner, J. Kampmeier, M. Lanius, E. Neumann, C. Weyrich, M. Gehlmann, P. Gospodarič, S. Döring, G. Mussler, N. Demarina, M. Luysberg, G. Bihlmayer, Th. Schäpers, L. Plucinski, S. Blügel, M. Morgenstern, C. M. Schneider, & D. Grützmacher. Realization of a vertical topological p-n junction in epitaxial Sb₂Te₃/Bi₂Te₃ heterostructures. *Nature Communications* **6**, 8816 (2015)
- A.4 M. Gehlmann, G. Bihlmayer, I. Aguilera, E. Młyńczak, **M. Eschbach**, S. Döring, P. Gospodarič, S. Cramm, B. Kardynal, L. Plucinski, S. Blügel, & C.M. Schneider. Quasi 2D electronic states with high spin-polarization in centrosymmetric MoS₂ bulk crystals. Accepted at: *Scientific Reports* (2015). Preprint: <http://arxiv.org/abs/1510.04101>
- A.5 J. Kellner, **M. Eschbach**, J. Kampmeier, M. Lanius, E. Młyńczak, G. Mussler, B. Holländer, L. Plucinski, M. Liebmann, D. Grützmacher, C.M. Schneider, & M. Morgenstern, Tuning the Dirac point to the Fermi level in the ternary topological insulator (Bi_{1-x}Sb_x)₂Te₃. *Applied Physics Letters* **107**, 251603 (2015).
- A.6 C. Weyrich, M. Drögeler, J. Kampmeier, **M. Eschbach**, G. Mussler, T. Merzenich, T. Stoica, I. Batov, J. Schubert, L. Plucinski, B. Beschoten, C.M. Schneider, C. Stampfer, D. Grützmacher, & T. Schäpers. Growth, characterization, and transport properties of ternary (Bi_{1-x}Sb_x)₂Te₃ topological insula-

tor layers. Submitted to: *Physical Review B* (2015).
Preprint: <http://arxiv.org/abs/1511.00965>

- A.7 H. Plank, L.E. Golub, S. Bauer, V.V. Bel'kov, T. Herrmann, P. Olbrich, **M. Eschbach**, L. Plucinski, J. Kampmeier, M. Lanius, G. Mussler, D. Grützmacher, & S.D. Ganichev. Photon Drag Effect in $(\text{Bi}_{1-x}\text{Sb}_x)_2\text{Te}_3$ Three-Dimensional Topological Insulators. Submitted to: *Physical Review X* (2015). Preprint: <http://arxiv.org/pdf/1512.07078v1.pdf>
- A.8 **M. Eschbach**, M. Lanius, E. Młyńczak, J. Kellner, C. Niu, P. Schüffegen, M. Gehlmann, P. Gospodarič, V. Heß, S. Königshofen, S. Döring, E. Neumann, M. Luysberg, B. Holländer, F. Matthes, G. Mussler, G. Bihlmayer, S. Blügel, D. Bürgler, M. Morgenstern, D. Grützmacher, L. Plucinski, & C.M. Schneider. Bi_1Te_1 : A dual topological insulator. Submitted to: *Nature Communications*. (2016) Preprint: <https://arxiv.org/abs/1604.08886>
- A.9 E. Młyńczak, **M. Eschbach**, S. Borek, J. Minár, I. Aguilera, G. Bihlmayer, S. Döring, M. Gehlmann, P. Gospodarič, S. Suga, L. Plucinski, S. Blügel, H. Ebert, & C.M. Schneider. Fermi surface manipulation by means of remanent magnetization by external magnetic field for a prototypical thin film ferromagnet. Submitted to: *Physical Review X* (2016)

Talks

- B.1 Epitaxial $\text{Sb}_2\text{Te}_3/\text{Bi}_2\text{Te}_3$ heterostructures: a new (route to) topological p-n junction. *VITI-Spinograph school, Aachen, Germany* (2014)
- B.2 Realization of a vertical topological p-n junction in epitaxial $\text{Sb}_2\text{Te}_3/\text{Bi}_2\text{Te}_3$ heterostructures. *DPG spring meeting, Berlin, Germany* (2015)
- B.3 Angle-resolved Photoemission Spectroscopy on 3D Topological Insulators. *Virtual Institute for Topological Insulators & Elitenetzwerk Bayern spring meeting, Mauterndorf, Austria* (2015)

Poster contributions

- C.1 Sb_2Te_3 ultrathin films on Si(111): magnetic surface doping and circular dichroism compared to spin-polarization in ARPES. *DPG spring meeting, Dresden, Germany* (2014)
- C.2 Epitaxial $\text{Sb}_2\text{Te}_3/\text{Bi}_2\text{Te}_3$ heterostructures: a new (route to) topological p-n junction. *Workshop on New Trends in Topological Insulators, Berlin, Germany* (2014)

Curriculum Vitae

Personal Data

Name	Markus Eschbach
Adress	Bahnhofstraße 18 52064 Aachen
E-Mail	eschbach.markus@googlemail.com
Birthday	07.02.1987
Birthplace	Lindlar
Nationality	German

Education

02/2013 - 02/2016	Ph.D. work at PGI-6, Forschungszentrum Jülich on Band Structure Engineering in 3D Topological Insulators by Angle-Resolved Photoemission Spectroscopy
11/2011 - 12/2012	Masters Thesis at PGI-6, Forschungszentrum Jülich on Magnetic Circular Dichroism in Laser-induced Threshold Photoemission Electron Microscopy
11/2010 - 12/2012	Master of Science in Physics at RWTH Aachen
07/2007 - 10/2010	Bachelor of Science in Physics at RWTH Aachen
07/1997 - 05/2006	Abitur at Engelbert-von-Berg Gymnasium Wipperfürth
07/1993 - 06/1997	Primary school in Lindlar

Danksagung

An dieser Stelle möchte ich mich bei einigen Menschen bedanken, ohne die diese Arbeit niemals zustande gekommen wäre und denen ich viel verdanke.

Zunächst möchte ich mich bei meinem Doktorvater **Prof. Claus M. Schneider** recht herzlich bedanken, der mir seit nun bereits 4 Jahren - inklusive meiner Masterarbeit - die Möglichkeit bietet mich im PGI-6 zu entfalten und zu verwirklichen. Insbesondere dank der Freiheit und der experimentellen Möglichkeiten, die er den Wissenschaftlern bietet, konnte ich hier sehr viel lernen!

Des Weiteren möchte ich **Prof. Markus Morgenstern** von der RWTH Aachen dafür danken, dass er meine Arbeit als Zweitgutachter bewertet.

My heartfelt and sincere thanks goes to the **photoemission group!**

Dr. Lukasz Plucinski is the best experimental scientist and one of the most special minds that I ever got to know closer. Although your way of teaching was not always immediately obvious for me, I learned and gained a lot in the time working together with you and I will always miss our debates and your extraordinary character. I salute your passion and commitment to everything you start working on!

Further, I want to express my sincere gratefulness to **Dr. Ewa Młyńczak**, who, after she joined our group two years ago, quickly became my first reference person whenever Lukasz was not available. Thank you very much for being my 'big sister'. I really enjoyed working and discussing with you!

Moreover, I deeply thank **Pika Gospodarič** (my small sister), **Mathias Gehlmann** and **Dr. Sven Döring** for the great and fruitful teamwork, the countless discussions and the shared beamtimes in the lab as well as at the synchrotrons! I wish all of you only the best and that all of your future plans and objectives may become true!

Ohne die permanente Unterstützung von technischer Seite, hätte ich in den vergangenen 3 Jahren wohl sicher kein einziges Spektrum gemessen.

Dafür danke an erster Stelle **Bernd Küpper!** Alles was ich über Vakuumtechnologie, eine konzeptionelle Herangehensweise an technische Aufgabenstellungen und nicht zuletzt "Maschinenästhetik" weiß, habe ich von dir gelernt. Neben deiner schnellen und professionellen Hilfe, weiß ich zu schätzen, dass du mich charakterlich durch gelegentliche Konfrontationen und Dispute gestärkt und geformt hast. Danke dafür!

Gleichermaßen möchte ich mich auch bei **Jürgen Lauer, Arnd Bremen, Heinz Pfeiffer**

sowie **Thomas Jansen** für ihre kompetente Hilfe bei allen technischen und elektronischen Problemen bedanken.

Ein wichtiger Faktor der zum Gelingen dieser Arbeit beigetragen hat, waren die großartigen Proben, die in dieser Arbeit untersucht wurden. Zum größten Teil waren dies MBE-gewachsene Dünnschichtproben, die von **Jörn Kampmeier** und später **Martin Lanius**, mit Unterstützung von **Peter Schüffegen** und unter der Regie von **Dr. Gregor Mussler** und **Prof. Detlev Grützmacher** hergestellt worden sind. Vielen Dank für die fantastischen Proben und die erfolgreiche Zusammenarbeit!

Außerdem möchte ich die Charakterisierung mittels elektronischer Transport-Messungen von **Christian Weyrich** und **Prof. Thomas Schäpers** dankend hervorheben.

Weitere unbezahlbare strukturelle Untersuchungen wurden von **Dr. Martina Luysberg** mit Vorarbeit von **Martin Lanius** und **Dr. Elmar Neumann** an einem der weltbesten Transmissionselektronenmikroskope durchgeführt.

Auch bei **Dr. Steffen Schreyeck** möchte ich mich für die besten Bi_2Se_3 Proben bedanken.

Einen enormen Beitrag zum Erfolg meiner Arbeit haben **Dr. Gustav Bihlmayer**, einer der führenden Wissenschaftler auf dem Gebiet der topologischen Isolatoren, sowie seine Kollegen **Dr. Irene Aguilera**, **Dr. Chengwang Niu** und **Prof. Stefan Blügel**. Es war mir eine Ehre mit euch zusammenarbeiten zu dürfen und von euch (ein paar) Einblicke in die theoretische Festkörperphysik und die DFT zu bekommen.

Die enge Zusammenarbeit mit **Jens Kellner** und der AG von **Prof. Markus Morgenstern** im Allgemeinen war eine der wissenschaftlich ergiebigsten und produktivsten. Vielen Dank für alle Diskussionen und gemeinsamen Messungen!

Luckily, I was able to go to the ELETTRA synchrotron in Trieste several times as well as to DIAMOND in Oxford during my PhD, where I could gather invaluable experiences with different experimental setups, synchrotron radiation beamlines and had the chance to look into various scientific topics beyond my own research. During those beamtimes we were supported by **Giovanni Zamborlini**, **Dr. Vitaliy Feyer** and **Dr. Slavomir Nemsak**. Thank you very much for the great time!.

Also, I would like to acknowledge the collaboration, discussions and experiences with the great and world-famous scientists **Prof. Shigemasa Suga**, **Prof. Chuck Fadley** and **Prof. Hans Lüth**.

For proofreading of this thesis I gratefully thank Lukasz, Ewa, Pika, Mathias, Moritz, Christoph, as well as my uncle, **Konrad Eschbach**.

Last but not least, möchte ich meinen thematisch (und auch sonst) am nahestehenden Kollegen **Christoph Schmitz** und **Moritz Plötzing** danken, dass ich sowohl wis-

senschaftlich als auch darüber hinaus mit euch diskutieren konnte und ihr mir immer gute Freunde wart!

Außerdem gilt mein Dank allen anderen Kollegen des PGI-6 und Freunden aus der **“the-one-and-only-Kaffeerunde”**, **Marten Patt, Christian Weier, Michael Schnee, Fabian Fritz, Dr. Sarah Fahrendorf, Volkmar Heß, Timm Gerber, Dr. Roman Adam, Dr. Robert Frielinghaus, Moritz von Witzleben, Eugen Michel, Daniel Simon** sowie **Dr. Carsten Wiemann**.

Abschließend möchte ich mich von ganzem Herzen bei **meinen Eltern** und meiner Familie bedanken, denen ich einfach alles zu verdanken habe und die mich immer bei allem unterstützt haben. Ich kann nicht ansatzweise beschreiben wie großartig es ist euer Sohn zu sein. Vielen Dank!

Keine Worte dieser Welt reichen aus, um meiner Verlobten **Julia** genug für ihre Unterstützung und Liebe zu danken. Ich denke ein Satz, den sie mir einmal mitgab, beschreibt die Kraft, die sie mir gibt, sehr gut: “Always believe in yourself, have dedication and pride, have faith in your abilities and let my love for you be your motivation and support.”

Vielen Dank für Alles!

Band / Volume 112

Silicon nanowire structures for neuronal cell interfacing

S. Pud (2015), 153 pp

ISBN: 978-3-95806-089-0

Band / Volume 113

Memristive Phenomena –

From Fundamental Physics to Neuromorphic Computing

Lecture Notes of the 47th IFF Spring School 2016

22 February – 04 March 2016, Jülich, Germany

ed. by R. Waser and M. Wuttig (2016), ca 1000 pp

ISBN: 978-3-95806-091-3

Band / Volume 114

**Single-Cell Analysis of Microbial Production Strains
in Microfluidic Bioreactors**

A. M. Grünberger (2015), XIX, 225 pp

ISBN: 978-3-95806-092-0

Band / Volume 115

**Magnetic order and spin dynamics in the
extended kagome system $\text{CaBaCo}_2\text{Fe}_2\text{O}_7$**

J. Reim (2015), viii, 144 pp

ISBN: 978-3-95806-097-5

Band / Volume 116

**Structural and electronic investigations on homo- and hetero-organic
layers involving CuPc on silver single crystal surfaces**

K. M. Schönauer (2015), x, 148 pp

ISBN: 978-3-95806-112-5

Band / Volume 117

**First-principles investigation of inelastic magnetic excitations
in nanostructures deposited on surfaces**

B. J. Schweflinghaus (2016), v, 204 pp

ISBN: 978-3-95806-115-6

Band / Volume 118

Magnetic, structural, and electronic properties of NiFe_2O_4 ultrathin films

M. Hoppe (2016), vii, 118 pp

ISBN: 978-3-95806-122-4

Band / Volume 119

First-principle investigation of displacive response in complex solids

D. A. Klüppelberg (2016), xi, 179 pp

ISBN: 978-3-95806-123-1

Band / Volume 120

**Beam Cooling at COSY and HESR – Theory and Simulation –
Part 1 Theory**

H. Stockhorst, T. Katayama and R. Maier (2016), v, 192 pp

ISBN: 978-3-95806-127-9

Band / Volume 121

**Scanning tunneling microscopy of single-molecule magnets and hybrid-
molecular magnets: Two approaches to molecular spintronics**

V. Heß (2016), x, 127 pp

ISBN: 978-3-95806-128-6

Band / Volume 122

**Bulk and surface sensitive energy-filtered photoemission microscopy
using synchrotron radiation for the study of resistive switching memories**

M. C. Patt (2016), viii, 247 pp

ISBN: 978-3-95806-130-9

Band / Volume 123

Group IV Epitaxy for Advanced Nano- and Optoelectronic Applications

S. Wirths (2016), vi, 116, XXX pp

ISBN: 978-3-95806-132-3

Band / Volume 124

**Strained Silicon-Germanium/Silicon Heterostructure Tunnel FETs
for Low Power Applications**

S. Blaeser (2016), iv, 91, xvii pp

ISBN: 978-3-95806-135-4

Band / Volume 125

**Nanocavity Arrays for Extracellular Recording and Stimulation of
Electroactive Cell Systems**

A. Czeschik (2016), x, 162 pp

ISBN: 978-3-95806-144-6

Band / Volume 126

**Band Structure Engineering in 3D Topological Insulators Investigated
by Angle-Resolved Photoemission Spectroscopy**

M. Eschbach (2016), VIII, 153 pp

ISBN: 978-3-95806-149-1

Schlüsseltechnologien /
Key Technologies
Band / Volume 126
ISBN 978-3-95806-149-1

